



Dissertation

Zunhao Wang

Surface-Controlled Adsorption of Plasmonic DNA Origami Nanostructures for Single-Molecule Surface-Enhanced Raman Spectroscopy (SERS)

DOI 10.7795/110.20240208

ISSN 2941-1297

ISBN 978-3-944659-31-2

Physikalisch-Technische Bundesanstalt

Dissertationen

PTB-Diss-3

Braunschweig, Januar 2024

Zunhao Wang

Surface-Controlled Adsorption of Plasmonic DNA Origami Nanostructures for Single-Molecule Surface-Enhanced Raman Spectroscopy (SERS)

DOI 10.7795/110.20240208

ISSN 2941-1297

ISBN 978-3-944659-31-2

Empfohlene Zitierweise/recommended citation

Wang, Z., 2024. *Surface-Controlled Adsorption of Plasmonic DNA Origami Nanostructures for Single-Molecule Surface-Enhanced Raman Spectroscopy (SERS)*.

Dissertation, Technische Universität Braunschweig.

Braunschweig: Physikalisch-Technische Bundesanstalt.

PTB-Bericht Diss-3. ISBN 978-3-944659-31-2.

Verfügbar unter: <https://doi.org/10.7795/110.20240208>

Herausgeber:

Physikalisch-Technische Bundesanstalt

ISNI: 0000 0001 2186 1887

Presse und Öffentlichkeitsarbeit

Bundesallee 100

38116 Braunschweig

Telefon: (05 31) 592-93 21

Telefax: (05 31) 592-92 92

www.ptb.de

Surface-Controlled Adsorption of Plasmonic DNA Origami Nanostructures for Single-Molecule Surface-Enhanced Raman Spectroscopy (SERS)

Von der Fakultät für Lebenswissenschaften

der Technischen Universität Carolo-Wilhelmina zu Braunschweig

zur Erlangung des Grades

eines Doktors der Naturwissenschaften

(Dr. rer. nat.)

genehmigte

D i s s e r t a t i o n

von Zunhao Wang
aus Heilongjiang / China

1. Referent: Professor Dr. Christoph R. Jacob
2. Referent: Professor Dr. Ilko Bald
eingereicht am: 04.09.2023
mündliche Prüfung (Disputation) am: 13.12.2023

Druckjahr 2024

Dissertation an der Technischen Universität Braunschweig,
Fakultät für Lebenswissenschaften

Vorveröffentlichungen der Dissertation

Teilergebnisse aus dieser Arbeit wurden mit Genehmigung der Fakultät für Lebenswissenschaften, vertreten durch den Mentor der Arbeit, in folgenden Beiträgen vorab veröffentlicht:

Publikationen

Wang, Z., Liu, Z., Dempwolf, W., Molle, J., Kanehira, Y., Kogikoski Jr, S., Etzkorn, M., Bald, I., Stosch, R., Wundrack, S.: Surface Enhanced Raman Spectroscopy on Selective Adsorbed Plasmonic Nanostructures Using Polar Surface Arrays. *ACS Appl. Nano Mater.* **6** (16), 14645-14655 (2023), DOI: 10.1021/acsanm.3c01776.

Liu, Z., **Wang, Z.**, Guckel, J., Park, D., Lalkens, B., Stosch, R., Etzkorn, M.: Positional Control of DNA Origami based Gold Dimer Hybrid Nanostructures on Pre-Structured Surfaces. *Nanotechnology* **34** 425301 (2023), DOI: 10.1088/1361-6528/ace726.

Tagungsbeiträge

Wang, Z., Liu, Z., Molle, J., Wundrack, S., Etzkorn, M., Stosch, R.: Improving single-molecule detection: Polar surface array for controlling the adsorption of plasmonic DNA origami nanostructures. (Talk)

DNA Nanotechnology 2022, Jena (2022).

Wang, Z., Liu, Z., Molle, J., Wundrack, S., Etzkorn, M., Stosch, R.: Surface-controlled adsorption of plasmonic DNA origami nanostructures for single-molecule detection using polar surface array substrates. (Talk)

27th International Workshop on “Single Molecule Spectroscopy and Super-resolution Microscopy”, Berlin (2022).

Posterbeiträge

Wang, Z., Molle, J., Wundrack, S., Stosch, R.: Toward single molecule detection: surface enhanced Raman spectroscopy (SERS) of biological markers on DNA Nanobreadboards. B-IGSM Metrological Summer School “Perspectives of Modern Metrology”, Online (2021).

Wang, Z., Molle, J., Wundrack, S., Stosch, R.: Toward single molecule detection: surface enhanced Raman spectroscopy (SERS) of biological markers on DNA Nanobreadboards. 26th International Workshop on “Single Molecule Spectroscopy and Super-resolution Microscopy”, Berlin (2021).

Wang, Z., Molle, J., Wundrack, S., Stosch, R.: Toward single molecule detection: surface enhanced Raman spectroscopy (SERS) of biological markers on DNA Nanobreadboards. International Symposium on Nanometrology 2021, Online (2021).

Wang, Z., Liu, Z., Wundrack, Molle, J., S., Etzkorn, M., Stosch, R.: Controlling the selective adsorption of plasmonic DNA origami nanostructures using polar surface arrays. B-IGSM Summer School of Metrology “Robust Precision Experiments”, Ilseburg (2022).

Wang, Z., Liu, Z., Molle, J., Wundrack, S., Etzkorn, M., Stosch, R.: Surface-controlled adsorption of plasmonic DNA origami nanostructures for single-molecule detection using polar surface array substrates.

18th Confocal Raman Imaging Symposium, Ulm (2022).

Wang, Z., Liu, Z., Kogikoski, S., Bald, I., Stosch, R., Wundrack, S.: Controlling the selective adsorption of plasmonic DNA origami nanostructures using polar surface arrays. Molecular Plasmonics 2023, Jena (2023).

Table of Contents

Abstract	III
Zusammenfassung	IV
List of Abbreviation	V
1. Introduction	1
2. Theoretical Background	6
2.1. Raman Scattering Effect	6
2.2. Single-Molecule Raman Experiments.....	10
2.3. Optical Properties and Plasmonic Effect of Metallic Nanoparticles	11
2.4. Surface-Enhanced Raman Scattering Effect.....	16
2.5. Density Functional Theory.....	20
2.6. Finite-Difference Time-Domain Method	23
2.7. The Principle of DNA-Origami.....	24
3. Materials and Methods	26
3.1. DNA Origami Design and Synthesis.....	27
3.2. AuNP-DNA Origami Hybridization.....	29
3.3. Purification of DNA Origami and Hybrid Nanostructure.....	30
3.4. EBL Fabrication of PSA and Nanostructure Adsorption.....	32
3.5. Sample Storage and Preparation for Measurements.....	35
3.6. Characterization Methods.....	37
4. Plasmonic AuNP-DNA-Origami Hybrid Nanostructure	39
4.1. DFT Analysis of Potential Raman Marker Candidate	39
4.2. FDTD Simulation of Hybrid Nanostructures.....	41
4.3. Hybrid Nanostructure Design and Characterization	43
4.4. Correlated AFM/SERS Measurement	49
5. Controlled Adsorption of Hybrid Nanostructures on PSA	55
5.1. Selective Adsorption on a Substrate.....	56
5.2. DFT Simulation of DNA Origami Adsorption on PSA.....	61
5.3. Surface Characterization of the Polar Surface Array	67

5.4. Single Hybrid Nanostructure Isolation on PSA.....	69
5.4.1. Tuning the PSA Field Size	69
5.4.2. Hybrid Nanostructure Concentration Variation	70
5.4.3. Incubation Time	74
5.4.4. Mg Ion Concentration.....	75
5.5. SERS from a Single Hybrid Nanostructure.....	76
5.6. Isotope Dilution SERS with DTNB at Single-Molecule Level	81
6. Summary and Outlook.....	90
References	92
Appendix.....	99
A1: Design of the Rectangular DNA Origami	99
A2: Estimation of Maximum TNB Molecules on an Au DONA	103
A3: List of Atoms in the Bader Charge Analysis.....	105
A4: Single Molecule Detection with Star DONAs.....	108
A5: Time Series of ¹⁴ N-TNB and ¹⁵ N-TNB coated Au DONA.....	109
Acknowledgments	111
Curriculum Vitae.....	113

Abstract

The quantitative detection of biomolecules, such as proteins and peptides, at low concentration levels plays a crucial role in facilitating early diagnosis and monitoring of prevalent diseases. Given the increasing utilization of metrological quantification in life sciences and the mandatory quality assurance requirements in routine laboratories, the need for SI-traceable methods to quantify such biomarkers has become urgent.

This thesis aims to investigate the quantification of substances at the single-molecule level using Surface-enhanced Raman Spectroscopy (SERS), with a specific focus on employing the Polar Surface Array (PSA) as a selective-adsorbing substrate for single-molecule studies. The primary objective is to overcome the challenges associated with nanostructure agglomeration and establish a reliable and efficient SERS-based method for the detection and quantification of individual molecules.

The results in this thesis involve the preparation of DNA origami-based hybrid nanostructures, the fabrication of the PSA using electron beam lithography, and the subsequent selective adsorption of hybrid nanostructures onto the PSA. The SERS technique, combined with Atomic Force Microscopy, was employed to quantify substances at the single-molecule level. Key findings include the successful isolation and identification of single hybrid nanostructures on the PSA. Moreover, this research introduces the application of the isotope dilution method at the single-molecule level by verifying and quantifying the isotopologue of molecules through the utilization of SERS in conjunction with the PSA.

This research presents a pioneering approach for the quantification of single molecules through SERS on an adsorption-controlled and tuneable substrate. By overcoming the challenge of nanostructure agglomeration, the PSA provides a highly effective and reliable platform for quantification of molecules at extremely low concentrations, and studying the over-time dynamics of single plasmonic hot spots. Furthermore, the research sheds light on the principles and benefits of SERS for single-molecule analysis, thus highlighting its specificity and its potential, in combination with the isotope dilution method, for metrological molecular quantification.

Zusammenfassung

Die quantitative Detektion von Biomolekülen wie Proteinen und Peptiden in geringen Konzentrationen spielt eine entscheidende Rolle bei der Früherkennung und Überwachung von Krankheiten. Angesichts der zunehmenden Anwendung metrologischer Quantifizierungsmethoden in den Lebenswissenschaften sowie der gesetzlich vorgeschriebenen Qualitätssicherungsanforderungen in der Routinelabor besteht ein dringender Bedarf an SI-rückführbaren Methoden zur Quantifizierung solcher Biomarker.

Das Ziel dieser Arbeit ist die Untersuchung der Quantifizierung von Substanzen auf Einzelmolekülebene mithilfe der oberflächenverstärkten Raman-Spektroskopie (SERS) und insbesondere die Verwendung des Polar Surface Arrays (PSA) als selektiv adsorbierendes Substrat für Einzelmolekülstudien. Das Hauptziel besteht darin, die mit der Agglomeration von Nanostrukturen verbundenen Herausforderungen zu überwinden und eine zuverlässige und effiziente SERS-basierte Methode zur Detektion und Quantifizierung einzelner Moleküle zu etablieren.

Die Ergebnisse dieser Arbeit umfassen die Herstellung von DNA-Origami-basierten hybriden Nanostrukturen, die Herstellung des PSA mittels Elektronenstrahlithografie und die anschließende selektive Adsorption hybrider Nanostrukturen auf dem PSA. Die SERS-Technik in Kombination mit der Rasterkraftmikroskopie wurde zur Quantifizierung von Substanzen auf Einzelmolekülebene verwendet. Wesentliche Ergebnisse umfassen die erfolgreiche Isolierung und Identifizierung einzelner hybrider Nanostrukturen auf dem PSA. Darüber hinaus führt diese Arbeit die Anwendung der Isotopenverdünnungsmethode auf Einzelmolekülebene ein, indem die Isotopologe von Molekülen durch die Verwendung von SERS in Verbindung mit dem PSA verifiziert und quantifiziert werden.

Diese Arbeit präsentiert einen wegweisenden Ansatz zur Quantifizierung einzelner Moleküle mittels SERS auf einem adsorptionsgesteuerten und einstellbaren Substrat. Durch Überwindung der Herausforderung wie Agglomeration von Nanostrukturen bietet das PSA eine äußerst effektive und zuverlässige Plattform zur Quantifizierung von Molekülen in extrem niedrigen Konzentrationen sowie zur Untersuchung der zeitlichen Entwicklung von einzelnen plasmonischen Hot Spots. Darüber hinaus wirft die Forschung Licht auf die Prinzipien und Vorteile von SERS für die Einzelmolekülanalyse und betont dessen Spezifität und Potenzial in Kombination mit der Isotopenverdünnungsmethode zur metrologischen molekularen Quantifizierung.

List of Abbreviation

AFM	Atomic Force Microscopy
AuNP	Gold nanoparticle
BEM	Boundary Element Method
BSPP	Bis(p-sulfonatophenyl)phenylphosphine dihydrate dipotassium
CCD	Charge-coupled devices
CDD	Charge density difference
CGPM	General Conference of Weights and Measures (English)
	Conférence générale des poids et mesures (French)
DFT	Density functional theory
DNA	Deoxyribonucleic acid
DONA	DNA nanofork antenna
DTNB	Dithionitrobenzoic acid
EBL	Electron beam lithography
EF	Enhancement factor
EM	Electromagnetism
FDTD	Finite-difference time-domain
FIB	Focus Ion Beam
hGH	Human growth hormone
HMDS	Hexamethyldisilazane
ID	Isotope dilution
LSP	Localized surface plasmon
LSPR	Localized surface plasmon resonance
M_w	Molecular weight
NA	Numerical aperture
NMP	N-Methyl-2-pyrrolidone
NRO	New rectangular origami
PSA	Polar Surface Array
PVD	Physical vapor deposition
SEM	Scanning electron microscopy
SERS	Surface-enhanced Raman spectroscopy

	International System of Units (English)
SI	Système international d'unités (French)
TAMRA	5-Carboxytetramethylrhodamine
TERS	Tip-Enhanced Raman Spectroscopy
TMP	Thymidine monophosphate
TNB	2-Nitro-5-thiobenzoic acid
T-SEM	Transmission scanning electron microscopy
Tween 20	Polyoxyethylene (20) sorbitan monolaurate
UCSF	University of California, San Francisco
	International Vocabulary of Metrology (English)
VIM	Vocabulaire international de métrologie (French)
wt.%	Percentage by mass

1. Introduction

Accurate measurement and quantification play a crucial role in scientific research and various disciplines of metrology. The ability to precisely determine the quantities of substances enables advancements in fields such as chemistry, biology, nanotechnology, and materials science. In recent years, there has been a significant focus on molecule quantification at the single-molecule level, leading to a deeper understanding of molecular behavior and enabling an unprecedented level of detection limit. This introduction chapter will highlight the significance of the SI unit “mol” and the increasing importance of counting-based measurement in scientific research and metrology. Furthermore, this chapter will delve into the concept and methodologies of quantifying individual molecules, with specific emphasis placed on spectroscopic techniques like surface-Enhanced Raman Spectroscopy (SERS).

Metrology and the Redefinition of SI Units

“To measure is to know”, a renowned statement attributed to William Thomson, later known as Lord Kelvin, aptly captures the essence of scientific development over the course of human history. Throughout history, humans have recognized the intrinsic need to understand and quantify the world around them. From ancient civilizations using rudimentary measuring tools to the sophisticated instruments and methodologies of modern science, measurement has been the cornerstone of scientific progress. Lord Kelvin's quote emphasizes the profound connection between measurement and knowledge, implying that by measuring, we gain insights and an understanding of the natural world. Over time, this realization led to the establishment of metrology, the science of measurement.

In contemporary times, metrology assumes a fundamental role in scientific and technological advancement. Its primary objective is to establish precise, accurate, and traceable measurement methods that ensure consistency and reliability across various domains. A significant milestone in the field of metrology occurred at the 26th General Conference of Weights and Measures (CGPM) in 2018, with the redefinition of the International System of Units (SI). One highlight of the redefinition of the SI unit was the realization of the kilogram using a silicon-28 sphere. This approach relies on the exact determination of the Avogadro constant, thereby eliminating the reliance on the physical prototype previously used.¹

The redefinition of SI units aimed to anchor the definitions of these units in fundamental constants of nature, ensuring greater stability and universality. The changes in the definitions of SI units have far-reaching implications for metrology, promoting advancements in precision and accuracy.

The SI Unit “Mole” and the Emergence of Counting-Based Measurement

Among the SI units, the mole holds a central position, representing the amount of a substance. The mole was formally defined at the 14th CGPM in 1971, as “the amount of substance of a system which contains as many elementary entities as there are atoms in 0.012 kg of carbon-12”.² The definition of the mole in 1971 and its redefinition at the 26th CGPM in 2018, which linked it to the Avogadro constant, granted the mole its own dimension as a number of elementary entities.³ This distinguished the mole as an extensive property of a material, departing from previous terms like the gram-molecule (in German: Grammmolekül), which describes a material’s intensive property that was used by Planck and Einstein.^{4,5} As an extensive property, the mole becomes a quantifiable property that is additive for subsystems, whose value is proportional to the size of the system it describes.⁶

Traditionally, chemical quantities were measured based on mass or volume, assuming a perfect correlation between these measurement results and the amount of substances present. However, advancements in scientific understanding and technological capabilities have revealed the limitations of these assumptions. While the mole is suitable for macroscopic quantities of substances, it becomes impractical and less precise when dealing with extremely low amounts, especially in the nanoscale or single-entity contexts. For instance, in the field of nanotechnology, the concept of “single-electron transfer” or “single-molecule manipulation” is employed to describe processes at the level of individual entities. Consequently, counting-based measurement approaches have gained increasing importance in scientific research and metrology.⁷⁻⁹

The adoption of counting-based measurement in metrology has introduced several notable advantages. Firstly, quantifying substances by counting individual entities offers improved accuracy. By directly assessing the quantity through counting, reliance on assumptions regarding mass or volume is mitigated, resulting in more precise determinations and reduced uncertainties. Additionally, counting-based methods contribute to enhanced precision by circumventing systematic errors that may arise from bulk measurements, as each individual entity is accounted for independently. Moreover, the inherent traceability of counting-based measurement is a significant benefit, as it relies on the direct enumeration of molecules that provides a clear and unambiguous reference point for calibration and comparison.⁹ This traceability ensures the establishment of reliable measurement standards and facilitates the reproducibility of results, ultimately enhancing the reliability and credibility of scientific and industrial metrology practices.

Measuring and Counting

Before delving into counting-based measurement in metrology, it is crucial to understand the meaning of counting and measuring. According to the International Vocabulary of Metrology (VIM, 3rd version), measurement is defined as the “process of experimentally obtaining one or more quantity values that can reasonably be attributed to a quantity”. This definition encompasses counting entities as a form of measurement. Consequently, the outcome of measurement or counting is not solely a numerical value but also emphasizes the knowledge about the type of quantity or entity being measured, which presuppose the specificity (Figure 1).

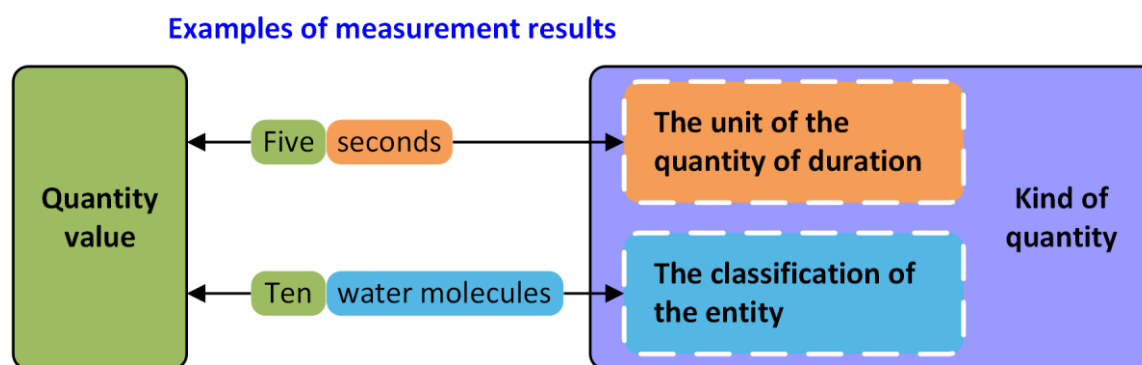


Figure 1: Two examples illustrating the measurement result, each comprising a quantity value (number) and the kind of quantity.

In the context of counting-based measurement of the amount of substance, it is essential to establish clarity regarding what is being measured. The (physical or chemical) phenomenon employed to identify and quantify the substance must be specific to the entity being measured. The following section will present a few examples to elucidate this point further.

Quantification and Counting at Single-Molecule Level

As advancements in technology and scientific understanding continue to push the limit of the measurable, metrology has shifted its focus towards quantifying the amount of substance by counting single entities. Various techniques based on counting have emerged as powerful tools for single-molecule detection and quantification by pushing the limits of the detection capabilities of instruments. These techniques enable precise determination of molecular characteristics in a given sample, thereby deepening our understanding of molecular behavior and interactions.

One example of such a technique is scanning tunneling microscopy, which utilizes a sharp metal tip to detect the presence of a molecule.¹⁰ The measured tunneling current reveals the electron density distribution of the molecule, enabling the reconstruction of its structure. Spectroscopic methods, particularly those based on light-molecule interactions, are widely employed for single-molecule detection and quantification. Single-molecule fluorescence spectroscopy is a

prominent candidate in this regard, as it detects the fluorescence signal generated by light-induced electron transitions.

Among these methods, surface-enhanced Raman spectroscopy (SERS) has emerged as a prominent approach for the determination of the amount of substance at the single-molecule level.¹¹ SERS offers exceptional sensitivity and selectivity, making it an invaluable tool for the quantification of molecules in complex systems. By exploiting the phenomenon of localized surface plasmon resonance, SERS enhances the weak Raman scattering signal of molecules adsorbed on metallic surfaces, enabling their detection and quantification even at low concentrations. The application of SERS has been further advanced by the development of quantification methods such as isotope dilution SERS. This approach, pioneered by Bernd Güttler and Rainer Stosch, combines the advantages of SERS with the precision of isotope dilution techniques, achieving accurate and absolute quantification of target molecules by incorporating isotopically labeled molecules as internal standards.¹²⁻¹⁴

The principles underlying SERS analysis are rooted in the specific interactions between molecules and nanostructured surfaces. The plasmonic hot spots generated by these surfaces create highly localized electromagnetic fields, leading to the enhancement of the molecule's vibration that is detected as Raman scattering.¹⁵ The unique vibrational energy exhibited by each type of molecule ensures the specificity of Raman scattering, allowing for the identification and quantification of target molecules even within complex mixtures.¹⁶ Moreover, precise positioning and control of molecule arrangement on surfaces, such as through the use of DNA origami techniques, further enhance the accuracy and reliability of single-molecule SERS-based quantification.^{17,18}

However, it is essential to acknowledge the challenges and limitations associated with single-molecule spectroscopic quantification. Factors such as photobleaching, photodegradation, and non-reproducibility of plasmonic hot spots can impact the reliability and accuracy of measurements, thereby affecting the quality of quantification at the single-molecule level. Ongoing efforts aim to overcome these challenges and establish standardized protocols for single-molecule quantification, ensuring reproducibility and traceability of results, which also aligns with the objective of this thesis.

Objective and Structure of This Dissertation

The objective of this dissertation is centered around advancing the field of single-molecule quantification using SERS with a particular focus on the development of a selective-adsorbing substrate known as the Polar Surface Array (PSA) as a measurement platform. The subsequent chapters of this dissertation will delve into various aspects, each contributing to the overall understanding and progress of single-molecule quantification.

A significant portion of this dissertation will be dedicated to an in-depth exploration of the development of single-nanostructure SERS experiments involving DNA origami-based plasmonic hybrid nanostructures, abbreviated as hybrid nanostructures (chapter 4). Furthermore, the fabrication process of the PSA will be presented, accompanied by a detailed examination of the adsorption mechanism of hybrid nanostructures on the PSA (chapter 5). The application of counting-based measurement techniques for single-molecule quantification will be demonstrated, and an initial approach to integrating single-molecule SERS with the isotope dilution method will be introduced (section 5.6).

Throughout the dissertation, the methodologies utilized, such as correlated atomic force microscopy (AFM)/SERS measurement, will be thoroughly discussed to ensure a comprehensive understanding of the experimental approaches.

These studies contribute to the understanding of location-controlled adsorption, and the potential for large-scale scans using PSA as a selective-adsorbing substrate. The findings presented in this dissertation pave the way for further advancements in single-molecule quantification and its applications in metrology.

2. Theoretical Background

This chapter will provide an overview of the background of Raman spectroscopy, emphasizing the development of single-molecule quantification and the role played by surface-enhanced Raman spectroscopy (SERS). The chapter further introduces the application of density functional theory (DFT) for the theoretical calculation of molecular properties and elucidates the finite-difference time-domain method (FDTD) as a powerful tool for understanding the interaction between light and materials. Finally, the chapter briefly introduces DNA origami as a biological, self-assembled nanostructure, and highlights its potential for the bottom-up nanofabrication of plasmonic nanocavities that can enhance the SERS effect.

2.1. Raman Scattering Effect

The Raman scattering effect, as described by quantum theory, represents an inelastic light scattering phenomenon wherein a photon interacts with a molecule. During this interaction, a portion of the incident photon energy (E_I) is absorbed and converted to the molecule's vibrational energy, leading to the molecule's temporary excitation into a virtual excited state. This excited state decays instantaneously, resulting in an inelastic photon scattering by releasing a new photon with a different frequency and energy (E_S) compared to the absorbed photon, as illustrated in Figure 2. The shift in vibrational frequencies of the molecule (ν_{Vib}) is known as the Raman shift, and the difference in energy between the initial and the scattered photon ($h\nu_{Vib}$) is equivalent to the vibrational energy of the molecule.^{19,20} Notably, in the scenario of elastic light scattering, where no energy exchange occurs between the incident photon and the molecule, the incident and scattered light possess identical energies, a phenomenon known as Rayleigh scattering.

The Raman shift is typically divided into two categories: the Stokes shift and the anti-Stokes shift (Figure 2).¹⁹ The Stokes shift is characterized by a frequency shift of the scattered light to a lower energy, resulting in a longer wavelength compared to the incident light. Conversely, the anti-Stokes shift refers to the frequency shift of the scattered light to higher energy. Both the Stokes and anti-Stokes Raman shifts provide valuable information about the vibrational modes and vibrational energy levels of molecules. The anti-Stokes signal is usually weaker than the Stokes signal and is more sensitive to temperature changes, this feature is utilized to estimate the temperature of a molecule.²¹

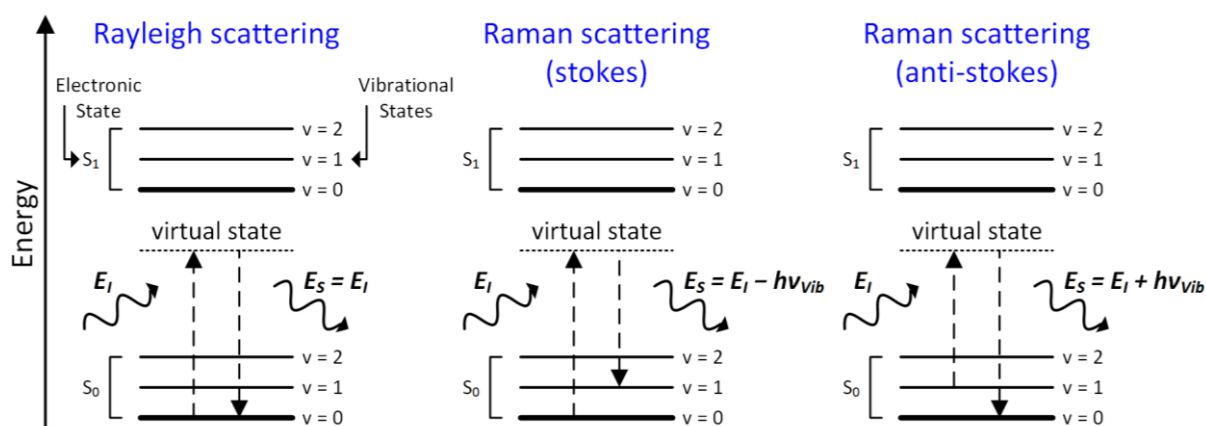


Figure 2: Simplified Jablonski diagram of Rayleigh and Raman scattering process.

The classical Raman scattering effect arises from the interaction between light and the electron cloud of a molecule (eq. (1)), while the external light source can be modeled as an incident oscillating electric field (E).¹⁹ This interaction induces changes in the molecule's polarization (P), resulting in the creation of a dipole moment that triggers characteristic molecular vibrations at specific frequencies.²² The molecule's ability to generate induced electric dipole moments when subjected to an electric field is quantified by its polarizability (α), which determines whether the molecule exhibits Raman activity.¹⁹

$$P = \alpha \cdot E \quad (1)$$

The oscillation of the induced electrical field is defined by its amplitude (E_0) and the frequency (ν_0) of the laser, as given in eq. (2).

$$E = E_0 \cdot \cos 2\pi\nu_0 t \quad (2)$$

Similarly, the molecular vibration can be broken down into i -normal modes (Q_i), with a total of $3N-6$ (or $3N-5$ for a linear molecule) normal modes in a molecule containing N atoms.

$$Q_i = Q_i^0 \cdot \cos 2\pi\nu_i t \quad (3)$$

Here, ν_i denotes the characteristic harmonic frequency of the molecule's i^{th} normal mode. Consequently, the polarizability of the molecule is expressed as a sum of normal modes, as given in eq. (4).

$$\alpha = \alpha_0 + \left(\frac{\partial\alpha}{\partial Q_i}\right) Q_i + \dots \quad (4)$$

From eq. (1), the molecular polarization corresponding to the i^{th} normal mode is described as the product of equations (2) and (4). This leads to the expression of the P in eq. (5), after noting that $\cos a \cdot \cos b = [\cos(a+b) + \cos(a-b)]/2$.

$$P = \alpha_0 \cdot E_0 \cdot \cos 2\pi\nu_0 t + E_0 \cdot Q_i^0 \left(\frac{\partial\alpha}{\partial Q_i}\right) \frac{\cos 2\pi(\nu_0 + \nu_i)t + \cos 2\pi(\nu_0 - \nu_i)t}{2} \quad (5)$$

Within eq. (5), the term marked in blue corresponds to Rayleigh scattering. The green term signifies vibration with a higher frequency, known as anti-Stokes scattering, while the orange term represents the lower-frequency Stokes scattering.

The Raman scattering effect is the fundamental phenomenon behind Raman spectroscopy, an analytical technique that collects and analyzes Raman scattering using a spectrometer that separates the scattered light into its component wavelengths. The scattered light emitted due to the vibrational motion contains valuable information about the molecular composition and structure of the sample, making it a useful tool for identifying and characterizing the sample. The Raman signal is usually very weak, necessitating the use of a sensitive spectrometer and sensor (such as charge-coupled devices, CCD) for detection.²³

Raman spectroscopy is a non-destructive technique that can analyze samples in their natural state, without the need for modification or preparation, providing information about the molecular vibrations and structure of a sample.²⁴⁻²⁶ This technique is highly specific, enabling the identification of specific molecules in complex mixtures, as each molecule has a unique Raman spectrum acting as a fingerprint.²⁷ Furthermore, Raman spectroscopy is versatile, making it useful for analyzing a wide range of samples, including solids, liquids, and gases. It is also applicable for studying materials under different conditions, such as at different temperatures and pressures.²⁸

Confocal Raman Spectroscopy

Confocal Raman spectroscopy is a technique that combines Raman spectroscopy with confocal microscopy. In this methodology, a focused laser is utilized to excite the Raman scattering of the sample, while the scattered light is collected and analyzed using a confocal microscope.²⁹ The primary advantage of confocal Raman spectroscopy over conventional Raman spectroscopy is its ability to provide higher spatial resolution and depth profiling of the sample using a confocal aperture (pinhole).³⁰ This is primarily due to the confocal microscope's ability to spatially isolate the region of the sample being analyzed, enabling three-dimensional imaging and characterization.^{29,31}

$$R = \frac{0.61 \cdot \lambda}{NA} \quad (6)$$

The superior resolution (R) performance of confocal Raman spectroscopy can be attributed to several factors, including the wavelength of the laser (λ) used and the numerical aperture (NA) of the microscope objective (eq. (6)).³² Here, it was assumed that the condenser and the objective of the microscope were the same. An empirical value of 0.61 was used in the equation to describe the shortest distance between two distinguishable spots in the microscope, where the intensity in-between the two signals is about 80% of the maxima. This concept is illustrated in Figure 3b.³³

Higher spatial resolution in confocal Raman spectroscopy can be achieved by using shorter laser wavelength, which offers higher spatial resolution but increases the potential for photodamage to the sample. The numerical aperture (Figure 3a) of the microscope objective also plays a critical role in determining spatial resolution, as higher numerical aperture objectives result in narrower beam waists and, therefore, higher spatial resolution. The confocal aperture size is another factor affecting the spatial resolution.^{34,35} A smaller confocal aperture can provide a more precise localization of the laser beam, effectively suppressing signals originating from regions outside the optical focus. However, a smaller aperture may also reduce the amount of scattered light collected, leading to a lower signal-to-noise ratio.³⁶

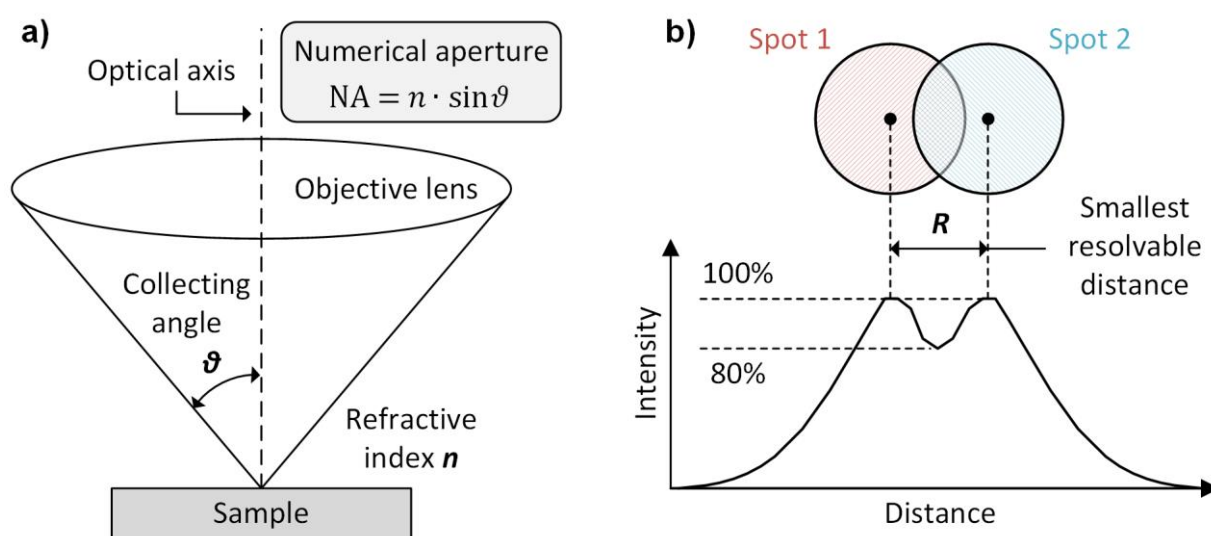


Figure 3: (a) Schematic representation of the collection optics in a typical confocal Raman scattering experiment. (b) The spatial resolution R is illustrated from two overlapping spots in a measurement.

The selection of an appropriate laser wavelength, microscope objective, and confocal aperture size is critical in optimizing the spatial resolution of confocal Raman spectroscopy for a specific application. Confocal Raman spectroscopy can be used for single-molecule Raman spectroscopy, although there are several challenges associated with this approach.³⁷ One of the primary challenges is the low signal-to-noise ratio due to the weak Raman signal from a single molecule, which can be overwhelmed by the background noise. Furthermore, the laser power required for single-molecule Raman spectroscopy may cause photodamage to the sample, which can result in changes to its chemical structure or lead to decomposition.³⁸ Consequently, low laser powers are often used to minimize these effects, but it will further reduce the signal-to-noise ratio. To enhance the signal-to-noise ratio and measurement speed, charge-coupled devices (CCD) are frequently utilized for multichannel detection.¹⁹ The sample's size and shape can also affect the performance of confocal Raman spectroscopy for single-molecule detection, with agglomerated molecules often presenting overlapping Raman peaks that make it challenging to identify the Raman signal to a single molecule.

Overall, confocal Raman spectroscopy is an advanced technique with high potential for single-molecule Raman spectroscopy, but several challenges must be addressed to achieve reliable and accurate results.

2.2. Single-Molecule Raman Experiments

The history of single-molecule Raman experiments can be traced back to the late 1990s when researchers first began exploring the potential of Raman spectroscopy to study individual molecules. In 1997, Nie and Emory conducted pioneering research that marked the first successful single-molecule Raman experiment by detecting plasmonic-enhanced Raman signals from a single rhodamine 6G molecule adsorbed on silver nanoparticles.³⁹ In the same year, Kneipp and coworkers observed the surface-enhanced Raman scattering (SERS)-based single-molecule detection of a crystal violet molecule in an aqueous colloidal silver solution and correlated the detected Raman intensity with the number of detected molecules.⁴⁰ Subsequently, researchers continued to refine the experimental techniques for single-molecule Raman spectroscopy, including the use of SERS to amplify the Raman signal from individual molecules. Recent advancements in single-molecule Raman spectroscopy have focused on enhancing the sensitivity and selectivity of the technique, with notable attention on utilizing SERS to amplify the Raman signal of individual molecules.^{41–43} This technique involves positioning the molecule of interest on a roughened metal surface or in-between nanoparticles, which can enhance the Raman signal by several orders of magnitude.^{44–46} Another noteworthy development is the use of artificially fabricated plasmonic nanocavities, which can enhance the Raman signal of individual molecules by trapping them within a small volume and focusing the excitation light to increase the Raman scattering.^{47,48} Similarly, tip-enhanced Raman spectroscopy (TERS), which involves positioning a metallic nanoparticle at the end of a scanning probe microscope tip, has also proven useful in amplifying the Raman signal of individual molecules.⁴⁹ TERS has been used to achieve sub-nanometer spatial resolution in single-molecule Raman spectroscopy.⁵⁰ In addition to the aforementioned SERS-based techniques, recent advancements in single-molecule Raman spectroscopy have leveraged the advantages of DNA origami as a platform for molecular sensing (section 2.7).⁵¹ DNA origami is a flexible platform that enables precise modification of nanoparticles and molecules of interest to specific locations on the structure.⁵² The resulting structure can be used as a template for single-molecule experiments by fluorescence spectroscopy and Raman spectroscopy, allowing for the detection and characterization of individual molecules with high sensitivity and specificity.¹⁸ The use of DNA origami as a template for single-molecule Raman experiments offers a promising avenue for advancing the sensitivity and selectivity of the technique.⁵³

2.3. Optical Properties and Plasmonic Effect of Metallic Nanoparticles

Metals, such as gold or silver, are known for their efficient light reflectivity, as well as good electrical conductivity. These properties have their origin in the presence of free-conduction electrons. The free electrons are moving in a matrix of fixed positive (metal) ions and form, by definition, a (solid-state) plasma. The optical response of this solid-state plasma is described in its dielectric function and will govern all the optical properties of metals, at least in the visible part of the spectrum where its characteristic resonant energies reside.²³

The Polarizability Described With the Drude-Lorentz Model

The optical property of a material can be expressed using the Lorentz oscillation model, which treats the interaction of an electromagnetic wave (E) with a specific electronic state as a classical (damped) harmonic oscillator and a natural frequency of ω_0 .²³ Equation (7) represents the equation of motion for a small charge displacement (r) in an external electrical field, with e as the elementary charge and m^* as the effective mass of the electron.²³

$$-\frac{e}{m^*}E(t) = \frac{d^2r}{dt^2} + \omega_0^2 r + \Gamma \frac{dr}{dt} \quad (7)$$

The solution to eq. (7) can be obtained using the complex notation for time-harmonic fields (eq. (8)), yielding the stationary solution for the equation of motion (eq. (9)).

$$E(t) = E_0 \cdot e^{-i\omega t} \quad \text{and} \quad r(t) = r_0 \cdot e^{-i\omega t} \quad (8)$$

$$r_0 = \frac{-e}{m^* \cdot (\omega_0^2 - \omega^2 - i\Gamma\omega)} \cdot E_0 \quad (9)$$

Consequently, the (complex) electric dipole moment (P_0) is expressed as $P_0 = -e \cdot r_0$. Subsequently, the (complex) optical polarizability $a(\omega)$ is denoted following eq. (1).

$$a(\omega) = \frac{e^2}{m^* \cdot (\omega_0^2 - \omega^2 - i\Gamma\omega)} \quad (10)$$

Dielectric Function of a Metal

In electromagnetism, the polarization exhibited by a dielectric material within a homogeneous medium aligns with and is directly proportional to the applied electric field E , and the permittivity $\varepsilon(\omega)$ is a measure of the electric polarizability of a dielectric.²³

$$P = \varepsilon(\omega) \cdot E - \varepsilon_0 \cdot E = \varepsilon_0 \cdot [\varepsilon_r(\omega) - 1] \cdot E \quad (11)$$

Here, ε_0 is the vacuum permittivity, and $\varepsilon_r(\omega)$ is the relative permittivity (dielectric constant), expressed as the permittivity of a material in a ratio to the electric permittivity of a vacuum. The polarization can also be expressed as the polarizability (a) of the total charge (n) induced by the external electric field.

$$P = n \cdot \alpha \cdot E \quad (12)$$

Under the assumption of negligible mutual interactions between atoms or molecules (i.e. in a dilute medium), the relative permittivity $\varepsilon_r(\omega)$ is derived as the combination of equations (11) and (12).

$$\varepsilon_r(\omega) = 1 + \frac{n \cdot \alpha}{\varepsilon_0} = 1 + \frac{n \cdot e^2}{m^* \cdot \varepsilon_0 \cdot (\omega_0^2 - \omega^2 - i\Gamma\omega)} \quad (13)$$

In metals, the free electrons, which are mainly contributing to the optical properties, can be considered to have a natural frequency of $\omega_0 = 0$. Thus, eq. (13) can be simplified to:

$$\varepsilon_r(\omega) = \varepsilon_b(\omega) - \frac{n \cdot e^2}{m^* \cdot \varepsilon_0 \cdot (\omega^2 + i\Gamma\omega)}. \quad (14)$$

$\varepsilon_b(\omega)$ represents the contribution of the inter-band transition of electrons, which is the electron transition from the valence band to the conduction band. This term is element specific and influences the effectiveness of the polarization of free electrons when subjected to an incident electric field.

From eq. (14), we can simplify the material-specific plasma frequency ω_p , which characterizes the oscillation of charge density in a metal (eq. (15)).²³

$$\omega_p = \sqrt{\frac{n \cdot e^2}{m^* \cdot \varepsilon_0}} \quad (15)$$

From Plasmon to Localized Surface Plasmon Resonance (LSPR)

The term “plasmon” was introduced by Pines in 1956 to describe the elementary excitations, or modes, of the charge density oscillations in a plasma.⁵⁴ A plasmon can be likened to the plasma charge density in the same way that photons are to the electromagnetic field.²³ From classical electromagnetism, the propagation of electromagnetic waves in a dielectric can be described using Maxwell’s equations, which induce internal polarization or magnetization of the dielectric. The energy of such is shared between electromagnetic field oscillations and internal excitations of the dielectric, termed “polaritons”.²³ The collective oscillation of free conduction electrons with respect to the fixed background of positive nuclei is referred to as bulk plasmons.²³ Since bulk plasmons are longitudinal waves, they can be excited by particle collisions, such as an electron beam, rather than transverse electromagnetic waves.⁵⁵

Another type of plasmon, introduced by Ritchie in 1957, corresponds to longitudinal charge density waves propagating at a planar metal/dielectric interface.⁵⁶ Due to retardation effects, these charge density waves cannot exist independently and must be associated with an incident transverse electromagnetic wave (photon). Consequently, they are referred to as “surface plasmon-polaritons” (SPPs).^{23,57}

For small metallic objects, particularly nanoparticles, the propagation of SPPs is restricted due to the loss of translational invariance of the plane wave vector (k).²³ As a result, SPPs become highly localized on the metal/dielectric interface and are known as “localized SPPs” (LSPs), with their properties influenced by the optical properties of the surrounding medium.²³

The interaction between light and metallic nanoparticles is commonly described using the Mie theory (Mie scattering), a well-established model that characterizes the scattering of electromagnetic waves by quasi-spherical particles whose diameter is much smaller than the wavelength of the incident light. The Mie theory provides an analytical solution to Maxwell’s equations for spherical objects, that can be employed to investigate the phenomenon of localized surface plasmon resonance (LSPR), which arises from the light-induced, collective oscillation of conduction band electrons on the metal nanoparticle surface.²³ LSPR are radiative modes that appear in an efficient coupling (absorption and scattering) of the LSPs, resulting in a resonant optical response at the plasma frequency (equations (15) and (16)).²³ This can be described as an oscillation of charges on the nanoparticle surface, as illustrated in Figure 4, in the form of an electric dipole or multipole.

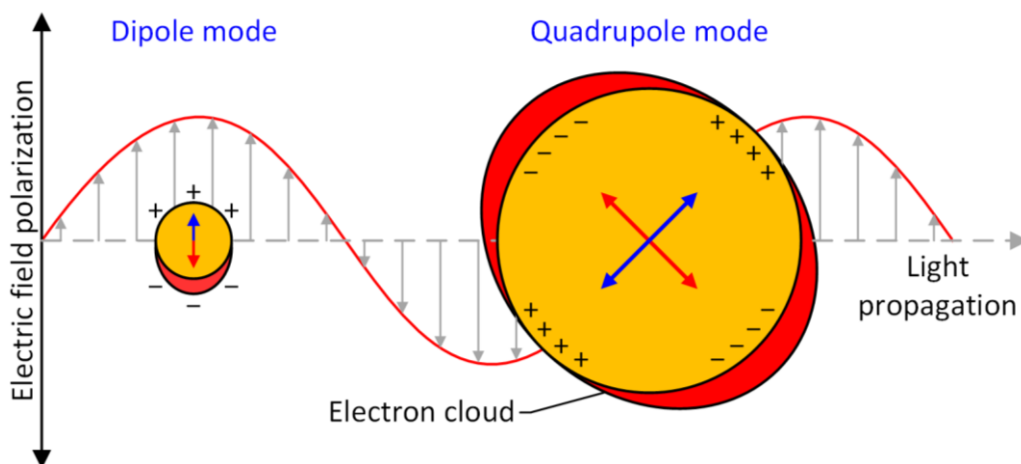


Figure 4: The dipolar and quadrupolar LSPR mode from a plasmonic nanoparticle in an external electric field. The gray arrow indicates the polarization of the external field while the red and blue arrow show the oscillating surface charges of the plasmonic nanoparticle.

The Mie theory offers a quantitative description for comprehending the scattering and absorption of light by nanoparticles, considering various factors such as their size, shape, composition, and incident light wavelength.⁵⁸ In particular, this theory predicts the LSPR wavelength (ω_{LSPR}), that is the wavelength at which the scattering and absorption of light by the nanoparticle are most pronounced.²³

$$\omega_{LSPR} = n_0 \cdot \omega_p \cdot \frac{l}{2l + 1} \quad (16)$$

Equation (16) shows that the LSPR wavelength is influenced by the dielectric function of the material, as well as the refractive index of the dielectric medium surrounding the metallic sphere (n_0). In addition, eq. (16) reveals that a metallic sphere exhibits multiple LSPR

wavelengths, with different l -order resonances characterized by their respective radiation properties. These resonances correspond to different LSPR modes in the nanoparticle and contribute to its unique optical properties.²³

The Mie Scattering of Silver and Gold Nanoparticle

The LSPR is a plasmon-induced scattering of the optical cross-sections, including extinction, scattering, and absorption.⁵⁹ When normalized to the geometrical cross-section of the sphere, the corresponding (extinction, scattering, and absorption) efficiencies, Q_{ext} , Q_{sca} , and Q_{abs} , are expressed with the following equations.⁵⁹

$$Q_{ext} = \frac{2}{x^2} \sum_{m=1}^{\infty} (2m + 1) \cdot \text{Re}(a_m + b_m) \quad (17)$$

$$Q_{sca} = \frac{2}{x^2} \sum_{m=1}^{\infty} (2m + 1) \cdot (|a_m|^2 + |b_m|^2) \quad (18)$$

$$Q_{abs} = Q_{ext} - Q_{sca} \quad (19)$$

Here, $x = 2\pi R/\lambda$ representing the geometrical factor (R is the radius of the sphere, and λ is the wavelength of the incident light in the surrounding medium). The coefficients a_m and b_m correspond to the m^{th} order electric and magnetic multipolar contributions, and are defined as:

$$a_m = \frac{\psi'_m(nx) \cdot \psi_m(x) - n\psi_m(nx) \cdot \psi'_m(x)}{\psi'_m(nx) \cdot \zeta_m(x) - n\psi_m(nx) \cdot \zeta'_m(x)} \quad (20)$$

$$b_m = \frac{n\psi'_m(nx) \cdot \psi_m(x) - \psi_m(nx) \cdot \psi'_m(x)}{n\psi'_m(nx) \cdot \zeta_m(x) - \psi_m(nx) \cdot \zeta'_m(x)}, \quad (21)$$

where $n = \sqrt{\varepsilon(\omega)}$ represents the metal's refractive index and ψ_m and ζ_m are the Ricatti-Bessel functions.⁵⁹

Figure 5 illustrates the behavior of the extinction efficiency (Q_{ext}), scattering efficiency (Q_{sca}), and absorption efficiency (Q_{abs}) for gold and silver nanoparticles of varying radii (5 nm and 50 nm).^{*} For silver nanoparticles, a sharp LSPR (extinction) band is observed in the near-UV region (Figure 5a and 5b). The LSPR band of small silver nanoparticles (Figure 5a) is primarily influenced by absorption phenomena. However, as the nanoparticle size increases, the LSPR maximum is red-shifted, and scattering becomes the dominant process (Figure 5b). The single-particle scattering efficiency (Q_{sca}) of the $r = 50$ nm silver nanoparticle is much stronger than that of the $r = 5$ nm silver nanoparticle, indicating the presence of a strong radiative (dipolar) mode of the surface plasmon.

^{*} Here, I used a modified Matlab script based on the work of Prof. Andrea Baldi.
Link: https://github.com/andrea-baldi/Mie_Scattering_and_Absorption_Sphere

On the other hand, gold nanoparticles exhibit a broad absorption band in the UV region (Figure 5c and 5d), primarily attributed to inter-band transitions. The LSPR band of gold nanoparticles falls within the visible spectrum and is broader than that of silver nanoparticles. According to Mie theory, the LSPR scattering of gold is weaker than that of silver, especially in the spectrum range between 350 and 600 nm. This is due to the energy dissipation characteristics of gold in this spectrum region, which is described by the imaginary part of the material's dielectric function.^{60,61}

For larger spherical nanoparticles, or non-spherical nanoparticles such as nanorods, nanocubes, or nanostars, the LSPR can exhibit multiple modes due to the increasing size and anisotropic shape of the particle.⁶² In addition to the dipole mode, these particles can also support quadrupole mode and higher-order modes (Figure 5b), which correspond to the oscillation of the electron cloud in higher-order multipoles (Figure 4). These higher-order modes are also radiative modes, but they have a larger absorptive character compared to the dipolar modes. This means that the proportion of losses through absorption, as opposed to radiation, is larger for higher-order modes, leading to weaker radiation.²³

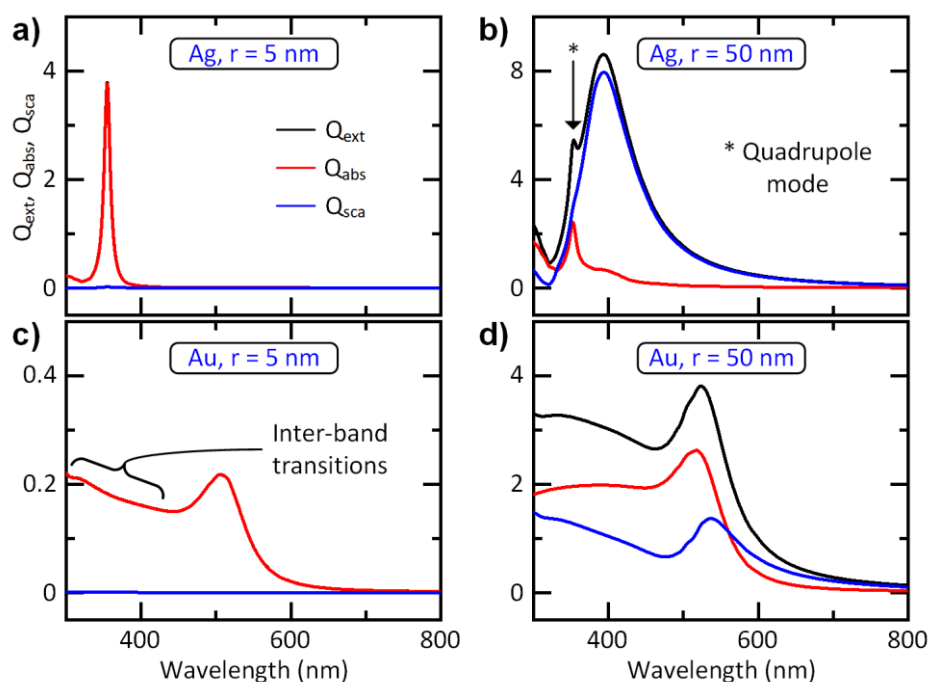


Figure 5: (a–d) Mie scattering of silver (Ag) and gold (Au) nanoparticles with a radius of $r = 5$ nm and $r = 50$ nm, respectively. The extinction efficiency Q_{ext} (black), absorption efficiency Q_{abs} (red), and scattering efficiency Q_{sca} (blue) are plotted against the excitation wavelength.

2.4. Surface-Enhanced Raman Scattering Effect

Surface-enhanced Raman spectroscopy (SERS) is a powerful analytical technique that provides highly sensitive detection and specific identification of molecules.⁶³ This technique relies on the amplification of the Raman scattering signal of a molecule adsorbed onto a metallic nanoparticle, which exhibits a localized surface plasmon resonance (LSPR) in the visible or near-infrared range of the electromagnetic spectrum, as discussed in section 2.3.

In SERS, a metallic nanoparticle, usually made of gold or silver, is used to enhance the Raman signal of the target molecule. The LSPR generated by the metallic nanoparticle generates a strong plasmonic field enhancement in the vicinity of its surface, enhancing the Raman signal of the adsorbed molecule by several orders of magnitude.⁶⁴ This effect is referred to as electromagnetic enhancement, which will be discussed in the following paragraph. The LSPR in SERS is critical in achieving high electromagnetic enhancement. By controlling the size, shape, and composition of the metallic nanoparticle, the LSPR wavelength can be tuned to selectively excite specific Raman-active vibrational modes of the target molecule.^{65,66}

The Electromagnetic Enhancement

The enhancement of the Raman scattering signal in SERS results from two primary mechanisms: electromagnetic enhancement and chemical enhancement.²³ The electromagnetic enhancement in SERS arises due to the LSPR's interaction with the incident electromagnetic field, inducing a localized surface plasmon (LSP) on the nanoparticle's surface, this is also known as the local field enhancement (EF_{Loc} , Figure 6a). The electric field component of the LSP induces an oscillating dipole moment in the adsorbed molecule, resulting in the enhancement of the Raman scattering signal of the molecule. This enhancement arises due to an increase in the excitation rate of the Raman-active vibrational modes of the molecule and an enhancement of the collection efficiency of the scattered photons. The magnitude of the electromagnetic enhancement in SERS depends on various factors, including the metallic nanoparticle's size, shape, material, the distance between the molecule and the nanoparticle's surface, and the molecule's orientation relative to the electric field of the LSP.⁶⁷

Another significant mechanism responsible for the enhancement of the Raman signal is known as radiation enhancement (EF_{Rad} , Figure 6b), which occurs when the Raman dipole radiates in close proximity to the metal (i.e., in SERS condition). If the Raman dipole is oriented perpendicular to the metal surface, the Raman emission will show a higher amplitude in compare with the same Raman dipole radiating in free-space due to the influence of the LSPR dipole, which is also perpendicular to the metal surface.

The electromagnetic enhancement in SERS can be improved by using a pair of plasmonic nanoparticles or nanoparticle agglomerations, a phenomenon known as “hot spot” formation (Figure 6a).²³ When two plasmonic nanoparticles are in close proximity, they can interact through their localized surface plasmon resonances, resulting in a strong electromagnetic field

enhancement at the gap between the particles. This enhancement can increase the Raman scattering signal intensity by several orders of magnitude and depends on the size, shape, and gap distance between the particles.⁶⁸ Moreover, nanoparticle agglomerations can also create hot spots due to the proximity of multiple nanoparticles.⁶⁹ By controlling the distance and arrangement of the nanoparticles, it is possible to create highly localized and intense hot spots, leading to significant enhancement in SERS signals. The use of plasmonic nanoparticle pairs or agglomerations has been demonstrated to be effective in various applications, including trace detection of biomolecules and environmental pollutants.^{70,71}

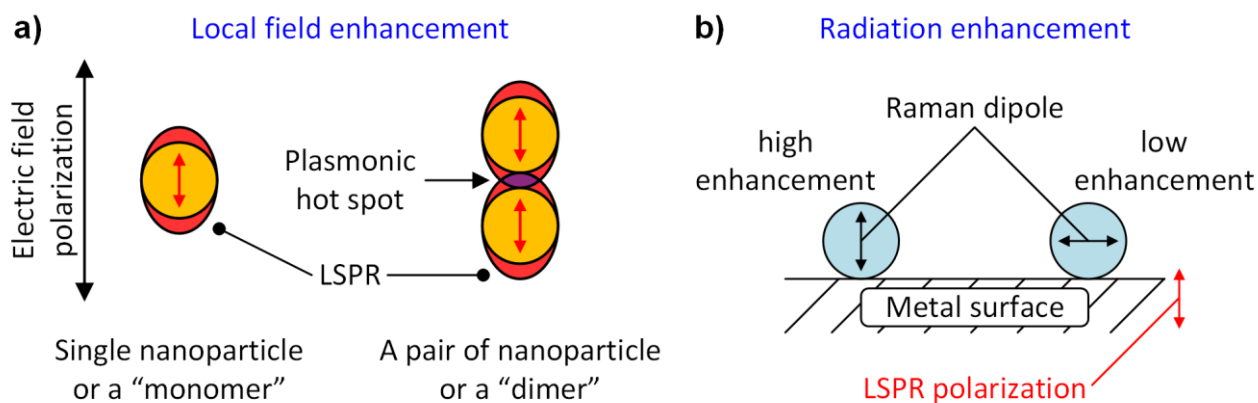


Figure 6: Illustration of the two mechanisms in the electromagnetic SERS enhancement: (a) the local field enhancement from a monomer and a dimer, and (b) the radiation enhancement of the Raman dipole on a metal surface.

The Chemical Enhancement

Chemical enhancement, in general, is referred to the changing nature and the identity of the adsorbate due to the adsorption and formation of a complex between the adsorbate and the metal. The most studied mechanism for chemical enhancement is the so-called charge-transfer mechanism, which describes the adsorbate's changing electron distribution or the polarizability due to the direct or indirect binding to the metal.^{72,73}

The mechanism of chemical enhancement in SERS is complex and not fully understood. Nevertheless, it is generally believed that the charge transfer complex modifies the polarizability of the adsorbed molecule that changes its Raman scattering cross-section, leading to an enhancement or quenching of the Raman scattering signal.^{74,75} This complex may also alter the symmetry of the molecule, leading to a selective enhancement of certain vibrational modes.

Estimation of the Enhancement Factor

Theoretical estimation of the enhancement of Raman scattering signal in surface-enhanced Raman spectroscopy (SERS) can be accomplished through various methods. One widely employed approach is to calculate the electromagnetic enhancement factor, which represents

the increase in Raman scattering due to the interaction of the incident electromagnetic field with the metallic nanoparticle.

The SERS enhancement factor (EF_{SERS}) is contributed by the factor of local field enhancement (EF_{Loc}) and the radiation enhancement (EF_{Rad}), which can be expressed with eq. (22).

$$EF_{SERS} \approx EF_{Loc} \cdot EF_{Rad} \quad (22)$$

The EF_{Loc} is associated with the LSPR and signifies the local electric field intensity on the plasmonic nanoparticle surface (eq. (23)). It is the square of the ratio between the local field amplitude (E_{Loc}) and the incident field amplitude (E_{Inc}).

$$EF_{Loc} = \left(\frac{|E_{Loc}|}{|E_{Inc}|} \right)^2 \quad (23)$$

The contribution of the radiation enhancement EF_{Rad} to the SERS enhancement is more difficult to estimate because it involves calculating the emission of the Raman dipole in a specific SERS environment, rather than the external excitation. Additionally, this electromagnetic problem must be solved for at least three perpendicular spatial directions, which becomes in most cases intractable. To avoid these complications, it is often assumed that $EF_{Rad} \approx EF_{Loc}$, which simplified the SERS enhancement factor as:

$$EF_{SERS} \approx EF_{Loc} \cdot EF_{Rad} \approx \left(\frac{|E_{Loc}|}{|E_{Inc}|} \right)^4 \quad (24)$$

The SERS enhancement factor in eq. (24) is referred to as the E^4 -approximation in literature, as it provides a simple estimation of the single-molecule enhancement factor from a calculation of the local field at the excitation wavelength.^{15,76}

The electromagnetic enhancement factor can be calculated using numerical simulations, such as finite-difference time-domain (FDTD) simulations or boundary element method (BEM) simulations, which model the electromagnetic field distribution around the nanoparticle.⁷⁷

Distance Dependence of the SERS Enhancement

The previous E^4 -approximation for the SERS enhancement factor only considers the enhancement when the molecule adsorbs on the metal surface. Understanding the variation of the local field enhancement as a function of distance from the surface is however important when the molecule is not directly adsorbed on the metal surface.

The LSPR dipole mode of a spherical metal nanoparticle can be simplified as an electrostatic dipole located at the sphere center. The electric field outside the sphere decay at a rate of $1/(r+d)^3$, where r is the sphere radius, and d is the distance from the sphere surface. Consequently, the local field amplitude should decay as $1/(r+d)^6$ and the SERS enhancement factor as $1/(r+d)^{12}$, following the assumption in equations (23) and (24). Despite this, the decay rate of the SERS enhancement factor is less dramatic than it might look.

As illustrated in Figure 7a, the EF_{SERS} is normalized to 1 at the nanoparticle surface and decreases by only half at a distance of $d = 0.06 \cdot r$, corresponding to a distance of 3 nm from the surface of a nanoparticle with radius $r = 50$ nm. At a distance of $d = 0.2 \cdot r$, which corresponds to a distance of 10 nm from the surface of the same nanoparticle, the SERS enhancement is reduced to 10%. This decay rate clearly shows that SERS is a near-field effect and a high enhancement factor can be achieved when the molecule is placed close to the nanoparticle surface. The distance dependency of SERS enhancement decay is less severe on large nanoparticles compared with small nanoparticles, since the ratio d/R (with $R = r + d$) would be smaller at constant d . Nonetheless, the strong distance dependency of the SERS enhancement factor remains an important criterion to achieve a high SERS enhancement.

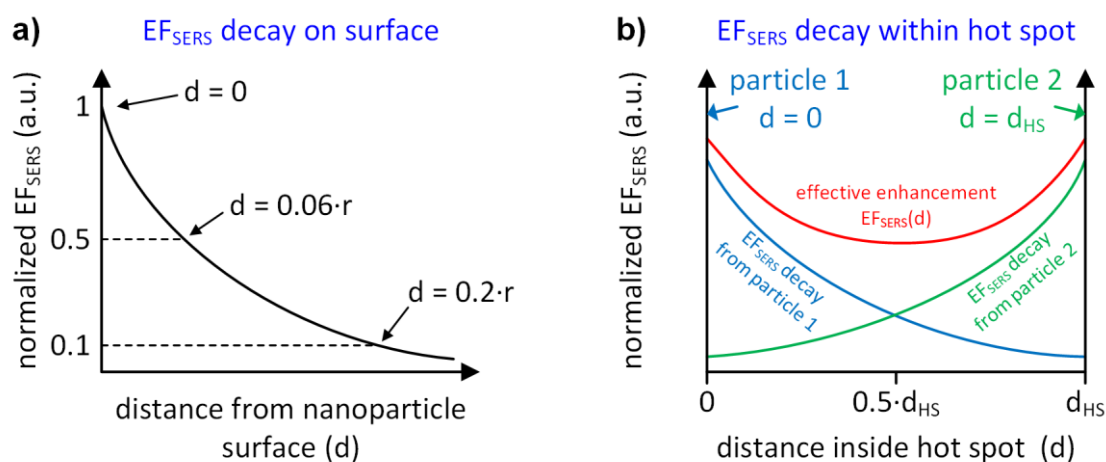


Figure 7: The distance dependence of the SERS enhancement (a) from the surface of a plasmonic nanoparticle and (b) within a plasmonic hot spot.

In contrast to the SERS enhancement decay on an isolated spherical metal nanoparticle, the situation inside a SERS hot spot, i.e., in-between two nanoparticles in close vicinity, is markedly different. Figure 7b presents the simplest case, where two nanoparticles with equal radii have a surface-to-surface distance of d_{HS} , thus creating a hot spot with this distance. The distance-dependent SERS enhancement, denoted as $EF_{SERS}(d)$, is a function of the distance from the nanoparticle surface (d), which can be described as the sum of SERS enhancement from each nanoparticle.

$$EF_{SERS}(d) = EF_{SERS}^1(d) + EF_{SERS}^2(d) \quad (25)$$

The highest SERS enhancement is expected to occur on the surface of both nanoparticles, as given by eq. (26).

$$EF_{SERS}(d = 0 \text{ or } d_{HS}) = \left(\frac{|E_{Loc}|}{|E_{Inc}|} \right)^4 \cdot \left(1 + \frac{1}{R + d_{HS}} \right) \quad (26)$$

On the other hand, the lowest SERS enhancement is expected to be at the center of the hot spot, with an enhancement factor given by eq. (27).

$$EF_{SERS}(d = 0.5 \cdot d_{HS}) = \left(\frac{|E_{Loc}|}{|E_{Inc}|} \right)^4 \cdot \left(\frac{2}{R + 0.5 \cdot d_{HS}} \right) \quad (27)$$

Despite the anticipated reduction of SERS enhancement in the hot spot center, the two nanoparticles can create a capacitor in the nanoscale, allowing the enhancement in the hot spot to remain considerable (Figure 7b). Therefore, the plasmonic hot spot represents a more reliable source of SERS than isolated metal nanoparticles, in addition to the already increased SERS enhancement in the hot spot.

It should be noted that the LSPR wavelength of a nanoparticle dimer is typically red-shifted (depending on the hot spot distance), relative to the LSPR wavelength of a single nanoparticle with the same size. Hence, the local field enhancement of a monomer and a dimer at the same excitation wavelength cannot be directly compared, as the SERS enhancement is higher when the excitation wavelength matches the LSPR wavelength.

In conclusion, obtaining high SERS enhancement involves a number of critical factors, such as the appropriate choice of SERS substrate with optimal surface morphology or hot spot, and the selection of an appropriate analyte molecule with a high Raman scattering crosssection.^{39,78} The use of highly roughened substrates, such as nanosphere lithography or electrochemical deposition, can significantly increase the number of hot spots on the surface, resulting in efficient electromagnetic enhancement.⁷⁹⁻⁸² Moreover, optimization of the laser excitation wavelength, power, and polarization can contribute to achieving a high SERS enhancement. The integration of these factors can lead to highly sensitive and selective SERS measurements, making SERS a powerful analytical tool for a variety of applications.⁸³⁻⁸⁵

2.5. Density Functional Theory

Density functional theory (DFT) is a quantum mechanics-based computational method used in condensed matter physics, chemistry, and materials science to study the electronic structure of atoms, molecules, and solids. The theory provides a way to calculate the electronic structure of a material based on the distribution of electrons in its system. It allows the prediction of material properties, such as their electronic, magnetic, and structural properties.

Multiple theoretical models are available to describe atomic interactions within a molecule, three of which are schematically shown in Figure 8. One such approach is the force field method, which relies on classical physics to characterize atom interactions. This method considers the attracting London dispersion force and the Pauli repulsion, resulting in the well-known Lennard-Jones potential.⁸⁶ This many-body problem can be expressed with Newtonian mechanics, where the force (F) acting on a particle is the sum of the external force (\vec{F}_E) and the force (\vec{F}_{ij}) between particles i and j .⁸⁷ This resultant force governs the change of momentum (p) over time (t).

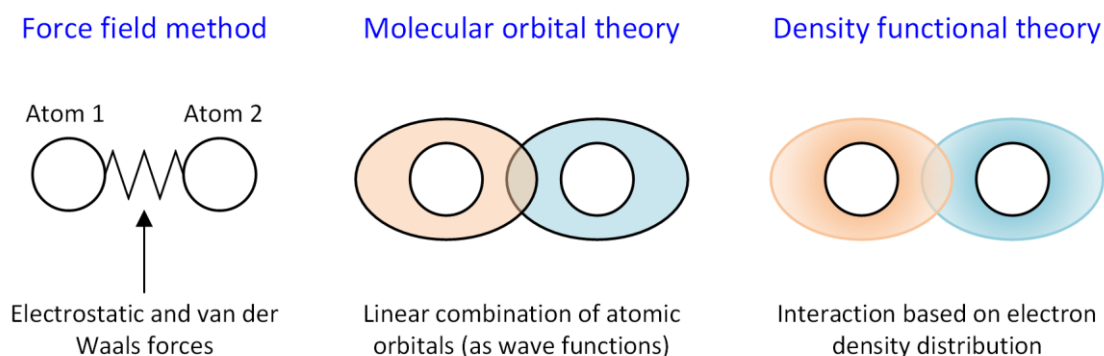


Figure 8: Theoretical models that describe the interaction between atoms.

$$\vec{F} = \frac{d\vec{p}_i}{dt} = \vec{F}_E + \sum_{i \neq j} \vec{F}_{ij} \quad (28)$$

In quantum mechanics, calculating the movement of light particles, especially electrons, requires solving the Schrödinger equation. The energy of a system containing N electrons can be described using the time-independent Schrödinger equation (eq. (29)). Here, the behavior of electrons is represented by the wave function (Ψ), which expresses the spatial distribution of electron density through the probability density function ($P = |\Psi|^2$).⁸⁸

$$\hat{H}\Psi(r_1, r_2, \dots, r_N) = E\Psi(r_1, r_2, \dots, r_N) \quad (29)$$

In this equation, the Hamiltonian operator (\hat{H}) is the sum of all energy components in the system. This includes the kinetic energy of nuclei (T_N), the kinetic energy of electrons (T_e), the nucleon-nucleon repulsion (V_{NN}), the electron-electron repulsion (V_{ee}), and the electron-nucleon attraction (V_{eN}).⁸⁸

Solving the Schrödinger equation and determining the wave function and energy of a quantum many-body system can be achieved through the Hartree-Fock method.⁸⁸ This method constructs a wave function as a Slater determinant of one-electron orbitals, albeit neglecting electron correlation effects.⁸⁹ While this simplification makes calculations more manageable for many-body systems, it may introduce inaccuracies in strongly correlated systems. For such cases, more sophisticated methods like density functional theory (DFT) are better suited to address the intricacies of electron correlation.⁸⁹

DFT is based on the idea that the total energy of a system can be expressed as a functional of the electron density.⁸⁸ This means that material electronic properties can be determined by calculating the electron density at each point in space, rather than relying on the wavefunctions of individual electrons, which is the basis of the Hartree-Fock molecular orbital theory.⁸⁸ This approach reduces computational complexity and improves calculation efficiency. The energy expressed in DFT is a function of the electron density, with the density itself being a function of three-dimensional spatial coordinates, referred to as “functionals” or “density functionals”.⁸⁸

Density functional theory can be used to estimate a stable molecular structure by minimizing the total energy of the system with respect to the positions of the atoms. The calculation starts with an initial guess for the atom position and then iteratively adjusts the positions until a minimum energy state of the system is found. Once a minimum energy state is found, the optimized molecular structure can be used to calculate other properties of the system, such as the electron density distribution via Bader charge analysis and the molecule's vibrational frequencies.^{90–93}

The distribution of electron density within a molecule can be assessed quantitatively using the Bader charge analysis, also known as Bader analysis or AIM (Atoms in Molecules) analysis.⁹⁴ This computational method, developed by Henk Bader, allows for the assignment of partial charges to individual atoms based on the surrounding electron density.⁹⁵ By utilizing a mathematical algorithm, the electron density is divided into regions referred to as “atomic basins” or “atomic volumes”, with each basin corresponding to a specific atom.⁹⁵

Initially, the electron density is determined through quantum mechanical techniques such as density functional theory (DFT), which quantifies the probability of electron presence at defined spatial coordinates. Following this, critical points in the electron density distribution are identified as extrema. The extrema comprise maximum points that are associated with the position of atomic nuclei, minimum points are found in non-bonding regions or the spaces between atoms, and saddle points delineate the boundaries between atomic basins. Through the Bader analysis algorithm, these critical points are attributed to individual atoms, effectively partitioning the electron density into distinct regions associated with each atom. Consequently, the atom-specific electron density can be determined, enabling the calculation of partial charges.^{95,96} Bader charge analysis provides valuable insights into the redistribution of electron density within the molecule, thereby clarifying the polar and covalent characteristics of chemical bonding.

The vibrational modes of a molecule can be simulated with DFT by computing the molecular Hessian matrix, which describes the second derivative of the total energy with respect to the atomic displacements.⁹⁷ To perform this simulation, the initial molecular geometry is first optimized using DFT to obtain the minimum energy state of the molecule. Then, the molecule's Hessian matrix is calculated to obtain the eigenvalues (vibrational frequencies) and eigenvectors (normal modes). The vibrational frequencies represent the frequency of each vibrational mode, and the eigenvectors describe the displacement pattern of the atoms in each mode.

The accuracy of density functional theory (DFT) simulations compared to experimental results depends on several factors, such as the complexity of the system and the choice of functional.^{98,99} There are many different functionals available, each with its own strengths and weaknesses. Some functionals are better suited for certain types of systems or properties than others and choosing the correct functional can have a significant impact on the accuracy of the results.

2.6. Finite-Difference Time-Domain Method

The finite-difference time-domain (FDTD) method is a numerical approach commonly utilized to solve electromagnetic field problems. This method is capable of simulating various electromagnetic phenomena, such as wave propagation, light scattering, and interaction with materials.

The FDTD method is a direct solution for Maxwell's equations, which describe the interactions of electric (E) and magnetic (H) fields with one another. In particular, the time evolution of the fields is expressed through equations (30) and (31).¹⁰⁰

$$\frac{\partial H}{\partial t} = -\frac{1}{\mu}(\nabla \times E) - \frac{\sigma^*}{\mu}H \quad (30)$$

$$\frac{\partial E}{\partial t} = -\frac{\sigma}{\varepsilon}E + \frac{1}{\varepsilon}(\nabla \times H) \quad (31)$$

FDTD computes the interaction between light and material by simulating the propagation of electromagnetic waves within a grid of small cells that comprise the material. As the propagating light enters a cell with material, its electric and magnetic fields interact with the material, resulting in light absorption, reflection, and transmission. The material properties are incorporated into the simulation through the permittivity and permeability values inside the simulation cells, which are referred to as the Yee-cell.¹⁰¹ The FDTD method computes the light-material interaction and updates it over time using finite-difference approximations to the time derivatives of Maxwell's equations. By iteratively solving this process over time, the FDTD method accurately simulates the propagation of the electromagnetic fields as they interact with the material.

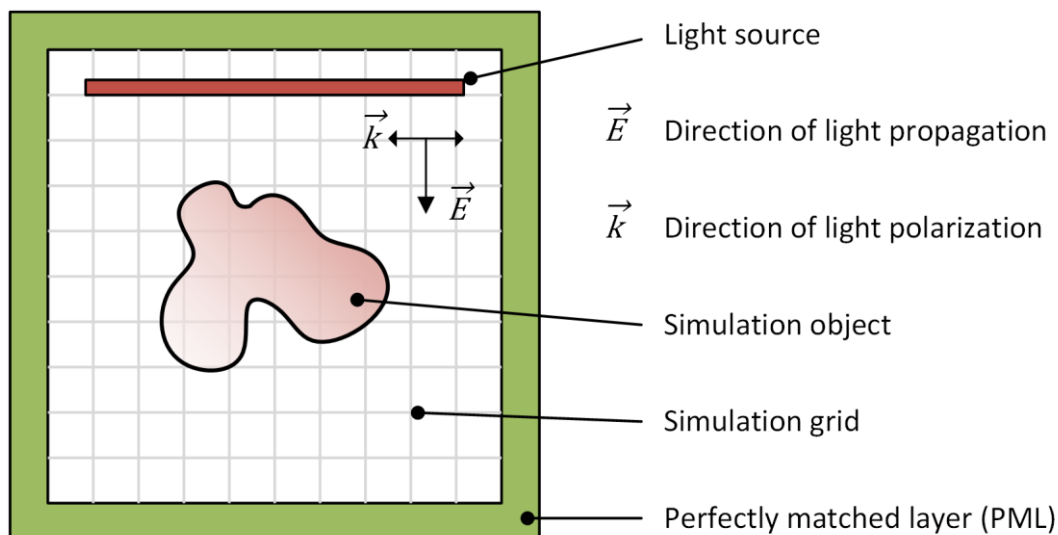


Figure 9: The typical simulation field of an FDTD simulation.

In this study, the FDTD method is employed to investigate the electromagnetic behavior of plasmonic structures under light irradiation (section 2.4). Specifically, the localized surface plasmon resonance (LSPR) and its associated surface-enhanced Raman spectroscopy (SERS)

enhancement are of interest for optimizing nanoantenna design and predicting the local SERS enhancement. Figure 9 schematically illustrates an FDTD simulation, which includes all relevant components, primarily the light source and the simulation object. The simulation domain is discretized into a mesh and is surrounded by a perfectly matched layer to mitigate boundary reflections. The light source is represented as a plane wave with a defined direction of propagation, wavelength, and polarization.

The FDTD method confers numerous advantages, such as its ability to handle complex geometries and materials, and its capability to simulate a broad range of electromagnetic phenomena.¹⁰² Furthermore, the FDTD method employs a time-domain approach, which facilitates the investigation of the dynamic behavior of electromagnetic fields over time, providing valuable insights into their temporal behavior. However, one notable disadvantage of the FDTD method is its computational cost, which may be prohibitive when modeling high-frequency phenomena or geometric features with many details, necessitating a fine grid resolution. Additionally, the FDTD method employs Cartesian grids, which result in rectangular-shaped Yee-cells. Consequently, modeling curved or circular geometries may produce surface artifacts. Nonetheless, despite these limitations, the FDTD method remains a popular and widely used numerical approach to solving electromagnetic field problems.

2.7. The Principle of DNA-Origami

DNA origami is a versatile technique that enables the precise folding of DNA into complex and custom-designed shapes. Developed in 2006 by computer scientist and biologist Paul Rothemund, this technique utilizes short, synthetic DNA strands called “staple strands” binding to a longer, single-stranded DNA known as the “scaffold strand” and dictating its folding pattern.¹⁰³ The resulting structures can be tailored to meet specific applications in fields such as nanotechnology, biosensing, and biomedicine.^{104–106}

One important application of DNA origami is in single-molecule detection.¹⁰⁷ This technique allows for the precise placement of functional molecules, such as fluorescent dyes or enzymes, at specific locations on a DNA nanostructure. This enables the development of highly sensitive biosensors that can detect low concentrations of target molecules with high specificity and selectivity.¹⁰⁸ DNA origami-based biosensors can immobilize multiple copies of a detection molecule at high density, increasing the probability of binding events and amplifying the detection signal.¹⁸ Additionally, the use of DNA origami as a sensing platform offers a high degree of flexibility in the design of the sensing probe, allowing for the optimization of binding affinity, sensitivity, and specificity.^{109,110}

Moreover, DNA origami structures allow for highly sensitive single-molecule detection platforms due to precise control over their size and shape.^{111,112} By attaching fluorophore or other reporter molecules to specific locations on the DNA origami structure, local single-molecule phenomena can be observed with high spatial and temporal resolution.¹¹³

DNA origami is easy to modify due to the flexibility and programmability of DNA as a material.^{112,114} The modular nature of DNA origami structures allows for the rapid and easy incorporation of new components or modifications. The “staple strands” used to fold the DNA into specific shapes can be easily designed and synthesized to contain additional functional elements, such as aptamers, enzymes, or other functional groups.^{115,116} The spatial arrangement of these molecules on the DNA origami structure can be precisely controlled, allowing for the development of tailored sensing platforms.¹¹⁷

The combination of DNA origami and confocal Raman spectroscopy provides a highly precise and customizable approach for single-molecule detection. The Raman-active molecule can be attached to a specific location on the DNA origami structure, and additional metallic nanoparticles attached to the same DNA origami can enhance the Raman signal of the molecule.^{68,118–120} When the Raman-active molecule is excited with a laser, it produces a characteristic Raman scattering signal that can be analyzed to identify the molecule and its location. This approach has been demonstrated in studies using surface-enhanced Raman spectroscopy (SERS) to detect single DNA origami structures. The use of DNA origami as a scaffold for single-molecule detection offers several advantages, including precise control over the position of the Raman-active molecule and the ability to tailor the size and shape of the DNA origami structure for optimal SERS enhancement. Overall, the combination of DNA origami and Raman spectroscopy provides a powerful analytical tool for single-molecule detection with potential applications in fields such as molecular biology, biophysics, and nanotechnology.¹²¹

3. Materials and Methods

This chapter presents the fabrication process of the DNA origami-based plasmonic hybrid nanostructures (in the following: hybrid nanostructures) and the Polar Surface Array (PSA). The general workflow for the preparation of hybrid nanostructures is shown in Figure 10. A list of the chemicals and buffer solutions used for the synthesis are listed in Table 1 and Table 2, respectively.

In this chapter, DNA origamis were self-assembled (section 3.1), hybridized with DNA-coated gold nanoparticles (section 3.2), and purified by different methods (section 3.3). The fabrication and adsorption of the Polar Surface Array (PSA) are described in section 3.4 for experiments using the PSA as the substrate. In section 3.5, important details for sample preparation and storage are listed.

The characterization methods of the synthesized hybrid nanostructures are listed in section 3.6. The hybrid nanostructures are characterized by SERS, AFM, and electron microscopy. The quantification of gold nanoparticles, DNA origami, and hybrid nanostructures was conducted by UV/Vis spectroscopy.

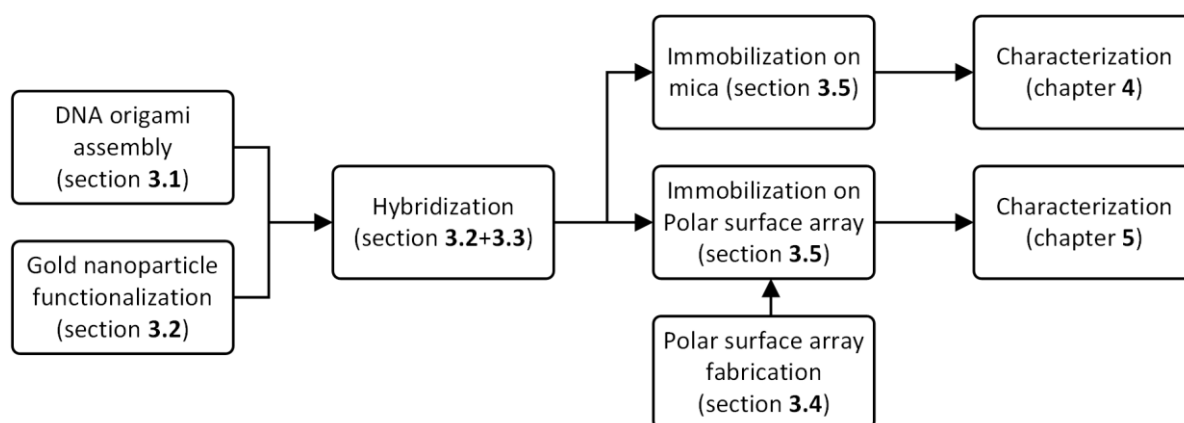


Figure 10: Sample preparation workflow for single-molecule Raman experiments.

Table 1: List of chemicals and buffers used for the synthesis.

Name	Supplier
10× TAE buffer	<i>Carl Roth</i>
10× TBE buffer	<i>Carl Roth</i>
Tris base	<i>Carl Roth</i>
MgCl ₂ ×6H ₂ O	<i>Carl Roth</i>
Tween 20	<i>Carl Roth</i>
10× Loading buffer	<i>Invitrogen</i>

Table 2: The names and composition of buffers used in this work.

Description	Composition
1× TAE buffer	1 L (pH = 7.6) contains 40 mM tris base, 20 mM acetic acid, 1 mM EDTA
Folding buffer	1 L (pH = 7.6) contains 0.5× TAE buffer and 11 mM MgCl ₂
Buffer A	1 L (pH = 8.3) contains 40 mM tris base and 40 mM MgCl ₂
Buffer B	1 L (pH = 8.3) contains 40 mM tris base, 40 mM MgCl ₂ , and 0.07 wt.% Tween 20
Buffer C	1 L (pH = 8.9) contains 40 mM tris base and 35 mM MgCl ₂
1× Loading buffer	1 L (pH = 7.6) contains 1 mM tris-HCl, 6 mM EDTA, 0.003% bromophenol blue, 6% glycerol

3.1. DNA Origami Design and Synthesis

The DNA origami employed in this study was designed using the *caDNA* software, an open-source program developed and maintained by Nick Conway (Wyss Institute) and Shawn Douglas (UCSF). This software allows for the planar visualization of DNA frameworks and provides tools for their modification.

Figure 11 illustrates the *caDNA* design of a miniaturized rectangular DNA origami constructed from a scaffold and four staples. The scaffold, which served as the backbone of the DNA origami, consists of a 208-base-long single-stranded DNA (ss-DNA). The position and DNA sequence of the scaffold are shown in blue. The rectangular structure of this DNA origami was achieved by joining specific positions of the scaffold with complementary ss-DNA strands, known as staples, each indicated by a distinct color. Notably, each ss-DNA has a starting position (5'-end) and an ending position (3'-end) denoted by square and rectangle symbols, respectively.

The position of each sequence was defined by the rows and columns in the design scheme. For instance, the red staple in Figure 11 initiates at the 5'-end (red square) located at row Nr.1, column Nr. 20. Its starting position is, therefore, 1[20]. Similarly, the end position of the red staple is at the 3' position (red rectangle), which is at position 0[28].

The DNA sequence of the four staples was specifically chosen to locally form double helices with the scaffold, which was folded into four parallel rows, as shown in Figure 11. Upon importing the scaffold sequence into the *caDNAno* program, the staple sequences were automatically generated and can be exported directly, as detailed in Table 3. It is possible to manually add further functionalization, such as dye molecules or extended ss-DNA strands, to a staple.

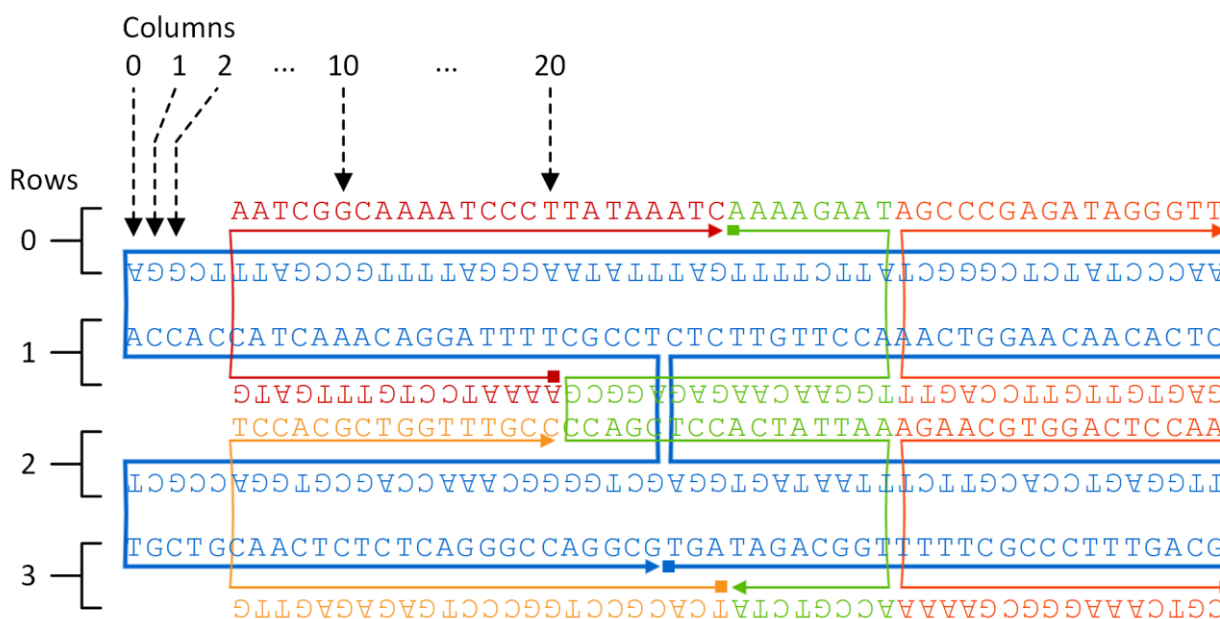


Figure 11: *caDNAno* design of a miniaturized rectangular DNA origami.

For the synthesis of rectangular DNA origami, single-stranded scaffold DNA, type p7249 (M13mp18) was purchased from *tilibit nanosystems*, and staples were purchased from *Eurofins Genomics*. The design scheme, scaffold sequences, and synthesis protocol are listed in Appendix A1.

The rectangular DNA origami was produced by mixing scaffold with staples in a molar ratio of 1:20 in the folding buffer (Table 2). An excess of staples was utilized to enhance the yield of DNA origami and accelerate the reaction speed. The mixture of staples and scaffold was subjected to heating up to 90°C in a thermocycler (*Bio-Rad*) and then cooled down to room temperature over a period of 70 minutes, with a cooling rate of 1°C per minute. After synthesis, the mixture was either purified directly or stored at -20°C.

Table 3: Staple sequences of the rectangular DNA origami in Figure 11.

Start	End	Staple sequence from 5'-end to 3'-end
0[29]	3[29]	AAAAGAATTGGAACAAGAGAGGGCGCCAGCTCCACTATTTAAACCG TCTA
1[20]	0[28]	AAAATCCTGTTTGTATGAATCGGCAAAATCCCTTATAAATC
3[28]	2[20]	TCACGCCTGGCCCTGAGAGAGTTGTCCACGCTGGTTTGCC
3[52]	0[52]	CGTCAAAGGGCGAAAAAGAACGTGGACTCCAAGAGTGTGTTGCC AGTTAGCCCGAGATAGGGTT

3.2. AuNP-DNA Origami Hybridization

Various techniques have been developed to modify DNA origami structures. One of the most commonly used approaches involves attaching a pair of complementary DNA strands, where one strand is linked to the DNA origami and the other to the modifier.^{122,123} An alternative method is the strain-promoted alkyne azide cycloaddition (Copper-free Click Chemistry), which can create a strong covalent bond between the DNA origami and the modifier.^{124,125} In this study, we employed a modification protocol adapted from Gür et al. to bind gold nanoparticles to DNA origami through complementary DNA strands.¹²³

We mixed 20 mL of citrate-capped gold nanoparticles (with an optical density of $OD = 1$) together with 150 μ L of 100 mM Bis(p-sulfonatophenyl)phenylphosphine dihydrate dipotassium (BSPP) and incubated overnight. 5 M NaCl was gradually added to the nanoparticle colloid until the color changed from red to blue, followed by centrifugation at 5000 rcf for 20 min. The supernatant was removed, and the pellet was suspended in 2.5 mM BSPP. This process was repeated once, and the concentration of the remaining gold nanoparticles was determined by measuring the extinction at a wavelength of $\lambda = 450$ nm using UV/Vis spectrometry (section 3.6).

Gold nanoparticles (AuNPs) modified with BSPP were mixed with thiolated T₁₉ single-stranded DNA in a molar ratio of 1:2400 (for AuNPs with a diameter of 30 nm) in 0.5 \times TAE. 5 M NaCl was added to this mixture, followed by sonication for 10 s, and shaken for 10 minutes. This step was repeated four times until a final NaCl concentration of 500 mM was reached, and the mixture was shaken overnight before being collected by centrifugation at 10000 rcf using Amicon Ultra-0.5 mL Centrifugal Filters. The resulting T₁₉-functionalized gold nanoparticles were then mixed with A₁₉-modified DNA origami in a molar ratio of 50:1 and shaken for 90 min. Finally, we used gel electrophoresis (see section 3.3) to separate unreacted gold nanoparticles from gold nanoparticle-functionalized DNA origami. The same protocol was applied for all hybridization syntheses in this work.

After the hybridization, AFM and SEM were applied for the characterization of hybrid nanostructures. Figure 12a exemplary shows an AFM measurement of hybrid nanostructures

with two 15 nm AuNPs. Unbounded AuNPs (①) and rectangular DNA origamis (②) were observed as well as hybrid nanostructures with one (③) or two AuNPs (④). The ratio of the correctly formed and non-ideal hybrid nanostructures was used to evaluate the experiments' success. The same evaluation was also feasible with SEM measurements (Figure 12b), where the position of AuNPs (white dots) and DNA origami (dark rectangles) were visualized.

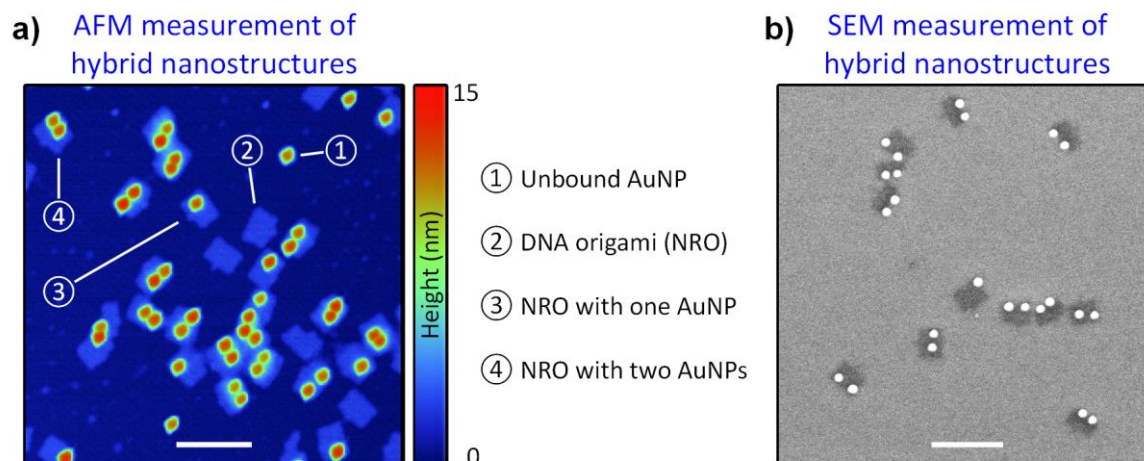


Figure 12: (a) AFM and (b) SEM characterization of hybrid nanostructures (two 15 nm AuNP binding on an NRO). Scale bars are 200 nm in both images.

3.3. Purification of DNA Origami and Hybrid Nanostructure

To ensure the high purity of the synthesized DNA origami and the DNA-functionalized gold nanoparticles, two purification techniques, gel electrophoresis, and centrifugation, were employed. This was crucial for removing excess staples from DNA origami, which could interfere with the yield determination, AFM characterization, and subsequent modification steps. The hybrid nanostructure, however, was only purified with gel electrophoresis to separate the final product from unreacted gold nanoparticles.

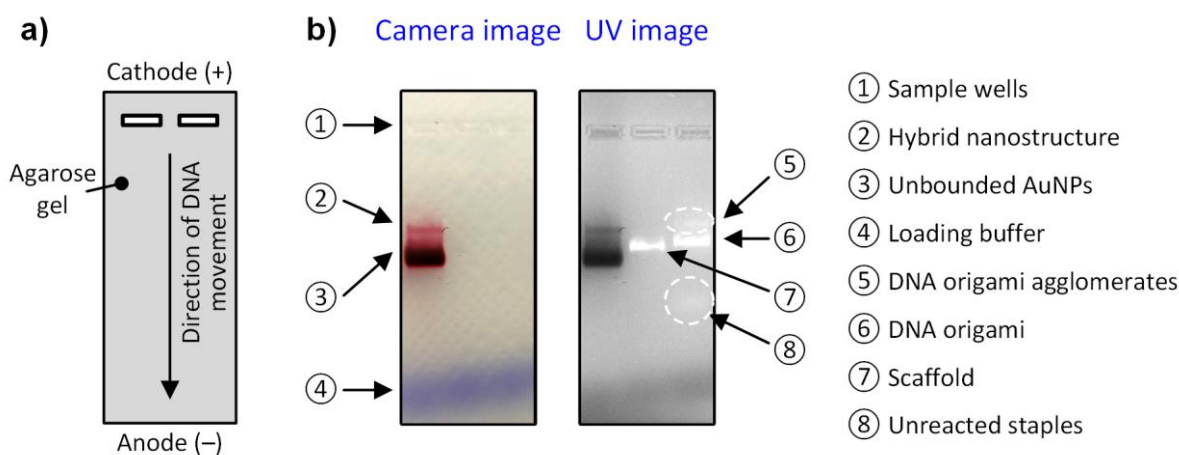


Figure 13: (a) Working principle of the gel electrophoresis. (b) White light camera image and UV image of a gel, which was used to purify DNA origami and hybrid nanostructures.

Electrophoresis with agarose gel was the primary method for DNA origami purification in this study. Alternatively, the purification was conducted via centrifugation, which is explained later in this section. The agarose gel has a porous structure and forms a mesh of holes in an aqueous solution through hydrogen bond cross-linking of the agarobiose chain. The typical pore size ranges between 50 nm and 2000 nm and is inversely proportional to the mass percentage of the agarose, which is typically in the range of 0.5 to 3 wt.%. The agarose gel used in this work was made by dissolving 0.75 wt.% agarose powder (Biozym Gold Agarose, *Biozym*) with $0.5\times$ TAE buffer, microwave heating will accelerate the dissolving process. After the agarose was fully dissolved, the transparent liquid was cooled down to $\sim 40^{\circ}\text{C}$, and MgCl_2 was added to reach an Mg^{2+} concentration of 11 mM. The warm gel was poured into a rectangular gel chamber with a gel comb designed to create equidistant chambers for the synthesized DNA origami. Once the gel was cooled and solidified at room temperature, it was placed in a gel box (Mini-Sub cell GT, *Bio-Rad*) filled with folding buffer, and the gel comb is carefully removed. About 30 μL of the synthesized DNA origami was mixed with 5 μL $1\times$ Loading buffer (BlueJuiceTM, *Invitrogen*) before injected into the sample wells.

The electrophoresis process was initiated by applying a constant voltage of 70 V across the gel, while a current of 0.1 mA was set throughout the process. The movement direction of the negatively charged DNA origami and the DNA-functionalized gold nanoparticles was illustrated in Figure 13a. After a certain time, negatively charged DNA would move to the anode, and staples would travel a greater distance compared with scaffold and folded DNA origami due to a smaller hydrodynamic radius. To mitigate any potential damage to the gel and the samples due to electrical resistance and heat generation, the gel was kept at 0°C using an ice-water mixture. Additionally, fluorescence marking could be achieved by incorporating a fluorescent dye such as peqGREEN[®] (*PEQLAB*) into the synthesized DNA origami. This dye binds to nucleic acids and enables their detection using UV light, for instance, using a Gel Documentation System (Gel Doc XR+, *Bio-Rad*).

Figure 13b depicted the successful purification of the synthesized hybrid nanostructures through agarose gel electrophoresis. The synthesized hybrid nanostructure was loaded into the designated sample wells (①) and was separated into two distinct bands, one contained the hybrid nanostructure (②) and the other was the unbounded DNA-functionalized gold nanoparticles (③). The deprotonated bromophenol blue dye used in the loading buffer (④) enabled visualization of the negatively charged ions' movement during electrophoresis. PeqGREEN[®] labeling facilitated the visualization of the DNA in the UV image of the gel. The position of the scaffold (⑦) served as an internal standard because the structure of DNA origami has a similar size but is more rigid, and therefore DNA origami should travel a shorter distance (⑥) in compare with the scaffold. The UV image on the right-most column of Figure 13b illustrated the separation of the synthesized DNA origami, while unreacted staples (⑧) and agglomerated DNA origami (⑤) were also visible.

Following electrophoresis, the gel fragment containing the folded DNA origami was separated from the gel by carefully excising it using a scalpel. The DNA origami was subsequently extracted by collecting the liquid obtained by squeezing the gel fragment between two glass slides. The yield of the extracted DNA origami could be determined using UV-Vis spectrometry, as described in section 3.6.

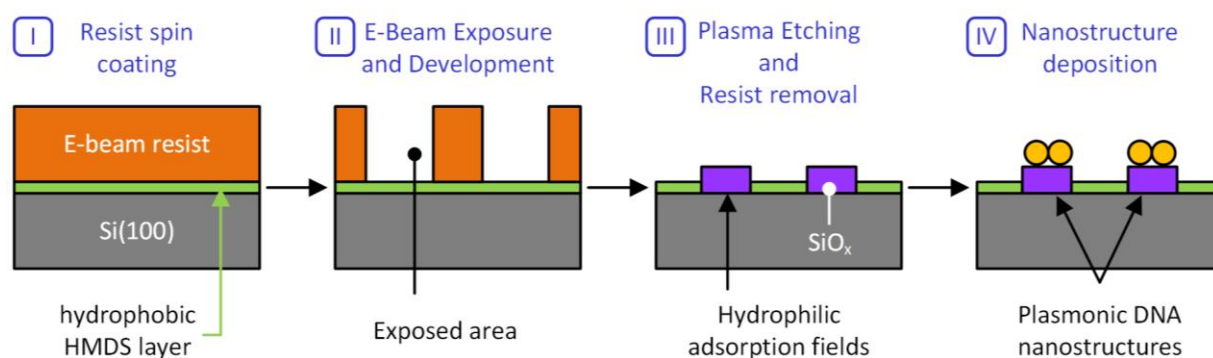
An alternative approach for purifying synthesized DNA origami was centrifugation using centrifugal filters, such as the Amicon Ultra 100k manufactured by *Merck Millipore*. To begin, the DNA origami was placed in a washed filter device and centrifuged at 10,000 rcf for 150 seconds. Multiple rounds of centrifugation, typically ranging from 4 to 8, were necessary to sufficiently remove the excess staples. For quality control purposes, the ss-DNA concentration in the supernatant was determined using UV-Vis spectrometry.

While electrophoresis was the preferred method for DNA origami purification, due to its ability to separate samples by charge and size, it does have the downside of a longer preparation and postprocessing time, totaling approximately two hours. In contrast, purification via centrifugation was much faster, taking approximately 30 minutes, but was incapable of sorting out non-ideal or agglomerated DNA origami, resulting in lower purification quality. In general, the DNA origami yield was approximately 10-20% with electrophoresis purification, while centrifugation yielded around 50%.

3.4. EBL Fabrication of PSA and Nanostructure Adsorption

The process of creating PSA on a silicon wafer using electron beam lithography (EBL) was depicted in Figure 14a. A p-doped (100) Si wafer (*Plano*) measuring 1×1 cm was subjected to O₂ plasma treatment at 150 W for 20 s using a 100-E Plasma etcher (*TEPLA*) to clean the surface, before the deposition of Hexamethyldisilazane (HMDS) at 150°C for 100 s via physical vapor deposition (PVD) to form a hydrophobic monolayer on the Si surface (Figure 14a, I). After that, a 120 nm thick PMMA layer was spin-coated on the Si wafer using E-beam resist AR-P 672.02 (*Allresist*) at 1000 rpm for 60 s, followed by baking at 150°C for 180 s to eliminate residual solvent. Laser lithography (imageGEO193, *Elemental Scientific Lasers*) was then employed to create markers on the wafer to facilitate the identification of the region of interest for further processing. Subsequently, EBL was carried out using a Helios 5 UX dual beam (*Thermo Scientific*), a Focus Ion Beam Scanning Electron Microscope (FIB-SEM), operated at 30 keV and 1.6 pA electron beam current (Figure 14a, II). The E-beam dosage for rectangular patterns of sizes (100×70) nm², (70×50) nm², and (50×40) nm² was about 240 μC·cm⁻², with dwell times of 600, 1200, and 2400 ns, respectively. The E-beam exposed PMMA was removed by immersing the wafer in a 1:3 mixture of the developer AR 600-55 (*Allresist*) and 2-propanol for 30 s, followed by immersion in the stopper AR 600-60 (*Allresist*) for 30 s. The wafer is then washed with deionized water and dried with an N₂ stream.

a) EBL fabrication of a polar surface array



b) Dark-field microscopy before resist removal c) Cr deposition + Lift-off to confirm PSA size

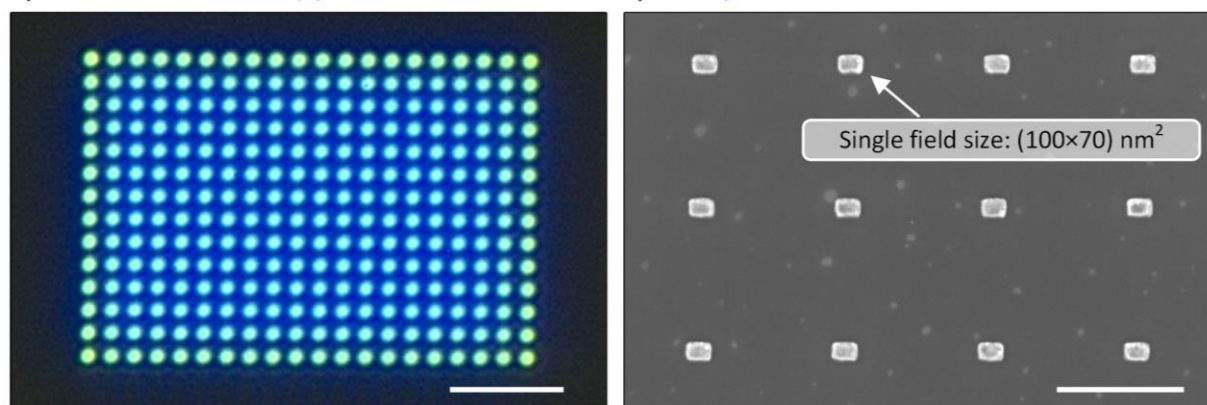


Figure 14: (a) The four-step EBL fabrication process for the polar surface array. (b) Dark-field microscope measurement of the substrate after step II in (a). (c) SEM image of Chromium-deposited PSA fields, created by the Lift-off process. The scale bar is 4 μm in (b) and 500 nm in (c).

The next step involved removing the uncovered HMDS surface with O₂ plasma treatment at 150 W for 20 s, which made the surface hydrophilic. The remained PMMA was removed via ultrasonic for 25 minutes in N-Methyl-2-pyrrolidone (NMP) at 55°C, leaving behind an array of hydrophilic patterns surrounded by hydrophobic surfaces (Figure 14a, III). The PSA was used immediately after fabrication for adsorption experiments (Figure 14a, IV).

To assess the manufacturing quality of the PSA chip, dark-field microscopy (DM2700 M, *Leica*) provided a rapid and effective means. Figure 14b shows a dark-field image of a well-shaped array after E-beam exposure and development. The dark area corresponds to the light-absorbing resist, and the bright spots indicate the scattering of cavities created after the resist development.

Experimental parameters were optimized to achieve a constant and controlled PSA field size. The size of the PSA field can be determined by depositing metal (aluminium, chromium) on the substrate after step II in Figure 14a, followed by the removal of the metal-coated resist. In this process, the deposited metal on the E-beam exposed area remains, and its size can be examined by electron microscopy (Figure 14c), known as the lift-off process.

Possible Reasons for Incorrect PSA Field Sizes:

Poor E-beam focus: The resolution and accuracy of E-beam exposure rely on proper focusing of the E-beam onto the substrate surface. Poor focus often leads to patterns that are too large. Small scratches or impurities near the to-be-exposed area can be helpful in adjusting the focus.

Too small pitch size: The E-beam exhibits a Gaussian-shaped electron density distribution, with the highest intensity at the center. This is similar to the intensity distribution of a focused laser. Typically, only the E-beam intensity at the focus is sufficient for exposure. However, if the distance between two exposed areas (i.e., the pitch) is too small, the area in between may receive sufficient dosage and become developed. This can result in the unwanted inter-connection of neighboring exposed areas. Hence, it is essential to inspect the developed area during EBL fabrication to avoid this effect. Dark-field microscopy is a suitable technique for visualizing the exposed area after development (see Figure 14b).

Improprate E-beam intensity: Insufficient E-beam dosage leads to resist that cannot be removed after exposure since the polymer chain wasn't broken into short-chained oligomers, whereas excessive dosage will create a larger exposed area and increases the PSA field size undesirably. Thus, adjusting the E-beam dosage via dose-testing in combination with the Lift-off process is critical (see Figure 14c).

Incorrect resist thickness: For the EBL fabrication of PSAs, the E-beam dosage in this section was optimized for a resist thickness of 120 nm. If the resist thickness significantly differs from the expected value, e.g., 200 nm instead of 120 nm, the applied E-beam dosage may be insufficient for exposure, resulting in patterns that are typically much smaller or even non-existent. Here, measuring the resist thickness with a profilometer (Tencor P-10 Surface Profiler, *TENCOR*) is recommended.

Note that the E-beam resist AR-P 672.02 contains 2 wt.% PMMA ($M_w \sim 950k$) dissolved in a mixture of chlorobenzene, anisole, and ethyl lactate. If the resist is stored in a sealed container with a significant amount of air, the solvent mixture will evaporate, leading to an increase in PMMA mass fraction and therefore an incorrect resist thickness after spin-coating.

Incomplete resist development and removal: After step II in Figure 14a, the E-beam exposed substrate was developed, and the exposed area should be resist-free. If the development was incomplete and a thin layer of resist remained on the exposed area, this will significantly impact the O₂ plasma etching required to locally remove the hydrophobic HMDS coating. Possible causes are either a too-short development time or an expired developer, as the vapor pressure of 2-propanol and AR 600-55 was different, and the mixing ratio may change over time due to evaporation.

Possible Reasons for Poor Polarity Control on the Substrate:

Deposit HMDS via spin-coating instead of physical vapor deposition (PVD): The HMDS deposition on the substrate via spin-coating would result in a thin layer of physisorbed HMDS that is only weakly attached to the substrate and is unsuitable for further spin-coating of the E-beam resist. On contrary, PVD-deposited HMDS forms a stable chemisorbed $\text{Si}(\text{CH}_3)_3$ monolayer by reacting with the surface Si–OH groups.

No O_2 plasma treatment before HMDS deposition: HMDS only reacts with the surface Si–OH groups at high temperatures (typically $\sim 150^\circ\text{C}$). The natural oxide layer on the Si substrate does not contain sufficient Si–OH groups to form a large-area $\text{Si}(\text{CH}_3)_3$ monolayer. Therefore, an O_2 plasma treatment of the Si substrate before the HMDS deposition is crucial to increase the number of Si–OH groups and remove organic impurities on the surface.

3.5. Sample Storage and Preparation for Measurements

The proper storage and handling of samples is a crucial step that is often overlooked in the process of synthesis and characterization. Inadequate sample treatment may result in contamination, artifacts, and sample decomposition over time. In this section, we present guidelines for the storage and preparation of different samples applied in this work.

Storage of DNA Origami and Its Precursor

The building blocks for DNA origami, i.e., staples and scaffolds, are single-stranded DNA chains. These molecules should be stored at -20°C in their original container upon receipt. Synthesized DNA origami structures can be stored in small plastic tubes, such as *Eppendorf* PCR Tubes with a volume of 0.2 mL. It is recommended that DNA origami be used immediately after synthesis for either characterization or functionalization. In case long-term storage is required, the structures should be stored at -20°C . However, extended storage may result in the adsorption of the DNA origami on the plastic tube and may lead to sample loss. Additionally, freeze-thaw cycles can cause damage to the DNA origami structures, resulting in structural damage and degeneration over time, as observed by AFM after several months of storage.

Storage of DNA-Functionalized AuNPs and Hybrid Nanostructures

Unfunctionalized citrate-capped gold nanoparticles (AuNPs) possess a high degree of solution stability for an extended duration. However, after functionalization with BSPP (a prerequisite for DNA functionalization, as outlined in section 3.2), the colloidal suspension of AuNPs exhibits reduced stability, with a propensity for agglomeration over time. While DNA-functionalized AuNPs may be stored in a refrigerated environment (4°C) for months, the DNA strands attached to the AuNP surface can gradually desorb. Furthermore, it is common to

observe DNA-functionalized AuNPs adsorption onto the plastic tube wall, particularly for particles exceeding 30 nm in diameter. Thus, it is advisable to use DNA-functionalized AuNPs immediately after preparation or be stored in glass tubes at 4°C. To eliminate any unbound ss-DNA in the solution, centrifugation with an Amicon filter must be performed before the AuNPs are subjected to further experimentation.

Hybrid nanostructures can be stored in sealed glass tubes at 4°C. After a few days, precipitation often occurs, and the sample can be retrieved by gently agitating the mixture using a vortex shaker.

Storage of Adsorbed Hybrid Nanostructures on PSA

Following the adsorption of hybrid nanostructures on PSA, storing the sample in a small, sealed container, such as a centrifugation tube or a gel box, is recommended to prevent damage from dust and light.

Sample Preparation for AFM and SERS Measurements on Mica

To enable high-resolution imaging of dried DNA origami or hybrid nanostructures using atomic force microscopy (AFM) and surface-enhanced Raman spectroscopy (SERS), a freshly cleaved mica surface is a suitable substrate. Typically, a droplet of the sample (5-10 μL) was deposited on the substrate and then incubated for five minutes in a humidity chamber. After removing the droplet by rinsing in Milli-Q water and drying with nitrogen stream, the sample is ready for measurement. Alternatively, for AFM imaging in an aqueous environment, the sample was prepared similarly to the in-air imaging method, but instead of drying with nitrogen, a droplet of folding buffer (~ 300 μL) was added after removing unbound samples with Milli-Q water.

Sample Preparation for AFM and SERS Measurements on PSA

A small volume of the nanostructure colloid (~ 0.5 μL) was deposited onto a freshly prepared PSA. The Si chip was then placed in a homemade humid chamber, and after incubation, the chip was washed sequentially with Buffer A, B, and C for five minutes each. The chip is then transferred to 50% aqueous EtOH and incubated for 10 s, followed by 75% EtOH for 20 s and 85% EtOH for two minutes. Finally, the chip was air-dried and ready for measurement. Note that all experiments conducted in this study used an incubation time of 60 min and an Mg^{2+} ion concentration of 40 mM unless otherwise stated.

Sample preparation for electron microscopy

Hybrid nanostructures adsorbed on Si substrate can be directly used for scanning electron microscopy (SEM). It is recommended to use the washing protocol described in section 3.4 to remove buffer (salt) contamination on the sample after drying. DNA origami can be visualized together with gold nanoparticles at low voltage (2-3 kV) and high magnification (typically

above 80,000 \times) with properly adjusted image contrast. Alternatively, transmission SEM (T-SEM) can be utilized for imaging, which requires a transmission electron microscopy (TEM) grid as the substrate. In this case, it is recommended to dilute the DNA origami or hybrid nanostructure with Milli-Q water (at least 10-fold in volume) to minimize salt contamination on the TEM grid.

3.6. Characterization Methods

SERS Imaging

SERS spectra were acquired using a confocal Raman microscope system (alpha300 RA, *WITec*), which was outfitted with an upright optical microscope. The spectra were acquired using a 633 nm excitation laser, which was coupled into a single-mode optical fiber and focused through a 100 \times objective (EC “Epiplan-Neofluar”, NA = 0.9, *Zeiss*). The laser power and integration time were set to 0.05 mW and 2 s, respectively, in conjunction with a dispersive grating of 300 grooves $\cdot\text{mm}^{-1}$ for 2D mappings, unless otherwise stated. The step size was set to 100 nm in both the X and Y directions. The software *Project Five 5.3* was utilized to process the collected SERS spectra, wherein cosmic ray removal was applied, and the background was subtracted.

Alternatively, SERS measurements were also conducted using a confocal Raman Microscope Labram Aramis (*Horiba*), which was equipped with a 633 nm laser source. The incident laser was focused using a 100 \times objective with NA = 0.9 (*Olympus* “MPlan N”, NA = 0.9). The laser power was reduced to \sim 0.01 mW by utilizing a 100 μm slit and a D3 filter. The SERS spectrum was collected over 6 accumulations, each with a 10 s integration time, along with a dispersive grating of 600 grooves $\cdot\text{mm}^{-1}$. The step size for mapping was set to 250 nm in both the X and Y directions.

Atomic Force Microscopy

In this study, Atomic Force Microscopy (AFM) measurements were performed using a Dimension Icon (*Bruker*) instrument. The instrument was operated in ScanAsyst mode with SCANASYST-AIR cantilevers (*Bruker*) for measurements in dried conditions. The ScanAsyst mode is a non-contact mode with automatic parameter adjustment. An integrated algorithm facilitates finding the optimum force, setpoint, and gain. The AFM phase image was obtained using Tapping mode and TESPA-V2 cantilever (*Bruker*). AFM measurements in liquid were conducted using the SNL-10 cantilever (*Bruker*). The typical measurement parameters included a scan speed of 1 line per second and 1024 \times 1024 lines on an area of 3 \times 3 μm . AFM data were processed using *Gwyddion 2.55* software.

Electron Microscopy

Electron microscopy images were obtained using a Focused Ion Beam-Scanning Electron Microscopy (FIB-SEM) (Helios 5 UX DualBeam, *Thermo Fischer*) instrument, with an acceleration voltage of 3 kV. Scanning electron microscopy (SEM) was primarily employed for the characterization of the position of AuNPs and the formation of dimers in this study, in addition to AFM. Furthermore, SEM was able to visualize the DNA origami with proper sample preparation (section 3.5).

UV-Vis Spectroscopy

In this study, the concentration of DNA and AuNPs was determined using an Eppendorf Bio Spectrometer[®] basic (*Eppendorf*) and an Eppendorf μ Cuvette[™] (*Eppendorf*) with a path length of 1 mm, requiring only 3 μ L of the sample. Prior to each measurement, a baseline was recorded with the same solvent as in the sample. The concentration of ss-DNA was estimated by multiplying the extinction at 260 nm by the factor 37 $\mu\text{g}\cdot\text{mL}^{-1}$. The concentration of double-stranded DNA (ds-DNA) and DNA origami was determined with the same method by multiplying with a factor of 50 $\mu\text{g}\cdot\text{mL}^{-1}$.

The concentration of AuNP colloids was calculated using eq. (32), adapted from the work of Haiss et al.¹²⁶ Here, the extinction at $\lambda = 450$ nm (A_{450}) was measured with a path length of 10 mm and divided by the extinction coefficient ϵ_{450} . ϵ_{450} of selected AuNP diameter is listed in Table 4. Using eq. (32), the concentration (c) of the hybrid nanostructure was estimated by the AuNP concentration, assuming that each hybrid nanostructure contains two AuNPs.

$$c = \frac{A_{450}}{\epsilon_{450}} \quad (32)$$

Table 4: Molar decadic extinction coefficient at $\lambda = 450$ nm (ϵ_{450}) for selected AuNP size.

AuNP diameter (nm)	ϵ_{450} ($\text{M}^{-1}\text{cm}^{-1}$)
15	2.18×10^8
20	5.41×10^8
30	1.96×10^9
40	4.92×10^9
60	1.73×10^{10}
80	3.89×10^{10}

4. Plasmonic AuNP-DNA-Origami Hybrid Nanostructure

This chapter presents experimental findings related to single-molecule detection utilizing hybrid nanostructures. The suitable Raman marker was selected through the application of DFT calculation (section 4.1), and the design of the hybrid nanostructure with high Raman enhancement was accomplished through FDTD simulation (section 4.2). The hybrid nanostructure was designed and characterized in section 4.3. The chemical identification of the Raman marker as enabled through the combination of Raman spectroscopy and atomic force microscopy (section 4.4). The benefits and challenges of using Raman spectroscopy for single-molecule detection were highlighted through the results obtained, which build upon established ideas in the literature (section 2.2).

4.1. DFT Analysis of Potential Raman Marker Candidate

In order to achieve successful single-molecule SERS detection, it is essential to carefully select a suitable Raman marker. Several conditions must be considered, including a high Raman scattering cross-section, photostability, and a distinct signal pattern from the surrounding environment, among others. Additionally, it is advantageous if the Raman data for the molecule is available in the literature and if it can be modified on the hybrid nanostructure with ss-DNA.

After careful consideration, the molecule ATTO-633 was selected as a potential subject for single-molecule Raman experiments. The fluorophore ATTO-633 exhibits high photostability and a reduced risk of photodegradation. Furthermore, ATTO-633 can be functionalized with ss-DNA, allowing for its modification on DNA origami. Unfortunately, there was no known Raman spectrum of ATTO-633 available, and therefore DFT was used to predict the Raman spectrum of this molecule.

It is important to note that in a SERS measurement, any substance near the plasmonic hot spot may contribute to the measured Raman spectra, potentially leading to an incorrect interpretation of the measurement data. According to the hybrid nanostructure design (section 4.3), the Raman marker ATTO-633, DNA sequences (adenine, cytosine, guanine, and thymine), and BSPP (a surfactant for AuNP stabilization) were all present in the hot spot. Before conducting any experiments, the Raman spectrum of these molecules was simulated and compared using DFT simulation. Overlapping Raman bands were used as a criterion to rule out inappropriate marker molecules for Raman detection.

The DFT simulation was performed using the software *ORCA 4.1*, utilizing the *BP86* functional and the *def2-TZVP* basis set for molecule structure optimization and calculation of vibration wavenumbers with corresponding Raman activity (S_i). The calculated Raman activity was converted into relative Raman intensity I_i concerning the excitation wavelength using eq. (33), which provides a more accurate intensity ratio between Raman bands.¹²⁷

$$I_i = \frac{f \cdot S_i \cdot (v_0 - v_i)^4}{v_i [1 - e^{(-h \cdot c \cdot v_i / k \cdot T)}]} \quad (33)$$

Equation (33) was adapted from the work of Ciubuc et al.¹²⁷ In this equation, v_0 denotes the excitation frequency, specifically set to 633 nm (equivalent to 15797.79 cm^{-1}). v_i represents the vibrational wavenumber of the i^{th} vibration mode, h is the Planck constant, c is the speed of light, and k is the Boltzmann constant. A normalization factor $f = 10^{-15}$ was used for all peak intensities, as well as a temperature (T) of 293.15 Kelvin.

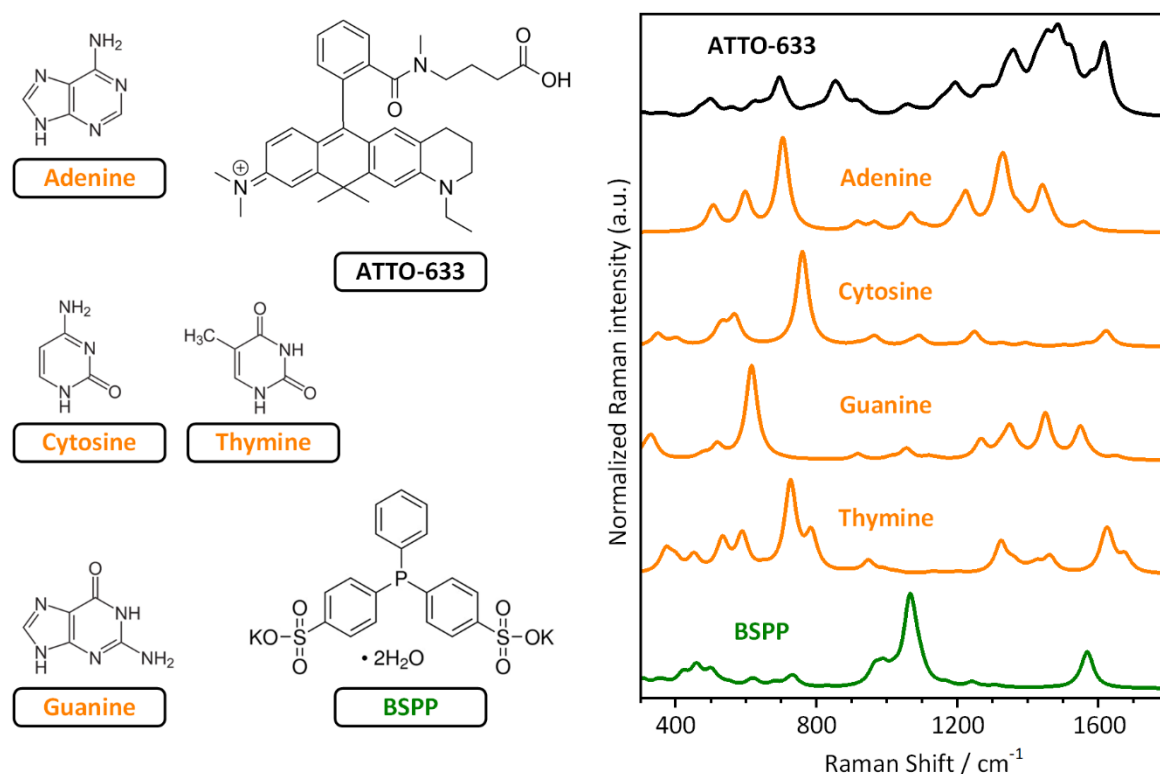


Figure 15: Molecular structures (left) and DFT simulated Raman spectra (right) of the Raman marker candidate ATTO-633 (black spectrum), the four DNA nucleotides (orange spectra), and the AuNP surfactant BSPP (green spectrum).

Subsequently, the calculated Raman intensity was used to generate a spectrum by plotting the calculated vibrational modes, with each vibrational mode set to have an FWHM of 20 cm^{-1} for a more realistic spectrum. Figure 15 displays the molecular structure and DFT-simulated Raman spectra of molecules present in the hot spot that may be detected by SERS. Notably, ATTO-633 exhibits strong vibrational modes between 1400 cm^{-1} and 1600 cm^{-1} . The strongest modes of the four DNA nucleotides were found between 600 cm^{-1} and 800 cm^{-1} , where the potential Raman markers do not show any discernible Raman modes. Moreover, the strongest

Raman band of BSPP was around 1100 cm^{-1} , and its other modes are much less intense, making it distinguishable from ATTO-633.

In summary, the DFT-calculated Raman spectrum of ATTO-633 suggests that it is a suitable Raman marker candidate for modification on hybrid nanostructures for single-molecule investigation.

4.2. FDTD Simulation of Hybrid Nanostructures

Strong Raman signal enhancement is required for the detection of single molecules through Raman spectroscopy. One effective and commonly used technique to achieve this is by employing plasmonic nanostructures, such as surface-enhanced Raman spectroscopy (sections 2.3 and 2.4). In this work, a nanometer-scale cavity was fabricated between two gold nanoparticles using DNA origami techniques to create a plasmonic “hot spot”. The localized surface plasmon resonance (LSPR) on the gold nanoparticle surface increases the amplitude of the electric field, thereby enhancing the Raman signal of any substance present in the hot spot (section 2.4). This is referred to as electromagnetic (EM) enhancement in the literature.²³ The EM enhancement factor, which is the ratio of the enhanced E-field amplitude (E^2) to the E-field amplitude without the plasmonic particle (E_0^2), as shown in eq. (34), was used to quantify this enhancement.

$$EM\text{ enhancement factor} = \frac{E^2}{E_0^2} \quad (34)$$

The EM enhancement factor from an AuNP dimer was simulated using the FDTD method in this section. The highest attainable EM enhancement in the simulation was achieved by varying the hot spot size and AuNP diameters. The simulation region was divided into a cartesian computational grid (mesh), which determines the simulation's resolution. The space inside each grid unit, referred to as a Yee-cell, contains circulating electric and magnetic field components. In the simulation, physical objects were defined by Yee-cells, whose properties include the material's dielectric function. Light is represented by the (time-dependent) propagation of an electromagnetic field. Maxwell's equations are solved within each Yee-cell to calculate the interaction between physical objects and light (section 2.6).

An FDTD simulation of the EM enhancement was conventionally carried out using a non-uniform mesh to reduce computational costs. In order to enhance simulation accuracy and reduce artifacts, the mesh size around the hot spot was set to 0.25 nm. The simulation was performed in a vacuum environment with a pair of AuNP dimers present, possessing diameters varying from 10 nm to 300 nm, and a hot spot size ranging from 2 nm to 15 nm. The excitation light source was a total-field scattered-field source having a wavelength of 633 nm. The refractive index of the AuNP, which determine the material's optical properties, was established based on the work of Johnson and Christy.⁶⁰ As illustrated in Figure 16a, the hot spot area between two 100 nm AuNPs was presented as an example, where the hot spot size

was 10 nm and local EM enhancement was presented by the colored scale. As described in section 2.4, the maximum EF was expected at the surface of an AuNP in the hot spot region. Nevertheless, the cartesian mesh of the FDTD simulation produced an imperfectly smooth AuNP surface, leading to calculation artifacts with abnormally high EM enhancement. To obtain a more representative result, the EM enhancement factor of the 100 nm AuNP dimer shown in Figure 16a was determined by the enhancement at the hot spot center, yielding a value of approximately 73.

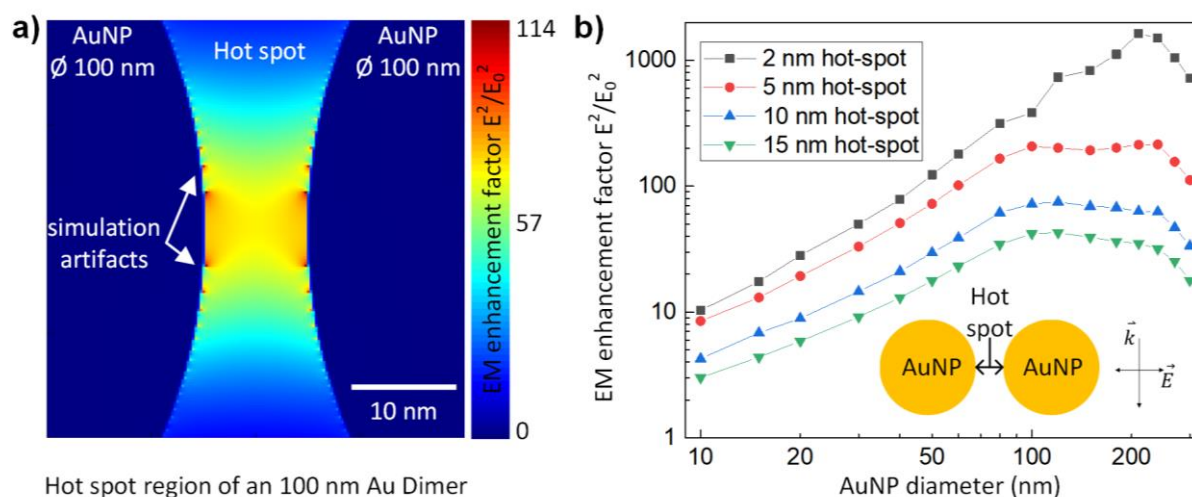


Figure 16: (a) A section of the FDTD simulated EM enhancement between two 100 nm AuNPs with a gap of 10 nm. (b) The FDTD simulated EM enhancement between a pair of AuNPs with various hot spot sizes and AuNP diameters.

Figure 16b displays a plot of the EM enhancement factor for dimers with various diameters and hot spot sizes. Higher EM enhancement was achieved with a smaller hot spot compared to a larger one. The observed trend can be explained by the $1/r^{12}$ decay of the E-field outside a spherical plasmonic nanoparticle, which is very sensitive to any distance change (section 2.4). With a constant hot spot size, the EM enhancement initially increased with increasing AuNP diameter, plateaus between 100 nm and 200 nm AuNP diameter, and then decreases rapidly. This can be attributed to the shifting wavelength of the LSPR mode, which leads to an increase in EM enhancement. As the AuNP diameter increases, the LSPR resonance wavelength approaches the excitation wavelength, thereby enhancing the effectiveness of the EM enhancement.¹²⁸ A larger particle size also leads to increased scattering efficiency and higher EM enhancement, as explained by the Mie theory (section 2.3). Similar observations were made in the study by Liu et al., where the EM enhancement of AuNP dimers with constant gap size and various AuNP diameters is evaluated by FEM simulation and SERS measurements.¹²⁹

In large plasmonic nanoparticles, the interaction with light also stimulates higher-order plasmonic modes, in addition to dipole resonance. However, these high-order plasmonic resonances are only noticeable when the AuNP diameter exceeds 80 nm and do not contribute to the EM enhancement in the hot spot. Consequently, the EM enhancement factor in the hot spot does not increase continuously with increasing AuNP diameter.

4.3. Hybrid Nanostructure Design and Characterization

This section presents the design and characterization of hybrid nanostructures, which were synthesized following the protocol described in section 3.2.

Design of a Hybrid Nanostructure

The significance of a high-EF hot spot for single molecule detection is discussed in section 4.2, where the relationship between AuNP size and the Raman enhancement is examined using FDTD simulation. High EM enhancement can be achieved with a hot spot between a pair of larger AuNPs at a close distance, but at the same time, the synthesis of such AuNP dimers becomes more challenging. Electrostatic repulsion makes it more difficult to immobilize AuNPs with larger sizes on DNA origami and increases the likelihood of AuNP aggregation. In experiments, a hybrid nanostructure containing two 15 nm AuNPs was synthesized with an excellent yield ($> 80\%$ dimers). However, the yield of AuNP dimers decreased significantly with increasing AuNP sizes, with a yield of approximately 30% for two 30 nm AuNPs and less than 10% for two 60 nm AuNPs. Additionally, the synthesis was more likely to yield DNA origami with one AuNP (monomers) instead of two AuNPs (dimers) due to electrostatic repulsion between the AuNPs. Monomers were hard to separate from dimers in gel electrophoresis and they did not provide sufficient EM enhancement for single-molecule Raman detection. As a trade-off between EM enhancement and dimer yield, hybrid nanostructures with a pair of 30 nm AuNPs were selected for the single-molecule experiments in this chapter.

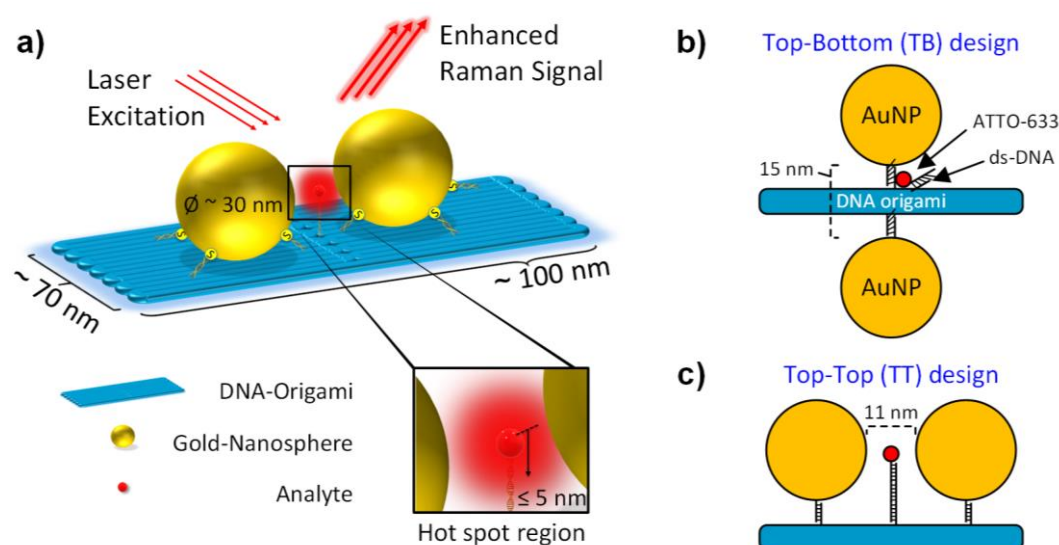


Figure 17: (a) Basic concept of the hybrid nanostructure design. (b, c) Two different binding concepts for the gold nanoparticle on rectangular DNA origami.

The immobilization of plasmonic nanoparticles using DNA origami is a widely recognized method for generating plasmonic hot spots in experimental settings. The hybrid nanostructure employed in this study is illustrated in Figure 17a, where a pair of 30 nm gold nanoparticles were immobilized using a template made from a rectangular DNA origami (NRO). The gold

nanoparticles were functionalized with thiolated ss-DNA and bound with complementary ss-DNA strands that are modified on the DNA origami. One ATTO-633 molecule was placed in the hot spot as the Raman marker. Two different designs for plasmonic hot spots are shown in Figure 17b and 17c. The Top-Bottom design (TB, Figure 17b) entails two AuNPs bound from different sites at the same location on the DNA origami. The ATTO-633 molecule was modified to be at the DNA origami surface, positioned between the AuNPs. The theoretical size of the hot spot in the TB design should be less than 15 nm, which represents the maximum possible distance between the two AuNPs. Conversely, the AuNPs and ATTO-633 molecules were bound to the same site in the Top-Top design (TT, Figure 17c). The anticipated size of the hot spot in the TT design was determined by the AuNP diameter (30 nm) and the binding position of both AuNPs, which possess a distance of 41 nm. Consequently, the projected size of the hot spot in the TT design was 11 nm. Both designs have been synthesized and the results are shown in this section.

The mobility and stability of DNA-functionalized gold nanoparticles during synthesis were highly dependent on the DNA sequence used for the surface modification of AuNPs. According to research conducted by Storhoff et al., thymine exhibits relatively low affinity toward the gold surface, whereas other DNA bases display higher affinity and tend to adsorb on the gold surface.¹³⁰ This important criterion for the selection of ss-DNA surface modification of AuNPs was demonstrated in an experiment depicted in Figure 18. The experiment compared the mobility of AuNPs that were modified with two different thiolated ss-DNA sequences using gel electrophoresis. One ss-DNA sequence consisted of a 30-based oligomer with 10 repetitions of cytosine-cytosine-adenine units and thiol modification at the 5'-end, denoted as $(CCA)_{10}$. The other sequence denoted as T_{19} , comprised a 19-based thymine oligomer with thiol modification at the 5'-end.

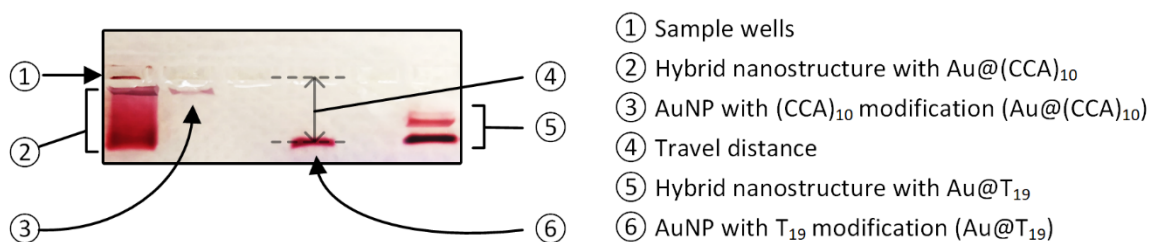


Figure 18: An image of the gel electrophoresis purification of hybrid nanostructures. $(CCA)_{10}$ binding strands used for the AuNP immobilization on DNA origami showing poor binding quality while T_{19} binding strands performed well.

The mobility of the DNA-functionalized AuNPs was evaluated qualitatively by the travel distance in the agarose gel. Experiments demonstrate that gold nanoparticles modified with the thiolated $(CCA)_{10}$ ss-DNA strands (Au@CCA₁₀) exhibit low mobility in gel electrophoreses (Figure 18 ③), in contrast to particles modified with T_{19} strands (Au@T₁₉, Figure 18 ⑥). Au@CCA₁₀ precipitated almost entirely in the sample well (Figure 18 ③), indicating low stability and a high propensity for agglomeration. Consequently, the hybrid nanostructures

made from Au@CCA₁₀ couldn't be purified using gel electrophoresis to segregate dimers from unbound Au@CCA₁₀ (Figure 18 ②).

On the other hand, the purification of hybrid nanostructures with Au@T₁₉ (the right-most column in Figure 18) was successful. The bottom band in Figure 18 ⑤ denotes the unreacted Au@T₁₉, they display the same travel distance as the sample in Figure 18 ⑥, which serves as an internal standard for the travel distance of Au@T₁₉. The hybrid nanostructures formed the second bottom band in Figure 18 ⑤, they had a reduced travel distance in the gel as compared to unbounded Au@T₁₉ due to steric hindrance. Occasional agglomeration of hybrid nanostructures resulted in an even shorter travel distance and produces a weak band at the top of Figure 18 ⑤. Based on these findings, the stable T₁₉ functionalized AuNPs were employed for the fabrication of all hybrid nanostructures in chapter 4.

Characterization of Synthesized NRO and Hybrid Nanostructures

In this section, hybrid nanostructures were synthesized following the TT and the TB design. The geometry of the synthesized NRO, as well as hybrid nanostructures, were characterized by SEM and AFM. The SEM and AFM samples were prepared as described in section 3.5.

Figure 19a depicts the hybrid nanostructures with TT and TB designs after purification using gel electrophoresis. The unbound gold nanoparticles were successfully separated from the hybrid nanostructure, and the two designs did not differ noticeably during the purification process. The scaffold was used as an internal benchmark for the travel distance (Figure 19a ④). Compared to the scaffold, the hybrid nanostructures (Figure 19a ②) exhibited a shorter travel distance, while unbound gold nanoparticles (Figure 19a ③) showed a longer travel distance. The same distance traveled by the loading buffer from each sample well indicated a homogeneous gel without any significant defects caused by gel cracks or electrode damage.

The hybrid nanostructure was obtained after purification with gel electrophoresis, followed the instruction in section 3.3. The synthesis yield and the hot spot size of the hybrid nanostructure were analyzed using transmission scanning electron microscopy (T-SEM). T-SEM images of hybrid nanostructures with 30 nm AuNPs, prepared using the TT and TB designs, are presented in Figure 19b and 19c, respectively. The images contain gold dimers, some of which are marked by red circles. The T-SEM images also show a significant number of isolated gold nanoparticles, as explained in the section above. The T-SEM image analysis revealed that about 40% of AuNPs contributed to dimers with the TB design, while a comparable share of ~33% AuNPs formed a dimer with the TT design (Table 5). The hot spot size of a hybrid nanostructure was typically below 10 nm, as observed in the T-SEM images, which is consistent with expectations. A few hybrid nanostructures exhibited a tiny hot spot, they are anticipated to have high Raman enhancement and are suitable for single-molecule Raman measurements.

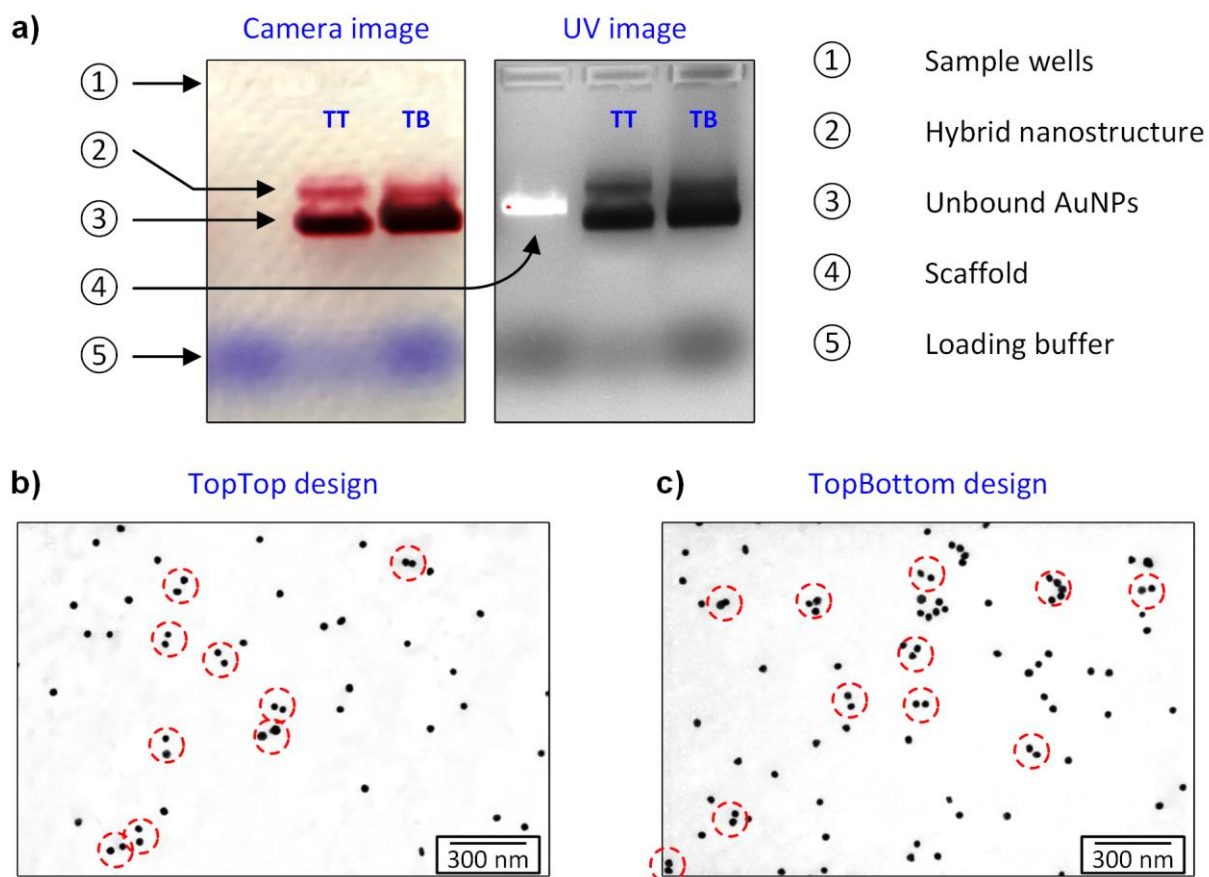


Figure 19: (a) Gel electrophoresis of hybrid nanostructures with the TopTop (TT) and the TopBottom (TB) design. T-SEM images show the extracted hybrid nanostructures with (b) TT and (c) TB designs.

AFM was utilized to visualize the topography of the DNA origami both in liquid and in dried condition. A noteworthy observation is the anisotropic shrinking of rectangular DNA origami after drying. NROs were displayed in Figure 20a when measured in liquid. The size of an NRO was found to be approximately $(95 \times 71) \text{ nm}^2$, which closely matches the theoretical size $(87 \times 71) \text{ nm}^2$. After drying, the size of NRO slightly decreased to $(95 \times 61) \text{ nm}^2$ compared to the AFM measurement in liquid (Figure 20b). It was observed that the structural shrinking was limited to only one direction, which is along the shorter side. The phenomenon could be explained based on the structural construction of NRO, specifically the arrangement of the double-stranded DNA in NRO.

Table 5: The percentage of isolated AuNPs and AuNP dimers from hybrid nanostructures following the TopTop (TT) and the TopBottom (TB) design.

	TT design	Percentage	TB design	Percentage
Number of Total AuNPs	427	100%	445	100%
Isolated AuNPs	285	67%	269	60%
AuNPs that formed dimers	142 (71 dimers)	33%	176 (88 dimers)	40%

The *caDNA* design of the NRO (Appendix A1) revealed that its rectangular structure was composed of 24 double helices of ds-DNA that were parallel-arranged and connected. Each double helix was 256 bases long, equal to 87 nm in length (0.34 nm per base). Additionally, a 32-base single-stranded DNA loop was located at the end of each double helix, which slightly increases the measured length of the double helix. According to an experiment by Rothmund et al., single ds-DNA showed a diameter of approximately 2 nm, and the interhelix gap between adjacent ds-DNAs was 1 nm.¹⁰³ Consequently, an NRO has a total width of 71 nm (24 double helix and 23 gaps).

The shorter side of the NRO was observed to have been reduced from 71 nm to approximately 61 nm after the drying process. It is plausible that the reduction of the interhelix gap causes this phenomenon. In liquid, electrostatic repulsion between negatively charged double helices was compensated by cations, resulting in an equilibrium state of the interhelix gap as observed by Rothmund et al. However, upon drying, attractive interactions such as the capillary force between neighboring ds-DNAs could further reduce the interhelix gap. It should be noted that the anisotropic shrinkage of the NRO is weak and only appears along the shorter axis. Therefore, this effect was not expected to have an impact on the AuNP modification.

The positions of AuNPs and the DNA origami in hybrid nanostructures could be simultaneously determined using AFM measurements. This approach offered more detailed information compared to T-SEM, as it enabled the identification of whether an AuNP was attached to DNA origami or not. Following purification by gel electrophoresis, the hybrid nanostructures were examined via AFM, as depicted in Figure 20c. The results revealed a mixture of hybrid nanostructures, including those containing two AuNPs, one AuNP, and DNA origami without any attached AuNPs. The AFM tip geometry may result in a lateral size of AuNPs that is slightly larger than the actual size, while the measured height was deemed accurate. Therefore, the AuNPs may appear to have a lateral size greater than 30 nm, as illustrated in Figure 20d and 20e.

Two regions from Figure 20c, each denoted by a white square, were enlarged and displayed in Figure 20d. The top image from Figure 20d present a hybrid nanostructure with two AuNPs and a DNA origami without any attached AuNPs, where the outline of the DNA origami underneath the AuNPs remains visible. The height profiles of both nanostructures, marked with a white line in Figure 20d, are displayed in Figure 20e. The top graph of Figure 20e shows a pair of AuNPs from the hybrid nanostructure with a height of approximately 30 nm, and the DNA origami beneath the AuNPs is represented as the shoulder adjacent to the AuNPs. The bottom graph of Figure 20e presents the height of the DNA origami, which is roughly 2 nm and corresponds to literature descriptions.

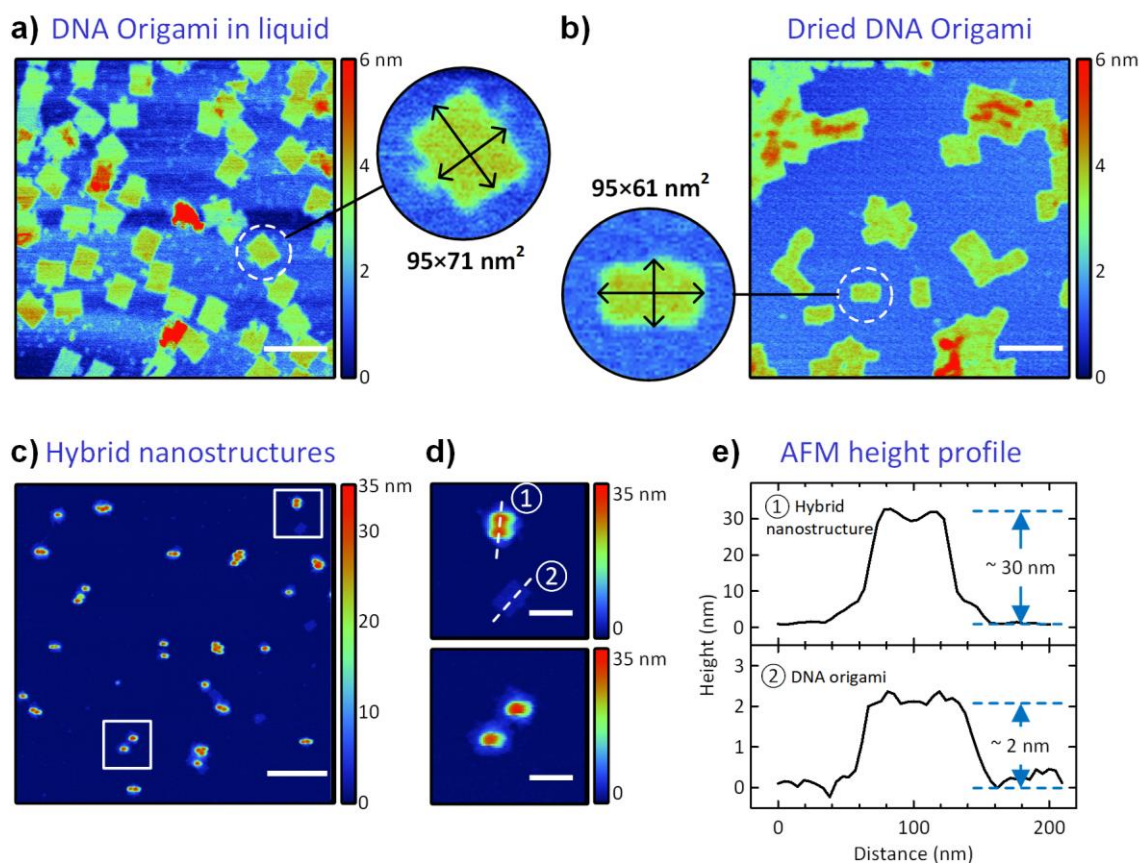


Figure 20: AFM measurement of DNA origami (a) in liquid and (b) in dried condition on mica. (c) AFM measurement of dried hybrid nanostructures on mica. (d) Two enlarged areas display a hybrid nanostructure and a DNA origami (top image), and two unideal hybrid nanostructures with only one gold nanoparticle (bottom image). (e) The height profile of a hybrid nanostructure (top) and a DNA origami (bottom), the line profiles are marked as white lines in the top image of (d). Scales bar are 200 nm in (a, b), 400 nm in (c), and 100 nm in (d).

Both hybrid nanostructures, as well as isolated AuNPs, were present in T-SEM images and AFM measurements. Synthesizing hybrid nanostructures with larger AuNPs (diameter > 30 nm) typically resulted in a higher yield of hybrid nanostructures with only one AuNP instead of the intended two, compared to using smaller AuNPs (diameter < 15 nm). One possible explanation is that the negatively charged, DNA-functionalized AuNPs experience stronger electrostatic repulsion when they are larger, especially when they are positioned at close distances. As a result, DNA origami is less likely to bind two large AuNPs rather than only one AuNP. Another reason for the mixed yield of hybrid nanostructures with one and two AuNPs is that their hydrodynamic radii are similar, making it difficult to separate them efficiently using gel electrophoresis.¹³¹

The findings of this section demonstrate the successful design and characterization of DNA origami and hybrid nanostructures. By combining DNA origami and AuNPs, a small plasmonic hot spot was formed. The following section presents an analysis of single-molecule Raman measurements performed on these hybrid nanostructures.

4.4. Correlated AFM/SERS Measurement

In this section, single-molecule SERS detection of ATTO-633 was performed on hybrid nanostructures. The combination of AFM and SERS measurements provides the advantage of precise local topography measurement and spectral identification of the Raman marker. This approach enables the assignment of the SERS spectrum to the correlated hybrid nanostructure. Two correlated AFM/SERS experiments of hybrid nanostructures are presented in this section. The first experiment successfully identified ATTO-633 molecule using the Raman spectroscope Labram Aramis, by the vibrational modes observed at 1195 cm^{-1} , 1264 cm^{-1} , 1362 cm^{-1} , and 1617 cm^{-1} . The second experiment, conducted with the spectroscope WITec alpha300 RA and the same hybrid nanostructure, was unable to identify ATTO-633. This is a common observation when performing single-molecule SERS experiments, attributed to photodegeneration.

ATTO-633 Identification with Hybrid Nanostructures

SERS mapping was conducted using the Labram Aramis measurement setup, as described in section 3.6, with sample preparation detailed in section 3.5.

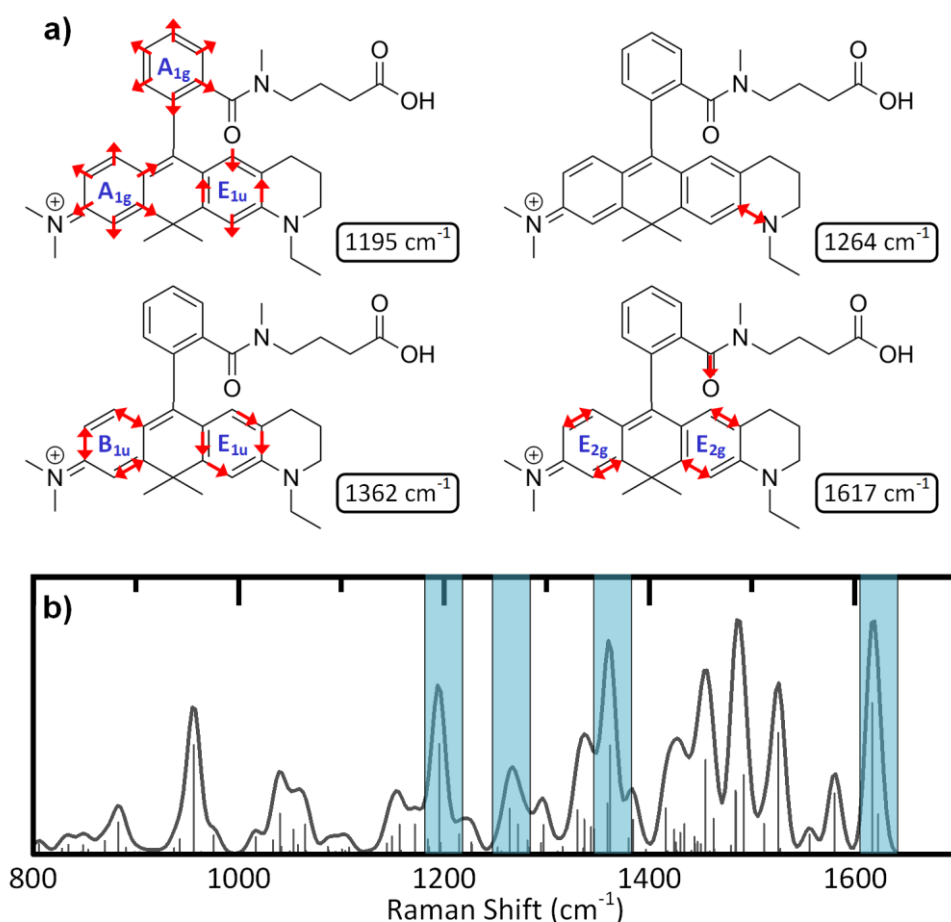


Figure 21: (a) Molecular vibration modes of ATTO-633 at selected vibrational frequencies and the vibrational symmetry of the phenyl-groups (in blue). (b) DFT simulated Raman spectrum of ATTO-633. Blue stripes mark the vibrational modes that were used to identify ATTO-633.

The DFT simulation (Figure 21b) was employed to determine the primary vibrational mode of the ATTO-633 molecule that generates the observed Raman signal. The four characteristic vibrational modes are presented in Figure 21a. The 1195 cm^{-1} band is primarily contributed by the phenyl groups, with two of them exhibiting ring breathing mode (A_{1g}), and one exhibiting ring stretching mode (B_{2u}). The piperidine group's C–N stretching generates the 1264 cm^{-1} mode. The 1362 cm^{-1} band is contributed by two ring stretching modes with different symmetries (B_{1u} and E_{1u}). Additionally, the 1617 cm^{-1} band is attributed to the C=O stretching of the amide group and the ring stretching mode (E_{2g}) of the two phenyl groups.

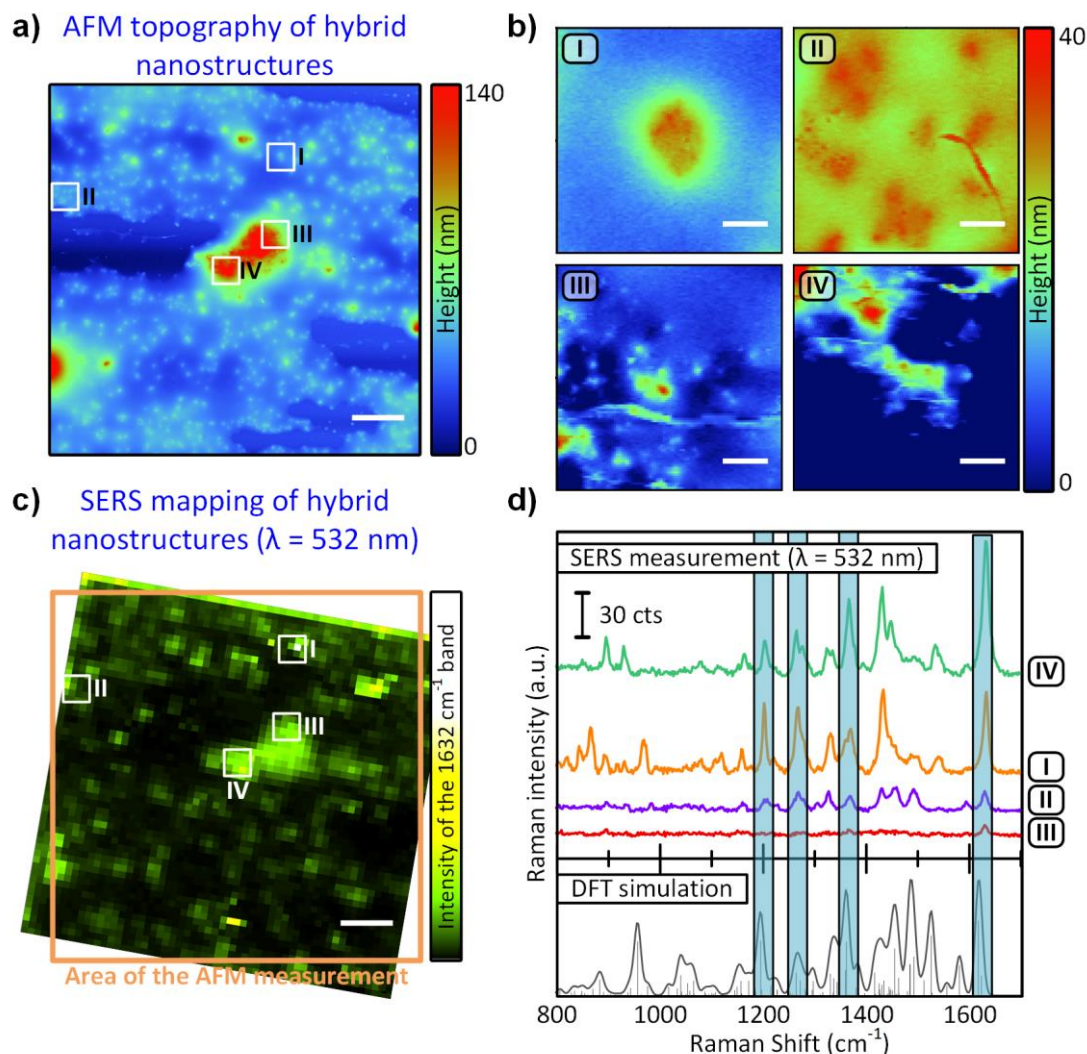


Figure 22: (a) AFM measurement of hybrid nanostructures deposited on mica substrate. (b) Magnification of four areas from (a) with Roman numerals I–IV. (c) SERS mapping of hybrid nanostructures, the orange frame marks the same area characterized by AFM. (d) SERS spectra from the marked area I–IV, compared with DFT-simulated Raman spectra of ATTO-633. The typical vibrational modes of ATTO-633 are marked with blue stripes. The vertical black lines are the position and the intensity of the DFT simulated vibrational modes. Scale bars are $2\text{ }\mu\text{m}$ in (a), 200 nm in (b), and $2\text{ }\mu\text{m}$ in (c).

Figure 22a displays the AFM measurement of hybrid nanostructures (light green dots), which were distributed over the entire mica substrate. Additionally, a thin layer (~10 nm thickness) of an unknown substance covered the measured area. This substance was believed to be residual salts and organics from the TAE buffer, which were not entirely removed during the sample preparation process. The region in the center of Figure 22a indicates the presence of a cluster of hybrid nanostructures mixed with salts and organics from the buffer.

Four areas with hybrid nanostructures were identified in Figure 22b, which showed SERS signals of ATTO-633. These areas are also marked in Figure 22a and 22c and labeled with Roman numerals. Due to the thin layer of salts, AFM couldn't clearly resolve the hybrid nanostructures. Nonetheless, some agglomerated nanostructures were recognizable in Figure 22b (I) by the red dots, and Figure 22b (II) contains numerous nanostructures within a small area. Unfortunately, the plasmonic nanostructures were not clearly visible in Figure 22b (III, IV). However, we could infer that each image contains a dozen nanostructures.

The SERS mapping results are presented in Figure 22c, with the area of AFM measurement (Figure 22a) indicated by an orange rectangle. The intensity and location of the SERS signal at 1632 cm^{-1} , which was utilized for identifying ATTO-633, are represented by green-yellow pixels. The overlap between the AFM and SERS measurements reveals several regions (white rectangles) that possess hybrid nanostructures and simultaneously display the characteristic ATTO-633 SERS signals. Particularly strong SERS signals were observed from the cluster of hybrid nanostructures located at the center and bottom-left of Figure 22a.

The SERS spectra of areas I–IV from Figure 22c were compared with the DFT-simulated Raman spectrum of ATTO-633 in Figure 22d. The blue stripes indicate the four typical vibrational modes of ATTO-633, which were visible in all four SERS spectra, although their intensity varies considerably. Despite containing a smaller number of hybrid nanostructures, area (I) exhibited a SERS intensity four times higher than that of area (II) (Figure 22b).

Similar results were observed when comparing the SERS spectra from regions (III) and (IV) shown in Figure 22d. Although both spectra were obtained from a large, agglomerated cluster of hybrid nanostructures, the SERS intensity of (III) was barely above the detection limit and was much weaker than that of (IV). The substantial difference in intensity was most likely due to the variations in the size of the hot spots rather than the measurement of a different number of hybrid nanostructures. This observation is supported by the following estimation: varying hot spot sizes ranging from a few nm to 10 nm were observed in the T-SEM images presented in section 4.3. According to the FDTD simulation (Figure 16), the EF enhancement (E^2/E_0^2) of a 2 nm hot spot was approximately 3.3 times greater than that of a 10 nm hot spot (AuNP diameter = 30 nm). As a result, the E^4 -approximation (section 2.4) estimates that the SERS enhancement at the 2 nm hot spot was about 11 times higher. This demonstrates the high sensitivity of the SERS intensity to the hot spot size and highlights that a single hybrid nanostructure with a small hot spot was more likely to be the source of high SERS intensity than multiple nanostructures with large hot spots.

Furthermore, a notable feature of the SERS spectra depicted in Figure 22d was the variation in the SERS peak ratio. The four marked Raman modes from (I, II) show roughly the same intensity. Conversely, the 1617 cm^{-1} band had the highest intensity in the spectra of (III, IV). This discrepancy suggests that either the steric hindrance of the ATTO-633 molecule or a charge transfer effect toward the gold nanoparticle could alter the C=O stretching band at 1617 cm^{-1} , thereby affecting the SERS intensity of this mode.

It is noteworthy that the SERS measurement appears to be unaffected by the buffer residue, which covered most of the hybrid nanostructures displayed by the AFM measurement. While TRIS and sodium acetate comprise the majority of the TAE buffer, the typical Raman signals of 1139 cm^{-1} and 1300 cm^{-1} for TRIS and 927 cm^{-1} for sodium acetate were not present in the SERS measurement.^{132,133}

Overall, the successful chemical identification of ATTO-633 with the synthesized hybrid nanostructures was demonstrated through the correlated AFM/SERS experiment. The SERS signal was generated by a small number of hybrid nanostructures, each containing a single ATTO-633 molecule, and the Raman peak position corresponded to the DFT-simulated Raman spectrum. The SERS spectra could be assigned to the corresponding hybrid nanostructures, which were confirmed with AFM. However, the agglomeration of hybrid nanostructures posed a hindrance to single-molecule detection with SERS, which remained a challenge in collecting the spectrum of a single hybrid nanostructure. It is important to note that the measured SERS intensity was determined by the hot spot size rather than the quantity of hybrid nanostructures. This aspect is crucial to consider when quantifying molecules at the single-molecule level, since the measured SERS intensity is not scaling with the number of detected entities.

Unexpected SERS Signals and Photodegeneration

The following experiment shows the correlated AFM/SERS mapping of the same sample that has been characterized in the section above. The measured area was marked by four laser ablation-generated spots as reference points for AFM and SERS mapping. The SERS spectra were acquired with WITec alpha300 RA using a 633 nm excitation laser and focused through a $100\times$ objective (Zeiss EC “Epiplan-Neofluar”, NA = 0.9). The laser power and integration time were set to 1 mW and 1 s, the step size was 100 nm in X and Y directions in combination with a dispersive grating of $1200\text{ grooves}\cdot\text{mm}^{-1}$.

Figure 23a illustrates the correlated AFM/SERS mapping of the same sample as in the preceding section, albeit at a different location. The AFM measurement result is displayed as a black-and-white image, where the hybrid nanostructures are depicted by white dots. In contrast to Figure 22a, no significant buffer residue was visible in the AFM measurement. The green clouds mark the locations of the SERS signals, which, unlike the previous experiment, illustrate the intensity of the entire Raman spectrum, regardless of its vibrational frequency. Notably, the positions of the green clouds align perfectly with the locations of the hybrid nanostructures, verifying that the Raman signals indeed originate from these areas.

The origin of the SERS signal from six hybrid nanostructures is marked by the red rectangles, and the spectra shown in Figure 23b. Figure 23c presents a magnified view of these regions, where the overlapping SERS signal and the hybrid nanostructure are shown in each image.

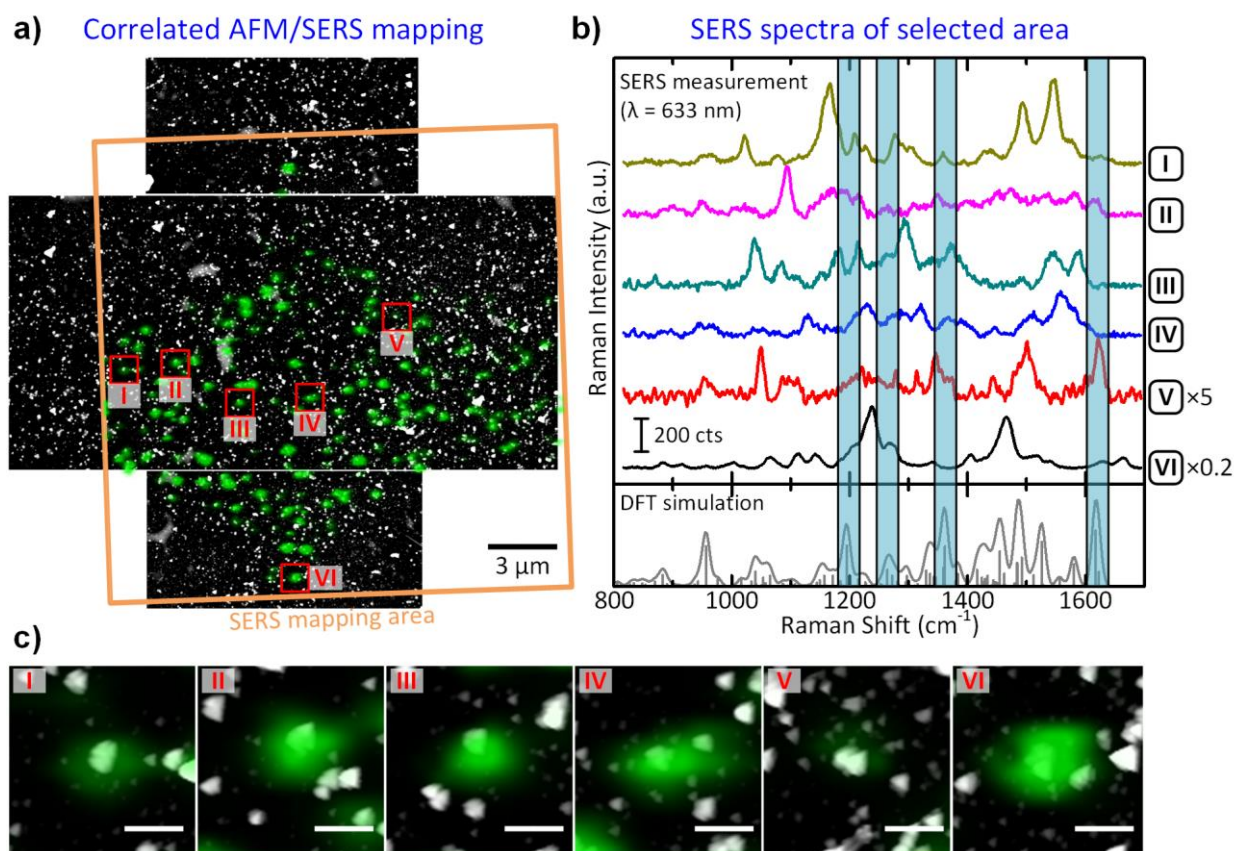


Figure 23: (a) Correlated AFM/SERS mapping of hybrid nanostructures with a single ATTO-633 molecule. The black/white image is the AFM measurement, each white dot shows the location of a gold nanoparticle. The green area shows the location of SERS signals. The SERS spectra from selected areas in (a) are presented in (b) and compared with the DFT simulation of ATTO-633. The typical vibrational modes of ATTO-633 were marked with blue stripes. (c) The overlap of AFM and SERS measurement of the six selected areas I–VI, the scale bars are 150 nm.

Notably, not every hybrid nanostructure in Figure 23a produced a detectable SERS signal, which could be attributed to two primary factors. Firstly, a highly focused UV laser was used to mark the four edges (which have been cropped out) of the measured area for AFM and SERS resulting in not only a ~5 μm hole in the substrate but also damaged any nearby organic substances. As a result, there was no detectable SERS signal around the four edges of the mapping area. Secondly, some hybrid nanostructures may not offer sufficient SERS enhancement due to their large hot spot size, which explains the absence of a detectable SERS signal in some of the hybrid nanostructures, as shown in Figure 23c.

Figure 23b exhibits the SERS spectra for the six marked areas and compares them with DFT simulated ATTO-633 Raman spectrum. The ATTO-633 typical vibrational bands, as previously discussed, were designated by blue stripes. Although all six SERS spectra had notable vibration bands, the number and the position of vibrational bands vary significantly.

Only spectra (II, V) were moderately similar to the DFT-calculated ATTO-633 spectrum, with the peak at 1617 cm^{-1} and 1362 cm^{-1} being distinguishable with some degree of imagination. The other four spectra showed intense Raman peaks at locations that are atypical for ATTO-633. In summary, the SERS signal obtained from the six areas were neither comparable nor can be unambiguously assigned to ATTO-633.

To understand why the results in this section differ from the successful identification from the previous section, it is necessary to analyze the measurement conditions and understand what could occur during the process. In contrast to the previous experiment, a considerably higher laser power (1 mW instead of 0.01 mW) was applied here. The increased laser power may lead to stronger plasmonic heating and photodegradation of organic substances such as ATTO-633, DNA fragments, and BSPP within the hot spot. Molecule fragments or even amorphous carbon may form in situ within the plasmonic hot spot. The non-reproducible spectra in Figure 23b were likely caused by the uncontrolled degradation, which results in the Raman detection of unknown species.

The phenomenon referred to as photocatalytic degradation was well documented in the literature, as described by Heck et al. in their SERS mapping of hybrid nanostructures using varying measurement setups, including different laser powers, laser wavelengths, and nanoparticle materials (gold and silver).³⁸ Their findings suggest that silver nanoparticle-containing hybrid nanostructures were more susceptible to photocatalytic degradation compared to gold nanoparticle-containing ones when subjected to the same laser power. Additionally, high laser power and excitation laser wavelength near the LSPR maximum could also cause undesired sample degeneration. These two observations correspond with the higher SERS efficiency of silver compared to gold, and higher SERS efficiency when the exciting laser wavelength was close to the LSPR band. Heck et al. provided two explanations for the photocatalytic degradation. The first explanation was the thermal excitation of plasmonic nanostructures, where photon energy was absorbed and converted into heat, leading to the thermal degeneration of molecules. The second explanation was the generation of hot electrons that are capable of ionizing organic molecules, resulting in molecular fragmentation.^{134,135}

In summary, this section illustrates a common issue that may lead to an inaccurate interpretation of SERS measurements. It is crucial to take preventive measures to avoid photodamage to the analyte molecule. Achieving an optimal result for single-molecule SERS measurements requires careful balancing of laser power and integration time. While high laser power can yield a good signal-to-noise ratio of the SERS spectrum, it also carries the risk of photodegradation. Similarly, combining low laser power and long integration times can lead to a good signal-to-noise ratio, but the laser power may not be adequate to generate a detectable SERS signal.

5. Controlled Adsorption of Hybrid Nanostructures on PSA

This chapter is dedicated to the development of the Polar Surface Array (PSA), a selective-adsorbing substrate for single-molecule SERS experiments. The adsorption mechanism of hybrid nanostructures on the PSA has been investigated both experimentally and by DFT simulation, shedding light on the controllability and precision of location-controlled adsorption. Furthermore, this chapter will delve into the application of PSA on SERS-based techniques for single-molecule quantification. Finally, an initial exploration of combining single-molecule SERS with the isotope dilution method will be presented, showcasing the potential for achieving SI-traceable quantification.

Results from section 4.4 demonstrated the successful identification of the ATTO-633 molecule by SERS measurement on hybrid nanostructures at extremely low molecule concentrations. However, the realization of true single-molecule SERS detection requires the spectrum of only one hybrid nanostructure. The natural tendency of nanostructure to form agglomeration, as demonstrated in the work of Bartschmid et al., is a hindrance to the single-molecule experiment in general (Figure 24a).¹³⁶ Since the spatial resolution of confocal Raman microscopy is limited by the Rayleigh criterion, which is controlled by the laser wavelength and the numerical aperture of the objective (section 2.1), the spectroscopy cannot resolve the signal from two neighboring nanostructures closer than the resolution limit (Figure 24d). Simply reducing the number of nanostructures by dilution does not guarantee agglomeration-free adsorption (Figure 24b and 24e). It rather reduces the chance of finding a plasmonic nanostructure and thereby increase the measurement time and the experimental effort.

One solution to overcome the agglomeration is to increase the resolution of the measurement method, e.g., super-resolution fluorescence spectroscopy. Unfortunately, this method is not applicable to Raman spectroscopy yet. An alternative way to overcome the resolution limitation is to ensure a minimum distance between each hybrid nanostructure, as schematically shown in Figure 24c. This ensures a controllable minimum distance that is greater than the Rayleigh criterion (Figure 24f). This idea is picked and followed in this chapter, and the substrate for such adsorption-controlled experiments was developed and referred to as Polar Surface Arrays (PSA).

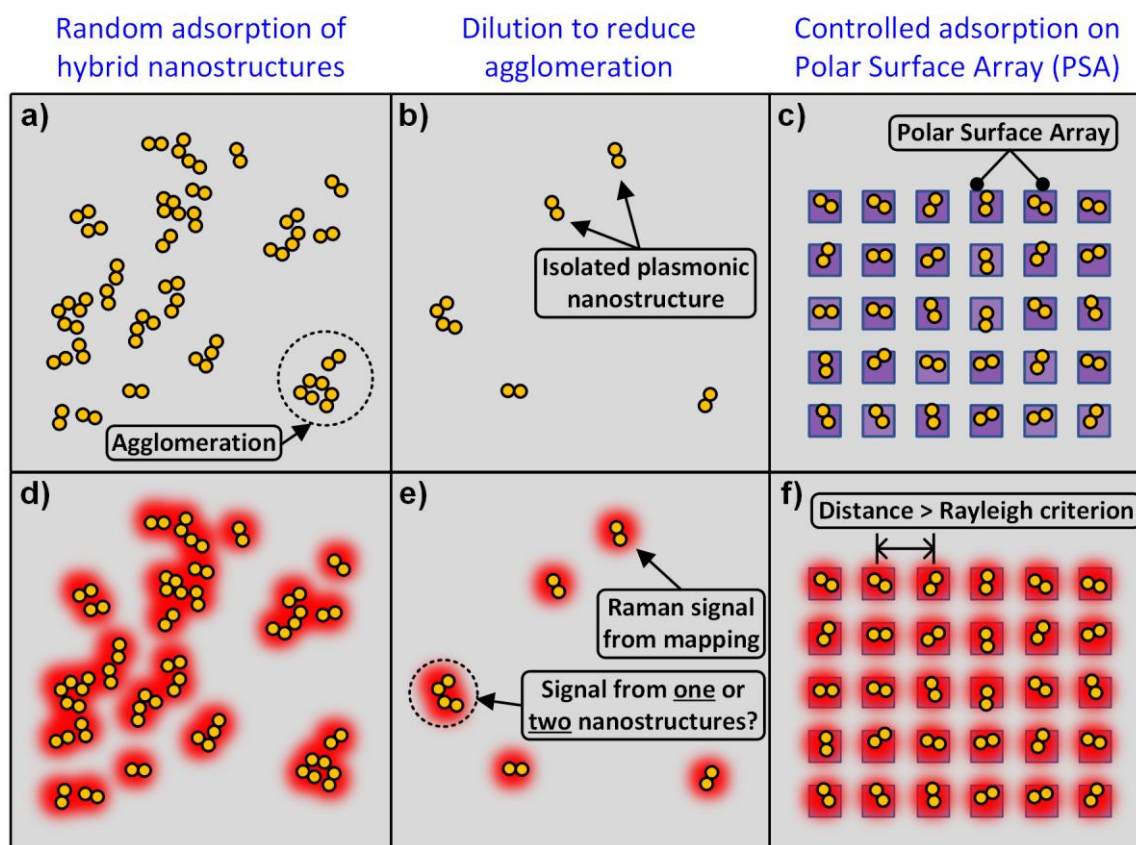


Figure 24: Hypothetical microscopy images and the corresponding Raman signal location, with (a, d) high concentrations of hybrid nanostructures, (b, e) low concentrations, or (c, f) placed on a Polar Surface Array with an inter-structural distance larger than the diffraction limit of Raman spectroscopy.

5.1. Selective Adsorption on a Substrate

The idea of selective adsorption is based on the assumption, that the adsorption location of hybrid nanostructures can be controlled with intrinsic properties (i.e., different adsorption energy on surfaces) on a large scale. The adsorption process should be thermodynamically driven and determined by the substrate-nanostructure interaction. Alternatively, external influence (like light trapping or the manual movement by AFM tip) could be applied to control the adsorption location, but this is difficult to implement on the nanoscale and uneconomical for up-scaling. In this chapter, we implemented the controlled adsorption of hybrid nanostructures by tuning the substrate polarity. This idea was inspired by the work of Kershner et al., who realized the controlled adsorption of DNA origami on a silicon-based hydrophilic substrate in 2009.¹³⁷

Selective Adsorption on Si–Au Substrates

The hybrid nanostructure used in this work was constructed on rectangular DNA origami, but the structure includes additional plasmonic nanoparticles which may influence the properties of the nanostructure (e.g. surface charge or the diffusion in liquid) and thus the adsorption behavior on a substrate. Here, a proof-of-concept experiment was conducted to validate the controlled adsorption of hybrid nanostructures on the hydrophilic and hydrophobic substrates. For this experiment, hybrid nanostructures with two 15 nm AuNPs were adsorbed on a silicon substrate which contained additional gold structures on the surface. The gold structures were created by the lift-off technique combined with E-beam lithography.

Naturally, the surface of Si and Au were both hydrophilic. To modify the surface polarity, the Si surface was selectively coated with a hydrophobic $\text{Si}(\text{CH}_3)_3$ monolayer by the thermal decomposition of Hexamethyldisilazane (HMDS) at 150 °C, while the Au surface remained hydrophilic. In this case, the Si surface was treated with an O_2 plasma before HMDS deposition to increase the number of Si–O and Si–OH groups on the Si surface, which reacts with HMDS. There were two advantages to using a substrate with two materials on the surface for the adsorption experiment. Firstly, the surface polarity could be tuned separately due to different material properties and secondly, it gave a good contrast for the visualization, showing a clear boundary between the materials and the between the hydrophilic and hydrophobic areas.

The hybrid nanostructures in suspension were deposited on the Si–Au surface by drop-casting and were placed in a humidity chamber for one-hour incubation (more details in section 3.5). The humidity chamber prevents the sample droplet from evaporation and drying out, which would otherwise accelerate the adsorption and lead to forced adsorption.

After the hybrid nanostructure deposition, the unbound nanostructures were removed by rinsing in water. The adsorbed hybrid nanostructures were characterized by AFM and the adsorption efficiency of the polar and apolar substrate (i.e., the number of adsorbed nanostructures divided by the substrate area) was compared qualitatively.

Figure 25a depicts the deposition of hybrid nanostructures on an untreated silicon-gold substrate. The sketch on the left side displays the observed binding results on the (both hydrophilic) Si and Au surface. Here, the AFM measurements on the right showed evenly distributed hybrid nanostructures on the whole substrate while both surfaces indicated comparable adsorption efficiency. After turning the polarity of the Si substrate to hydrophobic (Figure 25b) as described above, we observed that the hybrid nanostructures overwhelmingly adsorb on the hydrophilic Au surface while avoiding the hydrophobic Si surface. This observation corresponds with the experimental finding of Kershner et al. and confirmed the polarity-depending adsorption of hybrid nanostructures.¹³⁷

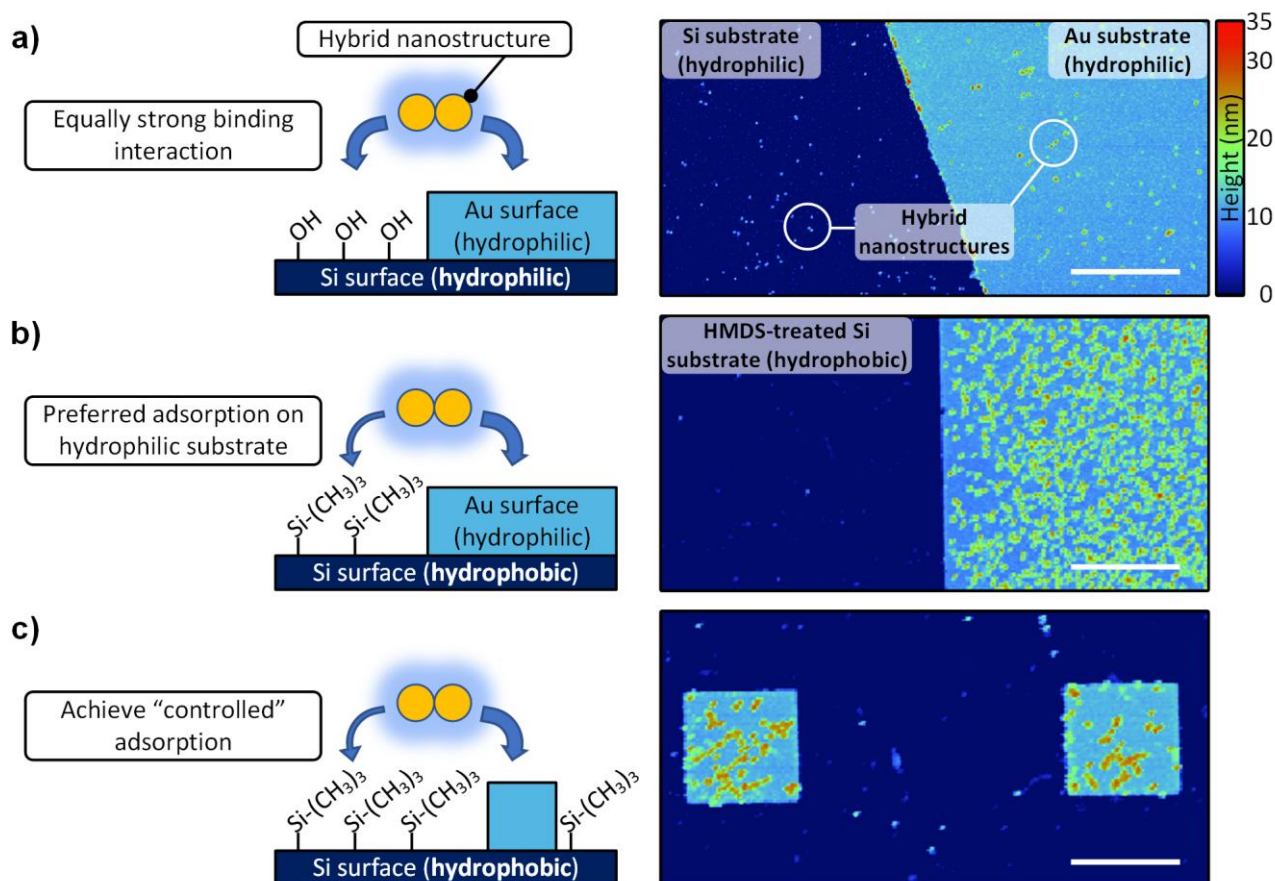


Figure 25: Sketches (left) and AFM measurements (right) of hybrid nanostructures adsorbing on different surfaces. (a) Adsorption on hydrophilic silicon and gold surfaces. (b) Adsorption on HMDS-treated hydrophobic silicon surface and hydrophilic gold surface. (c) Adsorption on HMDS-treated hydrophobic silicon surface and small hydrophilic gold islands. Scale bars in (a–c): 1 μm .

A first step toward the isolation of a single hybrid nanostructure was to reduce the area of adsorption as shown in Figure 25c. Here, the $1 \times 1 \mu\text{m}^2$ hydrophilic Au islands were surrounded by hydrophobic Si surfaces, and the selective adsorption of hybrid nanostructures was confirmed again. Only a very small number of hybrid nanostructures remained on the hydrophobic surface. This case is unfavorable from the aspect of adsorption energy (and will be discussed in section 5.2), but can be explained by either defect in the hydrophobic monolayer or low mobility of the nanostructure during the deposition that leads to a metastable adsorption condition (i.e. forced adsorption).

Selective Adsorption on Si Substrate

The last section described the polarity-depending adsorption of hybrid nanostructures on a silicon-gold substrate. With the aim of reducing the cost and workload of the substrate processing, an alternative concept of creating patterns with opposing polarity was applied on a pure Si wafer using E-beam lithography, as described in section 3.4. Here, the hydrophobic area on the Si substrate was covered by a Si(CH₃)₃ monolayer, created by HMDS decomposition.

The hydrophilic area contains Si–OH groups generated by position-restricted O₂ plasma treatment. The concept of creating a hydrophilic pattern directly on a Si wafer was also adapted from the work of Kershner et al., and the substrates created in this way were referred to as Polar Surface Array (PSA) in this work.¹³⁷

Figure 26a depicts the adsorption of hybrid nanostructures on a PSA, polar stripes with 400 nm width and 800 nm pitch between the stripes were created and surrounded by hydrophobic Si surfaces. Although the SEM measurement could not display the polarity of the surface directly, the selectively adsorbed hybrid nanostructures (white dots) clearly reveal the hydrophilic stripe pattern on the PSA substrate.

One phenomenon of hybrid nanostructure adsorption was that a small number of nanostructures remained on the hydrophobic surface, similar to the AFM results in Figure 25b and 25c. The undesired adsorption could be specifically removed by washing the hybrid nanostructure-loaded PSA with a buffer solution that contains 0.07 wt.% of Polysorbate 20 (Tween 20). This washing process (section 3.5) was adapted from the work of Shetty et al.¹³⁸

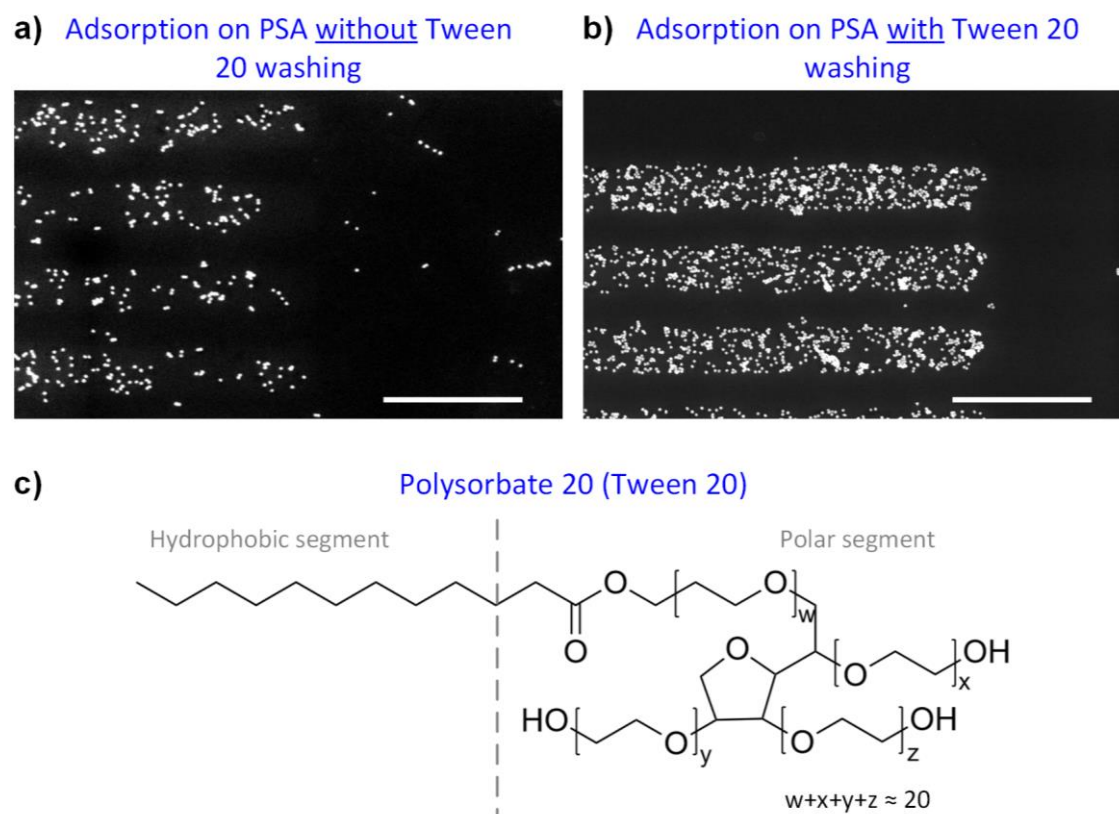


Figure 26: SEM image of hybrid nanostructures adsorption on a PSA with hydrophilic stripes, (a) without and (b) with Tween 20 washing. (c) Molecular structure of Polysorbate 20 (Tween 20). Scale bars are 1 μm in (a, b).

Figure 26b shows the hybrid nanostructure adsorption on PSA while adapting the Tween 20 washing process. Here, the contrast between the hydrophilic stripe pattern and the surrounding hydrophobic area was more pronounced and the undesired adsorption on the hydrophobic area (like in Figure 26a) was clearly confined. Tween 20 is a surfactant that has a high affinity

toward the hydrophobic $\text{Si}(\text{CH}_3)_3$ layer due to a long aliphatic chain (Figure 26c). This molecule substitutes the weakly bounded hybrid nanostructures on the hydrophobic area but does seem not to affect the hybrid nanostructures on the hydrophilic area. The result of the washing process indicates that the attractive interaction between the hydrophobic surface and Tween 20 was higher, while its binding attraction toward the hydrophilic surface was weaker compared with the adsorbed hybrid nanostructure. The Tween 20 washing process was applied for all experiments in sections 5.4, 5.5, and 5.6.

Selective Adsorption of Hybrid Nanostructure Components

Since the hybrid nanostructure consists of DNA origami and gold nanoparticles, we want to find out whether each of the single components has different adsorption behavior on the polar surface array, which may influence the adsorption mechanism. For this investigation, a PSA with an array of $(200 \times 200) \text{ nm}^2$ polar fields was used as an adsorption substrate, the pitch between each field was 500 nm. Rectangular DNA origami, as well as citrate capped AuNPs ($\text{O} 20 \text{ nm}$), were separately incubated on the PSA for one hour, followed by Tween 20 washing. AFM measurement was carried out for the localization of the adsorbates.

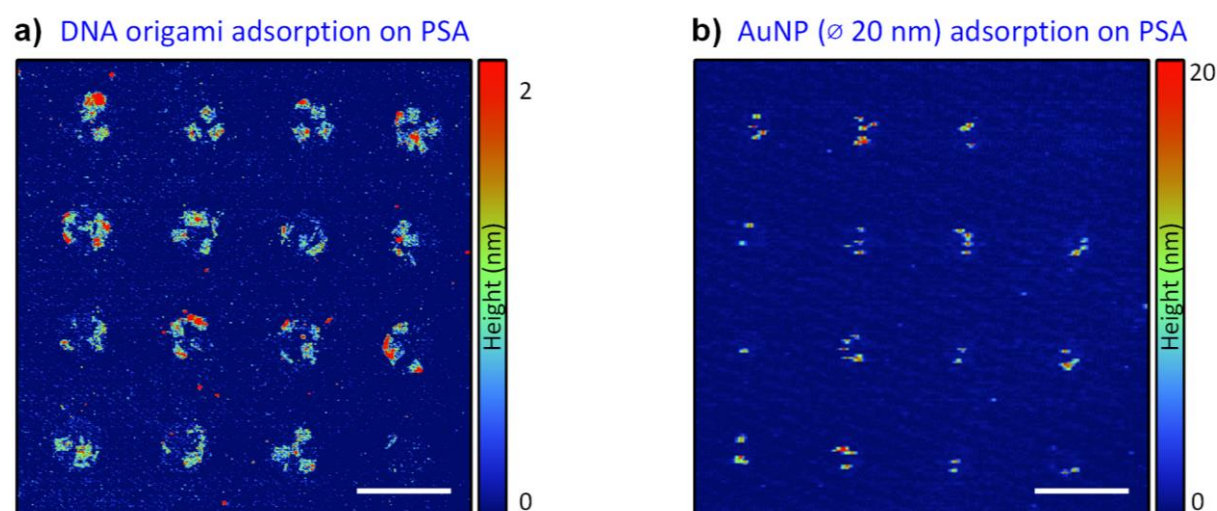


Figure 27: AFM image of the adsorption of (a) **unmodified DNA origami** and (b) **unmodified AuNPs** on PSA. Scale bars are 500 nm in (a, b).

In Figure 27a, the position of the polar adsorption fields was revealed by the position of DNA origami. Each adsorption field was occupied by approximately three to four DNA origamis, their rectangular shape was clearly visible, and exposes the 4×4 polar array in this image. Figure 27b depicts the adsorption of 20 nm AuNPs on a PSA, and the AuNPs were also exclusively adsorbed on the polar fields. The results here showcase the comparable selective adsorption of DNA origami as well as AuNPs on polar areas. Furthermore, the results demonstrate the application of polarity-driven adsorption for precise nanostructure positioning.

5.2. DFT Simulation of DNA Origami Adsorption on PSA

Experiments in section 5.1 revealed a favorable adsorption behavior of plasmonic DNA nanostructures on hydrophilic PSA fields, indicating a strong interaction on such surfaces (Figure 28a). On the contrary, only a weak binding interaction was expected toward a hydrophobic surface which results in a low adsorption efficiency. In this section, the interaction between the hydrophilic and hydrophobic interface of the PSA substrate and the DNA origami (represented by a thymidine monophosphate molecule, TMP) was investigated using DFT simulations. The binding energy as well as changes in electron distribution due to adsorption could be extracted from the DFT results, which would support the understanding of the adsorption process in addition to the experimental observations.

In this section, the geometric optimization of an isolated TMP was calculated using *ORCA* software, before applying it to adsorption simulations. DFT calculations were applied using the B3LYP hybrid functional with the Karlsruhe basis set of valence triple-zeta polarization (def2-TZVP) for all atom types. The self-consistent field convergence cut-off was set to 10^{-6} arb. units. The charge density difference of TMP on Si (100) substrate was performed using the *Quantum Espresso* software package. The molecule relaxation of TMP, lattice relaxation of the Si supercell ($16.4 \times 16.4 \times 35.0 \text{ \AA}^3$), and the subsequent physisorption of TMP were performed with a k-points distance of 0.2 \AA^{-1} , a k-point grid of $5 \times 5 \times 2$, and a force convergence threshold of $10^{-4} \text{ Ry} \cdot \text{Bohr}^{-1}$.¹³⁹

Figure 28b (black frame) shows that the phosphate groups within the DNA origami were mostly in close contact with the underlying Si substrate due to their local molecular position in the double-stranded DNA. Other molecular fragments were sterically inward from the DNA center and thus interact less with the Si substrate. For this reason, we simplified the DFT simulation and only considered the interaction between the hydrophilic silanol surface (Si–O) or the hydrophobic methyl surface (Si–CH₃) and the phosphate group. The modification on the hydrophobic surface, the Si(CH₃)₃ monolayer, was simplified to surface methyl groups (Si–CH₃) to reduce calculation time. In addition, we used a single thymidine monophosphate (TMP) from the DNA fragment to represent those interactions at the Si-substrate/phosphate interface (Figure 28c and 28d). However, other nucleotides could be considered in such DFT calculations as well.

Figure 28c and 28d depict the results of the two DFT simulations. Here, a three-layer Si supercell with a (100) orientation was applied to represent the Si substrate. Hydrogen atoms were used for the passivation of dangling bonds on the opposite substrate side for charge compensation.

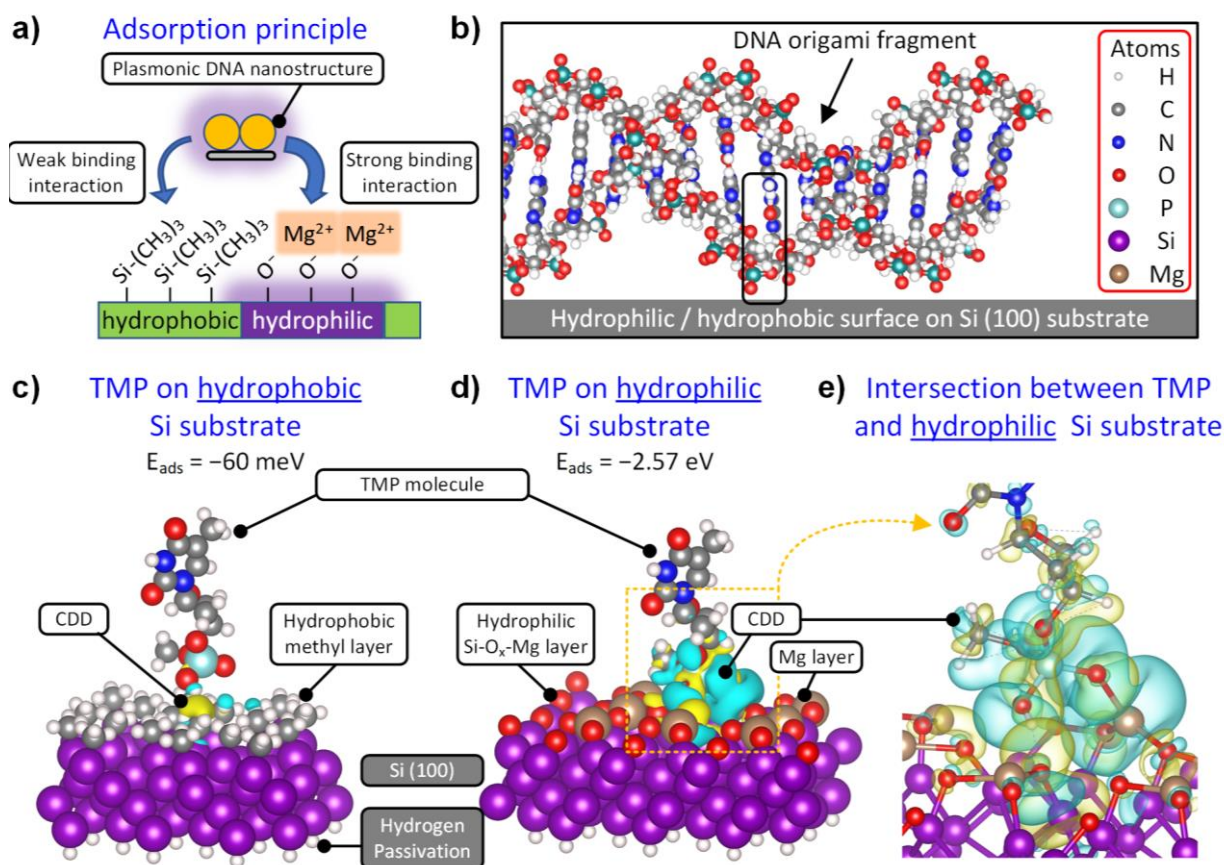


Figure 28: (a) Proposed adsorption behavior of plasmonic nanostructure adsorption on PSA. (b) Illustration of a double-stranded DNA laying on Si substrate. The black frame shows a section that is used for the DFT simulation. Different atoms were presented as colored spheres, and the same color scheme was used in (b–e). Result of the DFT simulation of a TMP molecule adsorbs on hydrophobic (c) and hydrophilic (d) Si (100) surface. The charge density difference (CDD) was represented by yellow (electron density accumulation) and cyan (electron density depletion) clouds, respectively. (e) Adsorption interface between TMP and hydrophilic Si surface. The CDD isosurface in (c–e) was normalized to $\pm 5 \cdot 10^{-4} a_0^{-3}$, a_0 is the Bohr radius.

In Figure 28c, the hydrophobic Si surface was functionalized using methyl groups ($-\text{CH}_3$) to denote the HMDS deposition. The hydrophilic surface was realized with silanol (SiO_x) groups on the Si surface (Figure 28d), representing the polar PSA fields after oxygen plasma treatment. To replicate the adsorption environment of DNA origami, silanol groups on the hydrophilic surface were deprotonated and the negative charge was compensated by a layer of Magnesium ions. The molecular adsorption process was calculated by positioning a single TMP molecule perpendicular to the Si substrate and the subsequent structural relaxation by DFT.

Equation (35) was used to determine the adsorption energy (E_{ads}) of the TMP molecule onto a Si substrate. This involves subtracting the sum of the total energy of the isolated substrate (E_{sur}) and the total energy of a single isolated TMP molecule (E_{TMP}) from the total energy of the adsorbed TMP molecule onto the Si substrate (E_{tot}).

$$E_{ads} = E_{tot} - (E_{TMP} + E_{sur}) \quad (35)$$

Based on the adsorption energy calculation, we have determined that the adsorption energy of a TMP molecule on the hydrophobic surface was only -60 meV (Figure 28c). This relatively weak binding energy is primarily due to van der Waals interactions.¹⁴⁰ In contrast, when TMP was adsorbed on a hydrophilic surface, the adsorption energy was significantly higher (-2.57 eV), indicating a strong Coulomb interaction between the molecule and the surface (Figure 28d).¹⁴⁰

The charge density difference (CDD) has been calculated to reveal electrostatic interactions at the interface between TMP and the Si substrate using eq. (36), illustrated in Figure 28c and 28d as cyan and yellow clouds, respectively. The CDD is the difference between the total charge density of the adsorbed TMP on the Si substrate (q_{tot}) and the sum of the charge densities of the isolated substrate (q_{sur}) and a single TMP molecule (q_{TMP}).

$$CDD = \rho_{tot} - (\rho_{TMP} + \rho_{sur}) \quad (36)$$

The colored region in Figure 28cs and 28d depicts the isosurface of charge density difference for the adsorbed TMP molecule on the substrate. The yellow cloud represents charge density accumulation, while the cyan clouds represent regions of density depletion. Only a small CDD was observed in Figure 28c between TMP and the hydrophobic surface, indicating the presence of an induced dipole. However, in Figure 28d, the CDD was much larger and primarily attributed to the phosphate group from TMP and the magnesium ions on the Si surface, indicating Coulomb interaction between these groups. Figure 28e provides a more detailed examination and revealed that the interaction depicted in Figure 28d was due to a cascade of dipole interactions between TMP and the magnesium-loaded hydrophilic Si surface.

In general, a larger CDD size corresponds with higher adsorption energy and indicates a stronger electrostatic interaction between TMP and the hydrophilic Si–O_x surface, in contrast to the adsorption on the hydrophobic Si–CH₃ surface.

Correlation Between Polarity-Driven Adsorption and Bader Charges

In the previous section, the preferential adsorption of a DNA fragment onto hydrophilic substrates, driven by polarity, was revealed through the analysis based on density functional theory (DFT). The electrostatic attraction between the TMP molecule and the substrate was facilitated by the presence of a silanol group, with the interaction further augmented by a layer of magnesium ions (Mg²⁺). These magnesium ions, along with other monovalent and bivalent cations, served to neutralize the negative charge of the DNA origami, thereby stabilizing its framework.¹⁴¹ Additionally, it has been documented that the presence of magnesium ions enhances the adsorption of DNA origami.¹⁴²

To investigate the influence of Mg²⁺ in the adsorption of DNA fragments, a DFT analysis was conducted, which encompassed an examination of the change in the charge density distribution (CDD) during TMP adsorption on magnesium-loaded hydrophilic and hydrophobic surfaces.

The CDD analysis enabled the examination of electron density shifts within the simulated structure, allowing for the identification of regions indicating Coulomb interactions associated with ionic binding. Furthermore, the Bader charge analysis (section 2.5) was performed to quantify the shift in electron density for each atom, thus providing insights into the Coulomb interactions within the adsorption model.^{95,96}

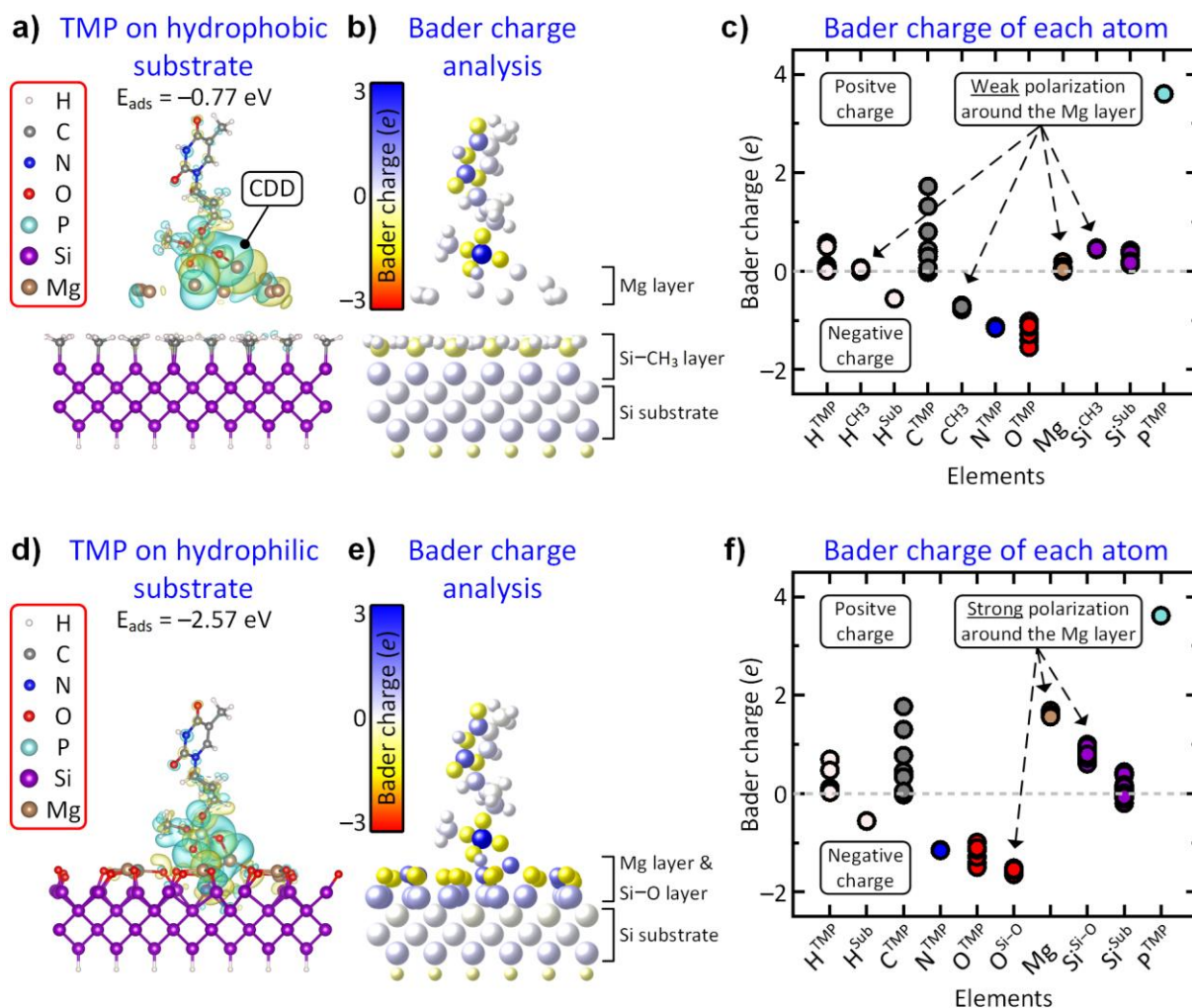


Figure 29: The charge density difference of a TMP molecule adsorbed on a magnesium-covered (a) hydrophobic and (d) hydrophilic Si substrate. The corresponding Bader charge of atoms was displayed in (b, e), respectively. The Bader charge of each atom was presented in (c, f), the atoms were grouped by the element and their position, as described in Table 6 and Table 7. The CDD isosurface in (c, e) was normalized to $\pm 5 \cdot 10^{-4} a_0^{-3}$, where a_0 is the Bohr radius.

Figure 29 depicted a comparison of the CDD and Bader charge analysis for the adsorption of TMP on hydrophilic and hydrophobic substrates. The normalized CDD isosurface was depicted as cyan and yellow clouds in Figure 29a and 29d, representing electron charge depletion and accumulation, respectively. In Figure 29a, a large CDD cloud was observed surrounding the phosphate group of the TMP molecule and the magnesium layer (represented by brown spheres), indicating a significant charge-shift between them. The calculated adsorption energy (E_{ads}) of -0.77 eV, determined using eq. (35), indicates a weak Coulomb interaction that favors the adsorption. Nonetheless, no CDD was observed between the magnesium layer and the

hydrophobic substrate, suggesting the absence of electronic interaction and, consequently, no favorable adsorption of magnesium onto the hydrophobic Si-CH₃ surface. Notably, the adsorption energy in Figure 29a was higher than the result in Figure 28c, where the magnesium layer was absent. Thus, the CDD and the calculated adsorption energy in Figure 29a imply an attractive interaction solely between TMP and magnesium layer, thereby accounting for the higher adsorption energy compared to the result in Figure 28c. In contrast, Figure 29d exhibited significantly higher adsorption energy (E_{ads} of -2.57 eV), suggesting a much stronger Coulomb interaction. Here, the CDD isosurface overlays the TMP molecule, the magnesium layer, and the hydrophilic surface. This demonstrates the positive synergy of magnesium bridging over the negatively charged DNA fragment and the equally negatively charged hydrophilic substrate.

The Bader charge analysis, depicted in Figure 29b and 29e, provides a quantification of the electron density shift for each atom upon TMP adsorption. The color bar represents the Bader charge of each atom, ranging from red (-3 Bader charges, equivalent to receiving three electrons) over white (no charge) to blue (+3 Bader charges). A comprehensive list of atoms with their corresponding Bader charges can be found in Appendix A3. The Bader charge of an atom was calculated as the difference between its valence electron number and its assigned electrons based on the Bader charge analysis. For instance, in Figure 29b, the phosphorus atom (represented by the blue sphere in the image center) had 5 valence electrons, but only approx. 1.40 electrons were assigned to it in the calculation, resulting in a Bader charge of approx. +3.60. This positive Bader charge for the phosphorus atom, with an electronegativity of $\Delta_{EN}(P) \sim 2.2$ (by Pauling), is reasonable considering its bonding with four oxygen atoms ($\Delta_{EN}(O) \sim 3.4$), leading to bonds with a polar covalent character.¹⁴³

To systematically analyze the Bader charge of different atoms, the atoms were classified into groups based on their element type and position within the adsorption system. The Bader charge distributions for these groups were presented in Figure 29c and 29f. Detailed information about the atom groups for TMP molecule adsorption on the hydrophobic and hydrophilic substrates can be found in Table 6 and Table 7, respectively.

Figure 29c and 29f illustrated that seven atom groups (H^{TMP} , H^{Sub} , C^{TMP} , N^{TMP} , O^{TMP} , Si^{Sub} , P^{TMP}) exhibit similar Bader charges in both simulations. These seven groups encompass all components of the TMP molecule and the Si substrate, excluding the hydrophilic and hydrophobic top layers. The consistency in Bader charges indicates that these groups experience similar chemical environments throughout the adsorption process, regardless of the polarity of the substrate.

Table 6: Group of atoms from the **TMP molecule** adsorption on the **hydrophobic substrate**, with their respective Bader charge. The four groups (H^{CH_3} , C^{CH_3} , Mg, Si^{CH_3}) at the boundary between TMP and the substrate are marked with color, according to the color bar in Figure 29b.

Group	No. of atoms	Average Bader charge (e)	Description
H^{TMP}	15	+0.13	H atoms of the TMP molecule
H^{CH_3}	54	+0.03	H atoms of the Si–CH₃ layer
H^{Sub}	18	−0.56	H atoms below the Si substrate
C^{TMP}	10	+0.54	C atoms of the TMP molecule
C^{CH_3}	18	−0.73	C atoms of the Si–CH₃ layer
N^{TMP}	2	−1.14	N atoms of the TMP molecule
O^{TMP}	7	−1.26	O atoms of the TMP molecule
Mg	9	+0.05	Mg atoms of the Mg monolayer
Si^{CH_3}	18	+0.46	Si atoms of the Si–CH₃ layer
Si^{Sub}	54	+0.24	Si atoms of the Si substrate
P^{TMP}	1	+3.60	P atom of the TMP molecule
	206	0	The sum of all atoms

Table 7: Group of atoms from the **TMP molecule** adsorption on the **hydrophilic substrate**, with their respective Bader charge. The three groups ($\text{O}^{\text{Si-O}}$, Mg, $\text{Si}^{\text{Si-O}}$) at the boundary between TMP and the substrate are marked with color, according to the color bar in Figure 29e.

Group	No. of atoms	Average Bader charge (e)	Description
H^{TMP}	15	+0.14	H atoms of the TMP molecule
H^{Sub}	18	−0.56	H atoms below the Si substrate
C^{TMP}	10	+0.54	C atoms of the TMP molecule
N^{TMP}	2	−1.15	N atoms of the TMP molecule
O^{TMP}	7	−1.25	O atoms of the TMP molecule
$\text{O}^{\text{Si-O}}$	18	−1.55	O atoms of the Si–O layer
Mg	9	+1.62	Mg atoms of the Mg monolayer
$\text{Si}^{\text{Si-O}}$	18	+0.79	Si atoms of the Si–O layer
Si^{Sub}	54	+0.17	Si atoms of the Si substrate
P^{TMP}	1	+3.62	P atom of the TMP molecule
	152	0	The sum of all atoms

In addition to these seven groups, four groups were observed specifically in the case of TMP adsorption on the hydrophobic substrate, namely the Mg layer and the three groups (H^{CH_3} , C^{CH_3} , Si^{CH_3}) that contribute to the construction of the hydrophobic surface. Here, the Mg layer displayed a negligible positive Bader charge of +0.05 (Table 6), indicating a minimal shift in electron density towards the TMP molecule. On the hydrophobic surface, the Si-CH₃ layer was charge neutral towards the outside (H^{CH_3} with +0.03 Bader charge, Table 6), while the carbon atoms (-0.73 Bader charge, Table 6) attracted some electron density from the silicon atoms (+0.46 Bader charge, Table 6), implying the presence of weakly polar C-Si bonds.

The Bader charge analysis presented in Figure 29e and 29f revealed a strongly positive charge on the magnesium layer (+1.62 Bader charge, Table 7) and a strong negative charge on the oxygen atoms ($\text{O}^{\text{Si-O}}$, -1.55 Bader charge, Table 7) on the hydrophilic substrate, indicating a significant Coulomb interaction between them. The electron density of the Si atoms in the Si-O layer ($\text{Si}^{\text{Si-O}}$, +0.79 Bader charge, Table 7) was shifted toward the $\text{O}^{\text{Si-O}}$ atoms. The Bader charges and electronegativity differences ($\Delta_{\text{EN}}(\text{Si}) \sim 1.9$, $\Delta_{\text{EN}}(\text{O}) \sim 3.4$) indicate the polar nature of the Si substrate with a Si-O layer on the surface.¹⁴³

In conclusion, our DFT calculations highlight the decisive role of the presence of magnesium in the adsorption of the DNA fragment, which is consistent with previous findings reported in the literature.¹⁴² The results demonstrate that the DNA fragment adsorption on the hydrophobic surface was not favored due to the weak interaction between the magnesium layer and the hydrophobic surface. The quantitative Bader charge analysis provides support for the observations made regarding the charge density distribution and highlights the presence of an attractive Coulomb interaction between the DNA fragment, the magnesium layer, and the polar (hydrophilic) surface.

5.3. Surface Characterization of the Polar Surface Array

The PSA chip was designed for the selective adsorption of DNA origami-based plasmonic nanostructures, which preferentially adsorb onto a hydrophilic surface, as introduced in section 5.1. It consists of an array of polar (hydrophilic) fields surrounded by non-polar (hydrophobic) areas, fabricated on a polished silicon (100) wafer. The high polarity of the hydrophilic area results from Si-O groups, which favor DNA origami adsorption due to electrostatic attraction (section 5.2). In this section, the surface properties of the hydrophilic and the hydrophobic surface were studied with high-resolution X-ray photoelectron spectroscopy (XPS) as well as Atomic force microscopy (AFM).

The surface composition of hydrophilic and hydrophobic Si (100) has been examined using high-resolution XPS. Both surfaces consist of a natural, amorphous SiO_x layer above the Si (100) substrate, while the hydrophobic surface has additional Si(CH₃)₃ groups due to the HMDS deposition. The measured binding energy of the three elements (Si, O, and C) has been extracted from the surface of the untreated Si wafer, on the Si wafer with HMDS coating, and

the Si wafer after HMDS removal, respectively. Each surface has been characterized at five different locations to ensure representative results. The XPS data did not show notable changes in the binding energy for the element Si and O (data not shown), which indicate a stable chemical composition of the SiO_x layer unaffected by the O_2 plasma treatment and HMDS deposition.

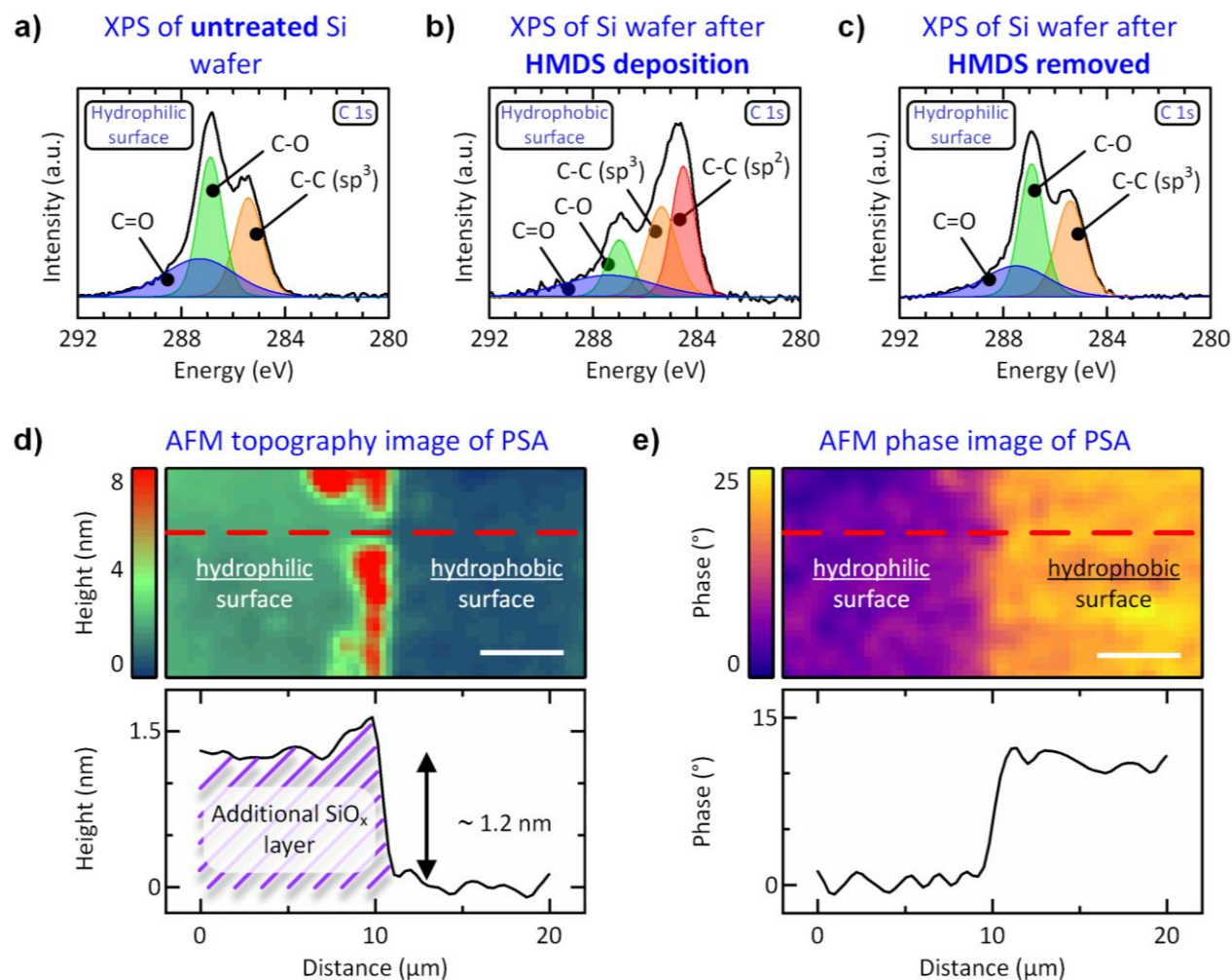


Figure 30: (a–c) XPS spectrum (C 1s region) of Si(100) surface. The data have been fitted with Gaussian functions. (d) AFM height image and (e) phase contrast image for discrimination of hydrophobic and hydrophilic surface areas. The red lines mark the path used to create the cross-sections in the diagrams below. Scale bars are $4\ \mu\text{m}$ in (d, e).

XPS spectra of the C 1s peak revealed a change in carbon composition before (Figure 30a), after HMDS coating (Figure 30b), and after HMDS was removed (Figure 30c). The aliphatic species (C-C , sp^3) at $h\nu = 285.4\ \text{eV}$, as well as carboxyl species (C-O , C=O) at $h\nu = 286.6\ \text{eV}$ and $287.4\ \text{eV}$ in Figure 30a–30c, were due to hydrocarbon contaminations between the sample preparation and the XPS measurement.¹⁴⁴ In Figure 30b, the deconvolution of the C 1s peaks confirmed an additional sp^2 carbon species at $h\nu = 284.5\ \text{eV}$, likely caused by X-ray beam damage of the HMDS monolayer.¹⁴⁵ This peak vanished after the removal of HMDS by the O_2 plasma, as shown in Figure 30c.

AFM inspection of the PSA chip revealed a 1.2 nm elevation of the hydrophilic areas compared to the surrounding hydrophobic substrate (Figure 30d). These elevations consist of SiO_x layers that were created by oxygen plasma treatment, in addition to the natural oxide layer (Figure 14). The differences in surface properties of the hydrophilic and hydrophobic areas also become evident from the phase contrast image (Figure 30e).¹⁴⁶ The phase contrast indicates a changing tip-surface interaction on the PSA due to different surface properties.¹³⁹

5.4. Single Hybrid Nanostructure Isolation on PSA

After successfully demonstrating the selective adsorption of hybrid nanostructures on a polar surface array, we optimized the experimental parameters with the aim of isolating single hybrid nanostructures on PSA fields. The adsorption behavior of plasmonic nanostructures on PSA has been investigated by tuning experimental parameters such as the nanostructure concentration (section 5.4.1), incubation time (section 5.4.2), adsorption field size (section 5.4.3), and Mg²⁺ ion concentration (section 5.4.4).

5.4.1. Tuning the PSA Field Size

The number of hybrid nanostructures (AuNP dimers) adsorbed on PSA ideally scales with the size of the adsorption fields, and a single nanostructure might be isolated with sufficiently small field size. In this section, hybrid nanostructure adsorption has been performed on four PSAs. Adsorption fields with a size of $A = (500 \times 400) \text{ nm}^2$, $(400 \times 200) \text{ nm}^2$, $(100 \times 70) \text{ nm}^2$, and $(50 \times 40) \text{ nm}^2$ were analyzed and hybrid nanostructure suspension with a concentration of $N = 7.1 \times 10^{11} \text{ AuNP dimer} \cdot \text{mL}^{-1}$ was used for the adsorption experiment.

Hybrid nanostructures adsorbed on the PSA were analyzed with SEM and the numbers of Au Dimers on each adsorption field (M) were determined using ImageJ. Electron microscopy images showed a declining number of hybrid nanostructures occupying an adsorption field alongside reducing field size (Figure 31a–31d). The size of a hybrid nanostructure is about $(100 \times 70) \text{ nm}^2$, but even a field size of $(50 \times 40) \text{ nm}^2$, four times smaller than a single nanostructure's size, attracted substantially more than one hybrid nanostructure and leads to agglomeration (Figure 31d).

In Figure 31e, the adsorption ratio M/M_{theo} is plotted against the area of a single adsorption field (A). M_{theo} is the expected number of hybrid nanostructures on one adsorption field (assuming monolayer coverage) and was shown as a red line. Multilayer coverage was observed among different field sizes. The adsorption on a large field was close to monolayer coverage, while the ratio M/M_{theo} raises significantly at smaller field sizes. The increasing adsorption ratio at small adsorption fields was possibly due to a higher perimeter-area ratio, where hybrid nanostructures were adsorbed on the edge of a PSA field.

Results in this section show that a hybrid nanostructure would adsorb on a PSA field with a significantly smaller area than itself. Reducing the adsorption field size only was not sufficient to isolate a single hybrid nanostructure, thus additional parameters must be taken into account.

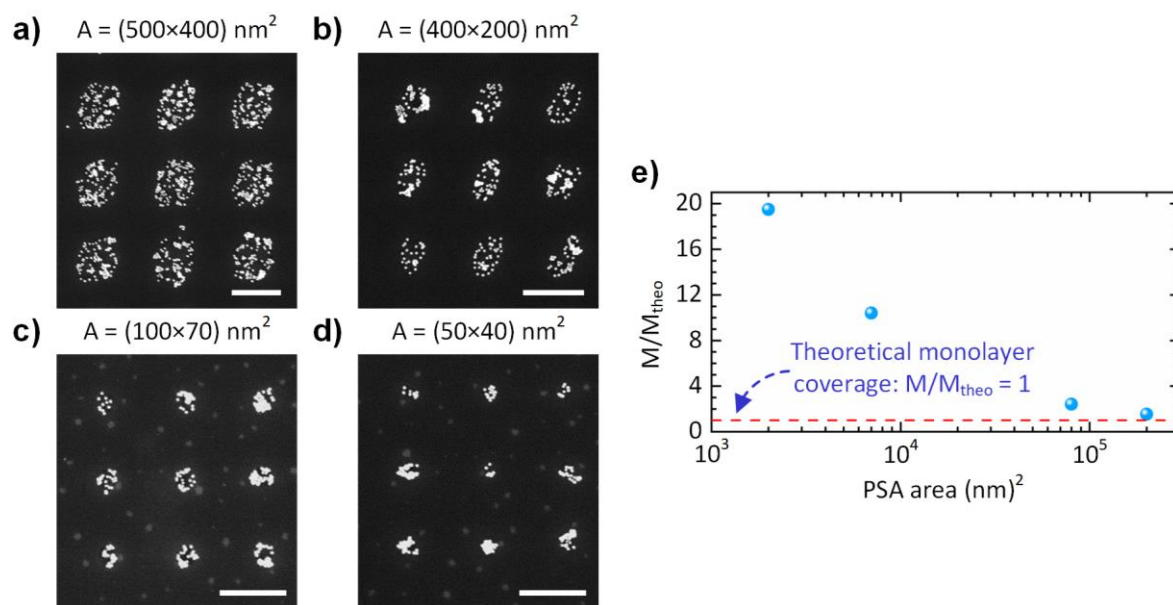


Figure 31: (a–d) SEM image of hybrid nanostructures adsorbed on the PSA; single field area (A) is listed in the caption. (e) The ratio between the average number of Au Dimers adsorbed on a single PSA field (M) and the theoretical monolayer coverage (M_{theo}), with different adsorption field sizes. 200 adsorption fields were analyzed for each experiment. Scale bars are $1 \mu\text{m}$ in (a–d).

5.4.2. Hybrid Nanostructure Concentration Variation

Experiments were carried out to investigate the impact of hybrid nanostructure concentration (N) to effectively isolate those nanostructures on PSA substrates for single-molecule experiments.¹³⁹ Here, the hybrid nanostructure concentration and the PSA area must be known in advance to determine the efficiency of adsorption of hybrid nanostructure structures on PSA fields. The concentration of N was determined utilizing UV-Vis spectroscopic measurements and showed a concentration range from 7.1×10^9 to 7.1×10^{11} AuNP dimer·mL⁻¹. Hybrid nanostructure was drop-casted on PSA fields (field size = $(100 \times 70) \text{ nm}^2$, 500 nm pitch) and the adsorption efficiency of PSA substrates has been evaluated through SEM measurements. Colored circles marked the position of PSA fields in the SEM images. Here, the number of hybrid nanostructures on PSA fields (M) was grouped into four classes: M_A ($M > 4$) for strong agglomerations, M_B ($2 \leq M \leq 4$) for fields with a limited number of hybrid nanostructures, M_C ($M = 1$) for isolated hybrid nanostructures, and M_D ($M = 0$) for empty PSA fields (Figure 32a).

Figure 32b and 32c are SEM images of two PSA substrates treated with rather high and low hybrid nanostructure concentrations ($N = 3.5 \times 10^{11}$ and 7.0×10^9 AuNP dimer·mL⁻¹). The small white dots in the SEM image depicted the adsorbed gold nanoparticles bonded to the DNA

origami. Due to the structural flexibility of DNA origami, the two AuNPs of the hybrid nanostructure did not show a constant distance, which varied between 0 and 30 nm. The DNA origamis were not observable in the SEM image as a result of low electron contrast. Both figures also exemplarily show the significant change in the adsorption efficiency behavior of hybrid nanostructure depending on the concentration. Furthermore, Figure 32b and 32c demonstratively show that hybrid nanostructures were adsorbed only on the hydrophilic area of the PSA which underpins the selective interaction to the hydrophilic/hydrophobic areas of the PSA substrate. The agglomerations consist of at least two hybrid nanostructures in the same PSA field, but can also be formed by considerably more structures. From Figure 32b it is evident that agglomeration of hybrid nanostructures dominates at high concentrations. The figure also reveals that a total of significantly more than four hybrid nanostructures (PSA fields marked with a blue circle in Figure 32b) have been adsorbed on each PSA field at high concentrations with a randomly spatial orientation to the substrate. Figure 32c shows that agglomeration vanished when the hybrid nanostructure concentration was significantly reduced to 7.0×10^9 AuNP dimer $\cdot \text{mL}^{-1}$. Simultaneously, the percentage of occupied fields decreased.

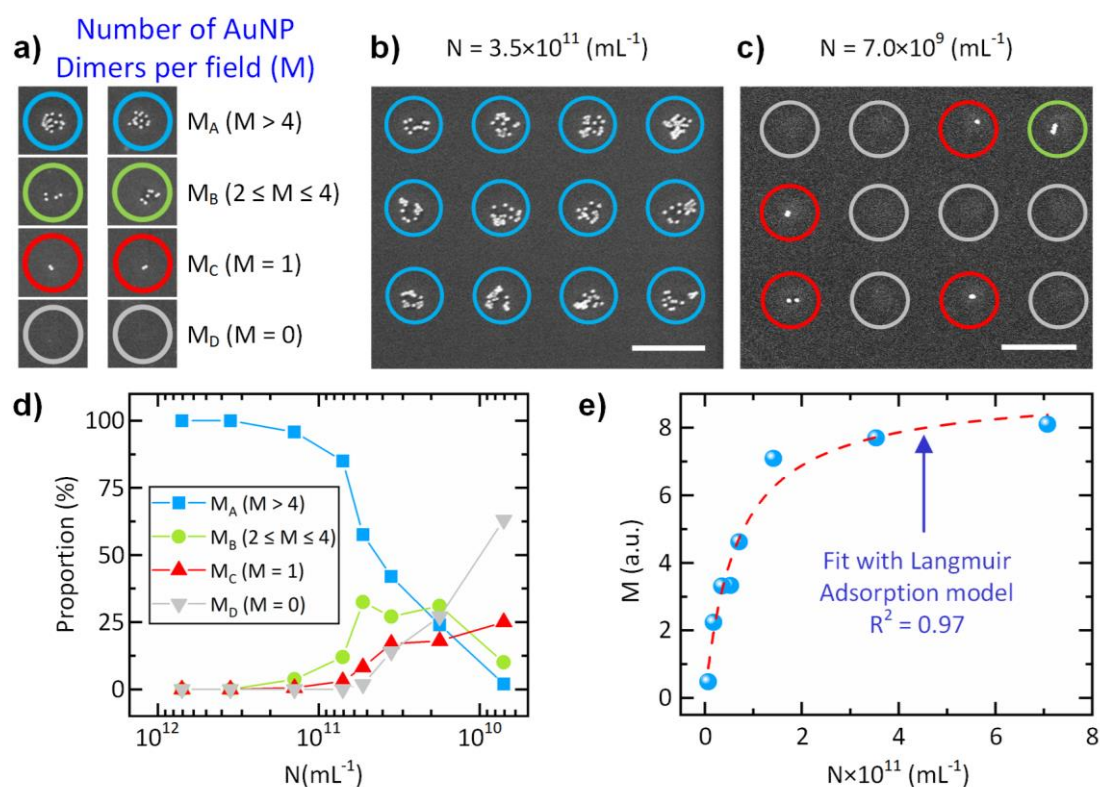


Figure 32: (a) Classification of the number of adsorbed AuNP dimer structures per PSA field, which has been mainly observed within the different DNA origami nanostructure concentrations. (b, c) SEM images of different concentrations of AuNP dimers adsorbed onto PSA. Colored circles refer to the four-level classification scheme describing the number of adsorbed AuNP dimer structures. (d) Proportional change of M_A , M_B , M_C , and M_D fields at on PSA fields as a function of nanostructure concentration. 400 adsorption fields were analyzed for each experiment. (e) Dependence of the number of AuNP dimers (M) on the AuNP dimer concentration (N) applied to the Langmuir adsorption model. Scale bars are $0.5 \mu\text{m}$ in (b, c).

Figure 32d depicts the relationship of the nanostructure adsorption on PSA as a function of the concentration. The PSA fields were divided into four classes (M_A , M_B , M_C , and M_D), regarding the number of adsorbed hybrid nanostructures. The results reveal two different types of adsorption behaviors depending on the hybrid nanostructure concentration (N), in a concentration range between 10^{12} and 10^{10} AuNP dimer·mL⁻¹. When N was between 10^{12} and 10^{11} AuNP dimer·mL⁻¹, PSA fields were predominantly loaded with four or more hybrid nanostructures (M_A), and only small changes were observed when reducing the concentration. When N was below 10^{11} AuNP dimer·mL⁻¹, the proportion of M_A fields decreases along reduced N and was substituted by M_B , M_C , and M_D fields, which occurs in parallel. Data show the percentage of M_B fields (with 2 to 4 hybrid nanostructures per PSA field) increased first and decreased with N below 10^{10} AuNP dimer·mL⁻¹, implying a gradual decrease of the agglomeration when reducing N . Furthermore, a steady increase in the proportion of M_C fields (one hybrid nanostructure per PSA field) was observed with decreasing N and was surpassed by M_D fields (empty PSA fields) whose proportion raised quickly. The proportion of empty PSA fields dominated when N was just below 10^{10} AuNP dimer·mL⁻¹, while roughly every fourth PSA field was loaded with one AuNP Dimer. The results implied that the effective adsorption efficiency of hybrid nanostructure per PSA field clearly decreases at low concentrations ($N < 10^{10}$ AuNP dimer·mL⁻¹), because of either concentration-dependent adsorption or concentration-dependent diffusion. PSA covered with AuNP Dimers and a DNA nanostructure concentration range $10^{11} \geq N \geq 10^{10}$ AuNP dimer·mL⁻¹, on the other hand, can represent a suitable sample for single-molecule SERS experiments. In order to avoid agglomeration, however, a high number of unoccupied PSA fields must be accepted.

Numerous researchers have comprehensively studied the adsorption behavior of DNA origami on various substrates.^{138,142,147-149} Gopinath and Xin have investigated DNA Origami adsorption by adjusting parameters such as salt concentrations, incubation times, and DNA origami concentrations. Fabrication of DNA monolayers and single DNA origami separation were both accomplished, whereas agglomeration and multilayer stacking was prevented under the right circumstances. In Hung's research, triangle DNA origamis had several 5 nm AuNPs attached to them; these triangle DNA origamis displayed nearly identical adsorption behavior as those that had not been modified by nanoparticles.¹⁴⁷

Although we followed Gopinath's methodology in our studies, our findings contradict the effect that has been shown in the literature.¹⁴⁸ Our research demonstrated that by adjusting the hybrid nanostructure concentration, it was possible to prevent the agglomeration of hybrid nanostructures. However, a single PSA field with a comparable surface area like the hybrid nanostructure ($A = (100 \times 70) \text{ nm}^2$) could be occupied by numerous nanostructures. This shows that the probability of hybrid nanostructure adsorption was similar between already occupied and vacant PSA fields. The additional plasmonic AuNP bonded to the DNA origami ultimately altered the adsorption behavior due to the change in geometry from the DNA origami to the hybrid nanostructure and influences the surface potential of the DNA origami. Attractive

interactions between each hybrid nanostructure might encourage aggregation. Similar results of cluster formation have been observed on silicon substrates by Bartschmid et al.¹³⁶ Compared with pure DNA origami, the adsorption behavior of hybrid nanostructures was impaired by the presence of gold nanoparticles. Nonetheless, PSA clearly demonstrated the capability of single nanostructure isolation for single-molecule experiments.

The Adsorption on PSA Evaluated by the Langmuir Isotherm

In the next step, we investigate the adsorption efficiency of hybrid nanostructures on PSA by consideration of adsorption isotherms.¹³⁹ The investigation of SEM images (Figure 32b) has already revealed that multiple hybrid nanostructures were adsorbed within one PSA field at high concentrations ($N = 3.5 \times 10^{11}$ AuNP dimer·mL⁻¹). Although the hybrid nanostructures formed clusters in some of the PSA fields, most hybrid nanostructures were spread in an area that indicates a monolayer at the highest possible surface coverage. We have analyzed the nanostructure adsorption with the Langmuir model (eq. (37)). This model implies a monolayer at the maximum adsorption and the adsorbate concentration was a crucial parameter in the surface coverage.^{150,151} In eq. (37), M_∞ is the maximum achievable adsorption density of Au Dimers and K is the Langmuir equilibrium constant.

$$M = M_\infty \frac{K \cdot N}{1 + K \cdot N} \quad (37)$$

The Langmuir isotherm was characterized by a separation factor (R_L), a dimensionless constant. R_L (eq. (38)) shows the isotherm's type depending on K and is listed in Table 8.¹⁵²

$$R_L = \frac{1}{(1 + K \cdot N)} \quad (38)$$

Table 8: Langmuir equilibrium constant (K) dependent effect of separation factor (R_L) on the isotherm type.

K value	R_L value	Type of isotherm
$K < 0$	$R_L > 1$	Unfavorable
$K = 0$	$R_L = 1$	Linear
$0 < K < 1$	$0 < R_L < 1$	Favorable
$K \rightarrow \infty$	$R_L = 0$	Irreversible

In Figure 32e, Langmuir isotherm (eq. (37)) was applied as a fitting model to evaluate the hybrid nanostructure adsorption on PSA. The average number of hybrid nanostructures per PSA field changes while the concentration increases, as shown by the blue data points. Here, the Langmuir isotherm showed a good correlation with the observed experimental data. The fitting function (eq. (37)) revealed a rapidly increasing adsorption of hybrid nanostructures along with rising N and reaches an equilibrium around $M_\infty = 9.2$ nanostructures per PSA field

(Figure 32e). Based on the fitting function, we calculated a Langmuir equilibrium constant of $K = 0.15 \times 10^{-10}$ AuNP dimer·mL⁻¹ and an R_L (Table 9) range from approx. 0.9 to 0.1. Favorable adsorption on PSA was confirmed with R_L between 0 and 1, which was in agreement for all concentrations in these experiments. Otherwise, lower R_L values (Table 9) indicate more favorable adsorption at high concentrations.

Table 9: Separation factor (R_L) at different nanostructure concentrations (N).

N in 10^{10} AuNP dimer·mL ⁻¹	R_L
70.76	0.086
35.38	0.159
14.15	0.320
7.08	0.485
5.31	0.557
3.54	0.653
1.77	0.790
0.71	0.904

The experiments carried out in this section have demonstrated that a single AuNP Dimer could be isolated in a controlled manner using PSA. In addition, the nanostructure concentration was essential to adjust the number of adsorbed nanostructures per PSA field. We assume that the diffusion of DNA origami nanostructures within the surrounding solution also has a significant impact on the adsorption efficiency of the PSA substrate, which was affected by the DNA origami concentration. However, this situation has not been considered within our model, but it should be investigated in further experiments.

5.4.3. Incubation Time

In the previous section, cluster forming was observed on PSA at a high hybrid nanostructure concentration. A high concentration could lead to a higher adsorption rate on the PSA as well as an agglomeration of nanostructures in the liquid. It's important to understand whether the cluster forming on PSA was consecutive, i.e., adsorption on an already occupied field, or abruptly, i.e. cluster forming in liquid prior to adsorption.¹³⁹

The time-dependency of hybrid nanostructure adsorption was imaged with SEM (Figure 33a–33c), using the same legend as in Figure 32a. Hybrid nanostructures were adsorbed on PSA ($A = (100 \times 70) \text{ nm}^2$) with three different incubation times: $t = 15$ min, 30 min, and 60 min. A nanostructure concentration of $N = 7.1 \times 10^{10}$ AuNP dimer·mL⁻¹ was applied for the adsorption because this concentration led to clusters forming on the PSA (incubation for 60 min), while fields with lower M were still present (Figure 33d).

The proportion of adsorption fields in classes M_A , M_B , M_C , and M_D were plotted in Figure 33d with corresponding incubation times. Over 50% of PSA fields were still unoccupied (class M_D) after 15 min incubation and most of the adsorbed hybrid nanostructures were isolated (class M_C). After 30 min, the proportion of empty fields drastically reduced while half of the PSA fields were filled with clusters (class M_A). Compared with incubation after 15 min, the proportion of class M_C fields decreased from 23% to 18%, while class M_B fields increased from 7% to 17%, indicating a steady growth of clusters. By $t = 60$ min, all PSA fields were occupied, and the class M_A field dominated, thus reproducing the result in Figure 32d. Here, a reduced incubation time showed a similar effect as reduced nanostructure concentration, which led to lower agglomeration and a higher number of isolated hybrid nanostructures on PSA.

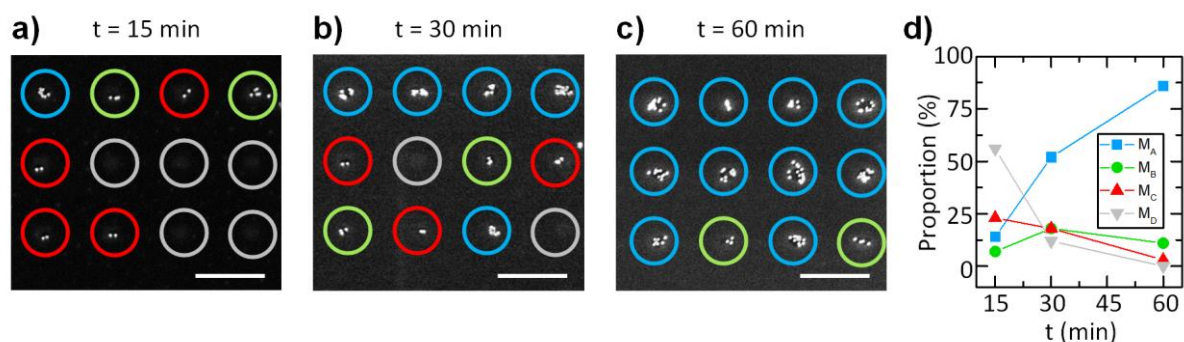


Figure 33: (a–c) SEM images of Polar Surface Array loaded with Au Dimers with different incubation times. (d) The proportion of M_A ($M > 4$), M_B ($2 \leq M \leq 4$), M_C ($M = 1$), and M_D ($M = 0$) fields at different incubation times. 200 adsorption fields were analyzed for each experiment. Scale bars are $0.5 \mu\text{m}$ in (a–c).

Cluster-forming prior adsorption would cause a parallel increase of M_A , M_B , and M_C fields. On the contrary, we observe a decreased proportion of M_C fields over time. In addition, the proportion of class M_B field increased until 30 min incubation and decreased after 60 min. These two observations support a consecutive cluster formation on PSA and indicated an attractive interaction causing adsorption on an already occupied PSA field, as discussed in section 5.4.2. In the work of Gopinath, the adsorption of triangular DNA origami over time was investigated with a similar result, where a longer incubation time leads to multiple binding of DNA origami on the same field.¹⁴⁸

5.4.4. Mg Ion Concentration

Magnesium ion was commonly used to stabilize the DNA origami structure by compensating the negative charge of the phosphate backbone. Magnesium ions were beneficial for DNA origami to adsorb on negatively charged surfaces, such as freshly cleaved mica or the PSA, this was demonstrated by the DFT simulation in section 5.2. The study by Shetty indicated that a minimum Mg^{2+} concentration of 5 mM was necessary for stable DNA origami adsorption.¹³⁸ Gopinath showed that Mg^{2+} concentration above 40 mM led to multilayer stacking of DNA origamis, while a lower Mg^{2+} concentration drastically reduced the adsorption rate.¹⁴⁸ The

results reported in the literature indicate an optimum range of Mg^{2+} concentration, while an excess or lacking magnesium ions would impede effective adsorption.

In this section, we studied the adsorption of nanostructures at low hybrid nanostructure concentration ($N = 7.1 \times 10^9$ AuNP dimer $\cdot \text{mL}^{-1}$) on the PSA (with (100×70) nm² field size) while varying the Mg^{2+} ion concentration from 20 mM to 80 mM. At this concentration, most adsorption fields were empty at 40 mM Mg^{2+} , as previous results in Figure 32d and Figure 33d show. A change in Mg^{2+} ion concentration might influence the adsorption behavior of the nanostructure and improve the chance of finding fields with isolated nanostructures.

Table 10: Percentage of nanostructures per field at various Mg^{2+} concentrations ($c_{\text{Mg}^{2+}}$). PSA fields were divided into four classes with a different number of adsorbed nanostructures, as explained in Figure 32a. 800 adsorption fields were analyzed for each Mg^{2+} concentration.

$c_{\text{Mg}^{2+}}$ (mM)	M_A ($M > 4$)	M_B ($2 \leq M \leq 4$)	M_C ($M = 1$)	M_D ($M = 0$)
20	2%	11%	20%	67%
40	3%	9%	13%	75%
60	4%	9%	13%	74%
80	1%	2%	13%	83%

The percentage of four adsorption field classes at different Mg^{2+} concentrations is listed in Table 10. Surprisingly, no major change was observed in the statistic. The adsorption rate at $c_{\text{Mg}^{2+}} = 20$ mM was comparatively higher, leading to a lower number of empty fields (M_D) and slightly more isolated nanostructures (M_C). In contrast to the observation of Gopinath, plasmonic nanostructures were less likely to adsorb on the PSA with increasing Mg^{2+} concentration. The results indicate that the hybrid nanostructure adsorption was only weakly influenced by a change in Mg^{2+} concentration at low nanostructure concentration. Adjusting Mg^{2+} concentration might show a higher impact at high hybrid nanostructure concentration.

As discussed in the previous section, the adsorption behavior of a plasmonic nanostructure was influenced by the presence of the attached gold nanoparticles. Therefore, a different adsorption behavior was possible compared with unmodified DNA origami.

5.5. SERS from a Single Hybrid Nanostructure

In this section, the application of PSA for single-molecule detection experiments was demonstrated with two hybrid nanostructures: Au DONA (Figure 34a) and Star DONA (Figure 34b), aiming at the isolation and SERS characterization of single hybrid nanostructures. The hybrid nanostructures were synthesized by Dr. Sergio Kogikoski Jr. and Yuya Kanehira from Uni Potsdam. The structure of Au DONA was based on a DNA nanofork antenna (DONA), modified with two 5-Carboxytetramethylrhodamine (TAMRA) coated AuNPs.¹⁷ This structure was used to showcase the ability of PSA to isolate a single plasmonic active

nanostructure, that was characterized by AFM and confocal Raman spectroscopy. The Star DONA was made from a DONA with two gold nanostars attached and a single TAMRA molecule in the plasmonic hot spot. TAMRA was bound to the Star DONA via a double-stranded DNA. These structures were designed for single-molecule SERS experiments, with PSA as an adsorption platform for nanostructure isolation and localization.¹³⁹

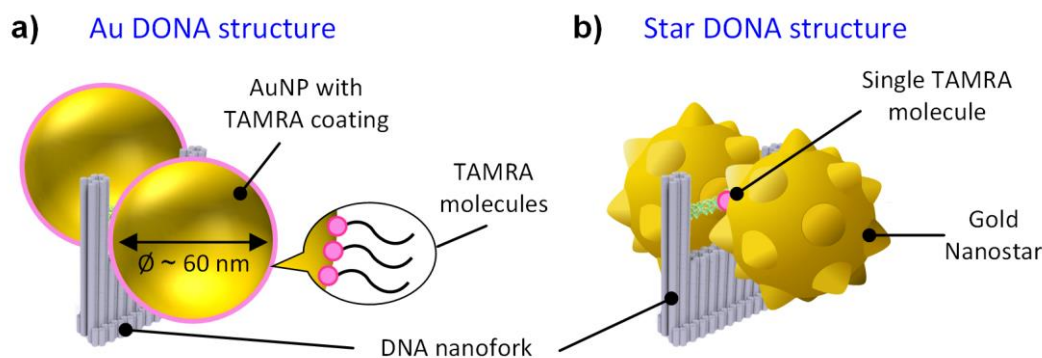


Figure 34: Two types of plasmonic DNA origami nanostructures used in this section.

The Raman signal enhancement of Au DONA and Star DONA was expected to be higher than the hybrid nanostructure used in section 4.4. This is due to a reduced hot spot size of $\sim 1\text{-}2$ nm and a larger gold nanoparticle size (as explained in sections 2.4 and 4.2).¹⁷

SERS Experiment with Au DONA

In this part, correlated AFM and surface-enhanced Raman spectroscopy (SERS) were applied to characterize a single Au DONA hybrid nanostructure. The characteristic Raman peak of the amide group (1657 cm^{-1}) was evaluated within the SERS spectrum for the identification of the TAMRA molecule. A reduced Au DONA concentration ($N = 4.1 \times 10^9$ AuNP dimer $\cdot\text{mL}^{-1}$) was selected based on the findings in section 5.4.2, to increase the share of PSA fields with only one nanostructure. Additionally, the PSA field size was increased to $A = (140 \times 100)\text{ nm}^2$, to slightly increase the adsorption efficiency.

Figure 35a shows the topography of the Au DONAs adsorbed on a PSA substrate, measured by AFM. Two white circles mark exemplary the adsorbed Au DONAs (Figure 35a, I) as well as an empty PSA field (Figure 35a, II). The position of Au DONAs (red dots) perfectly aligns with the PSA fields (light blue discs). Otherwise, no adsorption of Au DONAs has been observed on the HMDS-passivated non-polar surface that surrounds the PSA fields. The well-ordered, equidistant PSA adsorption fields were visible on the silicon wafer due to the additional oxide layer on the substrate created by the O_2 plasma (Figure 35a, light blue discs). The topography measurement of a single Au DONA is depicted in the right image of Figure 35c. The line profile through the Au DONA topography revealed as expected two AuNPs with a center-to-center distance of approx. 60 nm and a height and diameter of 60 nm (Figure 35c, left image), respectively. Unfortunately, the size of the local hot spot couldn't be resolved within the AFM measurement, since the AFM tip was not able to reach the gap between the

gold nanoparticles. However, we assumed that the hot spot distance should be below 2 nm. This small hot spot is in the range of the expected hot spot distance reported in the literature.¹⁷

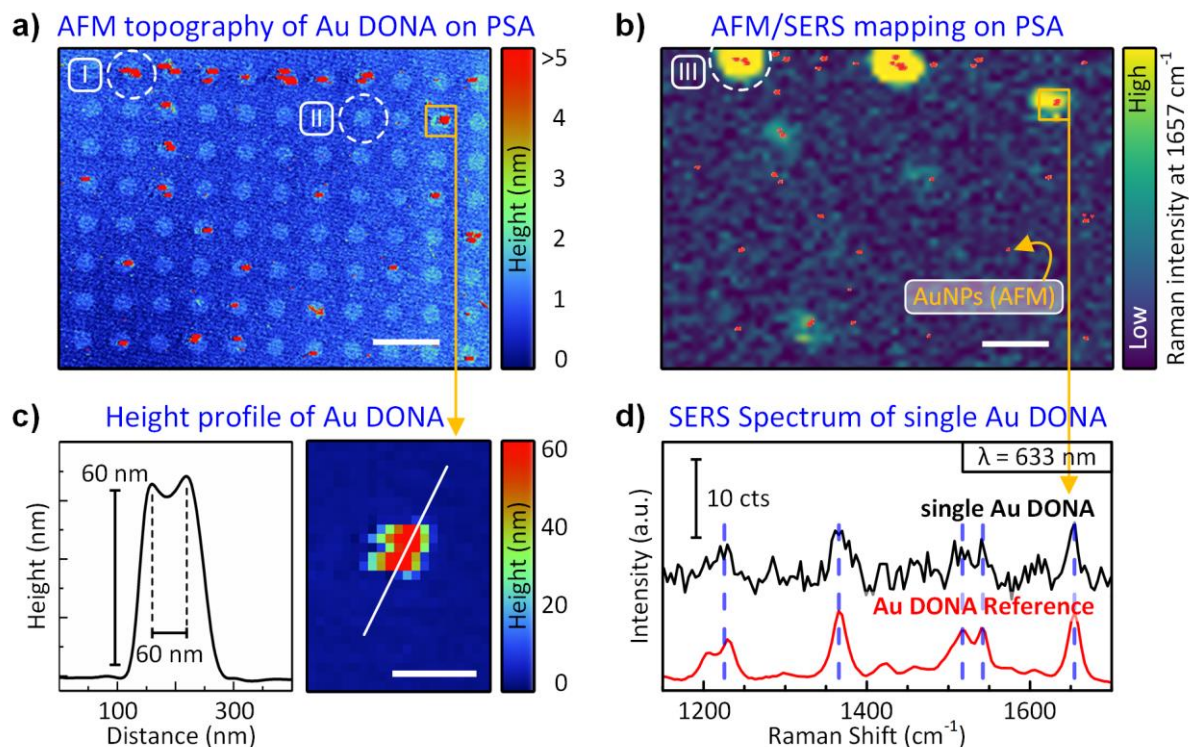


Figure 35: (a) Atomic force microscopy measurement and (b) AFM/SERS mapping at the same area on PSA. The red dots in (b) show the location of Au DONAs measured with AFM. (c) AFM measurement from a single Au DONA, the height profile (white line) is shown in the left image. (d) SERS signal of the Au DONA from (c), compared with reference spectrum from agglomerated Au DONAs. Scale bars are 1 μm for (a, b), and 200 nm for (c).

The overlap of the AFM measurement (red dots) and the Raman mapping (yellow-green image) on the same sample area (Figure 35b) show a good correlation between the local position of Au DONAs and the detected SERS signal of TAMRA. Figure 35d shows the SERS spectrum of the isolated Au DONA (orange box in Figure 35b) presented in Figure 35c. The Raman peak positions of the observed SERS spectrum clearly match the SERS reference spectrum of TAMRA. The reference spectrum was obtained by the SERS measurement of agglomerated Au DONAs, which was identical to the TAMRA spectra measured by Tapio and Prinz.^{17,153} Five Raman bands in the SERS spectra (marked with grey lines, Figure 35d) have been identified with DFT calculation (Figure 36). The vibrational bands at 1225 cm⁻¹ (B_{2u}), 1364 cm⁻¹ (B_{1u}), and 1542 cm⁻¹ (E_{1u}) describe the deformation of phenyl groups within the TAMRA molecule. Furthermore, the bands at 1518 cm⁻¹ and 1657 cm⁻¹ were assigned to the amide II band (C–N stretching) and the amide I band (C=O stretching), respectively. The overall signal-to-noise ratio of the SERS spectrum from a single Au DONA is, as expected, lower than that of agglomerated Au DONAs. Nonetheless, all significant Raman peaks of a TAMRA molecule were also observable from a single Au DONA. Neither the peak position nor the number of vibrational modes has changed, indicating that the molecule has not undergone

any major changes in molecular structure due to strain or charge carrier transfer within the Au DONA structure.

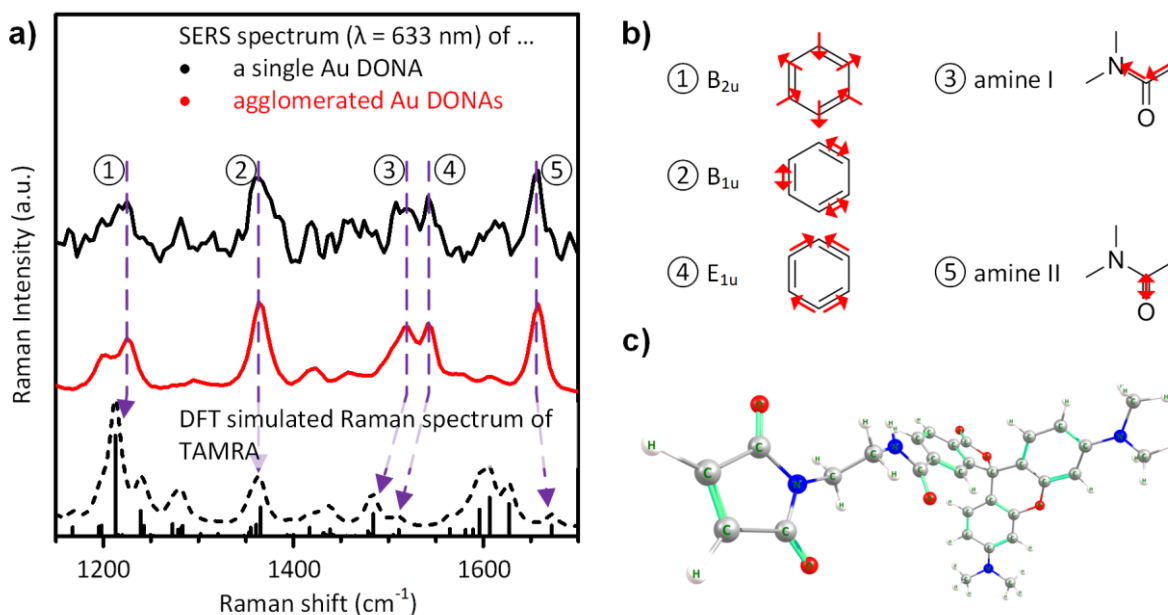


Figure 36: (a) Comparison of the measured SERS spectra from TAMRA (from Figure 35d) with the DFT simulated Raman spectrum of TAMRA. The five vibrational modes from (a) are marked and displayed in (b), the red arrows mark the atom displacement. (c) Molecular structure of TAMRA used for the DFT simulation.

Importantly, the SERS measurements underpin the spectral identification of TAMRA molecules coated on a single Au DONA on PSA substrates. On the other side, non-ideal Au DONAs with only one AuNP were not visible in the Raman measurement. We assume that the Raman signal amplification within those structures was significantly weaker compared to ideal Au DONA structures containing a plasmonic hot spot. As a result, the observed SERS enhancement was below the detection limit of the Raman spectroscopy.^{139,154}

The results in this section have revealed two benefits of the PSA substrate as a selective-adsorbing substrate for single-molecule detection applications. Firstly, the isolation of single hybrid nanostructures for SERS measurement was easily controlled, in contrast to the random nanostructure placement on an untreated substrate. The SERS signal of the plasmonic nanostructure collected on a PSA adsorption field was not affected by any other DNA nanostructures in the adjacent PSA field. Secondly, the PSA significantly reduces the available area for nanostructure adsorption, as Figure 35a demonstrates. This simplifies the search for adsorbed plasmonic nanostructures for single-molecule experiments.

First Approach Toward Single-Molecule SERS with Star DONA

Here, a single-molecule SERS experiment has been conducted with Star DONAs, using the same characterization method described in the section above. The SERS spectra were collected with a WITec alpha300R and measured by Yuya Kanehira from Uni Potsdam. The exchange

of spherical gold nanoparticles by gold nanostars in the Star DONA was expected to provide a higher plasmonic enhancement due to high aspect-ratio spikes on the nanoparticle surface. This has been shown experimentally in the work of Zhu et al.¹⁵⁵

Star DONAs were adsorbed and isolated on a PSA. The PSA fields were shown as bright rectangles in the AFM measurement and isolated Star DONAs were marked with white circles (Figure 37a). Some larger clusters and stripes on the array were present due to contamination, and a few broken Star DONAs with only one nanostar were observed as well. In general, the Star DONAs were successfully separated and most of the PSA fields were occupied by either one or none Star DONAs. The topography of a single Star DONA is shown in Figure 37b, the height of a nanostar was close to 70 nm while the center-to-center distance between the two nanostars was 65 nm. This suggests a very close distance between the nanostars, thus potentially creating a SERS hot spot with high Raman enhancement for the TAMRA molecule.

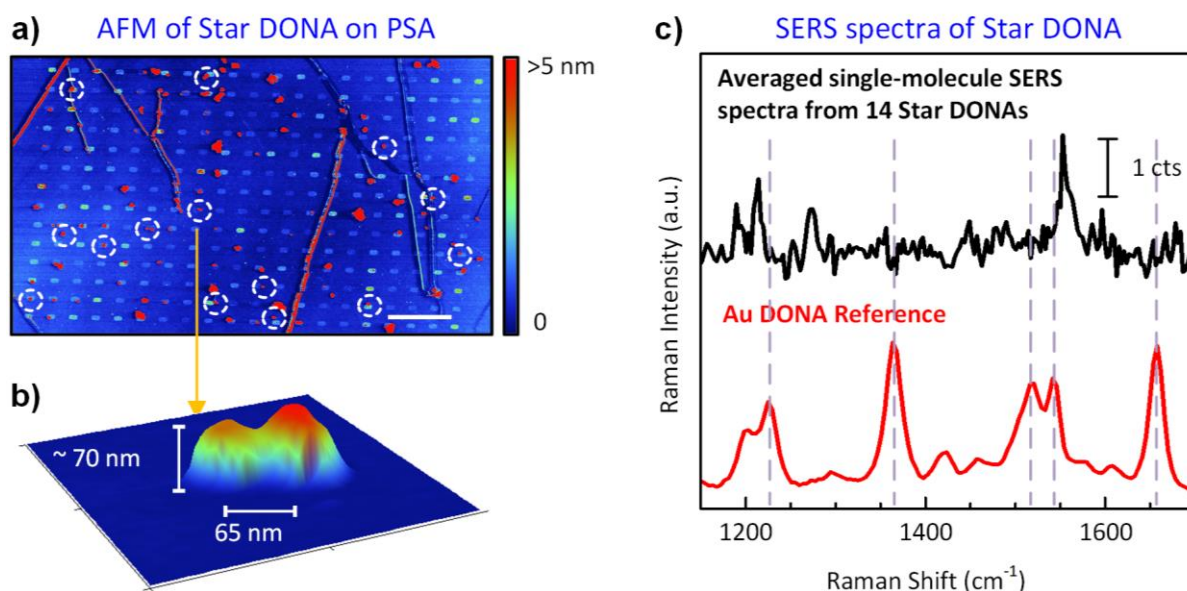


Figure 37: (a) AFM measurement of Star DONAs deposited on PSA, white circles mark Star DONAs for single-molecule SERS measurement. (b) 3D projected AFM measurement of a single Star DONA. (c) Averaged single-molecule SERS spectra of 14 Star DONAs, compared with spectra from reference measurement of agglomerated Au DONAs. Scale bar: 2 μm for (a).

Single-molecule SERS measurements have been performed with 14 Star DONAs as marked in Figure 37a. The averaged Raman spectra are shown in Figure 37c, which are poorly comparable with TAMRA spectra from the referent measurement. The characteristic Raman bands of TAMRA, which are marked with dash lines in Figure 37c, are not recognizable in the single-SERS spectrum of the Star DONAs. This result indicates that either the TAMRA molecule was not present at the plasmonic hot spot or the Raman enhancement of the Star DONA was insufficient to overcome the detection limit of the instrument.

In the work of Tapio et al., the single TAMRA molecule detection was successfully demonstrated with SERS on an Au DONA.¹⁷ Despite a low signal-to-noise ratio, three Raman bands at 1363 cm^{-1} , 1511 cm^{-1} , and 1662 cm^{-1} were recognizable and could be identified as the

TAMRA molecule.¹⁷ This result confirmed that hybrid nanostructures based on DONA DNA origami could provide sufficient Raman enhancement for the single-molecule detection of TAMRA using SERS.

Considering the measurement result of the Star DONA, two reasons could be responsible for the unsuccessful single-molecule detection in this section. Firstly, the highly unordered surface morphology of gold nanostars could increase the Raman enhancement of the Star DONA, but it also increased the complexity of placing a molecule exactly into the hot spot. The second reason was the high aspect ratio of the spikes on the nanostar surface, which led to a red shift of the LSPR band. If the LSPR spectra did not overlap with the exciting laser wavelength, as shown in the simulation in the work of Zhu et al., the LSPR efficiency of the nanostar will drop drastically.¹⁵⁶

Overall, the result in this section presents a first approach to combine single-molecule SERS measurement with a polar surface array. The PSA was a useful platform to isolate single nanostructures and suppress agglomeration, but the successful single-molecule analysis still relies on a suitable plasmonic nanostructure.

5.6. Isotope Dilution SERS with DTNB at Single-Molecule Level

The isotope dilution (ID) is a method of internal standardization, particularly in conjunction with mass spectrometry (MS), which offers exceptional precision and accuracy in determining sample concentrations. This method entails the addition of a known quantity of the analyte, referred to as a “spike”, to the original sample. Importantly, the spike possesses a distinct isotopic composition that differs from the natural state of the sample. By employing mass spectrometry to measure the ratio between the two isotopically distinct forms of the analyte, known as isotopologues, the concentration of the analyte in the sample can be accurately determined. However, while the combination of ID and MS enables the detection and quantification of extremely small amounts of substances, direct information about the molecular structure remains concealed.^{12–14}

Further advancement of the ID method involves its integration with spectroscopic techniques, such as surface-enhanced Raman Spectroscopy (SERS), which is known as ID-SERS. This combination capitalizes on the strengths of both methodologies, enabling not only the precise quantification of a specific molecule within a sample but also the identification of the molecule through its vibrational modes. Previous research using ID-SERS conducted by Fatemeh et al. exemplifies the quantification of urea and creatinine at concentrations ranging from 0.1 to 1 mM, as well as the quantification of the T6 and T13 peptide sequences within human growth serum (hGH) at a concentration of 50 nM.^{157,158}

In this section, our main objective is to investigate the feasibility of employing the Isotope Dilution-Surface-Enhanced Raman Spectroscopy (ID-SERS) technique at the single-molecule level, specifically targeting a singular hybrid nanostructure containing a limited number of

molecules within the plasmonic hotspot. Our selected molecule of interest for this study was **Dithionitrobenzoic acid (DTNB)**, which exhibits a high Raman cross-section attributable to its nitro group. Here, we have functionalized both natural DTNB (referred to as ^{14}N DTNB) and ^{15}N isotope-labeled DTNB (^{15}N DTNB) onto Au DONAs, aiming to evaluate the sensitivity of SERS in differentiating between the two DTNB isotopologues on a single Au DONA. Furthermore, we want to highlight the advantage of PSA in separating hybrid nanostructures by conducting ID-SERS mapping on a selective-adsorbing substrate.

During experimental procedures, the functionalization of DTNB onto gold surfaces results in the cleavage of the disulfide bond of DTNB, leading to the formation of stable gold-sulfide bonds between 2-Nitro-5-thiobenzoic acid (TNB) and the gold surface. For the purpose of clarity, throughout the remainder of section 5.6, we adopt the terminology “TNB coating” to denote the binding of DTNB on gold surfaces, while “ ^{14}N TNB” and “ ^{15}N TNB” refer to the binding of ^{14}N DTNB and ^{15}N DTNB on gold surfaces, respectively.

DFT Analysis of TNB Vibrational Mode Changes due to Isotope Exchange

Common isotope exchange for ID-SERS is performed on the carbon atom ($^{12}\text{C} \rightarrow ^{13}\text{C}$) or nitrogen atom ($^{14}\text{N} \rightarrow ^{15}\text{N}$) due to the high Raman scattering cross-section of the phenyl-group and the nitro-group.^{14,157} Here, DFT simulation was applied to simulate the impact of isotope exchange on the vibrational modes of TNB. The simulated Raman bands of TNB without isotope exchange (natural TNB) were compared with TNB where either all carbon atoms are exchanged to the isotope ^{13}C or nitrogen atoms are exchanged to ^{15}N .

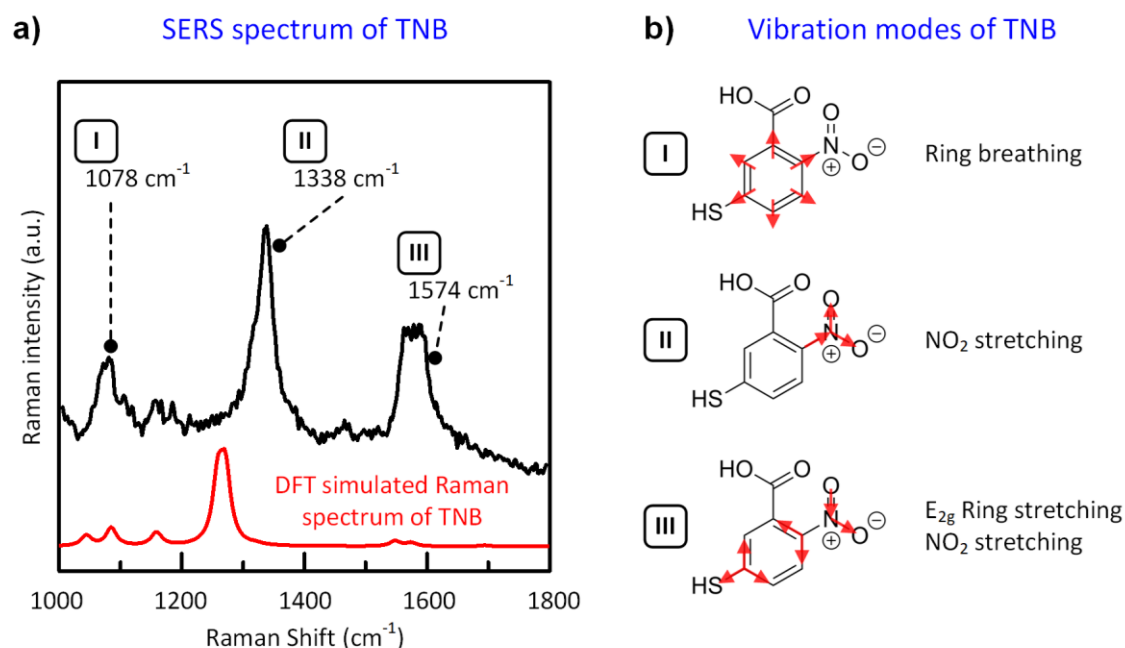


Figure 38: (a) SERS spectrum of TNB (in black) compared with DFT-simulated TNB Raman spectrum (in red). The Raman shift of three vibration modes from TNB is marked with Roman numerals in (a) and the corresponding atom displacement is schematically shown in (b).

Before simulating the isotope exchange, the SERS spectrum of the TNB molecule has been studied with DFT to identify which atoms and molecular fractions mainly contribute to the given vibrational mode. Figure 38a shows the DFT simulated Raman spectrum of TNB (red spectrum) compared with a measured SERS spectrum of TNB (black spectrum), that was deposited on a gold nanoparticle-loaded surface. The molecular vibration of the three most intense Raman bands has been identified by comparing them with the DFT simulated spectrum (Figure 38b). The Raman bands are: (I) the ring “breathing” mode at 1078 cm^{-1} , (II) the NO_2 stretching mode at 1338 cm^{-1} , and (III) the collective E_{2g} stretching mode of the phenyl ring with the NO_2 stretching mode at 1554 cm^{-1} .

It is notable that the measured SERS spectrum slightly differs from the DFT-simulated Raman spectrum. The main difference has been found at the NO_2 stretching mode, which locates at 1338 cm^{-1} in the measured SERS spectrum and at 1268 cm^{-1} in the DFT simulation. This rather large difference can be explained by the different environments in which the TNB molecule was located. In the DFT simulation, a TNB molecule was in a medium with a refractive index of 1 (i.e., in a vacuum), and no further molecules exist which prohibit intermolecular interactions. In contrast, the TNB molecules in SERS measurement were adsorbed on a gold nanoparticle surface, where the charge transfer from the electron-rich nitro-group toward the gold surface may influence the vibration frequency of TNB.

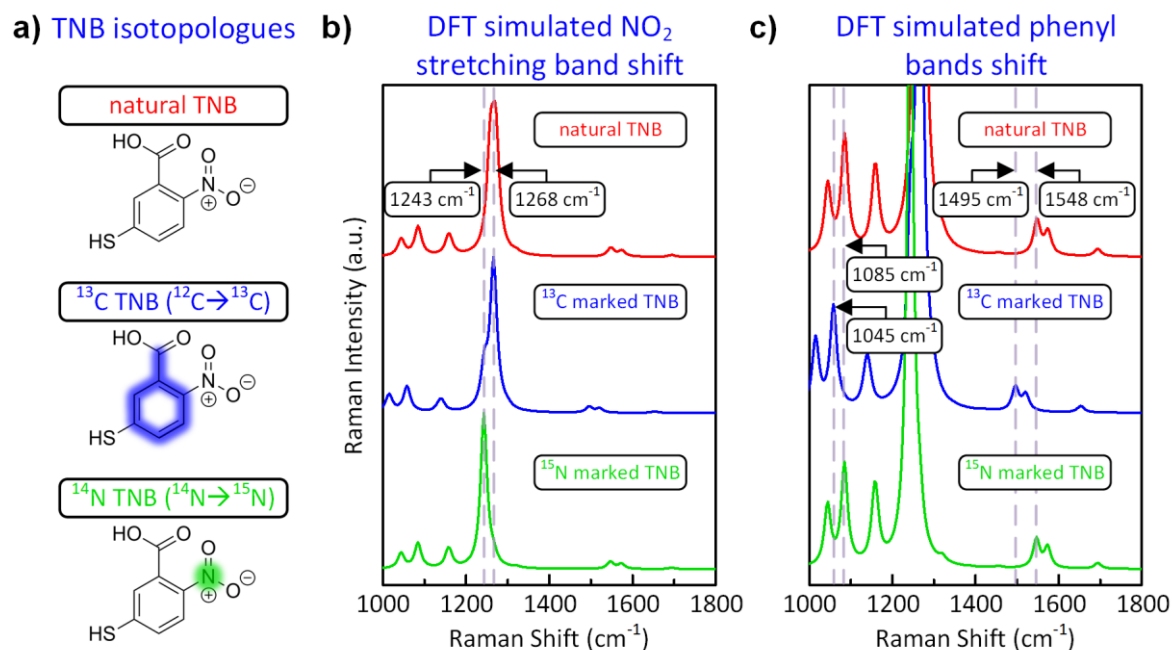


Figure 39: (a) The molecular structure of TNB, the blue and green clouds mark the position of isotope atoms if all carbon or nitrogen atoms were exchanged, respectively. (b, c) DFT simulated Raman spectra of natural TNB (red), ^{13}C marked TNB (blue), and ^{15}N marked TNB (green). Dash lines mark the Raman modes, which were red-shifted due to the isotope exchange.

The isotope exchange on TNB is schematically marked in Figure 39a, where the blue clouds show the position of ^{13}C atoms, and the green clouds mark the ^{15}N atom. Figure 39b and 39c depict the DFT-simulated Raman spectra of TNB, which shows the Raman band shift of the isotope-marked TNB in comparison with the spectrum of natural TNB. Notably, a prominent peak shift was observed in the NO_2 stretching mode, as denoted by dashed lines in Figure 39b. In the DFT simulation, the NO_2 stretching mode of natural TNB is situated at 1268 cm^{-1} , whereas the ^{13}C -labeled TNB exhibits an additional shoulder at approximately 1243 cm^{-1} . The ^{15}N -labeled TNB demonstrates a significant red-shift in the NO_2 stretching mode, with a maximum of 1243 cm^{-1} , which is 25 cm^{-1} lower than that of natural TNB. This red-shift in the NO_2 stretching mode of isotope-exchanged TNB can be attributed to the increased mass of carbon and nitrogen atoms, leading to a change in the frequency of molecular vibration.

This red-shift of vibrational modes related to the phenyl group was observed primarily with the ^{13}C -marked TNB (blue spectrum), depicted in Figure 39c. Both the ring breathing mode at 1085 cm^{-1} and the E_{2g} stretching mode at 1548 cm^{-1} were affected by the presence of ^{13}C isotopes, as evident in the figure.

Based on the DFT results, employing ^{15}N -labeled TNB as a candidate for isotope dilution SERS measurements would be more convenient. This is primarily due to the intense Raman shift observed in the NO_2 band, and the fact that exchanging one nitrogen atom is more cost-effective than replacing all seven carbon atoms for TNB molecules.

ID-SERS Measurement of Single TNB-Coated Au DONA

In this part, the SERS measurement on a single TNB-coated Au DONA was conducted, which was isolated on a PSA. The TNB-coated Au DONAs (Figure 40a) used in this section were provided by Yuya Kanehira from Uni Potsdam. The SERS spectra were obtained with WITec alpha300 RA using a 633 nm excitation laser with 1 mW power and 2 s integration time.

Figure 40b shows representative SERS spectra of single Au DONAs coated with different TNB isotopologues. The peak shift of the NO_2 stretching mode from 1338 cm^{-1} to 1314 cm^{-1} was the most significant spectral difference between ^{14}N and ^{15}N TNB-coated Au DONAs. The measured Raman shift change of the NO_2 stretching mode ($\Delta\omega \sim 24\text{ cm}^{-1}$) corresponds well with the red shift in the DFT simulation ($\Delta\omega \sim 25\text{ cm}^{-1}$). Further vibration modes of TNB related to the phenyl-ring stretching (bands I, III in Figure 38b) did not show significant peak shifts.

The SERS spectrum of an Au DONA with mixed ^{14}N and ^{15}N TNB (yellow spectrum in Figure 40b) shows vibrational bands from both $^{14}\text{NO}_2$ and $^{15}\text{NO}_2$ functional groups. This result indicates that the natural TNB, as well as the ^{15}N -labeled TNB, were both present within the plasmonic hot spot.

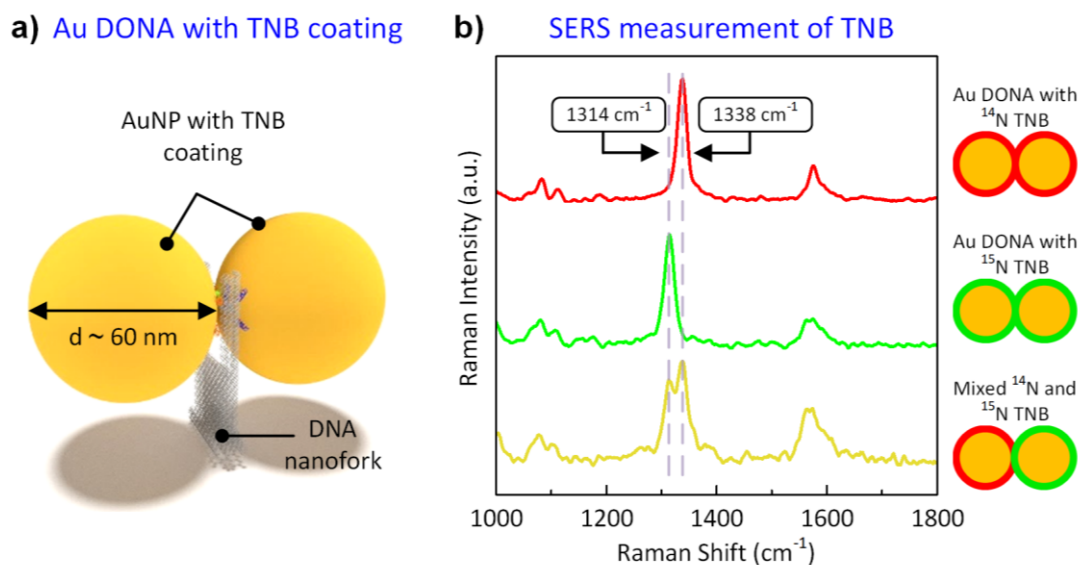


Figure 40: (a) Design of a TNB-coated Au DONA. (b) SERS measurement of Au DONAs with TNB coating. Dash lines show the Raman peaks that have been used to identify ^{14}N and ^{15}N TNB.

The results in this part underpin the low detection limit of SERS, which was capable to detect and identify different TNB isotopologues in an extremely low amount of substance. Unfortunately, it was not possible to directly link the TNB Raman intensity and the number of detected molecules, since the absolute number on the Au DONA surface was unknown. Nonetheless, we have estimated that no more than about 6000 molecules have contributed to the SERS signal of a single Au DONA (Appendix A2).

Correlated dark-field microscopy and SERS mapping of TNB-coated Au DONAs on PSA

In this section, the TNB-coated Au DONAs were selectively adsorbed on PSA and analyzed by correlated dark-field microscopy and SERS mapping. This is an important approach toward the statistical evaluation of isotope-dilution SERS on PSA, where both the spectral identification and the spatial resolution of the analysis method are requested.

Here, the dark-field imaging revealed the approximate positions of the Au DONAs on PSA while the SERS mapping showed the location of TNB signals. Dark-field microscopy presents a clear advantage over confocal microscopy, primarily attributed to its capacity for producing enhanced contrast in imaging. Unlike confocal microscopy, dark-field microscopy selectively detects scattered light (from unevenness, such as Au DONAs). The dark-field image exhibits Au DONAs as point sources of light scattering, with the scattered light being collected and the back-scattered light (mainly from the PSA substrate) being filtered out. The yellow-colored signals observed in the dark-field image (Figure 41) have resulted from the scattering of light emitted by the LED light source, which possesses a color temperature of 4500 K (with a spectral range of $\lambda \sim 530$ nm to 630 nm), thereby appearing yellowish.

According to the study of Pini et al., the gold nanoparticles comprising the Au DONAs can be viewed as polarizable electric point dipoles.¹⁵⁹ In the dark-field image, they appeared as yellowish circles rather than bright spots due to the excitation of the dipolar localized surface plasmon resonance (LSPR) mode of the gold nanoparticles.¹⁵⁹ The different brightness of the yellow circles indicated the relative intensity of the scattered light, which corresponds to the number of gold nanoparticles that contribute to the light scattering at the specific position. Thus, a non-ideal Au DONA with only one gold nanoparticle appeared darker than Au DONAs with two gold nanoparticles.

A total number of four samples were adsorbed on PSA and presented in Figure 41: Au DONAs coated with (a) ¹⁴N TNB, (b) ¹⁵N TNB, (c) a 1:1 mixture of both, and (d) Au DONA with one ¹⁴N TNB-coated AuNP and one ¹⁵N TNB-coated AuNP. Figure 41a–41d depicts the dark-field microscopy image and the SERS mapping of TNB-coated Au DONAs on PSA. The area with PSA is marked with white dash-lines. The adsorbed Au DONAs on PSA formed a rectangular array of yellow circles, that appear in the dark-scattering image. The arrays in Figure 41a and 41d were larger by design (~15×15 μm²), while Figure 41b and 41c show ~10×7 μm² arrays.

SERS mapping was conducted in the same area which has been shown in the dark-field images. In Figure 41a, the SERS mapping shows several red spots. Each red spot corresponds to one location, in which the SERS spectrum of ¹⁴N TNB was identified (maximum of the NO₂ stretching mode at 1338 cm⁻¹). The size of the red spots corresponds with the Raman signal intensity. It is noticeable that the number of SERS spots was inferior compared with Au DONAs identified by the dark-field image. This is due to the presence of Au DONAs with only one gold nanoparticle, which couldn't generate a sufficiently high SERS signal to be detected. By overlapping the SERS measurement and the dark-field image, the location of the SERS signals has been assigned to the corresponding spot in the dark-field image and was marked with red circles. The same comparison was performed in Figure 41b as well. The four green spots show the location of ¹⁵N TNB in the SERS mapping (maximum of the NO₂ stretching mode at 1314 cm⁻¹) and have been assigned to the respective Au DONAs in the dark-field image.

The PSA in Figure 41c was loaded with a mixture of Au DONAs that are fully coated with either ¹⁴N TNB or ¹⁵N TNB. The two types of Au DONAs are visually indistinguishable in the dark-field image, and common characterization methods like AFM, SEM, or fluorescence spectroscopy are not able to identify the isotopic composition of TNB molecules that was chemically coated on the Au DONA. Here, the combination of PSA and SERS allows the spatial separation of single Au DONAs and simultaneously the identification of the TNB isotopologue. The intensity ratio of the NO₂ stretching mode at 1314 cm⁻¹ / 1338 cm⁻¹ was the criteria for the spectrum identification and the color assignment in Figure 41c. The SERS mapping in Figure 41c clearly shows two Au DONAs with ¹⁴N TNB and two Au DONAs with ¹⁵N TNB on the PSA. These SERS spectra (Figure 41c, I–IV) are presented in Figure 42. The signal overlapping of ¹⁴N TNB and ¹⁵N TNB, which could be expected in the case of

agglomerating Au DONAs with different isotopologues, was prevented by selective adsorption on the PSA.

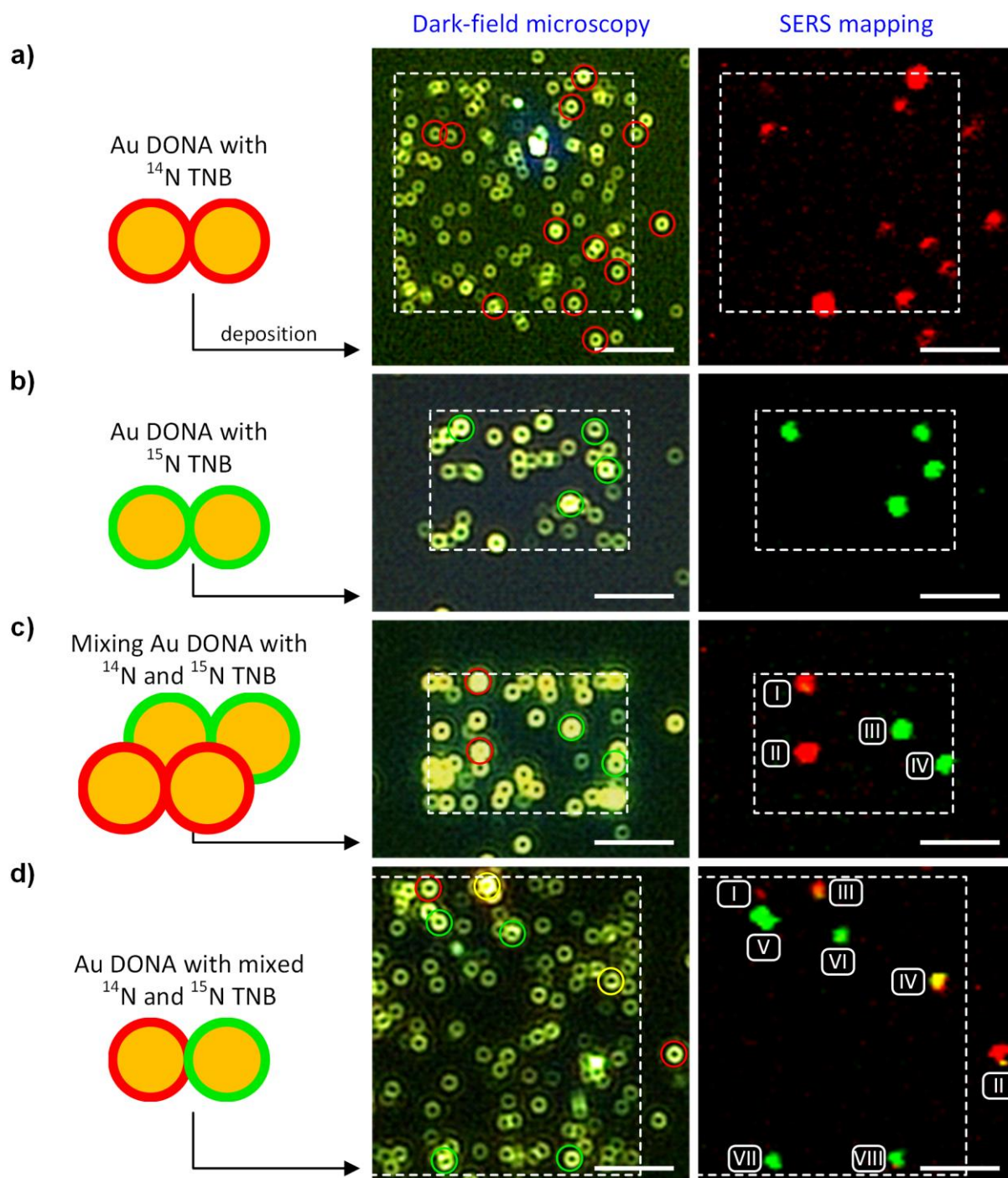


Figure 41: SERS mapping and dark-field microscopy image of Au DONAs with (a) ^{14}N TNB coating, (b) ^{15}N TNB coating, (c) a mixture of both, and (d) and mixed ^{14}N and ^{15}N TNB on PSA. The white rectangles mark the PSA area. The red color in the SERS mapping corresponds to the SERS signal of ^{14}N TNB, the corresponding position on the PSA is marked with a red circle in the dark-field image. The position of SERS signals originating from ^{15}N TNB and mixed ^{14}N and ^{15}N TNB are marked in the same way with green and yellow circles, respectively. Scale bars are 5 μm in (a) and 4 μm in (b–d).

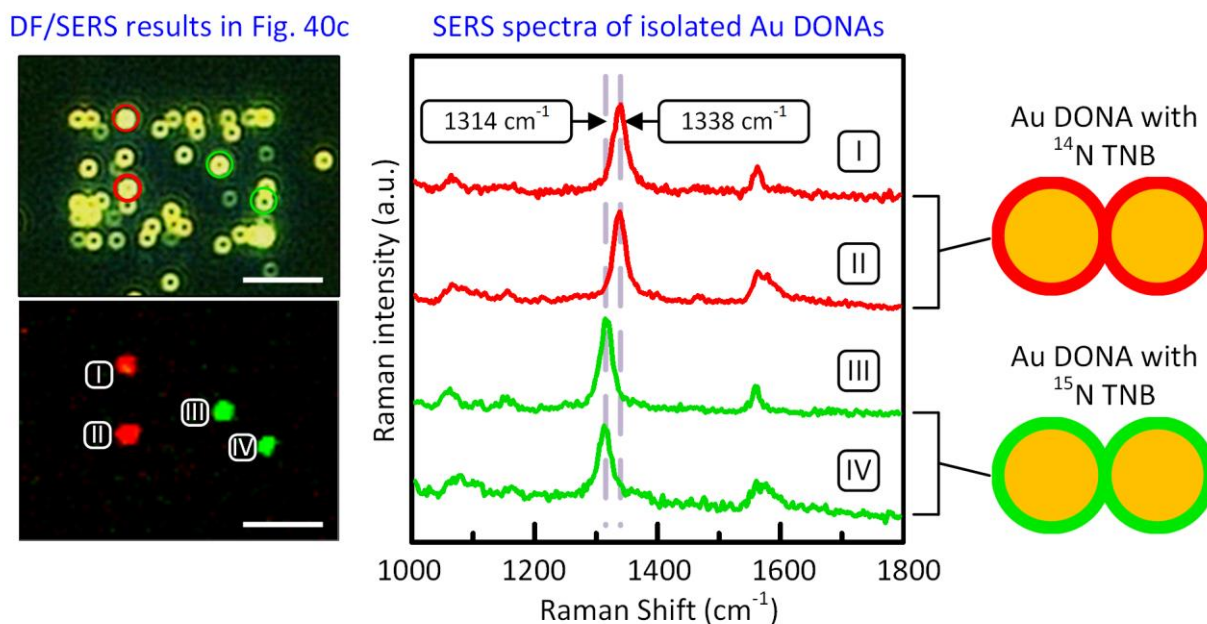


Figure 42: (left) Correlated dark-field/SERS results from Figure 41c, scale bars are 4 μm . (right) SERS spectra of selected Au DONAs. The Roman numerals (I–IV) of the SERS spectra correspond with the marked Au DONAs. The dash lines show the Raman peaks that have been used to identify ^{14}N and ^{15}N TNB.

In Figure 41d, the dark-field image and the SERS mapping show a PSA loaded with Au DONAs, that contains one ^{14}N TNB-coated AuNP and one ^{15}N TNB-coated AuNP. One would expect that the SERS mapping only shows the overlapping spectrum of the natural and the ^{15}N -marked TNB (like the yellow spectrum in Figure 40b). Instead, the SERS mapping in Figure 41d showed eight Raman active spots (marked with Roman numerals), where two have been identified as ^{14}N TNB, four spots show the spectrum of ^{15}N TNB, and two spots have characteristics of both ^{14}N TNB and ^{15}N TNB Raman signals.

The observed SERS result in Figure 41d may initially seem counterintuitive since the same sample displays different vibrational modes. However, considering that only TNB molecules within the hot spot effectively contribute to the SERS spectra, and given that the number of TNB molecules within the hot spot was extremely low, it is possible that the abundance of natural TNB outweighs the ^{15}N TNB isotopes or vice versa, while the about 50/50 isotopologue ratio was only observed in one case. This discrepancy in isotopologue composition could potentially account for the variation in the SERS spectra observed among different Au DONAs. Figure 43 displays the SERS spectra of the eight identified Au DONAs in Figure 41d, all SERS spectra were normalized to enable a better comparison. The signal-to-noise ratio of spectra (I, III) in Figure 43 appears to be lower due to the weak SERS intensity, probably caused by a slightly larger plasmonic hot spot. Among all spectra in Figure 43, it is notable that the ring breathing mode of TNB around 1040 cm^{-1} was often undetected, this band only appears in the spectra (II, V). Furthermore, the Raman intensity ratio between different vibrational modes may change greatly, for example, the E_{2g} stretching mode of the spectrum (II) at 1548 cm^{-1}

appears to be stronger than the NO_2 stretching mode, which is typically the most intense SERS band. These minor differences between the SERS spectra can be explained by the different binding orientations of TNB molecules toward the gold nanoparticle, as explained in section 2.4. Since the vibrational modes at 1040 cm^{-1} and 1550 cm^{-1} were caused by the phenyl ring stretching, these bands are expected to receive different SERS enhancement when the phenyl ring was either perpendicular or parallel oriented to the gold nanoparticle surface due to the radiation enhancement effect (Figure 6).

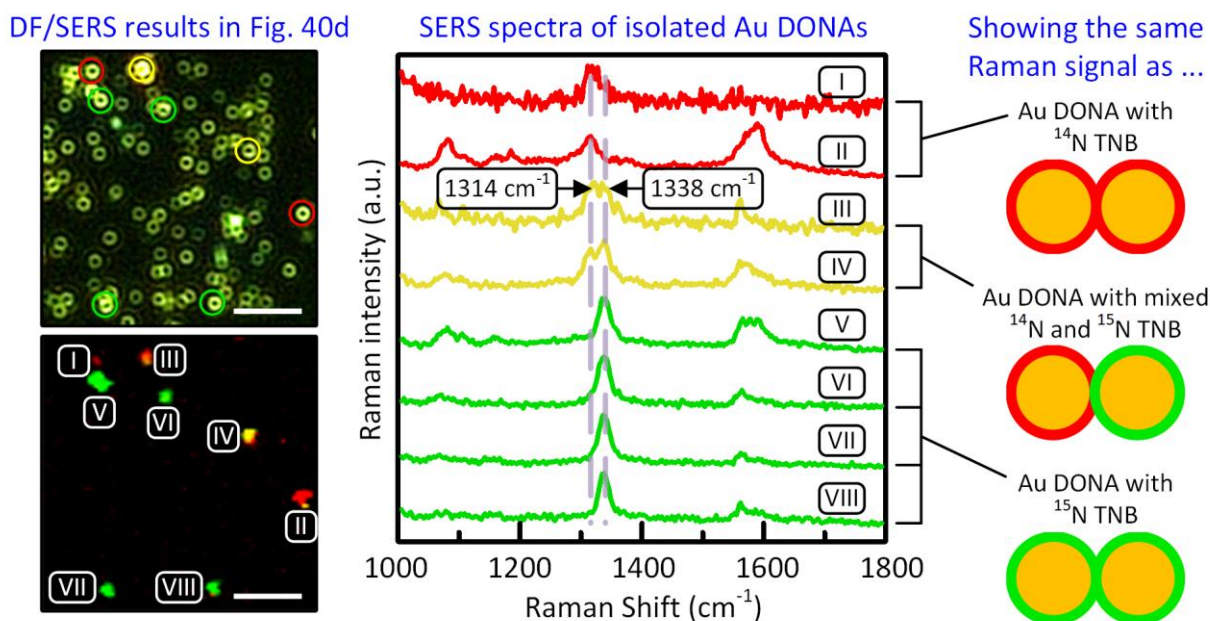


Figure 43: (left) Correlated Dark-Field/SERS results from Figure 41d, scale bars are $4\ \mu\text{m}$. (right) SERS spectra of selected Au DONAs. The Roman numerals (I–VIII) of the SERS spectra correspond with the marked Au DONAs. The dash lines show the Raman peaks that have been used to identify ^{14}N and ^{15}N TNB.

The phenomenon of the same sample showing different vibrational modes, as observed in Figure 41d, was further studied in cooperation with Yuya Kanehira (Uni Potsdam). Briefly, a SERS time series was conducted on isolated Au DONAs with one ^{14}N TNB-coated AuNP and one ^{15}N TNB-coated AuNP. The SERS spectra were collected over 300 seconds, and one spectrum is taken every second. The SERS time series (Appendix A5) reveals that the vibrational mode of a single Au DONA may change over time, e.g., the SERS spectrum showed signals of ^{14}N TNB at the beginning and switched to ^{15}N TNB signals during the time series or vice versa. This observation indicates either molecular migration on the Au DONA surface or the movement of gold nanoparticles that changes the hot spot location and therefore the TNB isotope stoichiometry within the hot spot. The ongoing investigation underpins the necessity of studying the influence on plasmonic hot spots and creating a basis for future ID-SERS-based single-molecule studies.

6. Summary and Outlook

This study successfully demonstrated the effective detection of individual molecules through correlated AFM and SERS analysis. Valuable insights into single-molecule detection with plasmonic hybrid nanostructures were provided by this work. The utilization of a DNA origami-based hybrid nanostructure showed promising capabilities in generating small plasmonic active hot spots, which resulted in the enhancement of SERS signals for single molecules.

In chapter 4, the design of a plasmonic hot spot for effective single-molecule SERS within the hybrid nanostructure was supported by DFT simulations. The SERS signal of hybrid nanostructures containing a single ATTO-633 molecule was collected by a confocal Raman spectroscopy, and the position of the hybrid nanostructures was determined using AFM. The correlated SERS/AFM measurement clearly confirmed the presence of the ATTO-633 molecule from a limited number of hybrid nanostructures. However, photodegradation was observed when increasing the laser power, resulting in non-reproducible and identifiable Raman signals.³⁸ Another challenge encountered in obtaining the SERS signal from a single hybrid nanostructure was agglomeration, which complicated the assignment of the detected SERS signal to a specific number of hybrid nanostructures. Consequently, the quantification of molecules becomes challenging since the number of hybrid nanostructures from one SERS signal cannot be controlled in advance.

To address the challenge of hybrid nanostructure agglomeration, a novel approach was adopted involving selective adsorption onto a Polar Surface Array (PSA) in chapter 5, developed in collaboration with the group of Dr. Markus Etzkorn from TU Braunschweig. Through DFT simulations, it was revealed that the attractive Coulomb interaction between the DNA origami fragment and the polar surface was further enhanced by a layer of magnesium cations, which was absent on the apolar surface.¹³⁹ The DFT results not only support but also contribute to the existing experimental findings by previous researchers who observed selective adsorption on substrates with varying polarities.^{137,138}

To achieve the isolation of a single hybrid nanostructure on the PSA, the adsorption behavior of hybrid nanostructures on the PSA was thoroughly examined by systematically varying several experimental parameters. These parameters included the concentration of the adsorbate, incubation time, PSA field size, and magnesium concentration. The concentration of the adsorbate emerged as a crucial factor in minimizing the likelihood of multiple hybrid nanostructures occupying the same PSA field, this observation is supported by analysis with the Langmuir adsorption model.¹³⁹

The hybrid nanostructure adsorption on PSA was further developed with the Etzkorn group, and an improved electron beam fabrication process elevated the probability of isolating a single hybrid nanostructure, resulting in an impressive yield of approximately 77% single occupation on PSA fields.¹⁶⁰ This has greatly improved the feasibility of isolating and studying individual hybrid nanostructures locally on the PSA, paving the way for more precise and controlled experimental investigations.

The experiments involving the single-molecule SERS on the PSA were conducted using Au DONAs (hybrid nanostructures with two 60 nm gold nanospheres coated with TAMRA) in section 5.5. Here, Au DONAs were successfully isolated on the PSA, which led to the identification of TAMRA-SERS signals originating from a single TAMRA-coated hybrid nanostructure through correlated AFM/SERS measurements. In an initial attempt to detect a single TAMRA molecule, Star Dimers (two 60 nm gold nanostars with a single TAMRA molecule in the hot spot) were employed on the PSA. Unfortunately, this approach did not verify the presence of a single TAMRA molecule yet. However, Yuya Kanehira et al. (Ph.D. student in Prof. Ilko Bald's group) further pursued the investigation with Star Dimers and succeeded in achieving the verification of a single TAMRA molecule using SERS. (Appendix A4)

In section 5.6, we expand the capabilities of ID-SERS by applying the PSA as a selective-adsorbing substrate to achieve single-molecule level detection combined with an isotope dilution (ID) approach. Au DONAs were coated with TNB molecules, as well as isotope-marked TNBs with ¹⁵N labeling. By utilizing the PSA substrate, SERS measurements on a single TNB-modified Au DONA were achieved, ensuring that the SERS signal originated from not more than approx. 6000 TNB molecules (Appendix A2). Furthermore, confocal Raman spectroscopy allowed for the identification of TNB isotopologues originating from a single hotspot, accommodating an extremely low number of molecules. This outcome establishes the foundation for conducting SERS measurements on single hybrid nanostructures and opens up possibilities for future investigations involving single-molecule ID-SERS experiments, which is a potential topic for a future Ph.D. thesis.

Overall, this study demonstrates that by utilizing the PSA as a selective-adsorbing substrate, the hindrance of agglomeration can now be overcome systematically. This leads to a significant increase in the probability of obtaining isolated hybrid nanostructures suitable for single-molecule experiments and enables more efficient and effective large-scale scans for molecule quantification. The achieved result represents a significant advancement towards the realization of single-molecule quantification via SERS on a large scale.

References

- (1) Bartl, G.; Becker, P.; Beckhoff, B.; Bettin, H.; Beyer, E.; Borys, M.; Busch, I.; Cibik, L.; D'Agostino, G.; Darlatt, E.; Luzio, M. Di; Fujii, K.; Fujimoto, H.; Fujita, K.; Kolbe, M.; Krumrey, M.; Kuramoto, N.; Massa, E.; Mecke, M.; Mizushima, S.; Müller, M.; Narukawa, T.; Nicolaus, A.; Pramann, A.; Rauch, D.; Rienitz, O.; Sasso, C. P.; Stopic, A.; Stosch, R.; Waseda, A.; Wundrack, S.; Zhang, L.; Zhang, X. W. A New ²⁸Si Single Crystal: Counting the Atoms for the New Kilogram Definition. *Metrologia* **2017**, *54* (5), 693. <https://doi.org/10.1088/1681-7575/aa7820>.
- (2) BIPM. *The International System of Units (SI)*, 8th ed.; STEDI Media: Paris, 2006.
- (3) Güttler, B.; Bettin, H.; Brown, R. J. C.; Davis, R. S.; Mester, Z.; Milton, M. J. T.; Pramann, A.; Rienitz, O.; Vocke, R. D.; Wielgosz, R. I. Amount of Substance and the Mole in the SI. *Metrologia* **2019**, *56* (4). <https://doi.org/10.1088/1681-7575/ab1fae>.
- (4) König, A. *Verhandlungen Der Deutschen Physikalischen Gesellschaft Im Jahre 1900*, 2nd ed.; 1900.
- (5) Einstein, A. Zur Theorie Der Brownschen Bewegung. *Ann. Phys.* **1906**, *324* (2), 371–381. <https://doi.org/10.1002/andp.19063240208>.
- (6) Engel, T.; Reid, P. *Physical Chemistry*; Benjamin Cummings, 2005.
- (7) da Silva, T. F. Photon-Counting-Based Optical Frequency Metrology. *Appl. Opt.* **2020**, *59* (36), 11232–11239. <https://doi.org/10.1364/AO.411171>.
- (8) Weis, J.; von Klitzing, K. Metrology and Microscopic Picture of the Integer Quantum Hall Effect. *Philos. Trans. R. Soc. A Math. Phys. Eng. Sci.* **2011**, *369* (1953), 3954–3974. <https://doi.org/10.1098/rsta.2011.0198>.
- (9) Price, G.; De Bièvre, P. Simple Principles for Metrology in Chemistry: Identifying and Counting. *Accredit. Qual. Assur.* **2009**, *14* (6), 295–305. <https://doi.org/10.1007/s00769-009-0529-4>.
- (10) Michnowicz, T.; Borca, B.; Pétuya, R.; Schendel, V.; Pristl, M.; Pentegov, I.; Kraft, U.; Klauk, H.; Wahl, P.; Mutombo, P.; Jelínek, P.; Arnau, A.; Schlickum, U.; Kern, K. Controlling Single Molecule Conductance by a Locally Induced Chemical Reaction on Individual Thiophene Units. *Angew. Chemie* **2020**, *132* (15), 6266–6271. <https://doi.org/10.1002/ange.201915200>.
- (11) Wallace, G. Q.; Graham, D. Pushing the Limits. *Nat. Rev. Chem.* **2022**, *6* (12), 842–843. <https://doi.org/10.1038/s41570-022-00444-z>.
- (12) Stosch, R.; Henrion, A.; Schiel, D.; Güttler, B. Surface-Enhanced Raman Scattering Based Approach for Quantitative Determination of Creatinine in Human Serum. *Anal. Chem.* **2005**, *77* (22), 7386–7392. <https://doi.org/10.1021/ac0511647>.
- (13) Zakeł, S.; Wundrack, S.; O'Connor, G.; Güttler, B.; Stosch, R. Validation of Isotope Dilution Surface-Enhanced Raman Scattering (IDSERS) as a Higher Order Reference Method for Clinical Measurements Employing International Comparison Schemes. *J. Raman Spectrosc.* **2013**, *44* (9), 1246–1252. <https://doi.org/10.1002/jrs.4349>.
- (14) Zakeł, S.; Rienitz, O.; Güttler, B.; Stosch, R. Double Isotope Dilution Surface-Enhanced Raman Scattering as a Reference Procedure for the Quantification of Biomarkers in Human Serum. *Analyst* **2011**, *136* (19), 3956–3961. <https://doi.org/10.1039/c1an15207f>.
- (15) Le Ru, E. C.; Meyer, M.; Blackie, E.; Etchegoin, P. G. Advanced Aspects of Electromagnetic SERS Enhancement Factors at a Hot Spot. *J. Raman Spectrosc.* **2008**, *39* (9), 1127–1134. <https://doi.org/10.1002/jrs.1945>.
- (16) Maurer, V.; Frank, C.; Porsiel, J. C.; Zellmer, S.; Garnweitner, G.; Stosch, R. Step-by-Step Monitoring of a Magnetic and SERS-Active Immunosensor Assembly for Purification and Detection of Tau Protein. *J. Biophotonics* **2020**, *13* (3). <https://doi.org/10.1002/jbio.201960090>.
- (17) Tapio, K.; Mostafa, A.; Kanehira, Y.; Suma, A.; Dutta, A.; Bald, I. A Versatile DNA Origami-Based Plasmonic Nanoantenna for Label-Free Single-Molecule Surface-Enhanced Raman Spectroscopy. *ACS Nano* **2021**, *15* (4), 7065–7077. <https://doi.org/10.1021/acsnano.1c00188>.
- (18) Fang, W.; Jia, S.; Chao, J.; Wang, L. L. L.; Duan, X.; Liu, H.; Li, Q.; Zuo, X.; Wang, L. L. L.; Wang, L. L. L.; Liu, N.; Fan, C. Quantizing Single-Molecule Surface-Enhanced Raman Scattering with DNA Origami Metamolecules. *Sci. Adv.* **2023**, *5* (9), eaau4506. <https://doi.org/10.1126/sciadv.aau4506>.
- (19) McCreery, R. L. *Raman Spectroscopy for Chemical Analysis*; 2001; Vol. 12. <https://doi.org/10.1088/0957-0233/12/5/704>.
- (20) Hesse, M.; Meier, H.; Zeeh, B. *Spektroskopische Methoden (IR, UV/ VIS) in Der Organischen Chemie*; 2012. <https://doi.org/10.1515/9783112648384>.

REFERENCES

- (21) Malyj, M.; Griffiths, J. E. Stokes/Anti-Stokes Raman Vibrational Temperatures: Reference Materials, Standard Lamps, and Spectrophotometric Calibrations. *Appl. Spectrosc.* **1983**, *37* (4), 315–333. <https://doi.org/10.1366/0003702834634325>.
- (22) Patnaik, P. *Dean's Analytical Chemistry Handbook*, 2nd ed.; 2004.
- (23) Ru, E. Le; Etchegoin, P. *Principles of Surface Enhanced Raman Spectroscopy*, 1st ed.; 2008.
- (24) Sidorov, T. A. Raman Spectra and Molecular Structure of Silicates. *Russ. J. Inorg. Chem.* **2007**, *52* (10), 1586–1594. <https://doi.org/10.1134/S0036023607100191>.
- (25) Wilson, E. B.; Decius, J. C.; Cross, P. C.; Sundheim, B. R. Molecular Vibrations: The Theory of Infrared and Raman Vibrational Spectra. *J. Electrochem. Soc.* **1955**, *102* (9), 235Ca. <https://doi.org/10.1149/1.2430134>.
- (26) Ling, Y.; Xie, W. C.; Liu, G. K.; Yan, R. W.; Wu, D. Y.; Tang, J. The Discovery of the Hydrogen Bond from P-Nitrothiophenol by Raman Spectroscopy: Guideline for the Thioalcohol Molecule Recognition Tool. *Sci. Rep.* **2016**, *6* (1), 31981. <https://doi.org/10.1038/srep31981>.
- (27) de Veij, M.; Vandenaabeele, P.; De Beer, T.; Remon, J. P.; Moens, L.; Veij, M. De; Vandenaabeele, P.; Beer, T. De; Paul, J.; Moens, L. Reference Database of Raman Spectra of Pharmaceutical Excipients. *J. Raman Spectrosc.* **2009**, *40* (3), 297–307. <https://doi.org/10.1002/jrs.2125>.
- (28) Hsieh, W.-P.; Zalden, P.; Wuttig, M.; Lindenberg, A. M.; Mao, W. L. High-Pressure Raman Spectroscopy of Phase Change Materials. *Appl. Phys. Lett.* **2013**, *191908* (October). <https://doi.org/10.1063/1.4829358>.
- (29) Vankeirsbilck, T.; Vercauteren, A.; Baeyens, W.; Van der Weken, G.; Verpoort, F.; Vergote, G.; Remon, J. . Applications of Raman Spectroscopy in Pharmaceutical Analysis. *TrAC Trends Anal. Chem.* **2002**, *21* (12), 869–877. [https://doi.org/10.1016/S0165-9936\(02\)01208-6](https://doi.org/10.1016/S0165-9936(02)01208-6).
- (30) Lewis, I. R.; Edwards, H. G. M. *Handbook of Raman Spectroscopy: From the Research Laboratory to the Process Line*, 1st ed.; Taylor & Francis, 2001.
- (31) Majzner, K.; Kaczor, A.; Kachamakova-Trojanowska, N.; Fedorowicz, A.; Chlopicki, S.; Baranska, M. 3D Confocal Raman Imaging of Endothelial Cells and Vascular Wall: Perspectives in Analytical Spectroscopy of Biomedical Research. *Analyst* **2013**, *138* (2), 603–610. <https://doi.org/10.1039/C2AN36222H>.
- (32) Barbillat, J.; Dhamelincourt, P.; Delhaye, M.; Da Silva, E. Raman Confocal Microprobing, Imaging and Fibre-Optic Remote Sensing: A Further Step in Molecular Analysis. *J. Raman Spectrosc.* **1994**, *25* (1), 3–11. <https://doi.org/10.1002/jrs.1250250103>.
- (33) Rottenfusser, R.; Wilson, E. E.; Davidson, M. W. *Education in Microscopy and Digital Imaging*. <https://zeiss-campus.magnet.fsu.edu/articles/basics/resolution.html>.
- (34) Breitenbach, J.; Schrof, W.; Neumann, J. Confocal Raman-Spectroscopy: Analytical Approach to Solid Dispersions and Mapping of Drugs. *Pharm. Res.* **1999**, *16* (7), 1109–1113. <https://doi.org/10.1023/A:1018956304595>.
- (35) Caspers, P. J.; Lucassen, G. W.; Puppels, G. J. Combined In Vivo Confocal Raman Spectroscopy and Confocal Microscopy of Human Skin. *Biophys. J.* **2003**, *85* (1), 572–580. [https://doi.org/10.1016/S0006-3495\(03\)74501-9](https://doi.org/10.1016/S0006-3495(03)74501-9).
- (36) Puppels, G. J.; Colier, W.; Olminkhof, J. H. F.; Otto, C.; de Mul, F. F. M.; Greve, J. Description and Performance of a Highly Sensitive Confocal Raman Microspectrometer. *J. Raman Spectrosc.* **1991**, *22* (4), 217–225. <https://doi.org/10.1002/jrs.1250220405>.
- (37) Michalet, X.; Weiss, S. Single-Molecule Spectroscopy and Microscopy. *Comptes Rendus Phys.* **2002**, *3* (5), 619–644. [https://doi.org/10.1016/S1631-0705\(02\)01343-9](https://doi.org/10.1016/S1631-0705(02)01343-9).
- (38) Heck, C.; Kanehira, Y.; Kneipp, J.; Bald, I. Amorphous Carbon Generation as a Photocatalytic Reaction on DNA-Assembled Gold and Silver Nanostructures. *Molecules* **2019**, *24* (12). <https://doi.org/10.3390/molecules24122324>.
- (39) Nie, S.; Emory, S. R. Probing Single Molecules and Single Nanoparticles by Surface-Enhanced Raman Scattering. *Science* **1997**, *275* (5303), 1102–1106. <https://doi.org/10.1126/science.275.5303.1102>.
- (40) Kneipp, K.; Wang, Y.; Kneipp, H.; Perelman, L. T.; Itzkan, I.; Dasari, R. R.; Feld, M. S. Single Molecule Detection Using Surface-Enhanced Raman Scattering (SERS). *Phys. Rev. Lett.* **1997**, *78* (9), 1667–1670. <https://doi.org/10.1103/PhysRevLett.78.1667>.
- (41) Koya, A. N. Plasmonic Nanoarchitectures for Single-Molecule Explorations: An Overview. *Adv. Photonics Res.* **2022**, *3* (3), 2100325. <https://doi.org/10.1002/adpr.202100325>.
- (42) Lindquist, N. C.; Bido, A. T.; Brolo, A. G. Single-Molecule SERS Hotspot Dynamics in Both Dry and Aqueous Environments. *J. Phys. Chem. C* **2022**, *126* (16), 7117–7126. <https://doi.org/10.1021/acs.jpcc.2c00319>.
- (43) Skolrood, L.; Wang, Y.; Zhang, S.; Wei, Q. Single-Molecule and Particle Detection on True Portable Microscopy Platforms. *Sensors and Actuators Reports* **2022**, *4*, 100063. <https://doi.org/10.1016/j.snr.2021.100063>.
- (44) Lu, X.; Punj, D.; Orrit, M. Two-Photon-Excited Single-Molecule Fluorescence Enhanced by Gold Nanorod Dimers. *Nano Lett.* **2022**, *22* (10), 4215–4222. <https://doi.org/10.1021/acs.nanolett.2c01219>.
- (45) Qiu, Y.; Kuang, C.; Liu, X.; Tang, L. Single-Molecule Surface-Enhanced Raman Spectroscopy. *Sensors* **2022**, *22* (13). <https://doi.org/10.3390/s22134889>.

- (46) Hao, Q.; Peng, Z.; Wang, J.; Fan, X.; Li, G.; Zhao, X.; Ma, L.; Qiu, T.; Schmidt, O. G. Verification and Analysis of Single-Molecule SERS Events via Polarization-Selective Raman Measurement. *Anal. Chem.* **2022**, *94* (2), 1046–1051. <https://doi.org/10.1021/acs.analchem.1c04015>.
- (47) Liu, B.; Zhan, C.; Yao, X.; Yan, S.; Ren, B. Nanobowtie Arrays with Tunable Materials and Geometries Fabricated by Holographic Lithography. *Nanoscale* **2020**, *12* (41), 21401–21408. <https://doi.org/10.1039/D0NR05546H>.
- (48) Jalali, M.; Hosseini, S. I. I.; AbdelFatah, T.; Montermini, L.; Hogiu, S. W.; Rak, J.; Mahshid, S. Nanobowtie Embedded Microfluidic Device for SERS Identification of Extracellular Vesicles from Synthetic Liposomes. In *2021 IEEE 21st International Conference on Nanotechnology (NANO)*; 2021; pp 400–402. <https://doi.org/10.1109/NANO51122.2021.9514348>.
- (49) Wang, R.-P.; Hu, C.-R.; Han, Y.; Yang, B.; Chen, G.; Zhang, Y. Y.; Zhang, Y. Y.; Dong, Z.-C. Sub-Nanometer Resolved Tip-Enhanced Raman Spectroscopy of a Single Molecule on the Si(111) Substrate. *J. Phys. Chem. C* **2022**, *126* (29), 12121–12128. <https://doi.org/10.1021/acs.jpcc.2c03614>.
- (50) Jiang, S.; Chen, Z.; Chen, X.; Nguyen, D.; Mattei, M.; Goubert, G.; Van Duyne, R. P. Investigation of Cobalt Phthalocyanine at the Solid/Liquid Interface by Electrochemical Tip-Enhanced Raman Spectroscopy. *J. Phys. Chem. C* **2019**, *123* (15), 9852–9859. <https://doi.org/10.1021/acs.jpcc.9b00513>.
- (51) Kaur, V.; Kaur, C.; Sen, T. Single-Molecule Fluorescence Enhancement Based Detection of ATP Using DNA Origami-Assembled Au@Ag Nanostar Optical Antennas. *J. Phys. Chem. C* **2023**. <https://doi.org/10.1021/acs.jpcc.3c00020>.
- (52) Niu, R.; Gao, F.; Wang, D.; Zhu, D.; Su, S.; Chen, S.; YuWen, L.; Fan, C.; Wang, L.; Chao, J. Pattern Recognition Directed Assembly of Plasmonic Gap Nanostructures for Single-Molecule SERS. *ACS Nano* **2022**, *16* (9), 14622–14631. <https://doi.org/10.1021/acsnano.2c05150>.
- (53) Dutta, A.; Tapio, K.; Suma, A.; Mostafa, A.; Kanehira, Y.; Carnevale, V.; Bussi, G.; Bald, I. Molecular States and Spin Crossover of Hemin Studied by DNA Origami Enabled Single-Molecule. **2022**, 26–31. <https://doi.org/10.1039/d2nr03664a>.
- (54) Pines, D. Collective Energy Losses in Solids. *Rev. Mod. Phys.* **1956**, *28* (3), 184–198. <https://doi.org/10.1103/RevModPhys.28.184>.
- (55) Kittel, C. *Introduction to Solid State Physics*, 8th ed.; 2005.
- (56) Ritchie, R. H. Plasma Losses by Fast Electrons in Thin Films. *Phys. Rev.* **1957**, *106* (5), 874–881. <https://doi.org/10.1103/PhysRev.106.874>.
- (57) Downing, C. A.; Mariani, E.; Weick, G. Retardation Effects on the Dispersion and Propagation of Plasmons in Metallic Nanoparticle Chains. *J. Phys. Condens. Matter* **2018**, *30* (2), 25301. <https://doi.org/10.1088/1361-648X/aa9d59>.
- (58) *Nanoscale Materials In Chemistry*; Klabunde, K. J., Ed.; John Wiley & Sons, Inc., 2001.
- (59) Rodríguez-Oliveros, R.; Paniagua-Domínguez, R.; Sánchez-Gil, J. A.; Macías, D. Plasmon Spectroscopy: Theoretical and Numerical Calculations, and Optimization Techniques. *Nanospectroscopy* **2015**, *1* (1), 67–96. <https://doi.org/10.1515/nansp-2015-0006>.
- (60) Johnson, P. B.; Christy, R. W. Optical Constants of the Noble Metals. *Phys. Rev. B* **1972**, *6* (12), 4370–4379. <https://doi.org/10.1103/PhysRevB.6.4370>.
- (61) Farooq, S.; Araujo, R. E. de. Engineering a Localized Surface Plasmon Resonance Platform for Molecular Biosensing. *Open J. Appl. Sci.* **2018**, *8* (3), 126–139. <https://doi.org/10.4236/ojapps.2018.83010>.
- (62) Baumberg, J. J.; Aizpurua, J.; Mikkelsen, M. H.; Smith, D. R. Extreme Nanophotonics from Ultrathin Metallic Gaps. *Nat. Mater.* **2019**, *18* (7), 668–678. <https://doi.org/10.1038/s41563-019-0290-y>.
- (63) Tian, T.; Yi, J.; Liu, Y.; Li, B.; Liu, Y.; Qiao, L.; Zhang, K.; Liu, B. Self-Assembled Plasmonic Nanoarrays for Enhanced Bacterial Identification and Discrimination. *Biosens. Bioelectron.* **2022**, *197*, 113778. <https://doi.org/10.1016/j.bios.2021.113778>.
- (64) Camargo, P. H. C.; Au, L.; Rycenga, M.; Li, W.; Xia, Y. Measuring the SERS Enhancement Factors of Dimers with Different Structures Constructed from Silver Nanocubes. *Chem. Phys. Lett.* **2010**, *484* (4), 304–308. <https://doi.org/10.1016/j.cplett.2009.12.002>.
- (65) Cathcart, N.; Chen, J. I. L.; Kitaev, V. LSPR Tuning from 470 to 800 Nm and Improved Stability of Au–Ag Nanoparticles Formed by Gold Deposition and Rebuilding in the Presence of Poly(Styrenesulfonate). *Langmuir* **2018**, *34* (2), 612–621. <https://doi.org/10.1021/acs.langmuir.7b03537>.
- (66) Harder, R. A.; Wijenayaka, L. A.; Phan, H. T.; Haes, A. J. Tuning Gold Nanostar Morphology for the SERS Detection of Uranyl. *J. Raman Spectrosc.* **2021**, *52* (2), 497–505. <https://doi.org/10.1002/jrs.5994>.
- (67) Chen, M.; Ye, Z.; Wei, L.; Yuan, J.; Xiao, L. Shining at the Tips: Anisotropic Deposition of Pt Nanoparticles Boosting Hot Carrier Utilization for Plasmon-Driven Photocatalysis. *J. Am. Chem. Soc.* **2022**, *144* (28), 12842–12849. <https://doi.org/10.1021/jacs.2c04202>.
- (68) Arbuz, A.; Sultangazyev, A.; Rapikov, A.; Kunushpayeva, Z.; Bukasov, R. How Gap Distance between Gold Nanoparticles in Dimers and Trimers on Metallic and Non-Metallic SERS Substrates Can Impact Signal Enhancement. *Nanoscale Adv.* **2022**, *4* (1), 268–280. <https://doi.org/10.1039/D1NA00114K>.

REFERENCES

- (69) Zhao, Q.; Hilal, H.; Kim, J.; Park, W. W.; Haddadnezhad, M.; Lee, J. J.-W.; Park, W. W.; Lee, J. J.-W.; Lee, S.; Jung, I.; Park, S. All-Hot-Spot Bulk Surface-Enhanced Raman Scattering (SERS) Substrates: Attomolar Detection of Adsorbates with Designer Plasmonic Nanoparticles. *J. Am. Chem. Soc.* **2022**, *144* (29), 13285–13293. <https://doi.org/10.1021/jacs.2c04514>.
- (70) Lee, C. H.; Tian, L.; Singamaneni, S. Paper-Based SERS Swab for Rapid Trace Detection on Real-World Surfaces. *ACS Appl. Mater. Interfaces* **2010**, *2* (12), 3429–3435. <https://doi.org/10.1021/am1009875>.
- (71) Xu, L.; Zhang, H.; Tian, Y.; Jiao, A.; Chen, F.; Chen, M. Photochemical Synthesis of ZnO@Au Nanorods as an Advanced Reusable SERS Substrate for Ultrasensitive Detection of Light-Resistant Organic Pollutant in Wastewater. *Talanta* **2019**, *194*, 680–688. <https://doi.org/10.1016/j.talanta.2018.10.060>.
- (72) Wu, D.-Y.; Duan, S.; Ren, B.; Tian, Z.-Q. Density Functional Theory Study of Surface-Enhanced Raman Scattering Spectra of Pyridine Adsorbed on Noble and Transition Metal Surfaces. *J. Raman Spectrosc.* **2005**, *36* (6–7), 533–540. <https://doi.org/10.1002/jrs.1353>.
- (73) Otto, A. Surface-Enhanced Raman Scattering: “Classical” and “Chemical” Origins BT - Light Scattering in Solids IV: Electronics Scattering, Spin Effects, SERS, and Morphic Effects; Cardona, M., Güntherodt, G., Eds.; Springer Berlin Heidelberg: Berlin, Heidelberg, 1984; pp 289–418. https://doi.org/10.1007/3-540-11942-6_24.
- (74) Liang, C.; Lu, Z.-A.; Zheng, M.; Chen, M.; Zhang, Y.; Zhang, B.; Zhang, J.; Xu, P. Band Structure Engineering within Two-Dimensional Borocarbonitride Nanosheets for Surface-Enhanced Raman Scattering. *Nano Lett.* **2022**, *22* (16), 6590–6598. <https://doi.org/10.1021/acs.nanolett.2c01825>.
- (75) Chen, R.; Jensen, L. Understanding Chemical Enhancements of Surface-Enhanced Raman Scattering Using a Raman Bond Model for Extended Systems. *J. Chem. Phys.* **2022**, *157* (18), 184705. <https://doi.org/10.1063/5.0124553>.
- (76) Le Ru, E. C.; Etchegoin, P. G. Rigorous Justification of the $|E|^4$ Enhancement Factor in Surface Enhanced Raman Spectroscopy. *Chem. Phys. Lett.* **2006**, *423* (1), 63–66. <https://doi.org/10.1016/j.cplett.2006.03.042>.
- (77) Myroshnychenko, V.; Rodríguez-Fernández, J.; Pastoriza-Santos, I.; Funston, A. M.; Novo, C.; Mulvaney, P.; Liz-Marzán, L. M.; García de Abajo, F. J. Modelling the Optical Response of Gold Nanoparticles. *Chem. Soc. Rev.* **2008**, *37* (9), 1792–1805. <https://doi.org/10.1039/b711486a>.
- (78) Rippa, M.; Sagnelli, D.; Vestri, A.; Marchesano, V.; Munari, B.; Carnicelli, D.; Varrone, E.; Brigotti, M.; Tozzoli, R.; Montalbano, M.; Morabito, S.; Zhou, J.; Zyss, J.; Petti, L. Plasmonic Metasurfaces for Specific SERS Detection of Shiga Toxins. *ACS Appl. Mater. Interfaces* **2022**, *14* (4), 4969–4979. <https://doi.org/10.1021/acsami.1c21553>.
- (79) Stankevicius, E.; Ignatjev, I.; Petrikaitė, V.; Selskis, A.; Niaura, G. Gold Nanoparticles Generated Using the Nanosecond Laser Treatment of Multilayer Films and Their Use for SERS Applications. *ACS Omega* **2021**, *6* (49), 33889–33898. <https://doi.org/10.1021/acsomega.1c05165>.
- (80) Golze, S. D. A Hybrid Nanofabrication Route for the Synthesis of Highly Ordered Large-Area Arrays of Planar and Chiral Nanostructures, University of Notre Dame, 2022. <https://doi.org/10.7274/sx61dj56g2p>.
- (81) Luo, S.; Mancini, A.; Wang, F.; Liu, J.; Maier, S. A.; de Mello, J. C. High-Throughput Fabrication of Triangular Nanogap Arrays for Surface-Enhanced Raman Spectroscopy. *ACS Nano* **2022**, *16* (5), 7438–7447. <https://doi.org/10.1021/acsnano.1c09930>.
- (82) Zheng, R.; Pan, R.; Sun, C.; Du, S.; Jin, A.; Li, C.; Geng, G.; Gu, C.; Li, J. Bidirectional Origami Inspiring Versatile 3D Metasurface. *Adv. Mater. Technol.* **2022**, *7* (8), 2200373. <https://doi.org/10.1002/admt.202200373>.
- (83) Li, X.; Lin, L.; Chiang, W.-H.; Chang, K.; Xu, H. Microplasma Synthesized Gold Nanoparticles for Surface Enhanced Raman Spectroscopic Detection of Methylene Blue. *React. Chem. Eng.* **2022**, *7* (2), 346–353. <https://doi.org/10.1039/D1RE00446H>.
- (84) Jang, A. S.; Praveen Kumar, P. P.; Lim, D.-K. Attomolar Sensitive Magnetic Microparticles and a Surface-Enhanced Raman Scattering-Based Assay for Detecting SARS-CoV-2 Nucleic Acid Targets. *ACS Appl. Mater. Interfaces* **2022**, *14* (1), 138–149. <https://doi.org/10.1021/acsami.1c17028>.
- (85) Turino, M.; Alvarez-Puebla, R. A.; Guerrini, L. Plasmonic Azobenzene Chemoreporter for Surface-Enhanced Raman Scattering Detection of Biothiols. *Biosensors*. 2022. <https://doi.org/10.3390/bios12050267>.
- (86) Atkins, P. W.; de Paula, J. *Physical Chemistry*, 8th ed.; W H Freeman & Co (Sd), 2006.
- (87) Demtröder, W. *Experimentalphysik 1*, 4th ed.; Springer Berlin Heidelberg New York, 2006.
- (88) Cramer, C. J. *Essentials of Computational Chemistry*, 2nd ed.; 2004.
- (89) David C. Young. *Computational Chemistry, A Practical Guide for Applying Techniques to Real-World Problems*; John Wiley & Sons, Inc., 2008.
- (90) Radilla, J.; Negrón-Silva, G. E.; Palomar-Pardavé, M.; Romero-Romo, M.; Galván, M. DFT Study of the Adsorption of the Corrosion Inhibitor 2-Mercaptoimidazole onto Fe(100) Surface. *Electrochim. Acta* **2013**, *112*, 577–586. <https://doi.org/10.1016/j.electacta.2013.08.151>.
- (91) Zoltowski, C. M.; Lalisie, R. F.; Hadad, C. M.; Schultz, Z. D. Plasmonically Generated Tryptophan Radical Anion on Gold Nanoparticles Investigated by Combined Surface-Enhanced Raman Scattering and Density Functional Theory Calculations. *J. Phys. Chem. C* **2021**, *125* (50), 27596–27606. <https://doi.org/10.1021/acs.jpcc.1c07840>.

REFERENCES

- (92) Shen, X.-M.; Zhang, Y. Y.; Zhang, S.; Zhang, Y. Y.; Meng, Q.-S.; Zheng, G.; Lv, S.; Wang, L.; Boto, R. A.; Shan, C.; Aizpurua, J. Optomechanical Effects in Nanocavity-Enhanced Resonant Raman Scattering of a Single Molecule. *Phys. Rev. B* **2023**, *107* (7), 75435. <https://doi.org/10.1103/PhysRevB.107.075435>.
- (93) Zayak, A. T.; Hu, Y. S.; Choo, H.; Bokor, J.; Cabrini, S.; Schuck, P. J.; Neaton, J. B. Chemical Raman Enhancement of Organic Adsorbates on Metal Surfaces. *Phys. Rev. Lett.* **2011**, *106* (8), 23–26. <https://doi.org/10.1103/PhysRevLett.106.083003>.
- (94) Koch, W.; Holthausen, M. C. *A Chemist's Guide to Density Functional Theory*, 2nd ed.; Wiley-VCH, 2001.
- (95) Bader, R. F. W. Atoms in Molecules. *Acc. Chem. Res.* **1985**, *18* (1), 9–15. <https://doi.org/10.1021/ar00109a003>.
- (96) Tang, W.; Sanville, E.; Henkelman, G. A Grid-Based Bader Analysis Algorithm without Lattice Bias. *J. Phys. Condens. Matter* **2009**, *21* (8), 84204. <https://doi.org/10.1088/0953-8984/21/8/084204>.
- (97) *Computational Organometallic Chemistry*; Cundari, T. R., Ed.; CRC Press Inc, 2001.
- (98) Wodrich, M. D.; Corminboeuf, C.; Schreiner, P. R.; Fokin, A. A.; Schleyer, P. von R. How Accurate Are DFT Treatments of Organic Energies? *Org. Lett.* **2007**, *9* (10), 1851–1854. <https://doi.org/10.1021/ol070354w>.
- (99) Brémond, E.; Savarese, M.; Adamo, C.; Jacquemin, D. Accuracy of TD-DFT Geometries: A Fresh Look. *J. Chem. Theory Comput.* **2018**, *14* (7), 3715–3727. <https://doi.org/10.1021/acs.jctc.8b00311>.
- (100) Kunz, K. S.; Luebbers, R. J. *The Finite Difference Time Domain Method for Electromagnetics*; CRC Press, 1993.
- (101) Taflove, A.; Hagness, S. C. *Computational Electrodynamics The Finite-Difference Time-Domain Method*, 3rd ed.; Artech House: Boston, London, 2005.
- (102) Joannopoulos, J. D.; Johnson, S. G.; Winn, J. N.; Meade, R. D. *Photonics Crystals*, 2nd ed.; Princeton University Press, 2008.
- (103) Rothmund, P. W. K. K. Folding DNA to Create Nanoscale Shapes and Patterns. *Nature* **2006**, *440* (7082), 297–302. <https://doi.org/10.1038/nature04586>.
- (104) Pitikultham, P.; Wang, Z.; Wang, Y.; Shang, Y.; Jiang, Q.; Ding, B. Stimuli-Responsive DNA Origami Nanodevices and Their Biological Applications. *ChemMedChem* **2022**, *17* (1), e202100635. <https://doi.org/10.1002/cmde.202100635>.
- (105) Liu, L.; Xiong, Q.; Xie, C.; Pincet, F.; Lin, C. Actuating Tension-Loaded DNA Clamps Drives Membrane Tubulation. *Sci. Adv.* **2023**, *8* (41), eadd1830. <https://doi.org/10.1126/sciadv.add1830>.
- (106) Sala, L.; Perecko, T.; Mestek, O.; Pinkas, D.; Homola, T.; Kočišek, J. Cisplatin-Cross-Linked DNA Origami Nanostructures for Drug Delivery Applications. *ACS Appl. Nano Mater.* **2022**, *5* (9), 13267–13275. <https://doi.org/10.1021/acsanm.2c02976>.
- (107) Hao, Y.; Li, M.; Zhang, Q.; Shi, J.; Li, J.; Li, Q.; Fan, C.; Wang, F. DNA Origami-Based Single-Molecule CRISPR Machines for Spatially Resolved Searching. *Angew. Chemie Int. Ed.* **2022**, *61* (34), e202205460. <https://doi.org/10.1002/anie.202205460>.
- (108) Büber, E.; Schröder, T.; Scheckenbach, M.; Dass, M.; Franquelin, H. G.; Tinnefeld, P. DNA Origami Curvature Sensors for Nanoparticle and Vesicle Size Determination with Single-Molecule FRET Readout. *ACS Nano* **2023**, *17* (3), 3088–3097. <https://doi.org/10.1021/acsnano.2c11981>.
- (109) Yao, C.; Xu, Y.; Hu, P.; Ou, J.; Yang, D. Gene-like Precise Construction of Functional DNA Materials. *Accounts Mater. Res.* **2022**, *3* (1), 42–53. <https://doi.org/10.1021/accountsmr.1c00164>.
- (110) Domljanovic, I.; Loretan, M.; Kempter, S.; Acuna, G. P.; Kocabey, S.; Ruegg, C. DNA Origami Book Biosensor for Multiplex Detection of Cancer-Associated Nucleic Acids. *Nanoscale* **2022**, *14* (41), 15432–15441. <https://doi.org/10.1039/D2NR03985K>.
- (111) Close, C.; Trofymchuk, K.; Grabenhorst, L.; Lalkens, B.; Glembocky, V.; Tinnefeld, P. Maximizing the Accessibility in DNA Origami Nanoantenna Plasmonic Hotspots. *Adv. Mater. Interfaces* **2022**, *9* (24), 2200255. <https://doi.org/10.1002/admi.202200255>.
- (112) Manuguri, S.; Nguyen, M.-K.; Loo, J.; Natarajan, A. K.; Kuzyk, A. Advancing the Utility of DNA Origami Technique through Enhanced Stability of DNA-Origami-Based Assemblies. *Bioconj. Chem.* **2023**, *34* (1), 6–17. <https://doi.org/10.1021/acs.bioconjchem.2c00311>.
- (113) Stein, J.; Stehr, F.; Jungmann, R.; Schwille, P. Calibration-Free Counting of Low Molecular Copy Numbers in Single DNA-PAINT Localization Clusters. *Biophys. Reports* **2021**, *1* (2), 100032. <https://doi.org/10.1016/j.bpr.2021.100032>.
- (114) Yin, J.; Xie, M.; Wang, J.; Cui, M.; Zhu, D.; Su, S.; Fan, C.; Chao, J.; Li, Q.; Wang, L. Gold-Nanoparticle-Mediated Assembly of High-Order DNA Nano-Architectures. *Small* **2022**, *18* (22), 2200824. <https://doi.org/10.1002/sml.202200824>.
- (115) Feng, N.; Zhang, L.; Shen, J.; Hu, Y.; Wu, W.; Kouadio Fodjo, E.; Chen, S.; Huang, W.; Wang, L. SERS Molecular-Ruler Based DNA Aptamer Single-Molecule and Its Application to Multi-Level Optical Storage. *Chem. Eng. J.* **2022**, *433*, 133666. <https://doi.org/10.1016/j.cej.2021.133666>.
- (116) Eklund, A. S.; Comberlato, A.; Parish, I. A.; Jungmann, R.; Bastings, M. M. C. Quantification of Strand Accessibility in Biostable DNA Origami with Single-Staple Resolution. *ACS Nano* **2021**, *15* (11), 17668–17677. <https://doi.org/10.1021/acsnano.1c05540>.

REFERENCES

- (117) Ye, Y.; Hou, S.; Wu, X.; Cheng, X.; He, S. Freeze-Driven Adsorption of Poly-A DNA on Gold Nanoparticles: From a Stable Biointerface to Plasmonic Dimers. *Langmuir* **2022**, *38* (15), 4625–4632. <https://doi.org/10.1021/acs.langmuir.2c00007>.
- (118) San Juan, A. M. T.; Chavva, S. R.; Tu, D.; Tircuit, M.; Coté, G.; Mabbott, S. Synthesis of SERS-Active Core-Satellite Nanoparticles Using Heterobifunctional PEG Linkers. *Nanoscale Adv.* **2022**, *4* (1), 258–267. <https://doi.org/10.1039/D1NA00676B>.
- (119) Li, Y.; Pei, J.; Lu, X.; Jiao, Y.; Liu, F.; Wu, X.; Liu, J.; Ding, B. Hierarchical Assembly of Super-DNA Origami Based on a Flexible and Covalent-Bound Branched DNA Structure. *J. Am. Chem. Soc.* **2021**, *143* (47), 19893–19900. <https://doi.org/10.1021/jacs.1c09472>.
- (120) Heuer-Jungemann, A.; Linko, V. Engineering Inorganic Materials with DNA Nanostructures. *ACS Cent. Sci.* **2021**, *7* (12), 1969–1979. <https://doi.org/10.1021/acscentsci.1c01272>.
- (121) Guo, J.; Liu, Y.; Ju, H.; Lu, G. From Lab to Field: Surface-Enhanced Raman Scattering-Based Sensing Strategies for on-Site Analysis. *TrAC Trends Anal. Chem.* **2022**, *146*, 116488. <https://doi.org/10.1016/j.trac.2021.116488>.
- (122) Vietz, C.; Lalkens, B.; Acuna, G. P.; Tinnefeld, P. Functionalizing Large Nanoparticles for Small Gaps in Dimer Nanoantennas. *New J. Phys.* **2016**, *18* (4), 1–16. <https://doi.org/10.1088/1367-2630/18/4/045012>.
- (123) Gür, F. N.; Schwarz, F. W.; Ye, J.; Diez, S.; Schmidt, T. L. Toward Self-Assembled Plasmonic Devices: High-Yield Arrangement of Gold Nanoparticles on DNA Origami Templates. *ACS Nano* **2016**, *10* (5), 5374–5382. <https://doi.org/10.1021/acsnano.6b01537>.
- (124) Lin, Z.; Xiong, Y.; Xiang, S.; Gang, O. Controllable Covalent-Bound Nanoarchitectures from DNA Frames. *J. Am. Chem. Soc.* **2019**, *141* (17), 6797–6801. <https://doi.org/10.1021/jacs.9b01510>.
- (125) Fantoni, N. Z.; El-Sagheer, A. H.; Brown, T. A Hitchhiker’s Guide to Click-Chemistry with Nucleic Acids. *Chem. Rev.* **2021**, *121* (12), 7122–7154. <https://doi.org/10.1021/acs.chemrev.0c00928>.
- (126) Haiss, W.; Thanh, N. T. K.; Aveyard, J.; Fernig, D. G. Determination of Size and Concentration of Gold Nanoparticles from UV-Vis Spectra. *Anal. Chem.* **2007**, *79* (11), 4215–4221. <https://doi.org/10.1021/ac0702084>.
- (127) Ciubuc, J. D.; Bennet, K. E.; Qiu, C.; Alonzo, M.; Durrer, W. G.; Manciu, F. S. Raman Computational and Experimental Studies of Dopamine Detection. *Biosensors* **2017**, *7* (4), 1–12. <https://doi.org/10.3390/bios7040043>.
- (128) Schlather, A. E.; Large, N.; Urban, A. S.; Nordlander, P.; Halas, N. J. Near-Field Mediated Plexcitonic Coupling and Giant Rabi Splitting in Individual Metallic Dimers. *Nano Lett.* **2013**, *13* (7), 3281–3286. <https://doi.org/10.1021/nl4014887>.
- (129) Liu, M.; Fang, L.; Li, Y.; Gong, M.; Xu, A.; Deng, Z. “Flash” Preparation of Strongly Coupled Metal Nanoparticle Clusters with Sub-Nm Gaps by Ag+ Soldering: Toward Effective Plasmonic Tuning of Solution-Assembled Nanomaterials. *Chem. Sci.* **2016**, *7* (8), 5435–5440. <https://doi.org/10.1039/C6SC01407K>.
- (130) Storhoff, J. J.; Elghanian, R.; Mirkin, C. A.; Letsinger, R. L. Sequence-Dependent Stability of DNA-Modified Gold Nanoparticles. *Langmuir* **2002**, *18* (17), 6666–6670. <https://doi.org/10.1021/la0202428>.
- (131) Ko, S. H.; Vargas-Lara, F.; Patrone, P. N.; Stavis, S. M.; Starr, F. W.; Douglas, J. F.; Liddle, J. A. High-Speed, High-Purity Separation of Gold Nanoparticle–DNA Origami Constructs Using Centrifugation. *Soft Matter* **2014**, *10* (37), 7370–7378. <https://doi.org/10.1039/C4SM01071J>.
- (132) National Institute of Advanced Industrial Science and Technology (AIST). *SDBS-4015*. <https://sdb.db.aist.go.jp/sdb/cgi-bin/landingpage?sdbno=4015>.
- (133) National Institute of Advanced Industrial Science and Technology (AIST). *SDBS-2981*. <https://sdb.db.aist.go.jp/sdb/cgi-bin/landingpage?sdbno=2981>.
- (134) Schürmann, R.; Bald, I. Real-Time Monitoring of Plasmon Induced Dissociative Electron Transfer to the Potential DNA Radiosensitizer 8-Bromo adenine. *Nanoscale* **2017**, *9* (5), 1951–1955. <https://doi.org/10.1039/c6nr08695k>.
- (135) Christopher, P.; Xin, H.; Marimuthu, A.; Linic, S. Singular Characteristics and Unique Chemical Bond Activation Mechanisms of Photocatalytic Reactions on Plasmonic Nanostructures. *Nat. Mater.* **2012**, *11* (12), 1044–1050. <https://doi.org/10.1038/nmat3454>.
- (136) Bartschmid, T.; Farhadi, A.; Musso, M. E.; Goerlitzer, E. S. A.; Vogel, N.; Bourret, G. R. Self-Assembled Au Nanoparticle Monolayers on Silicon in Two- and Three-Dimensions for Surface-Enhanced Raman Scattering Sensing. *ACS Appl. Nano Mater.* **2022**. <https://doi.org/10.1021/acsnm.2c01904>.
- (137) Kershner, R. J.; Bozano, L. D.; Micheel, C. M.; Hung, A. M.; Fornof, A. R.; Cha, J. N.; Rettner, C. T.; Bersani, M.; Frommer, J.; Rothmund, P. W. K.; Wallraff, G. M. Placement and Orientation of Individual DNA Shapes on Lithographically Patterned Surfaces. *Nat. Nanotechnol.* **2009**, *4* (9), 557–561. <https://doi.org/10.1038/nnano.2009.220>.
- (138) Shetty, R. M.; Brady, S. R.; Rothmund, P. W. K.; Hariadi, R. F.; Gopinath, A. Bench-Top Fabrication of Single-Molecule Nanoarrays by DNA Origami Placement. *ACS Nano* **2021**, *15* (7), 11441–11450. <https://doi.org/10.1021/acsnano.1c01150>.
- (139) Wang, Z.; Liu, Z.; Dempwolf, W.; Molle, J.; Kanehira, Y.; Kogikoski, S. J.; Etzkorn, M.; Bald, I.; Stosch, R.; Wundrack, S. Surface-Enhanced Raman Spectroscopy on Selectively Adsorbed Plasmonic Nanostructures Using Polar Surface Arrays. *ACS Appl. Nano Mater.* **2023**. <https://doi.org/10.1021/acsnm.3c01776>.

REFERENCES

- (140) Berg, JM; Tymoczko, J. S. *Biochemistry*; 2006.
- (141) Linko, V.; Keller, A. Stability of DNA Origami Nanostructures in Physiological Media: The Role of Molecular Interactions. *Small* **2023**. <https://doi.org/10.1002/smll.202301935>.
- (142) Xin, Y.; Martinez Rivadeneira, S.; Grundmeier, G.; Castro, M.; Keller, A. Self-Assembly of Highly Ordered DNA Origami Lattices at Solid-Liquid Interfaces by Controlling Cation Binding and Exchange. *Nano Res.* **2020**, *13* (11), 3142–3150. <https://doi.org/10.1007/s12274-020-2985-4>.
- (143) Mortimer, C. E.; Müller, U. *Chemie*, 10th ed.; Thieme, 2010.
- (144) Greczynski, G.; Hultman, L. C 1s Peak of Adventitious Carbon Aligns to the Vacuum Level: Dire Consequences for Material's Bonding Assignment by Photoelectron Spectroscopy. *ChemPhysChem* **2017**, *18* (12), 1507–1512. <https://doi.org/10.1002/cphc.201700126>.
- (145) Piao, H.; Fairley, N.; Walton, J. Application of XPS Imaging Analysis in Understanding Interfacial Delamination and X-Ray Radiation Degradation of PMMA. *Surf. Interface Anal.* **2013**, *45* (11), 1742–1750. <https://doi.org/10.1002/sia.5316>.
- (146) Martínez, N. F.; García, R. Measuring Phase Shifts and Energy Dissipation with Amplitude Modulation Atomic Force Microscopy. *Nanotechnology* **2006**, *17* (7). <https://doi.org/10.1088/0957-4484/17/7/S11>.
- (147) Hung, A. M.; Micheel, C. M.; Bozano, L. D.; Osterbur, L. W.; Wallraff, G. M.; Cha, J. N. Large-Area Spatially Ordered Arrays of Gold Nanoparticles Directed by Lithographically Confined DNA Origami. *Nat. Nanotechnol.* **2010**, *5* (2), 121–126. <https://doi.org/10.1038/nnano.2009.450>.
- (148) Gopinath, A.; Rothmund, P. W. K. Optimized Assembly and Covalent Coupling of Single-Molecule DNA Origami Nanoarrays. *ACS Nano* **2014**, *8* (12), 12030–12040. <https://doi.org/10.1021/nn506014s>.
- (149) Scheible, M. B.; Pardatscher, G.; Kuzyk, A.; Simmel, F. C. Single Molecule Characterization of DNA Binding and Strand Displacement Reactions on Lithographic DNA Origami Microarrays. *Nano Lett.* **2014**, *14* (3), 1627–1633. <https://doi.org/10.1021/nl500092j>.
- (150) Azizian, S.; Eris, S. Chapter 6 - Adsorption Isotherms and Kinetics. In *Adsorption: Fundamental Processes and Applications*; Ghaedi, M. B. T.-I. S. and T., Ed.; Elsevier, 2021; Vol. 33, pp 445–509. <https://doi.org/10.1016/B978-0-12-818805-7.00011-4>.
- (151) Islam, M. A.; Chowdhury, M. A.; Mozumder, M. S. I.; Uddin, M. T. Langmuir Adsorption Kinetics in Liquid Media: Interface Reaction Model. *ACS Omega* **2021**, *6* (22), 14481–14492. <https://doi.org/10.1021/acsomega.1c01449>.
- (152) Amenaghawon, A.; Aisien, F.; Agho, O. Adsorption of Toluene by Waste Tyre Rubber Granules: Effect of Operating Variables, Kinetic and Isotherm Studies. *Int. J. Sci. Res. Knowl.* **2013**, No. October, 427–438. <https://doi.org/10.12983/ijrsk-2013-p427-438>.
- (153) Prinz, J.; Heck, C.; Ellerik, L.; Merk, V.; Bald, I. DNA Origami Based Au-Ag-Core-Shell Nanoparticle Dimers with Single-Molecule SERS Sensitivity. *Nanoscale* **2016**, *8* (10), 5612–5620. <https://doi.org/10.1039/c5nr08674d>.
- (154) Le Ru, E. C.; Etchegoin, P. G. Single-Molecule Surface-Enhanced Raman Spectroscopy. *Annu. Rev. Phys. Chem.* **2012**, *63* (1), 65–87. <https://doi.org/10.1146/annurev-physchem-032511-143757>.
- (155) Zhu, J.; Wu, N.; Zhang, F.; Li, X.; Li, J.; Zhao, J. SERS Detection of 4-Aminobenzenethiol Based on Triangular Au-AuAg Hierarchical-Multishell Nanostructure. *Spectrochim. Acta Part A Mol. Biomol. Spectrosc.* **2018**, *204*, 754–762. <https://doi.org/10.1016/j.saa.2018.06.105>.
- (156) Zhu, S.-Q.; Bian, B.; Zhu, Y.-F.; Yang, J.; Zhang, D.; Feng, L. Enhancement in Power Conversion Efficiency of GaAs Solar Cells by Utilizing Gold Nanostar Film for Light-Trapping. *Front. Chem.* **2019**, *7*, 137. <https://doi.org/10.3389/fchem.2019.00137>.
- (157) Yaghobian, F.; Weimann, T.; Güttler, B.; Stosch, R. On-Chip Approach for Traceable Quantification of Biomarkers Based on Isotope-Dilution Surface-Enhanced Raman Scattering (IDSERS). *Lab Chip* **2011**, *11* (17), 2955–2960. <https://doi.org/10.1039/c1lc20032a>.
- (158) Yaghobian, F. ID-SERS Based Quantification of Biomarkers on a Single Chip, TU Braunschweig, 2011.
- (159) Pini, V.; Kosaka, P. M.; Ruz, J. J.; Malvar, O.; Encinar, M.; Tamayo, J.; Calleja, M. Spatially Multiplexed Dark-Field Microspectrophotometry for Nanoplasmonics. *Sci. Rep.* **2016**, *6* (December 2015), 1–10. <https://doi.org/10.1038/srep22836>.
- (160) Liu, Z.; Wang, Z.; Guckel, J.; Park, D.; Lalkens, B.; Stosch, R.; Etkorn, M. Positional Control of DNA Origami Based Gold Dimer Hybrid Nanostructures on Pre-Structured Surfaces. *Nanotechnology* **2023**, *34* (42), 425301. <https://doi.org/10.1088/1361-6528/ace726>.
- (161) Dileseigres, A. S.; Prado, Y.; Pluchery, O. How to Use Localized Surface Plasmon for Monitoring the Adsorption of Thiol Molecules on Gold Nanoparticles? *Nanomaterials* **2022**, *12* (2). <https://doi.org/10.3390/nano12020292>.

Appendix

A1: Design of the Rectangular DNA Origami

Table A1 lists all staples for the synthesis of rectangular DNA origami, which was applied to construct AuNP dimers. The start and end position of a staple is defined with the row number, followed by the position in the edge bracket. Example: the starting position 0[47] means that the 5' end of this staple is in the 0th row and the 47th base from the left. There are three magenta-colored staples and three staples in pink. These staples are extended with 12 adenine bases and are used to capture the 20 nm AuNPs with thymine modification.

Table A1: DNA sequences of a rectangular DNA origami which is used for the AuNP Dimer synthesis.

Start (5' end)	End (3' end)	Sequence (5' → 3')	Length (bases)
0[47]	1[31]	AAACTACAACGCCTGTAGCATTCTAAAGTTT	31
0[79]	1[63]	TGTACCGTAACTGAGTTTCGTCAATGAATT	32
0[111]	1[95]	TTTCAGGGATAGCAAGCCCAATAGAACTTTCA	32
0[143]	1[127]	GAACCGCCACCCTCAGAGCCACCAAAGGAAC	31
0[175]	0[144]	TAGTACCGCCACCCTCAGAACCGCCACCCTCA	32
0[207]	1[191]	GGAATAGGTGTATCACCGTACTCATTTAACGG	32
0[239]	1[223]	GCCGTCGAGAGGGTTGATATAAGCCGTATAA	31
0[271]	1[255]	GCGGGGTTTTGCTCAGTACCAGGCTCGGAACC	32
1[32]	3[31]	TGTCGTCAGTTGCGCCGACAATATTCGGTC	30
1[64]	3[71]	TTCTGTATGAGGTGAATTTCTTAAGGCCGCTTTTGCGGGA	40
1[96]	3[95]	ACAGTTTCTTTAATTGTATCGGTTGCGAAAGA	32
1[128]	3[127]	AACTAAAAATCTCCAAAAAAAAGGCTACAG	30
1[160]	2[144]	ACAGGAGTGCCTCATACATGGCTTATTTTTTC	32
1[192]	3[191]	GGTCAGTGAGCGCAGTCTCTGAATATCACCGG	32
1[224]	3[223]	ACAGTTACAAATAAATCCTCATCTCCCTCA	30
1[256]	3[263]	TATTATTCCAGGTCAGACGATTGGACCCTCAGAGCCACCA	40
2[47]	0[48]	ATACCGATTTTCCAGACGTTAGTAACCAGTAC	32
2[79]	0[80]	TTGCTTTTCGGGATTTTGCTAAACGAACCCA	30
2[111]	0[112]	AAGGAGCCAGCGGAGTGAGAATAGACCCTCAT	32
2[143]	1[159]	ACGTTGAAGGAATTGCGAATAATATTGATGAT	32
2[175]	0[176]	TCCAGTAAGTACTGGTAATAAGTGGAGGTT	30
2[207]	0[208]	GAATGGAACCTTGAGTAACAGTGCTATAGCCC	32
2[239]	0[240]	TTCACAAAATGCCCCCTGCCTATTGGATAAGT	32
2[271]	0[272]	GGTTGAGGTGAAACATGAAAGTAAGGATTA	30
3[32]	5[31]	GCTGAGGCAGCGATTATACCAAAATCGCCTG	30
3[96]	5[95]	CAGCATCGCGAAGGCACCAACCTAGCAGACGG	32
3[128]	5[127]	AGGCTTTTCATTAACGGGTAAACCAACTTT	30
3[160]	4[144]	TTTGCCATTCGGTCATAGCCCCCTTTCATGAG	32
3[192]	5[191]	AACCAGAGGTCAGACTGTAGCGCGGATTGAG	32
3[224]	5[223]	GAGCCGCCAGTAGCGACAGAATAATTATTC	30
4[47]	2[48]	TTGACCCCTTGCAGGGAGTTAAACAGCTTG	32
4[63]	6[56]	ACTAAAAACCTGCTCCATGTTACTCGTAACAAAGCTGCTC	40
4[79]	2[80]	AGAGGCAATCGTCACCCTCAGCATATCAGC	30
4[111]	2[112]	TGCCACTAGAACGAGGGTAGCAACGGCTCCA	32
4[143]	3[159]	GAAGTTTCGAGGACTAAAGACTTTTATTAGCG	32

APPENDIX

Start (5' end)	End (3' end)	Sequence (5' → 3')	Length (bases)
4[175]	2[176]	CGGCATTTCTTTTCATAATCAAATTACCGT	30
4[207]	2[208]	CCTTTAGCCCACCACCGGAACCGCTAAAGCCA	32
4[239]	2[240]	ACCGTAATCACCCCTCAGAACC GCCCCTTGATA	32
4[255]	6[248]	AACCATCGACCGACTTGAGCCATTAGCAAACGTAGAAAAAT	40
4[271]	2[272]	GAAACGTCCCCTCAGAGCCGCCAGACAGGA	30
5[32]	7[31]	ATAAAATTTTGCCCTGACGAGAATGGTTTAA	30
5[128]	7[127]	GAAAGAGGGCTGGCTGACCTCCGTTAATA	30
5[160]	6[144]	AAGACAAAAATTCATATGGTTTACACAGACCA	32
5[192]	7[191]	GGAGGGAAGAATAAGTTTATTTGTAGCTATC	32
6[47]	4[48]	AATAAGGCGTGTGCGAAATCCGCGAACTCATCT	32
6[79]	4[80]	CAAATCAATAGCCGGAACGAGGCAAACGAA	30
6[111]	4[112]	TAATCTTGAAGGGAACCGAACTGAATACGTAA	32
6[143]	5[159]	GGCGCATAGACAGATGAACGGTGTGACGCGCA	32
6[175]	4[176]	CAATAGAAAGGGCGACATTCAACTTTTCAT	30
6[207]	4[208]	ACACCACGGGTAAATATTGACGGACAAGTTTG	32
6[239]	4[240]	AAAGGTGGGTGAATTATCACCGTCATAGCAGC	32
6[271]	4[272]	AGTATGTTTGGGAATTAGAGCCAAAAGGCCG	30
7[32]	9[31]	TTTCAACAACCCTCGTTTACCATTGCAAA	30
7[56]	9[63]	TACCTTATGCGATTTTATTACGAGGCATAGTATAGTAAAA	40
7[128]	9[135]	AAACGAATTCATCAGTTGAGATCCCCCTCAAATGCTT	37
7[160]	8[144]	AGCAAGAAAAATTGAGTTAAGCCCAATTACAGG	32
7[192]	9[199]	TTACCGAAGAGCGCTAATATCAGAGCTAACGAGCGTCTTT	40
7[248]	9[255]	GGAAAACCGAGGAAACGAACAGGGAAGCGCATCCCAATCC	40
8[47]	6[48]	ACTATCATTTTAAATCATTGTGAATATTCAGTG	32
8[79]	6[80]	CAAAAGGAAAGAAGCTGGCTCATTCAATACC	30
8[111]	6[112]	ACCACATTTGGGAAGAAAAATCTAATCAAGAG	32
8[143]	7[159]	TAGAAAGACTAACGGAACAACATTATAATAAG	32
8[175]	6[176]	CCCACAAGACAATGAAATAGCAATCACAAAT	30
8[207]	6[208]	GGGTAATTGCCCTTTTTAAGAAAAACGCAAAAG	32
8[239]	6[240]	GAATTAACAACAAAAGTTACCAGAAAACATACAT	32
8[271]	6[272]	AACATAAAACAATAATAACGGAATATTACGC	30
9[32]	11[31]	AGAAGTTGCGTTTTAATTGAGAAACAGGTC	30
9[64]	11[63]	TGTTTAGAATTAAGAGGAAGCCCGCTCCTTT	32
9[96]	11[95]	AATCGTCAAGTCAAGAAAGCAAAGCGTGGCTTAG	32
9[160]	10[144]	ATTTTATCGTTGCTATTTTGCACCCGAGAATG	32
9[224]	11[223]	AAATAAACCGGAGGCGTTTTAGTATCATTCC	30
9[256]	11[255]	AAATAAGAAGATATAGAAGGCTTAACCGCACT	32
10[47]	8[48]	CAAATATCTTGCCAGAGGGGTAAAGAGCAAC	32
10[79]	8[80]	TCAAAAAGCTGGATAGCGTCCAAATAACGC	30
10[127]	12[120]	TCAGGTCTGTAGCTCAACATGTTGTTTCATTCCATATA	38
10[143]	9[159]	ACCATAAATAAACAGTTTCAGAAAACAGCTACA	32
10[175]	8[176]	CAAGATTACTGAATCTTACCAACGAGATAA	30
10[191]	12[184]	TTTGAAGCTAGAAAACCAATCAATATGCAGAACGCGCCTGT	40
10[207]	8[208]	CCGACTTGCCAGAGCCTAATTTGCAAGTCAGA	32
10[271]	8[272]	AGCAAATCAACGATTTTTTTGTTTAGAGAAT	30
11[32]	13[31]	AGGATTATAGCTATATTTTCATCTACTAAT	30
11[64]	13[63]	TGATAAGAAGATACATTTTCGCAAAAAATCATAAC	32
11[96]	13[95]	AGCTTAATTCTGCGAACGAGTAGAATTAAGCA	32
11[160]	12[144]	TCCCATCCAAGTCTGAAACAAGAAAGTACGGT	32
11[224]	13[223]	CAAGAACGACGACGACAATAAATATAAAGC	30
11[256]	13[255]	CATCGAGAAGTACCGACAAAAGGTTTGAGAAT	32
12[47]	10[48]	AACCTGTTGAGAGTACCTTTAATTAAGACTT	32
12[79]	10[80]	TGACCATTGGTCATTTTTGCGGAGATTGCA	30
12[111]	10[112]	TTCCCAATTGCTGAATATAATGCTTTACCCTG	32
12[143]	11[159]	GTCTGGAATTAATATGCAACTAAAAATAATA	32
12[175]	10[176]	CAATAGATTAATTTACGAGCATGCTTAAAT	30
12[207]	10[208]	TCAGCTAAATCGGCTGTCTTTCCCTCGAACCTC	32
12[239]	10[240]	TCTGTCCAGGGTATTAACCAAGTTCCGGTAT	32
12[271]	10[272]	GAAATATAAAACAAGCAAGCCGTTTAATAGCA	30
13[32]	15[31]	AGTAGTAGGTGAGAAAGGCCGACCGTTCT	30
13[64]	15[71]	AGGCAAGGGCCTGAGTAATGTGTAGGGTAGCTATTTTTGA	40
13[96]	15[95]	ATAAAGCCTTTTGAACCCTCATATATCAGGT	32
13[120]	15[127]	AATCGGTTGTACCAAGAAGCCTTTATTTTACAAGAGAA	38

APPENDIX

Start (5' end)	End (3' end)	Sequence (5' → 3')	Length (bases)
13[160]	14[144]	TAATTACTAAATAAGAATAAACACTAATACTT	32
13[184]	15[191]	AGTATCATATGCGTTAGAAATACCGACCGTGTAGATTAA	40
13[224]	15[223]	CAACGCTATTTTCATCTTCTGACATTTATCA	30
13[256]	15[263]	CGCCATATGCGAGAAAACTTTTTCTTTTTAACCTCCGGC	40
14[47]	12[48]	TTCAAAAGGCATTAACATCCAATATGGTCAAT	32
14[79]	12[80]	AATGCAATCAAAGAATTAGCAAATTTAGTT	30
14[111]	12[112]	ATAAAAATTCAGAGCATAAAGCTAACAGTTGA	32
14[143]	13[159]	TTGCGGGAAAAACATTATGACCCTGCGGAATCA	32
14[175]	12[176]	AAGGCGTTAGAAAAAGCCTGTTTTTATCAA	30
14[207]	12[208]	AATGGTTTTACAAATTCTTACCAGCAACATGT	32
14[239]	12[240]	TTTAGTTACAACAGTAGGGCTTAAAAAGTAAT	32
14[271]	12[272]	CAAAGAACTTAAACAACGCCAACAAATAAGA	30
15[32]	17[31]	AGCTGATCATTAAATTTTTGTTTCATCAAAA	30
15[96]	17[95]	CATTGCCTAAAACAGGAAGATTGTGAGTAACA	32
15[128]	17[127]	TCGATGATGTACCCCGGTTGATAAACGGCG	30
15[160]	16[144]	TCCTTGAAC TATTAATTAATTTTCTAGCATGT	32
15[192]	17[191]	GACGCTGAGAGTGAATAACCTTGCTTTACATC	32
15[224]	17[223]	AAATCATTAAATGGAAACAGTACTGATTGCT	30
16[47]	14[48]	AAAATTCGAAATTAATGCCGGAGAGGTAAAGA	32
16[63]	18[56]	ACGTTAATTAGCCAGCTTTCATCATCGCACTCCAGCCAGC	40
16[79]	14[80]	AATATTTAGAGATCTACAAAGGCTATTTTA	30
16[111]	14[112]	AAGCCCCAGAGAGTCTGGAGCAAAAACGCAAGG	32
16[143]	15[159]	CAATCATAACGGTAATCGTAAAAACCTTAGAA	32
16[175]	14[176]	AATCGTCGAACATAGCGATAGCTGATAAAT	30
16[207]	14[208]	ATATATGTGAAGAGTCAATAGTACTAAATTT	32
16[239]	14[240]	ACCTTTTTAGGTCTGAGAGACTACAAATATAT	32
16[255]	18[248]	CAATTTACGCAGAGGCGAATTATTCCTGATTGTTGGAT	40
16[271]	14[272]	AATTAATTTTAGGTTGGGTTATACGCAAGA	30
17[32]	19[31]	ATAATTCTGGTGCCGGAAAACTGTTGG	30
17[96]	19[95]	ACCCGTCGGGGGACGACGACAGTATGTGCTGC	32
17[128]	19[127]	GATTGACGCGCATCGTAACCGTAGGGTTTT	30
17[160]	18[144]	ATGAATATGTAGATTTTCAGGTTTACGTTGGT	32
17[192]	19[191]	GGGAGAAATTTGCACGTAAAAACGCGTATTAA	32
17[224]	19[223]	TTGAATAGGAAGGTTAGAACCTTTAAAAAG	30
18[47]	16[48]	ACCGCTTCGCGTCTGGCCTTCCTGATTTTGT	32
18[79]	16[80]	CAGGAAGAACATTAATGTGAGCATAAGCA	30
18[111]	16[112]	CAGTTTGAGATTCTCCGTGGGAACAATCAGAA	32
18[143]	17[159]	GTAGATGGCGTAATGGGATAGGTCAACGTCAG	32
18[175]	16[176]	GAAATTGCACAGTAACAGTACCTTTCTGTA	30
18[207]	16[208]	CAAAATTACAATAACGGATTCCGCATAAATCA	32
18[239]	16[240]	TGAATAATCCAAGTTACAAAATCGTTTGAATT	32
18[271]	16[272]	CAATATAATCATTTCAATTACCTAAAACAA	30
19[32]	21[31]	GAAGGGCCGCTCACAATTCACGCCTGGGG	30
19[56]	21[63]	TTGCTATTACGCCAGGTCATAGCTGTTTCCTCATTAAAT	40
19[96]	21[95]	AAGGCGATCCCGGTTACCGAGTCCCAGTCGG	32
19[128]	21[127]	CCCAGTCTTGCATGCCTGCAGGAATGAATC	30
19[160]	20[144]	ACTTTACACATTTGAGGATTTAGAACGGCCAG	32
19[192]	21[191]	ATCCTTTGACTAATAGATTAGAGCGAAGATAA	32
19[224]	21[223]	TTTGAGTGTTATCTAAAATATCAACACCGC	30
19[248]	21[255]	GGAAACAAAGAAACCACGGCAAATCAACAGTTGCCAGCAGC	40
20[47]	18[48]	TTGTTATCGATCGGTGCGGGCCTCTTCCGGC	32
20[79]	18[80]	TAATCATGCTGGCGAAAGGGGGATCGGCCT	30
20[111]	18[112]	AGAGGATCTAAGTTGGGTAACGCCGATCTGC	32
20[143]	19[159]	TGCCAAGCACGACGTTGTA AAAACGAGTATTAG	32
20[175]	18[176]	AGATAATAAAACAATTCGACAATAAATAAA	30
20[207]	18[208]	CACTAACACCCGAACGTTATTAATTACCATAT	32
20[239]	18[240]	TGAGGAAGAACATTATCATTTTGCTATACTTC	32
20[271]	18[272]	GGTCAGTTCAGAAAGGAGCGGAATAATTCAT	30
21[32]	23[31]	TGCCTAAGTTTGCCGACGAGGGGCAAAAT	30
21[64]	23[63]	GCGTTGCGCCTGAGAGAGTTGCAGCCGAGATA	32
21[96]	23[95]	GAAACCTGGGCAACAGCTGATTGCGAACAAAGA	32
21[128]	23[127]	GGCCAACCAGGGTGGTTTTTCTCCAACGTC	30
21[160]	22[144]	AAATACCGATAGCCCTAAAACATCTTTGCGTA	32

APPENDIX

Start (5' end)	End (3' end)	Sequence (5' → 3')	Length (bases)
21[192]	23[191]	AACAGAGGGAATGGCTATTAGTCTAGAACAAT	32
21[224]	23[223]	CTGCAACCGTAAGAATACGTGGAAAAACGC	30
21[256]	23[255]	AAATGAAACCAACAGAGATAGAACCCTCAAT	32
22[47]	20[48]	CCACGCTGTGAGTGAGCTAACTCAGTGTGAAA	32
22[79]	20[80]	CGCCTGGCCTCACTGCCCGCTTTGAATTTCG	30
22[111]	20[112]	GTGAGACGTCGTGCCAGTGCATTTGACTCT	32
22[143]	21[159]	TTGGGCGCGCGGGGAGAGGGCGGGCCATTAA	32
22[175]	20[176]	GCGAACTGAACGAACACCAGCAGCAGTCAAT	30
22[207]	20[208]	ATATTTTTTTGAGGCGGTCAGTATTTTTAGGAG	32
22[239]	20[240]	CCTGAAAGAGTGCCACGCTGAGAGAAAAGGAAT	32
22[271]	20[272]	CATTCTGGAATCTAAAGCATCACAATATCT	30
23[32]	22[48]	CCCTTATAAATCAAAAAGAATAGCCAAGCGGT	31
23[64]	22[80]	GGGTTGAGTGTGTTCCAGTTTGCCCTTAC	30
23[96]	22[112]	GTCCACTATTAAGAACGTGGACTTTTCACCA	32
23[128]	23[159]	AAAGGGCGAAAAACCGTCTATCAACTCAAAC	31
23[160]	22[176]	TATCGGCCTTGCTGGTAATATCCTTAATGC	30
23[192]	22[208]	ATTACCGCCAGCCATTGCAACAGGCACAGACA	32
23[224]	22[240]	TCATGGAAATACCTACATTTTGACCTTCTGA	31
23[256]	22[272]	CGTCTGAAATGGATTATTTACATAAAGGGA	30
5[96]	7[95]	TCAATCATAACAAGAACCGGATATTATACCAGTAAAAAAAAAAAAA	44
7[96]	9[95]	CAGGACGTCAACTAATGCAGATACTACTGCGGAAAAAAAAAAAAA	44
10[111]	8[112]	ACTATTATTAATATTCATTGAATTTAGGAATAAAAAAAAAAAAAA	44
5[224]	7[223]	ATTAAGCAACATATAAAGGAAGTAAGCAGAAAAAAAAAAAAA	42
7[224]	9[223]	ATAGCCGTGAACACCCTGAACACAGTTACAAAAAAAAAAAAA	42
10[239]	8[240]	TCTAAGAACAGCCATATTATTTATAGACGGGAAAAAAAAAAAAA	44

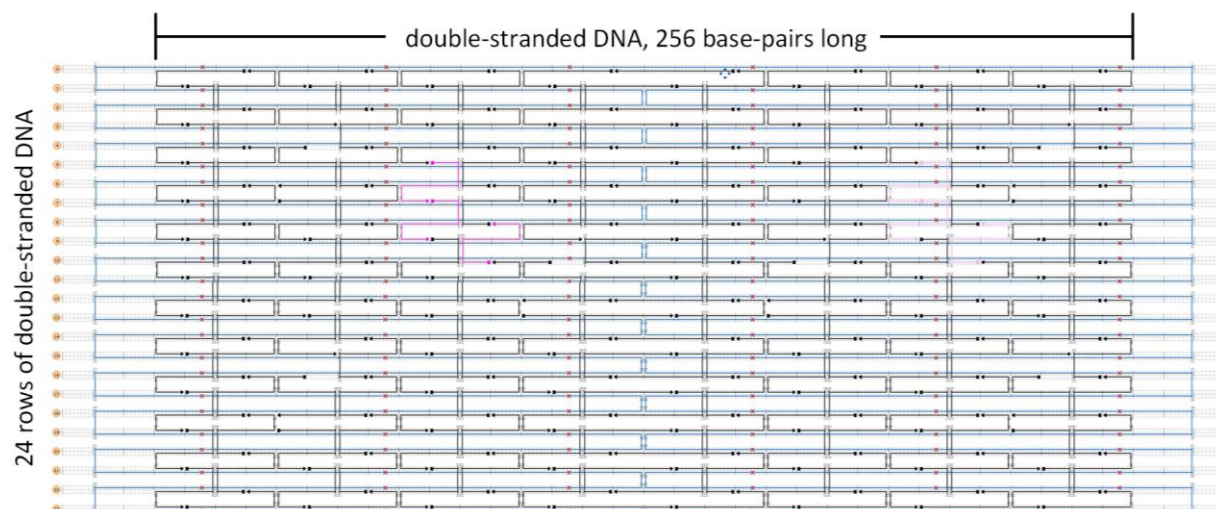


Figure A1: *caDNA*no design of a rectangular DNA origami, which is used for the synthesis of AuNP Dimers. The colored staples in magenta and pink correspond with the staples in Figure A1.

Figure A1 depicts a screenshot of the *caDNA*no-designed DNA origami. The DNA origami was made from an M13mp18 scaffold (the blue line), which was folded into 24 rows of double-stranded DNA (numbered 0 to 23). The unmodified staples are marked in black, while the staples for the AuNP modification are in magenta and pink.

A2: Estimation of Maximum TNB Molecules on an Au DONA

In this section, an estimation was made for the maximum number of TNB molecules that could contribute to the SERS signal of a 60 nm Au DONA in section 5.6. A maximum molecule density of 10 nm^{-2} on the surface of the gold nanoparticle was assumed, based on the investigation conducted by Dileseigres et al.¹⁶¹ Furthermore, it was assumed that half of the molecules were TNB, while the other half consisted of thiolated poly-Thymine ss-DNA strands. The surface area of an Au DONA, calculated from two particles with a diameter of 60 nm, was $22,608 \text{ nm}^2$. Consequently, a maximum load of 113,040 TNB molecules could be accommodated on the surface of an Au DONA.

It is important to note that the SERS enhancement provided by a single TNB-coated 60 nm gold nanoparticle was insufficient for the purpose of SERS detection, based on the results in section 5.6. Therefore, a minimum SERS enhancement factor (SERS-EF) must be established on the Au DONA surface in order to detect a SERS signal. In accordance with this notion, FDTD calculation was employed to determine the highest SERS-EF achievable on an AuNP with a diameter of $d = 60 \text{ nm}$, which was found to be 28 (Figures A2a, A2c). Subsequently, the SERS-EF of an Au DONA was computed, and two regions were identified on its surface that exhibited higher SERS-EF values than 28 (Figure A2d, e). These two regions were visually represented in Figure A2b. The orange region corresponds to the classical plasmonic hot spot, displaying a maximum SERS-EF in the order of 10^5 . Conversely, the blue region exhibits only a slightly higher maximum SERS-EF (105) compared to that of a single AuNP (Figure A2d). The surface areas (S) of the blue and orange regions, defined as spherical caps, were determined using eq. S1, where r denoted the radius of the sphere, and h represents the height of the cap. Specifically, the orange region had a cap height (h) of 3 nm, whereas the blue region had a cap height of 11 nm.

$$S = 2 \cdot \pi \cdot r \cdot h \quad (\text{S1})$$

Consequently, the surface area (S) of the orange region corresponds to 5.0% of the total surface area of the Au DONA, allowing for the potential placement of a maximum of 5,652 TNB molecules. On the other hand, the blue region accounted for 15.0% of the total surface area of the Au DONA, permitting the placement of up to 15,456 TNB molecules. However, considering the relatively low SERS enhancement observed in the blue region, it was deemed insignificant. Thus, the maximum number of TNB molecules that could contribute to the SERS signal of a 60 nm Au DONA is estimated to be approximately 6,000, specifically confined to the orange region in Figure A2b.

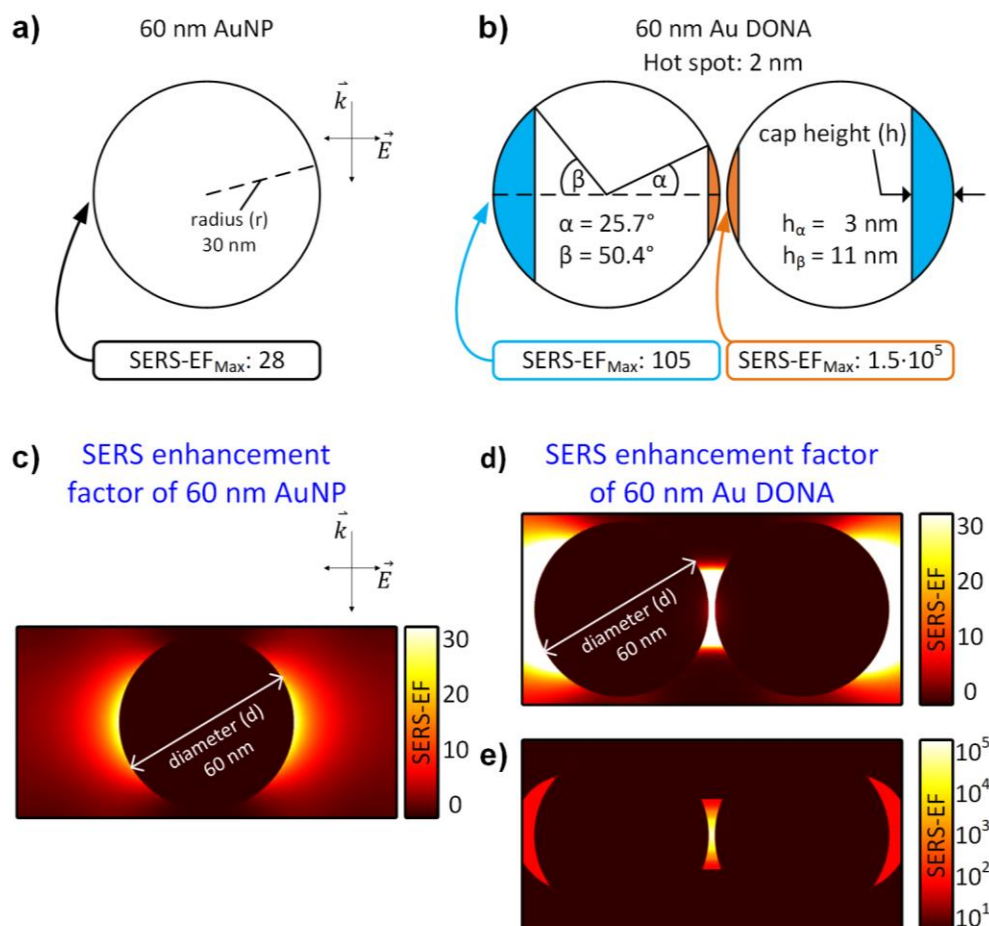


Figure A2: Sketch of the estimated area on an Au DONA which has a higher SERS enhancement factor (b) compared to a single 60 nm gold nanoparticle (a). The vector \vec{k} and \vec{E} showing the orientation of the laser polarization and the direction of propagation, respectively. The plane angles α and β describe the size of the sphere caps in orange and blue, these angles correspond to a solid angle of 0.154 sr (α) and 0.598 sr (β), which was used to calculate the surface area of the sphere cups in 3D. (c) FDTD simulated the SERS enhancement factor of 60 nm gold nanoparticle and (d, e) of 60 nm Au DONA. Note that the color bar for the SERS enhancement factor is from 0 to 30 in (c, d), whereas it has a logarithmic scale and covers a different range for (e). The color scales in (e) is selected in a way that only the areas with a SERS-EF > 28 are visualized.

A3: List of Atoms in the Bader Charge Analysis

Table A2: The Bader charge analysis of atoms from the **TMP** molecule adsorption on the hydrophilic substrate (section 5.2).

Element	Group	Bader charge (<i>e</i>)	Coordinate X-axis (Å)	Coordinate Y-axis (Å)	Coordinate Z-axis (Å)	Element	Group	Bader charge (<i>e</i>)	Coordinate X-axis (Å)	Coordinate Y-axis (Å)	Coordinate Z-axis (Å)
C	C ^{TMP}	0.344	11.636	12.122	26.325	P	P ^{TMP}	3.616	13.363	16.725	25.071
C	C ^{TMP}	-0.026	17.082	18.219	31.345	Si	Si ^{Sub}	0.086	2.584	7.751	12.032
C	C ^{TMP}	0.388	14.731	18.487	29.703	Si	Si ^{Sub}	0.151	2.584	18.085	12.032
C	C ^{TMP}	0.447	12.678	17.518	31.486	Si	Si ^{Sub}	0.154	2.584	28.420	12.032
C	C ^{TMP}	0.772	16.532	15.841	32.928	Si	Si ^{Sub}	0.110	12.918	7.751	12.032
C	C ^{TMP}	-0.009	16.264	19.443	41.636	Si	Si ^{Sub}	0.131	12.918	18.085	12.032
C	C ^{TMP}	1.767	19.658	14.392	36.029	Si	Si ^{Sub}	0.121	12.918	28.420	12.032
C	C ^{TMP}	1.302	19.602	16.217	40.423	Si	Si ^{Sub}	0.140	23.252	7.751	12.032
C	C ^{TMP}	0.334	16.531	17.516	37.295	Si	Si ^{Sub}	0.121	23.252	18.085	12.032
C	C ^{TMP}	0.044	17.415	17.742	39.691	Si	Si ^{Sub}	0.133	23.252	28.420	12.032
H	H ^{Sub}	-0.556	5.167	31.003	6.614	Si	Si ^{Sub}	-0.012	31.003	31.003	14.616
H	H ^{Sub}	-0.559	5.167	10.334	6.614	Si	Si ^{Sub}	0.108	31.003	10.334	14.616
H	H ^{Sub}	-0.560	5.167	20.669	6.614	Si	Si ^{Sub}	-0.020	31.003	20.669	14.616
H	H ^{Sub}	-0.559	15.502	31.003	6.614	Si	Si ^{Sub}	-0.019	10.334	31.003	14.616
H	H ^{Sub}	-0.557	15.502	10.334	6.614	Si	Si ^{Sub}	0.064	10.334	10.334	14.616
H	H ^{Sub}	-0.562	15.502	20.669	6.614	Si	Si ^{Sub}	0.009	10.334	20.669	14.616
H	H ^{Sub}	-0.561	25.836	31.003	6.614	Si	Si ^{Sub}	0.076	20.669	31.003	14.616
H	H ^{Sub}	-0.563	25.836	10.334	6.614	Si	Si ^{Sub}	0.026	20.669	10.334	14.616
H	H ^{Sub}	-0.563	25.836	20.669	6.614	Si	Si ^{Sub}	0.029	20.669	20.669	14.616
H	H ^{Sub}	-0.555	31.003	5.167	6.614	Si	Si ^{Si-O}	0.831	2.474	2.722	17.104
H	H ^{Sub}	-0.558	31.003	15.502	6.614	Si	Si ^{Si-O}	0.618	3.144	12.254	17.159
H	H ^{Sub}	-0.556	31.003	25.836	6.614	Si	Si ^{Si-O}	0.634	3.075	22.606	17.251
H	H ^{Sub}	-0.559	10.334	5.167	6.614	Si	Si ^{Si-O}	0.954	12.637	3.011	17.148
H	H ^{Sub}	-0.562	10.334	15.502	6.614	Si	Si ^{Si-O}	0.998	12.222	13.376	17.420
H	H ^{Sub}	-0.558	10.334	25.836	6.614	Si	Si ^{Si-O}	0.622	13.489	22.640	17.253
H	H ^{Sub}	-0.561	20.669	5.167	6.614	Si	Si ^{Si-O}	0.776	23.369	2.399	17.146
H	H ^{Sub}	-0.562	20.669	15.502	6.614	Si	Si ^{Si-O}	0.880	23.773	12.357	17.113
H	H ^{Sub}	-0.559	20.669	25.836	6.614	Si	Si ^{Si-O}	0.895	23.830	22.647	17.188
H	H ^{TMP}	0.696	16.549	16.537	22.157	Si	Si ^{Sub}	0.430	31.003	5.167	9.449
H	H ^{TMP}	0.079	12.796	11.989	28.041	Si	Si ^{Sub}	0.382	31.003	15.502	9.449
H	H ^{TMP}	0.086	9.765	11.313	26.675	Si	Si ^{Sub}	0.398	31.003	25.836	9.449
H	H ^{TMP}	0.078	12.537	11.168	24.727	Si	Si ^{Sub}	0.410	10.334	5.167	9.449
H	H ^{TMP}	0.100	14.371	20.415	29.032	Si	Si ^{Sub}	0.386	10.334	15.502	9.449
H	H ^{TMP}	0.113	17.359	14.139	32.085	Si	Si ^{Sub}	0.397	10.334	25.836	9.449
H	H ^{TMP}	0.076	18.809	18.029	30.223	Si	Si ^{Sub}	0.382	20.669	5.167	9.449
H	H ^{TMP}	0.057	17.268	19.884	32.570	Si	Si ^{Sub}	0.389	20.669	15.502	9.449
H	H ^{TMP}	0.053	11.042	16.689	30.520	Si	Si ^{Sub}	0.390	20.669	25.836	9.449
H	H ^{TMP}	0.034	12.012	19.105	32.670	Si	Si ^{Si-O}	0.829	7.928	7.636	17.102
H	H ^{TMP}	0.472	22.046	13.560	38.927	Si	Si ^{Si-O}	0.674	8.451	17.405	17.336
H	H ^{TMP}	0.076	14.874	18.559	36.659	Si	Si ^{Si-O}	0.605	8.437	27.904	17.310
H	H ^{TMP}	0.053	15.627	18.350	43.283	Si	Si ^{Si-O}	0.870	18.477	7.393	17.053
H	H ^{TMP}	0.048	17.663	20.802	42.346	Si	Si ^{Si-O}	0.898	17.741	18.699	17.158
H	H ^{TMP}	0.025	14.648	20.487	40.865	Si	Si ^{Si-O}	0.719	18.359	28.221	17.050
Mg	Mg	1.612	3.595	7.551	19.799	Si	Si ^{Si-O}	0.730	28.099	8.105	17.054
Mg	Mg	1.684	13.821	8.072	20.057	Si	Si ^{Si-O}	0.952	27.585	18.780	17.139
Mg	Mg	1.642	24.498	6.693	20.224	Si	Si ^{Si-O}	0.796	27.928	28.784	17.159
Mg	Mg	1.565	3.796	17.677	19.482	Si	Si ^{Sub}	0.438	5.167	31.003	9.449
Mg	Mg	1.687	10.404	20.632	21.457	Si	Si ^{Sub}	0.397	5.167	10.334	9.449
Mg	Mg	1.686	22.946	16.946	20.133	Si	Si ^{Sub}	0.424	5.167	20.669	9.449
Mg	Mg	1.602	3.282	27.792	19.432	Si	Si ^{Sub}	0.408	15.502	31.003	9.449
Mg	Mg	1.576	13.109	27.257	19.399	Si	Si ^{Sub}	0.388	15.502	10.334	9.449
Mg	Mg	1.560	23.983	27.054	19.987	Si	Si ^{Sub}	0.392	15.502	20.669	9.449
N	N ^{TMP}	-1.143	17.567	15.932	35.496	Si	Si ^{Sub}	0.368	25.836	31.003	9.449
N	N ^{TMP}	-1.157	20.521	14.641	38.483	Si	Si ^{Sub}	0.380	25.836	10.334	9.449
O	O ^{Si-O}	-1.517	1.783	4.373	19.575	Si	Si ^{Sub}	0.385	25.836	20.669	9.449
O	O ^{Si-O}	-1.541	2.575	14.210	19.565	Si	Si ^{Sub}	0.139	7.751	2.584	12.032

APPENDIX

Element	Group	Bader charge (<i>e</i>)	Coordinate X-axis (Å)	Coordinate Y-axis (Å)	Coordinate Z-axis (Å)	Element	Group	Bader charge (<i>e</i>)	Coordinate X-axis (Å)	Coordinate Y-axis (Å)	Coordinate Z-axis (Å)
O	O ^{Si-O}	-1.554	2.104	24.405	19.622	Si	Si ^{Sub}	0.145	7.751	12.918	12.032
O	O ^{Si-O}	-1.514	12.225	4.687	19.657	Si	Si ^{Sub}	0.176	7.751	23.252	12.032
O	O ^{Si-O}	-1.537	12.817	11.574	19.842	Si	Si ^{Sub}	0.137	18.085	2.584	12.032
O	O ^{Si-O}	-1.645	12.446	23.469	20.175	Si	Si ^{Sub}	0.137	18.085	12.918	12.032
O	O ^{Si-O}	-1.567	22.951	3.445	20.019	Si	Si ^{Sub}	0.138	18.085	23.252	12.032
O	O ^{Si-O}	-1.542	23.017	13.292	19.926	Si	Si ^{Sub}	0.112	28.420	2.584	12.032
O	O ^{Si-O}	-1.562	23.221	23.530	20.065	Si	Si ^{Sub}	0.127	28.420	12.918	12.032
O	O ^{Si-O}	-1.541	7.291	7.612	20.079	Si	Si ^{Sub}	0.135	28.420	23.252	12.032
O	O ^{Si-O}	-1.643	7.594	18.509	20.221	Si	Si ^{Sub}	-0.064	5.167	5.167	14.616
O	O ^{Si-O}	-1.554	6.664	28.992	19.670	Si	Si ^{Sub}	-0.088	5.167	15.502	14.616
O	O ^{Si-O}	-1.528	17.471	7.960	19.870	Si	Si ^{Sub}	-0.200	5.167	25.836	14.616
O	O ^{Si-O}	-1.538	19.148	17.772	19.807	Si	Si ^{Sub}	-0.064	15.502	5.167	14.616
O	O ^{Si-O}	-1.531	16.222	29.192	19.175	Si	Si ^{Sub}	0.013	15.502	15.502	14.616
O	O ^{Si-O}	-1.548	28.018	7.587	20.092	Si	Si ^{Sub}	-0.110	15.502	25.836	14.616
O	O ^{Si-O}	-1.528	26.592	18.066	19.980	Si	Si ^{Sub}	-0.040	25.836	5.167	14.616
O	O ^{Si-O}	-1.543	27.517	28.258	20.150	Si	Si ^{Sub}	-0.059	25.836	15.502	14.616
O	O ^{TMP}	-1.415	15.121	15.595	22.996	Si	Si ^{Sub}	-0.065	25.836	25.836	14.616
O	O ^{TMP}	-1.284	11.200	14.745	25.642						
O	O ^{TMP}	-1.501	12.075	19.199	24.445						
O	O ^{TMP}	-1.289	15.131	16.874	27.507						
O	O ^{TMP}	-0.993	13.832	15.598	33.019						
O	O ^{TMP}	-1.147	20.643	12.985	34.473						
O	O ^{TMP}	-1.105	20.621	16.228	42.505						

Table A3: The Bader charge analysis of atoms from the **TMP molecule adsorption** on the **hydrophobic** substrate (section 5.2).

Element	Group	Bader charge (<i>e</i>)	Coordinate X-axis (Å)	Coordinate Y-axis (Å)	Coordinate Z-axis (Å)	Element	Group	Bader charge (<i>e</i>)	Coordinate X-axis (Å)	Coordinate Y-axis (Å)	Coordinate Z-axis (Å)
C	C ^{CH3}	-0.731	2.692	2.690	20.795	H	H ^{Sub}	-0.560	20.669	5.167	6.614
C	C ^{CH3}	-0.720	2.639	13.114	20.791	H	H ^{Sub}	-0.560	20.669	15.502	6.614
C	C ^{CH3}	-0.731	2.672	23.309	20.795	H	H ^{Sub}	-0.560	20.669	25.836	6.614
C	C ^{CH3}	-0.740	12.931	2.708	20.797	H	H ^{CH3}	0.009	8.896	29.728	21.621
C	C ^{CH3}	-0.746	12.848	13.288	20.779	H	H ^{CH3}	0.029	8.021	26.490	21.529
C	C ^{CH3}	-0.716	12.946	23.424	20.792	H	H ^{CH3}	0.057	5.655	28.871	21.428
C	C ^{CH3}	-0.781	23.428	2.736	20.787	H	H ^{CH3}	0.007	18.758	30.058	21.620
C	C ^{CH3}	-0.696	23.384	12.709	20.787	H	H ^{CH3}	0.039	18.250	26.731	21.637
C	C ^{CH3}	-0.736	23.490	22.880	20.770	H	H ^{CH3}	0.040	15.659	28.822	21.229
C	C ^{CH3}	-0.738	7.625	7.630	20.793	H	H ^{CH3}	0.038	29.822	29.730	21.512
C	C ^{CH3}	-0.707	7.506	18.048	20.788	H	H ^{CH3}	0.034	28.906	26.502	21.524
C	C ^{CH3}	-0.715	7.566	28.374	20.793	H	H ^{CH3}	0.042	26.562	28.921	21.557
C	C ^{CH3}	-0.740	18.362	7.589	20.780	H	H ^{CH3}	0.045	25.124	23.926	21.499
C	C ^{CH3}	-0.705	18.001	18.213	20.793	H	H ^{CH3}	0.028	23.730	20.877	21.256
C	C ^{CH3}	-0.720	17.658	28.521	20.770	H	H ^{CH3}	0.026	21.781	23.573	21.723
C	C ^{CH3}	-0.745	28.273	7.656	20.791	H	H ^{CH3}	0.032	11.526	22.154	21.604
C	C ^{CH3}	-0.721	28.330	17.975	20.794	H	H ^{CH3}	0.014	12.528	25.352	21.428
C	C ^{CH3}	-0.723	28.418	28.384	20.799	H	H ^{CH3}	0.036	14.802	22.887	21.544
Si	Si ^{Sub}	0.134	2.584	7.751	12.032	H	H ^{CH3}	0.022	1.530	21.766	21.575
Si	Si ^{Sub}	0.166	2.584	18.085	12.032	H	H ^{CH3}	0.036	1.934	25.102	21.531
Si	Si ^{Sub}	0.197	2.584	28.420	12.032	H	H ^{CH3}	0.056	4.615	23.082	21.479
Si	Si ^{Sub}	0.135	12.918	7.751	12.032	H	H ^{CH3}	0.024	8.733	19.480	21.643
Si	Si ^{Sub}	0.165	12.918	18.085	12.032	H	H ^{CH3}	0.031	8.046	16.195	21.544
Si	Si ^{Sub}	0.198	12.918	28.420	12.032	H	H ^{CH3}	0.020	5.555	18.437	21.370
Si	Si ^{Sub}	0.197	23.252	7.751	12.032	H	H ^{CH3}	0.031	19.339	19.646	21.464
Si	Si ^{Sub}	0.198	23.252	18.085	12.032	H	H ^{CH3}	-0.003	18.529	16.387	21.625
Si	Si ^{Sub}	0.136	23.252	28.420	12.032	H	H ^{CH3}	0.054	16.109	18.711	21.482
Si	Si ^{Sub}	0.157	31.003	31.003	14.616	H	H ^{CH3}	0.026	29.499	19.476	21.610
Si	Si ^{Sub}	0.162	31.003	10.334	14.616	H	H ^{CH3}	0.048	29.018	16.148	21.495
Si	Si ^{Sub}	0.159	31.003	20.669	14.616	H	H ^{CH3}	0.030	26.391	18.238	21.483
Si	Si ^{Sub}	0.158	10.334	31.003	14.616	H	H ^{CH3}	0.034	24.885	13.939	21.513

APPENDIX

Element	Group	Bader charge (e)	Coordinate X-axis (Å)	Coordinate Y-axis (Å)	Coordinate Z-axis (Å)	Element	Group	Bader charge (e)	Coordinate X-axis (Å)	Coordinate Y-axis (Å)	Coordinate Z-axis (Å)
Si	Si ^{Sub}	0.163	10.334	10.334	14.616	H	H ^{CH3}	0.005	23.794	10.767	21.389
Si	Si ^{Sub}	0.159	10.334	20.669	14.616	H	H ^{CH3}	0.021	21.583	13.274	21.648
Si	Si ^{Sub}	0.166	20.669	31.003	14.616	H	H ^{CH3}	0.043	11.304	12.189	21.616
Si	Si ^{Sub}	0.145	20.669	10.334	14.616	H	H ^{CH3}	0.065	12.570	15.282	21.277
Si	Si ^{Sub}	0.149	20.669	20.669	14.616	H	H ^{CH3}	0.025	14.634	12.655	21.625
Si	Si ^{CH3}	0.454	2.584	2.584	17.199	H	H ^{CH3}	0.019	1.217	11.863	21.630
Si	Si ^{CH3}	0.456	2.584	12.918	17.199	H	H ^{CH3}	0.047	2.244	15.053	21.411
Si	Si ^{CH3}	0.457	2.584	23.252	17.199	H	H ^{CH3}	0.033	4.500	12.572	21.526
Si	Si ^{CH3}	0.449	12.918	2.584	17.199	H	H ^{CH3}	0.044	9.024	8.906	21.635
Si	Si ^{CH3}	0.447	12.918	12.918	17.199	H	H ^{CH3}	0.032	8.020	5.708	21.464
Si	Si ^{CH3}	0.459	12.918	23.252	17.199	H	H ^{CH3}	0.040	5.744	8.177	21.474
Si	Si ^{CH3}	0.470	23.252	2.584	17.199	H	H ^{CH3}	0.042	17.222	6.024	21.516
Si	Si ^{CH3}	0.438	23.252	12.918	17.199	H	H ^{CH3}	0.026	17.733	9.352	21.675
Si	Si ^{CH3}	0.464	23.252	23.252	17.199	H	H ^{CH3}	0.017	20.335	7.270	21.334
Si	Si ^{Sub}	0.380	31.003	5.167	9.449	H	H ^{CH3}	0.011	29.537	9.067	21.627
Si	Si ^{Sub}	0.393	31.003	15.502	9.449	H	H ^{CH3}	0.053	28.810	5.784	21.501
Si	Si ^{Sub}	0.398	31.003	25.836	9.449	H	H ^{CH3}	0.051	26.347	8.054	21.449
Si	Si ^{Sub}	0.381	10.334	5.167	9.449	H	H ^{CH3}	0.037	22.206	1.318	21.675
Si	Si ^{Sub}	0.362	10.334	15.502	9.449	H	H ^{CH3}	0.051	22.841	4.608	21.464
Si	Si ^{Sub}	0.356	10.334	25.836	9.449	H	H ^{CH3}	0.051	25.376	2.418	21.421
Si	Si ^{Sub}	0.372	20.669	5.167	9.449	H	H ^{CH3}	0.023	11.443	1.491	21.568
Si	Si ^{Sub}	0.396	20.669	15.502	9.449	H	H ^{CH3}	0.061	12.588	4.644	21.460
Si	Si ^{Sub}	0.388	20.669	25.836	9.449	H	H ^{CH3}	0.037	14.750	2.066	21.559
Si	Si ^{CH3}	0.457	7.751	7.751	17.199	H	H ^{CH3}	0.030	1.375	1.320	21.615
Si	Si ^{CH3}	0.456	7.751	18.085	17.199	H	H ^{CH3}	0.044	2.177	4.575	21.490
Si	Si ^{CH3}	0.460	7.751	28.420	17.199	H	H ^{CH3}	0.044	4.597	2.244	21.482
Si	Si ^{CH3}	0.453	18.085	7.751	17.199	Mg	Mg	0.031	2.128	8.546	27.912
Si	Si ^{CH3}	0.453	18.085	18.085	17.199	Mg	Mg	0.068	15.649	8.016	27.939
Si	Si ^{CH3}	0.466	18.085	28.420	17.199	Mg	Mg	0.052	21.437	9.627	27.713
Si	Si ^{CH3}	0.451	28.420	7.751	17.199	Mg	Mg	0.004	5.555	19.778	27.713
Si	Si ^{CH3}	0.449	28.420	18.085	17.199	Mg	Mg	0.187	10.069	21.580	31.047
Si	Si ^{CH3}	0.451	28.420	28.420	17.199	Mg	Mg	0.088	21.126	15.785	28.621
Si	Si ^{Sub}	0.398	5.167	31.003	9.449	Mg	Mg	0.000	5.994	25.424	29.398
Si	Si ^{Sub}	0.406	5.167	10.334	9.449	Mg	Mg	0.006	11.593	26.172	27.682
Si	Si ^{Sub}	0.363	5.167	20.669	9.449	Mg	Mg	0.025	21.631	27.115	27.852
Si	Si ^{Sub}	0.368	15.502	31.003	9.449	C	C ^{TMP}	0.372	11.603	12.159	34.847
Si	Si ^{Sub}	0.414	15.502	10.334	9.449	C	C ^{TMP}	-0.022	17.060	18.390	39.779
Si	Si ^{Sub}	0.421	15.502	20.669	9.449	C	C ^{TMP}	0.406	14.785	18.473	38.040
Si	Si ^{Sub}	0.380	25.836	31.003	9.449	C	C ^{TMP}	0.433	12.708	17.510	39.789
Si	Si ^{Sub}	0.369	25.836	10.334	9.449	C	C ^{TMP}	0.798	16.588	15.996	41.337
Si	Si ^{Sub}	0.358	25.836	20.669	9.449	C	C ^{TMP}	0.008	16.195	19.460	50.077
Si	Si ^{Sub}	0.167	7.751	2.584	12.032	C	C ^{TMP}	1.721	19.645	14.464	44.454
Si	Si ^{Sub}	0.198	7.751	12.918	12.032	C	C ^{TMP}	1.316	19.513	16.183	48.890
Si	Si ^{Sub}	0.197	7.751	23.252	12.032	C	C ^{TMP}	0.297	16.561	17.631	45.713
Si	Si ^{Sub}	0.196	18.085	2.584	12.032	C	C ^{TMP}	0.061	17.383	17.778	48.136
Si	Si ^{Sub}	0.133	18.085	12.918	12.032	H	H ^{TMP}	0.572	16.678	15.981	30.918
Si	Si ^{Sub}	0.166	18.085	23.252	12.032	H	H ^{TMP}	0.072	12.738	12.088	36.581
Si	Si ^{Sub}	0.200	28.420	2.584	12.032	H	H ^{TMP}	0.073	9.721	11.363	35.175
Si	Si ^{Sub}	0.197	28.420	12.918	12.032	H	H ^{TMP}	0.056	12.545	11.145	33.306
Si	Si ^{Sub}	0.166	28.420	23.252	12.032	H	H ^{TMP}	0.082	14.393	20.350	37.267
Si	Si ^{Sub}	0.160	5.167	5.167	14.616	H	H ^{TMP}	0.117	17.464	14.335	40.464
Si	Si ^{Sub}	0.156	5.167	15.502	14.616	H	H ^{TMP}	0.064	18.860	18.336	38.769
Si	Si ^{Sub}	0.159	5.167	25.836	14.616	H	H ^{TMP}	0.047	17.027	20.077	40.984
Si	Si ^{Sub}	0.169	15.502	5.167	14.616	H	H ^{TMP}	0.066	11.132	16.605	38.798
Si	Si ^{Sub}	0.159	15.502	15.502	14.616	H	H ^{TMP}	0.037	11.939	19.108	40.896
Si	Si ^{Sub}	0.155	15.502	25.836	14.616	H	H ^{TMP}	0.497	21.942	13.508	47.392
Si	Si ^{Sub}	0.157	25.836	5.167	14.616	H	H ^{TMP}	0.083	14.932	18.706	45.063
Si	Si ^{Sub}	0.167	25.836	15.502	14.616	H	H ^{TMP}	0.065	15.506	18.354	51.693
Si	Si ^{Sub}	0.169	25.836	25.836	14.616	H	H ^{TMP}	0.035	17.575	20.813	50.839
H	H ^{Sub}	-0.561	5.167	31.003	6.614	H	H ^{TMP}	0.008	14.607	20.524	49.277
H	H ^{Sub}	-0.560	5.167	10.334	6.614	N	N ^{TMP}	-1.124	17.612	16.072	43.900
H	H ^{Sub}	-0.561	5.167	20.669	6.614	N	N ^{TMP}	-1.157	20.446	14.629	46.935

Element	Group	Bader charge (e)	Coordinate X-axis (Å)	Coordinate Y-axis (Å)	Coordinate Z-axis (Å)	Element	Group	Bader charge (e)	Coordinate X-axis (Å)	Coordinate Y-axis (Å)	Coordinate Z-axis (Å)
H	H ^{Sub}	-0.560	15.502	31.003	6.614	O	O ^{TMP}	-1.405	15.110	15.139	31.527
H	H ^{Sub}	-0.559	15.502	10.334	6.614	O	O ^{TMP}	-1.294	11.201	14.766	34.093
H	H ^{Sub}	-0.560	15.502	20.669	6.614	O	O ^{TMP}	-1.549	12.443	19.153	32.797
H	H ^{Sub}	-0.559	25.836	31.003	6.614	O	O ^{TMP}	-1.286	15.294	16.740	35.946
H	H ^{Sub}	-0.560	25.836	10.334	6.614	O	O ^{TMP}	-1.021	13.888	15.675	41.406
H	H ^{Sub}	-0.559	25.836	20.669	6.614	O	O ^{TMP}	-1.137	20.627	13.068	42.888
H	H ^{Sub}	-0.560	31.003	5.167	6.614	O	O ^{TMP}	-1.108	20.475	16.116	50.996
H	H ^{Sub}	-0.560	31.003	15.502	6.614	P	P ^{TMP}	3.604	13.472	16.626	33.537
H	H ^{Sub}	-0.560	31.003	25.836	6.614						
H	H ^{Sub}	-0.559	10.334	5.167	6.614						
H	H ^{Sub}	-0.560	10.334	15.502	6.614						
H	H ^{Sub}	-0.561	10.334	25.836	6.614						

A4: Single Molecule Detection with Star DONAs

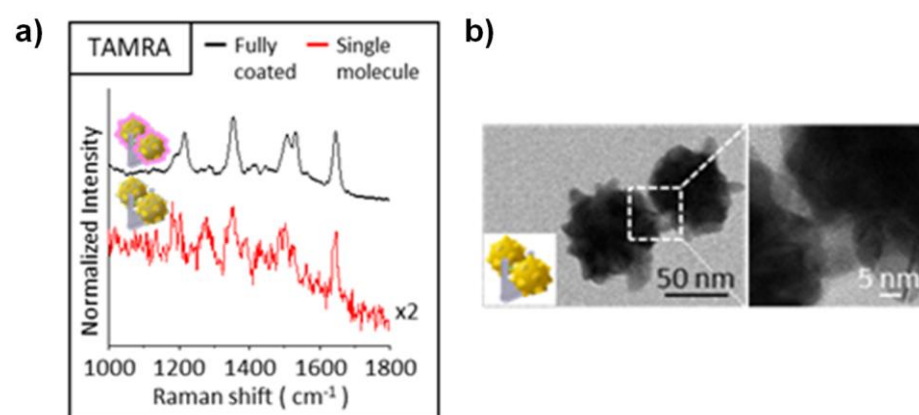


Figure A4: (a) SERS signals comparison between fully TAMRA-coated Star DONAs (black) and Star DONAs functionalized with a single TAMRA molecule (red). (b) High-resolution transmission electron microscopy (HRTEM) images of the Star DONAs.

Figure A4 presents data from an upcoming publication of Yuya Kanehira, a Ph.D. student from Prof. Ilko Bald's group at Uni Potsdam. Yuya successfully incorporated a single TAMRA molecule into the plasmonic hotspot of a Star DONA (depicted in Figure 34b) and showed a single-molecule SERS spectrum from this structure (red spectrum in Figure A4a). The structure of a Star DONA is depicted with high-resolution TEM in Figure A4b.

A5: Time Series of $^{14}\text{N-TNB}$ and $^{15}\text{N-TNB}$ coated Au DONA

Raman time series of a single $^{14}\text{N-TNB}$ and $^{15}\text{N-TNB}$ coated Au DONA

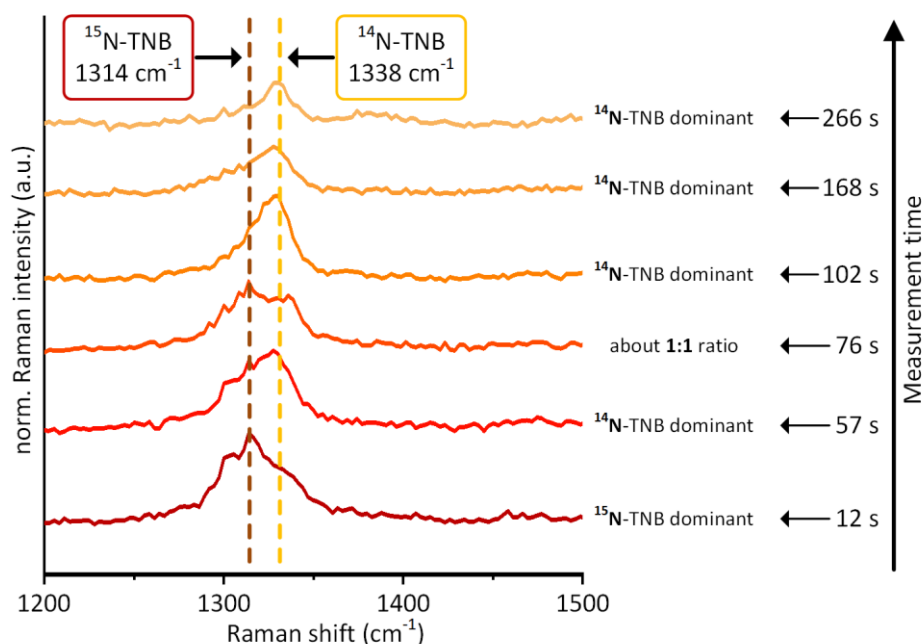


Figure A5: The Raman time series of a single Au DONA with $^{14}\text{N-TNB}$ and $^{15}\text{N-TNB}$ coating. The typical Raman shift of $^{14}\text{N-TNB}$ and $^{15}\text{N-TNB}$ were marked with dash lines.

In Figure A5, we present a Raman time series of an Au DONA composed of both $^{14}\text{N-TNB}$ coated AuNP and $^{15}\text{N-TNB}$ coated AuNP (the same sample as shown in Figure 41d and Figure 43). This result was obtained by Yuya Kanehira, a Ph.D. student from Prof. Ilko Bald's group at Uni Potsdam. The Raman time series was obtained by utilizing a confocal Raman spectroscope to collect the SERS signal of a single, isolated Au DONA over a 300-second period. During this time, a SERS spectrum was recorded every second.

At second 12, the dominant signal originates from $^{15}\text{N-TNB}$. However, as time progresses, the signal ratio between $^{15}\text{N-TNB}$ and $^{14}\text{N-TNB}$ undergoes multiple changes, and eventually, at second 266, only the $^{14}\text{N-TNB}$ signal remains observable. This indicates a change in TNB composition within the plasmonic hot spot, as mentioned in section 5.6.

Acknowledgments

An dieser Stelle möchte ich meine aufrichtige Dankbarkeit gegenüber allen, die in vielfältiger Weise zur Entstehung dieser Dissertation beigetragen haben, zum Ausdruck bringen.

Ein besonderer Dank gebührt Dr. Rainer Stosch und Stefan Wundrack für ihre hervorragende Betreuung während des gesamten Forschungsprozesses. Ebenso möchte ich meinen tiefen Dank an Prof. Christoph Jacob, Prof. Ilko Bald und Prof. Peter Walla aussprechen, die die Referate übernommen haben. Herzlicher Dank gilt auch Prof. Gavin O'Connor und Prof. Stefanie Tschierlei für ihre Beteiligung im Prüfungskomitee und ihr Interesse an dieser Forschung.

Dr. Julia Molle und Dr. Birka Lalkens danke ich herzlich für ihre einführende Unterstützung im Bereich DNA-Origami. Besonders loben möchte ich Stefan Wundrack, der mich in die faszinierende Welt der Raman-Spektroskopie und DFT-Simulationen eingeführt hat.

Mein Dank gilt auch Dr. Markus Etzkorn und Zhe Liu für unsere gemeinsame Entwicklung des Polar Surface Arrays. Ebenso gebührt der Arbeitsgruppe von Prof. Ilko Bald, insbesondere Dr. Sergio Kogikoski Jr. und Yuya Kanehira, großer Dank für die großzügige Bereitstellung der Au DONA und ihre wertvollen Diskussionen zur experimentellen Arbeit.

Ich möchte mich auch bei den Reinräumen des Instituts für Halbleitertechnik der TU Braunschweig und der PTB für die Möglichkeit bedanken, meine Arbeiten dort durchzuführen. Ebenso danke ich dem Rechencluster der PTB für die technische Unterstützung bei den DFT-Simulationen. Herzlicher Dank geht an die verschiedenen Arbeitsgruppen der PTB-Abteilungen 3, 4 und 5 sowie in LENA für ihre fachliche Unterstützung und inspirierende Zusammenarbeit.

Die Finanzierung dieser Forschungsarbeit erfolgte durch das DFG-Projekt GRK 1952 Metrologie komplexer Nanosysteme (NanoMet) und die Physikalisch-Technische Bundesanstalt. Die Graduiertenschule B-IGSM und GradTUBS möchte ich herzlich für die breite Palette an bereichernden Workshops danken, die meine persönliche Entwicklung neben dem Fachlichen gefördert haben.

Abschließend möchte ich meinen Eltern und meiner Freundin meinen tiefsten Dank aussprechen. Ihre bedingungslose Unterstützung, ihr Verständnis und ihre Geduld haben mich auf diesem Weg begleitet und gestärkt.

Curriculum Vitae

Personal Information

Name Zunhao Wang

Date of birth 25 April 1995

Work Experience

06/2016 – 12/2023 Research Associate at the Physikalisch-Technische Bundesanstalt (PTB)

01/2018 – 05/2018 Research internship at Bangor University in Prof. I. F. Perepichka's group

Education

06/2016 – 12/2023 Ph.D. in Chemistry at the Physikalisch-Technische Bundesanstalt (PTB)
Thesis: Surface-controlled adsorption of plasmonic DNA origami nanostructures for single-molecule surface-enhanced Raman Spectroscopy (SERS)
Supervisors: Prof. Christoph R. Jacob, Prof. Gavin O'Connor, Dr. Rainer Stosch

10/2016 – 05/2019 M.Sc. in Material chemistry und Nanochemistry at Leibniz Universität Hannover
Thesis: Wechselwirkung von plasmonischen Nanostrukturen und Halbleiter-Nanopartikeln
Supervisor: PD. Dr. Dirk Dorfs

10/2013 – 09/2016 Bachelor of Science in Dual Major Bachelor's Degree Chemistry/Physics at Universität Osnabrück
Thesis: Der Einfluss der Edukte bei der Synthese von KNbO_3
Supervisor: Dr. Karsten Kömpe

List of publications

Maurer, V., Zarinwall, A., **Wang, Z.**, Wundrack, S., Wundrack, N., Ag Seleci, D., Helm, V., Otenko, D., Frank, C., Schaper, F., Stosch, R., Garnweitner, G.: All-in-One Superparamagnetic and SERS-Active Niosomes for Dual-Targeted in Vitro Detection of Breast Cancer Cells. *Sensors & Diagnostics* **2022**, 1 (3), 469–484. DOI: 10.1039/d2sd00020b.

Syring, A., **Wang, Z.**, Molle, J., Keese, H., Wundrack, S., Stosch, R., Voss, T.: Confocal Raman Microscopy for the Analysis of the Three-Dimensional Shape of Polymeric Microsphere Layers. *Appl. Spectrosc.* **2022**, 76 (6), 678–688. DOI: 10.1177/00037028211067827.

Syring, A., **Wang, Z.**, Wundrack, S., Stosch, R., Voss, T.: Optical Tomography of Polymeric Microsphere Layers Using Confocal Raman Microscopy. *Appl. Spectrosc.* **2023**, 77 (7), 744–752. DOI: 10.1177/00037028231175922

Liu, Z., **Wang, Z.**, Guckel, J., Park, D., Lalkens, B., Stosch, R., Etzkorn, M.: Positional Control of DNA Origami based Gold Dimer Hybrid Nanostructures on Pre-Structured Surfaces. *Nanotechnology* **2023**, 34 425301, DOI: 10.1088/1361-6528/ace726.

Wang, Z., Liu, Z., Dempwolf, W., Molle, J., Kanehira, Y., Kogikoski Jr, S., Etzkorn, M., Bald, I., Stosch, R., Wundrack, S.: Surface Enhanced Raman Spectroscopy on Selective Adsorbed Plasmonic Nanostructures Using Polar Surface Arrays. *ACS Appl. Nano Mater.* **2023**, 6 (16), 14645-14655. DOI: 10.1021/acsnm.3c01776.



Herausgeber:

Physikalisch-Technische Bundesanstalt
ISNI: 0000 0001 2186 1887

Presse und Öffentlichkeitsarbeit

Bundesallee 100
38116 Braunschweig

Telefon: (05 31) 592-93 21
Telefax: (05 31) 592-92 92
www.ptb.de